The dissertation committee for Kerry Lynn Kreitman certifies that
this is the approved version of the following dissertation:

STRENGTHENING CONTINUOUS STEEL GIRDER BRIDGES WITH POST-INSTALLED SHEAR CONNECTORS AND INELASTIC MOMENT REDISTRIBUTION

Committee:

Michael D. Engelhardt, Co-Supervisor

Todd A. Helwig, Co-Supervisor

Eric B. Williamson

James O. Jirsa

Stelios Kyriakides

STRENGTHENING CONTINUOUS STEEL GIRDER BRIDGES WITH POST-INSTALLED SHEAR CONNECTORS AND INELASTIC MOMENT REDISTRIBUTION

by

Kerry Lynn Kreitman, B.S.C.E., M.S.E.

Dissertation

Presented to the Faculty of the Graduate School of

The University of Texas at Austin

in Partial Fulfillment

of the Requirements

for the Degree of

Doctor of Philosophy

The University of Texas at Austin

December 2016

Dedication

To my parents and sister, for their unconditional love and support in everything

Acknowledgements

First, I'd like to extend appreciation to the Texas Department of Transportation, particularly Yuan Zhao, Leon Flournoy, and Darrin Jenson, for providing the funding for this research and guidance along the way. I would also like to thank the faculty members involved with the research, Dr. Mike Engelhardt, Dr. Todd Helwig, and Dr. Eric Williamson, for their support and direction for the past five years. Additionally, I would like to thank my other committee members, Dr. Jim Jirsa and Dr. Stelios Kyriakides for their input and involvement, as well as Dr. Rich Klingner for his involvement in the early stages of the project.

I was lucky enough to get to work with Hemal Patel for a portion of this project, who is the best research partner I could have ever asked for, as well as a good friend. Hemal, I miss you and our weekly tennis matches, even though Kelly and Zach always beat us… Also, thanks to Amir Ghiami Azad, who picked up the research where Hemal left off. Of the several undergraduate students that helped out with the lab work, I'd like to extend a special thanks to Nick Kratkiewicz and Kyle Kishiyama for their hard work. Additionally, I greatly appreciate the help of all of the students at FSEL who leant a helping hand from time to time, especially during concrete pours. In particular, I'd like to thank Hossein Yousefpour for sharing his knowledge and giving advice on any and all topics.

The FSEL lab technicians were also vital to the success of this project. Special thanks goes to Blake Stasney and David Braley for putting up with me all the time. Additional thanks to Dennis Fillip, John Bacon and Joel Arredondo who do a great job of making the lab run smoothly. I must also thank the FSEL staff, namely Deanna Mueller and Michelle Damvar not only for their general assistance on everything administrative, but also for keeping me sane whenever I needed a break. Also, thanks to Mike Brown, whose motivational efforts ("Are you done yet? Do you have a job yet?") cannot be discounted.

Finally, I'd like to thank my family for their continued support throughout all aspects of my life. I would not be here without you guys and don't have the words to adequately express my thanks for everything…

August 20, 2016

STRENGTHENING CONTINUOUS STEEL GIRDER BRIDGES WITH POST-INSTALLED SHEAR CONNECTORS AND INELASTIC MOMENT REDISTRIBUTION

Kerry Lynn Kreitman, Ph.D.

The University of Texas at Austin, 2016

Co-Supervisor: Michael D. Engelhardt

Co-Supervisor: Todd A. Helwig

Many continuous steel bridges constructed prior to the 1970s have floor systems consisting of a non-composite concrete deck over steel beams with no shear connectors. While many of these bridges are still in good condition, the structures may not satisfy current load requirements and thus may need to be strengthened or replaced to avoid load-posting and to maintain structural safety. One potentially economical method of extending the service life of such bridges is to post-install adhesive anchor shear connectors to create composite action between the existing steel beams and concrete deck. This is efficient in regions dominated by positive flexural demands where the concrete deck is in compression. Inelastic moment redistribution away from the interior pier sections can be considered to address strength deficiencies in these regions, which are dominated by negative flexural demands.

This dissertation explores this method of strengthening continuous non-composite steel girder bridges. Of particular interest is the "shakedown" behavior of partially composite strengthened girders under large repeated loads requiring moment redistribution. These concepts are commonly referred to as "autostress" design. After conducting preliminary studies on the feasibility of this strengthening method for typical bridges in the state of Texas, an extensive large-scale experimental program was conducted in conjunction with finite element modeling. The results of the testing and modeling are discussed in detail. Design recommendations and a design example are also provided.

Table of Contents

CHAPTER 1: INTRODUCTION **1**

1.1 Overview 1

1.2 Objectives of Research 2

1.3 Scope of Dissertation 3

CHAPTER 2: BACKGROUND **4**

2.1 Overview 4

2.2 Composite Behavior 4

2.2.1 Full and Partial-Composite Behavior 4

2.2.2 Strength of Composite Girders 5

Interface Shear Force 6

Efficiency of Partial-Composite Behavior 8

2.2.3 Stiffness of Composite Girders 9

2.3 Post-Installed Shear Connectors 10

2.3.1 Types of Post-Installed Connectors Developed Previously 10

2.3.2 Previous Research at the University of Texas at Austin 12

Small-Scale Static and Fatigue Testing 14

Large-Scale Girder Testing 16

Implementation 17

2.4 Moment Redistribution and Shakedown 18

2.4.1 Shakedown Behavior 18

Illustrative Example 20

2.4.2 Shakedown Theorems 25

Upper-Bound Theorem Example 26

Lower-Bound Theorem Example 27

2.4.3 Previous Research on Shakedown of Steel and Composite Girders 30

2.5 Applicable AASHTO Design Provisions....31
2.5.1 Shear Connector Design....31
Fatigue Design....32
Strength Design....33
Other Requirements....33
2.5.2 Inelastic Moment Redistribution....33
2.6 Summary....36
CHAPTER 3: PRELIMINARY BRIDGE STRENGTHENING STUDIES....37
3.1 Overview....37
3.2 Bridge Survey....37
3.3 Concept Studies....38
3.3.1 Overview of Load Rating....38
Types of Load Rating and Limit States....38
Load Rating Procedures....40
3.3.2 Load Rating Results....41
3.3.3 Summary....43
CHAPTER 4: EXPERIMENTAL PROGRAM....44
4.1 Overview....44
4.2 Specimen Design....44
4.3 Laboratory Test Setup....47
4.4 Specimen Construction....49
4.4.1 Connector Installation....50
4.4.2 Material Testing....52
4.5 Instrumentation....53
4.6 Test Program....59
4.6.1 Elastic Testing....60
4.6.2 Fatigue Testing....60

First Specimen 60
Second Specimen 61
4.6.3 Shakedown Testing 61
4.6.4 Ultimate Strength Testing 64
4.7 Summary 64
CHAPTER 5: EXPERIMENTAL RESULTS 65
5.1 Overview 65
5.2 Fatigue Testing 65
First Specimen – South Span 65
First Specimen – North Span 66
Second Specimen – South Span 66
5.3 Shakedown Testing 67
5.3.1 Load-Deflection Behavior 67
First Specimen 67
Second Specimen 72
5.3.2 Inelastic Behavior 75
5.3.3 Composite Behavior 80
5.3.4 Shear Connector Behavior 83
5.4 Ultimate Strength Testing 86
5.4.1 Load-Deflection Behavior 86
First Specimen 86
Second Specimen 88
Both Specimens 90
5.4.2 Inelastic Behavior 91
5.4.3 Composite Behavior 96
5.4.4 Shear Connector Behavior 99

5.5 Summary 104

CHAPTER 6: FURTHER ANALYSIS OF EXPERIMENTAL RESULTS 105

6.1 Overview 105

6.2 Inelastic Behavior during Shakedown Loading 105

6.2.1 Method of Analysis 106

6.2.2 Plastic Rotations 108

6.2.3 Residual Moment Results 114

6.2.4 Discussion of Inelastic Analysis 118

6.3 Behavior within Connector Groups 119

6.3.1 Connector Force 119

Total Connector Force in a Group 119

Distribution of Force within a Group 122

6.3.2 Connector Slip 127

6.3.3 Cross-Sectional Behavior 130

Strain Profiles 131

Neutral Axis Locations 133

6.4 Summary 136

CHAPTER 7: FINITE ELEMENT MODELING 138

7.1 Overview 138

7.2 Modeling and Analysis Techniques 138

7.2.1 Steel Beam 139

7.2.2 Concrete Deck 140

Inelastic Concrete Material Models 140

Multilinear Elastic Material Model 141

7.2.3 Shear Connectors 143

7.2.4 Boundary Conditions and Applied Loads 145

7.2.5 Analysis Procedure 146

7.3 Elastic Distribution of Moments in Partially Composite Girders 147
7.3.1 Description of Models for Parametric Study 148
7.3.2 Results from Parametric Study 150
7.3.3 Analysis Recommendations 154
7.4 Inelastic Behavior of Strengthened Girders 154
7.5 Summary 161
CHAPTER 8: DESIGN APPROACH AND RECOMMENDATIONS 162
8.1 Overview 162
8.2 Recommended Strengthening Design Procedure 162
8.2.1 Conduct Live Load Analysis 162
8.2.2 Evaluate Existing Bridge 163
8.2.3 Set Targets for Strengthened Bridge 164
8.2.4 Conduct Additional Live Load Analysis (If Necessary) 164
8.2.5 Check Negative Moment Regions and Redistribute Moments 165
8.2.6 Design Connectors for Positive Moment Regions 166
8.2.7 Locate Connectors along Bridge 166
8.2.8 Check Fatigue Strength of Connectors 168

8.3 Recommended Connector Installation Procedure....169

8.4 Summary....172

CHAPTER 9: SUMMARY AND CONCLUSIONS....173

9.1 Summary....173

9.2 Conclusions....174

9.3 Recommendations for Future Research....175

APPENDIX A: EXPERIMENTAL PREDICTIONS....177

APPENDIX B: EQUATIONS USED IN FURTHER ANALYSIS OF EXPERIMENTAL RESULTS....207

APPENDIX C: FULL RESULTS OF PARAMETRIC STUDY....211

APPENDIX D: DESIGN EXAMPLE....215

REFERENCES....295

VITA....300

List of Tables

Table 2-1: Additional Theses and Dissertations Describing Research Involving Post-Installed Shear Connectors at the University of Texas at Austin 13

Table 4-1: Material Properties of the First Specimen 52

Table 4-2: Material Properties of the Second Specimen 52

Table 5-1: Summary of Loading for Shakedown Testing of First Specimen 70

Table 5-2: Summary of Loading for Shakedown Testing of Second Specimen.....73

Table 6-1: Estimated Order of Connector Failure during Ultimate Strength Testing of the Second Specimen 127

Table 7-1: Girder Geometry for Parametric Study 149

Table 7-2: Post-Installed Shear Connectors for Parametric Study 149

Table A-1: Section Properties for Both Specimens 177

Table A-2: Material Properties for the North Span of the First Specimen 178

Table A-3: Material Properties for the South Span of the First Specimen 190

Table A-4: Material Properties for the Second Specimen 197

Table D-1: Section Properties for Girders A and B 218

Table D-2: Unfactored Moments at Critical Sections and at Lateral Brace Locations around the Interior Pier Section in Girder B 220

Table D-3: Load Rating Results of Existing Non-Composite Girder B 232

Table D-4: Unfactored and Redistribution Moments at Critical Sections in Girder B....242

Table D-5: Results from Partially Composite Design Calculations for the Interior Span of Girder B 254

Table D-6: Load Rating Results of Strengthened Girder B 263

Table D-7: Unfactored Moments at Critical Sections and at Lateral Brace Locations around the Interior Pier Section in Girder B 266

Table D-8: Load Rating Results of Existing Non-Composite Girder A 267

Table D-9: Section Properties for Girder C 269

Table D-10: Unfactored Moments at Critical Sections and at Lateral Brace Locations around the Interior Pier Section in Girder C 270

Table D-11: Load Rating Results of Existing Non-Composite Girder C 271

Table D-12: Necessity of Moment Redistribution for Girder C 272

Table D-13: Results from Moment Redistribution Calculations for Girder C 274

Table D-14: Results from Partially Composite Design Calculations for Girder C.....276

Table D-15: Load Rating Results of Strengthened Girder C 279

Table D-16: Section Properties for Girder D 281

Table D-17: Unfactored Moments at Critical Sections and at Lateral Bracing in Girder D.....283

Table D-18: Load Rating Results of Existing Non-Composite Girder D.....284

Table D-19: Necessity of Moment Redistribution for Girder D.....285

Table D-20: Results from Moment Redistribution Calculations for Girder D 287

Table D-21: Results from Partially Composite Design Calculations for Girder D 288

Table D-22: Load Rating Results of Strengthened Girder D.....291

List of Figures

Figure 1-1: Adhesive Anchor Post-Installed Shear Connectors 2

Figure 2-1: Strain Distribution in Fully, Partially, and Non-Composite Girders 5

Figure 2-2: Plastic Stress Distributions in Composite Girders 6

Figure 2-3: Effect of Shear Connection Ratio on Strength (Kwon et al. 2007).....9

Figure 2-4: Post-Installed Connectors Tested by Klaiber et al. (1983) – (a) Double-nutted Connector and (b) Epoxied Bolt Connector.....11

Figure 2-5: Post-Installed Connectors Recommended by Dionne et al. (1997) – (a) Mechano-chemical Anchor with Abutment Sleeve and (b) Mechano-chemical Anchor with Inverted Conical Sleeve 11

Figure 2-6: Coiled Spring Pin Connectors in Pushout Tests by Buckby et al. (1997) 12

Figure 2-7: Post-Installed Connectors Recommended by Researchers at the University of Texas at Austin (Kwon et al. 2009) 13

Figure 2-8: Sample Direct-Shear Test Setup (Kayir 2006) 14

Figure 2-9: Results from Small-Scale Fatigue Testing of Adhesive Anchor Connectors – (a) Stress-based Approach and (b) Slip-based Approach 15

Figure 2-10: Test Setup and Results from Large-Scale Testing of Simply Supported Girders Strengthened with Post-Installed Shear Connectors (Kwon 2008).....17

Figure 2-11: Illustration of (a) Shakedown Behavior and (b) Incremental Collapse Behavior.....19

Figure 2-12: Shakedown of a Propped Cantilever with Moving Point Load – Moment Variation during the First Two Cycles.....21

Figure 2-13: Shakedown of a Propped Cantilever with Moving Point Load – Deflected Shapes during the First Two Cycles 22

Figure 2-14: Upper-Bound Method Example.....27

Figure 2-15: Lower-Bound Method Example.....29

Figure 2-16: AASHTO Moment Redistribution Procedure.....35

Figure 3-1: HS 20 Live Load (AASHTO 2002) 40

Figure 3-2: Load Rating Results 42

Figure 4-1: Cross Section View of Large-Scale Test Specimens 45

Figure 4-2: Elevation View of First Specimen – (a) North Span and (b) South Span 46

Figure 4-3: Elevation View of Second Specimen – (a) North Span and (b) South Span 46

Figure 4-4: 3D Rendering and Photos of Test Setup – (a) Overall View, (b) Interior Support, (c) End Support, (d) Load Frame, and (e) Lateral Bracing 48

Figure 4-5: Specimen Construction – (a) Steel Erection, (b) Splice Plates, (c) Deck Formwork, (d) Deck Reinforcement, and (e) Deck Casting 49

Figure 4-6: Connector Supplies – (a) Threaded Rod and (b) Adhesive 50

Figure 4-7: Connector Installation Process 51

Figure 4-8: Photos of Instrumentation – (a) 500-kip Load Cell with Spherical Head, (b) 200-kip Load Cell with Load Button, (c) String Potentiometer, (d) Linear Potentiometer for Deflection, (e) Strain Gages, and (f) Linear Potentiometer for Slip 54

Figure 4-9: Cross Section Strain Gage Locations around Connectors for the (a) First Specimen and (b) Second Specimen 56

Figure 4-10: Typical Setup for Optical Motion Tracking System 57

Figure 4-11: Marker Layout for Optical Motion Tracking System 58

Figure 4-12: Load Patterns for Shakedown Testing 62

Figure 4-13: Load Patterns for Ultimate Strength Testing 64

Figure 5-1: Adhesive Degradation during North Span Fatigue Test in First Specimen – (a) Schematic of Gap Formation and (b) Photograph of Typical Connector after Testing 66

Figure 5-2: Peak Load-Deflection Behavior during Shakedown Testing of the First Specimen 71

Figure 5-3: Change in Deflection between Consecutive Cycles during Shakedown Testing of the First Specimen – At the Shakedown Limit Load 71

Figure 5-4: Peak Load-Deflection Behavior during Shakedown Testing of the Second Specimen 74

Figure 5-5: Change in Deflection between Consecutive Cycles during Shakedown Testing of the Second Specimen – At the Shakedown Limit Load 74

Figure 5-6: Photographs of Yield Lines in Whitewash after Shakedown Testing and Curvature Distribution during Shakedown Testing at the Interior Support 78

Figure 5-7: Photographs of Deck Cracks at Interior Support after Shakedown Testing ... 79

Figure 5-8: Photographs of Typical Yield Lines in Whitewash at Loads A and D after Shakedown Testing in Both Specimens 79

Figure 5-9: Photographs of Typical Deck Cracking at Load A or Load D after Shakedown Testing 80

Figure 5-10: Neutral Axis Location during Shakedown Testing of the First Specimen ... 82

Figure 5-11: Neutral Axis Location during Shakedown Testing of the Second Specimen 83

Figure 5-12: Force-Slip Behavior of Connectors during Shakedown Testing of Both Specimens 85

Figure 5-13: Load-Deflection Behavior during Ultimate Strength Testing of the First Specimen 88

Figure 5-14: Load-Deflection Behavior during Ultimate Strength Testing of the Second Specimen 90

Figure 5-15: Photographs of Both Specimens after Ultimate Strength Testing 91

Figure 5-16: Photographs of Yield Lines in Whitewash after Ultimate Strength Testing at the Interior Support 93

Figure 5-17: Photographs of Local Buckling at Interior Support after Ultimate Strength Testing of the Second Specimen – (a) Flange Buckling and (b) Web Buckling 93

Figure 5-18: Photographs of Deck Cracking at Interior Support after Ultimate Strength Testing 94

Figure 5-19: Photographs of Yield Lines in Whitewash after Ultimate Strength Testing and Curvature Distribution during Ultimate Strength Testing at Loads A and D 95

Figure 5-20: Photographs of Deck Cracking at Load A or Load D after Ultimate Strength Testing – (a) Typical Cracking of Underside of Deck and (b) Crushing of Deck at Load D during Ultimate Strength Testing of First Specimen in the South Span.....96

Figure 5-21: Neutral Axis Location during Ultimate Strength Testing of First Specimen.....98

Figure 5-22: Neutral Axis Location during Ultimate Strength Testing of Second Specimen.....99

Figure 5-23: Force-Slip Behavior of Connectors during Ultimate Strength Testing of Both Specimens 102

Figure 5-24: Photographs of Failed Connectors and Underside of Deck at Connector Regions after Ultimate Strength Testing of Both Specimens 103

Figure 6-1: Deflected Shapes from Rotation of Plastic Hinges (a) at Load A in North Span, (b) at Interior Support, and (c) at Load D in South Span.....106

Figure 6-2: Elastic Deflected Shapes from Applied Load for (a) Load A in North Span, (b) Loads B and C in Both Spans, and (c) Load D in South Span.....108

Figure 6-3: Residual Rotations in Positive Bending during Shakedown Testing of Both Specimens 109

Figure 6-4: Residual Rotations in Negative Bending during Shakedown Testing of Both Specimens 110

Figure 6-5: Plastic Hinge Rotation at Critical Locations during Shakedown Testing of First Specimen 112

Figure 6-6: Plastic Hinge Rotation at Critical Locations during Shakedown Testing of Second Specimen.....113

Figure 6-7: Variation in Estimated Moment of Inertia during Shakedown Testing of Both Specimens 115

Figure 6-8: Variation in Estimated Redistribution Moment during Shakedown Testing of Both Specimens 117

Figure 6-9: Total Force Transmitted into the Deck in Each Shear Connector Group during Shakedown Testing of the Second Specimen 121

Figure 6-10: Total Force Transmitted into the Deck in Each Shear Connector Group during Ultimate Strength Testing of the Second Specimen.....122

Figure 6-11: Typical Distribution of Force within Connector Groups during Shakedown Testing of the Second Specimen 125

Figure 6-12: Distribution of Force within Connector Groups during Ultimate Strength Testing of the Second Specimen 126

Figure 6-13: Typical Distribution of Slip within Connector Groups during Shakedown Testing of the Second Specimen 129

Figure 6-14: Distribution of Slip within Connector Groups during Ultimate Strength Testing of the Second Specimen 130

Figure 6-15: Typical Variation of Strain Profiles between Connector Pairs 132

Figure 6-16: Typical Variation of Neutral Axis Location during Shakedown Testing of the Second Specimen 135

Figure 6-17: Typical Variation of Neutral Axis Location during Ultimate Strength Testing of the Second Specimen 136

Figure 7-1: Typical Finite Element Model 139

Figure 7-2: General Material Definition for Steel Beam 140

Figure 7-3: Equivalent Effective Deck Section for Multilinear Elastic Material Model. 142

Figure 7-4: Sample Material Definition for Concrete Deck – Multilinear Elastic Material Model 143

Figure 7-5: Force-Deformation Behavior of Shear Connector Springs 145

Figure 7-6: Connector Layout for 3D FEA Models in Parametric Study 149

Figure 7-7: Stiffness Distributions for Line Element Models in Parametric Study 150

Figure 7-8: Loading Cases for Parametric Study 150

Figure 7-9: Comparison of Peak Moments from 2D and 3D Analyses for Non-Composite and Strengthened Girder A 152

Figure 7-10: Comparison of Experimental and Computational Load-Deflection Behavior during Shakedown Loading 156

Figure 7-11: Comparison of Experimental and Computational Deflection Change at the Shakedown Limit Load during North Span Loading of the First Specimen 157

Figure 7-12: Comparison of Experimental and Computational Load-Deflection Behavior during Ultimate Strength Loading 158

Figure 7-13: Comparison of Experimental and Computational Connector Behavior during Shakedown Loading – (a) Poor Representation of Behavior due to Force Reversal, and (b) Good Representation of Behavior with No Force Reversal 159

Figure 7-14: Comparison of Experimental and Computational Connector Behavior during Ultimate Strength Loading – (a) Typical Intact Connector, and (b) Typical Failed Connector.....160

Figure 8-1: Design Procedure 162

Figure 8-2: Recommended Connector Layout.....168

Figure 8-3: Connector Installation 171

Figure A-1: Stress Distribution at Plastic Moment of Partially Composite Section with Neutral Axis in the Web of the Steel Beam.....183

Figure A-2: Dead Load Moments for First Specimen 185

Figure A-3: Load Pattern and Moment Diagrams for Shakedown Testing of the North Span of the First Specimen 186

Figure A-4: Shakedown Mechanism for the North Span of the First Specimen 187

Figure A-5: Ultimate Strength Loading for the North Span of the First Specimen.....189

Figure A-6: Ultimate Strength Mechanism for the North Span of the First Specimen ...189

Figure A-7: Load Pattern and Moment Diagrams for Shakedown Testing of the South Span of the First Specimen 194

Figure A-8: Shakedown Mechanism for the South Span of the First Specimen 195

Figure A-9: Ultimate Strength Loading for the South Span of the First Specimen.....196

Figure A-10: Ultimate Strength Mechanism for the South Span of the First Specimen .197

Figure A-11: Dead Load Moments for Second Specimen.....202

Figure A-12: Load Pattern and Moment Diagrams for Shakedown Testing of the Second Specimen.....203

Figure A-13: Shakedown Mechanism for the Second Specimen 204

Figure A-14: Ultimate Strength Loading for the Second Specimen.....205

Figure A-15: Ultimate Strength Mechanism for the Second Specimen 205

Figure B-1: Deflected Shapes from Rotation of Plastic Hinges (a) at Load A in North Span, (b) at Interior Support, and (c) at Load D in South Span.....207

Figure B-2: Elastic Deflected Shapes from Applied Load for (a) Load A in North Span, (b) Loads B and C in Both Spans, and (c) Load D in South Span.....209

Figure C-1: Comparison of Peak Moments from 2D and 3D Analyses for Non-Composite and Strengthened Girder A 212

Figure C-2: Comparison of Peak Moments from 2D and 3D Analyses for Non-Composite and Strengthened Girder B.....213

Figure C-3: Comparison of Peak Moments from 2D and 3D Analyses for Non-Composite and Strengthened Girder C.....214

Figure D-1: Cross Section View of Bridge.....215

Figure D-2: Half-Elevation View of Typical Girder 215

Figure D-3: Half-Elevation View of Girders A and B.....217

Figure D-4: Plot of Unfactored Moments for Girder B 220

Figure D-5: Plot of Unfactored and Redistribution Moments for Girder B 241

Figure D-6: Stress Distribution at Plastic Moment of Fully Composite Section – Exterior Span of Girder B 247

Figure D-7: Stress Distribution at Plastic Moment of Partially Composite Section – Exterior Span of Girder B 251

Figure D-8: Connector Layout for Girder B 255

Figure D-9: Results from Fatigue Analysis for Girder B 257

Figure D-10: Cross-Sectional Connector Layout 264

Figure D-11: Lever Rule for Distribution Factor Calculation for Girder A 265

Figure D-12: Plot of Unfactored Moments for Girder A 265

Figure D-13: Half-Elevation View of Girder C 268
Figure D-14: Plot of Unfactored Moments for Girder C 270
Figure D-15: Connector Layout for Girder C 277
Figure D-16: Results from Fatigue Analysis for Girder C 278
Figure D-17: Half-Elevation View of Girder D 280
Figure D-18: Plot of Unfactored Moments for Girder D 282
Figure D-19: Connector Layout for Girder D 290
Figure D-20: Results from Fatigue Analysis for Girder D 290
Figure D-21: Summary of Design for All Girders 293

CHAPTER 1: INTRODUCTION

1.1 OVERVIEW

Many continuous steel bridges constructed prior to the 1970s have floor systems consisting of a non-composite concrete deck over steel beams with no shear connectors. In these bridges, the deck serves primarily as a driving surface and helps to transfer the traffic loads to the girders, which are the primary load-resisting members. While many of these bridges are still in good condition, the structures may not satisfy current load requirements and thus may need to be strengthened or replaced to avoid load-posting, or restricting the axle weights allowed on the bridge, and to maintain structural safety.

Previous researchers have investigated the strengthening of simply supported steel girder bridges by creating composite action using "post-installed shear connectors" to provide a mechanical attachment between the existing concrete deck and steel beams (Kwon 2008). It was recommended that three different types of connectors be considered to create composite action, one of which is comprised of adhesive anchors, as shown in Figure 1-1. This connector type was chosen as the focus of the research reported in this dissertation because of its simple installation process that is done entirely from the underside of the bridge deck, which minimizes traffic disruption. By creating composite action, both the steel beams and the concrete deck contribute to resisting the loads on the bridge. In regions dominated by positive bending where the deck is in compression, this results in significant gains in strength and stiffness.

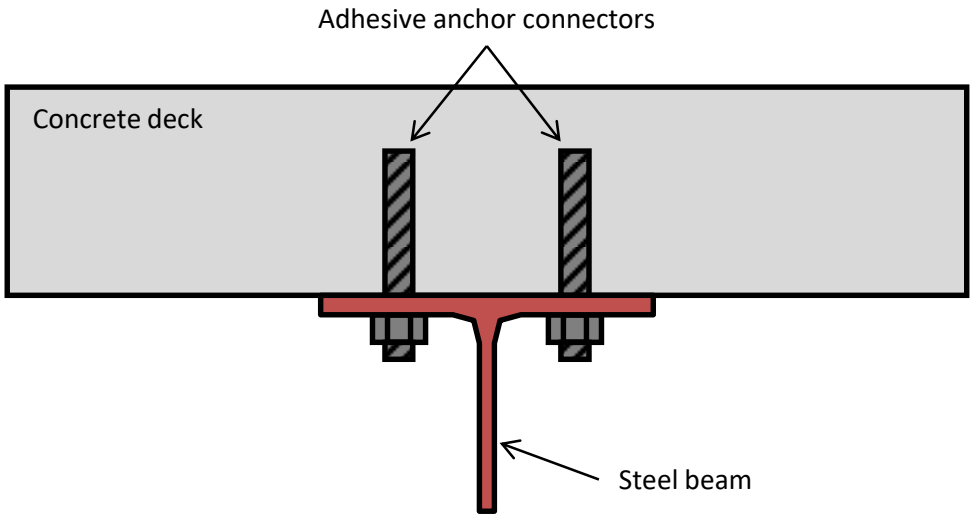

Figure 1-1: Adhesive Anchor Post-Installed Shear Connectors

However, for continuous girders, the low tensile strength of concrete and the minimal longitudinal deck reinforcement found in most older bridges prevent any significant benefits from composite action in negative bending. Thus, a different technique is needed to address any strength deficiencies in regions near the interior piers of a continuous girder bridge, which are dominated by negative flexural demands. This research investigates the use of inelastic moment redistribution from these interior piers to increase the overall load rating of the entire bridge. Moment redistribution means that yielding is allowed to occur at the interior piers under large loads, and excess moments are redistributed to the adjacent positive moment regions. This concept is commonly referred to as "autostress design" and is based on behavior at the shakedown limit state, which is the appropriate plastic limit state for statically indeterminate structures under repeated load patterns, such as traffic loading.

Thus, the overall approach to increasing the load rating of non-composite continuous steel girder bridges investigated in this research combines the use of inelastic moment redistribution in negative moment regions at interior supports with the use of post-installed shear connectors in the positive moment regions in the spans.

1.2 Objectives of Research

The research reported in this dissertation represents a portion of a 5-year project carried out at the Ferguson Structural Engineering Laboratory at the University of Texas

at Austin and funded by the Texas Department of Transportation (Kreitman et al. 2015, Kreitman et al. 2016). The overall objectives of this project were to:

1. Explore the feasibility of the proposed strengthening method for typical bridges in the state of Texas,
2. Investigate the behavior of representative strengthened girders, both experimentally and computationally, and
3. Provide detailed design recommendations for strengthening in-service non-composite continuous steel I-girder bridges.

This dissertation is focused on the behavior of strengthened girders under large loads at strength limit states. The fatigue behavior of the adhesive anchor connector is covered in detail by Patel (2013) and Ghiami Azad (2016).

1.3 Scope of Dissertation

Following this introductory chapter, Chapter 2 provides pertinent background information from the literature regarding composite behavior, post-installed shear connectors, and inelastic moment redistribution. A description of the initial studies that were conducted to evaluate the feasibility of the proposed strengthening method is provided in Chapter 3. Chapter 4 introduces the large-scale experimental program, while Chapter 5 and Chapter 6 discuss the experimental results in a general and more detailed sense, respectively. The details of the finite element modeling techniques and results from both a parametric study investigating the distribution of elastic moments in strengthened girders and the computational analysis of the experimental testing are provided in Chapter 7. Chapter 8 describes the design approach for the strengthening process and provides design equations for the static and fatigue strength of post-installed adhesive anchor shear connectors. Finally, Chapter 9 summarizes the work reported here and suggests some additional related topics for future research.

Calculations and equations used for data analysis, along with additional results not directly shown in the text are provided in Appendix A, Appendix B, and Appendix C. Appendix D is comprised of a detailed design example for strengthening a sample bridge.

CHAPTER 2: BACKGROUND

2.1 OVERVIEW

The proposed strengthening method combines several aspects of bridge design and structural behavior to create an efficient strengthening solution. This chapter presents the relevant background information pertaining to the general behavior of composite girders, previous research on post-installed shear connectors, principles of inelastic moment redistribution for bridges, and a summary of applicable AASHTO bridge design provisions.

2.2 COMPOSITE BEHAVIOR

A composite steel bridge has a floor system in which the concrete deck is mechanically attached to the steel beams so that the two elements bend together (Oehlers and Bradford 1995). This is illustrated in Figure 1-1. The shear connectors provide the mechanical attachment that transfers the horizontal shear force at the interface between the bottom of the concrete deck and the top flange of the steel beam. These connectors are typically headed studs that are welded to the top flange of the steel section and embedded into the concrete deck during casting. Historically, short channel sections and other shapes welded to the top flange have also been used as shear connectors. Composite girders are significantly stiffer and stronger in flexure compared to non-composite girders because more material is effective in the cross section. This is especially true for composite girders in positive bending where the concrete deck is in compression and the steel beam is primarily in tension.

2.2.1 Full and Partial-Composite Behavior

A fully composite girder has enough shear connectors to transfer the required horizontal interface shear force to develop the full plastic moment of the composite cross section. A condition where there is zero "slip", or relative longitudinal displacement, between the concrete deck and the steel beam, also known as "full interaction," is generally not possible to attain. However, the slip between the deck and the steel beam in a fully composite girder is generally considered negligible and ignored for analysis under service loads, although significant slip may occur at ultimate load. Thus, under service loads, a continuous strain distribution can be assumed throughout the entire composite section, as shown in Figure 2-1(a).

Conversely, a partially composite girder does not have enough shear connectors to transfer the horizontal shear required to develop the full plastic moment of the composite section. Instead, the strength of the section is controlled by the shear connection. A significant amount of slip occurs between the deck and the girder, even at service loads, and the strain distribution is discontinuous at the interface, as depicted in Figure 2-1(b). The amount of slip at a given section in a partially composite girder is determined by integrating the magnitude of this strain discontinuity along the length of the girder. A typical strain distribution in a non-composite girder is also shown in Figure 2-1(c). Although the slope of the strain profiles, or the curvatures, of the steel and concrete sections are generally assumed to be the same in all three cases shown in the figure, each element bends separately about its own neutral axis in a non-composite section. Interface slip also occurs in non-composite girders due to the strain discontinuity.

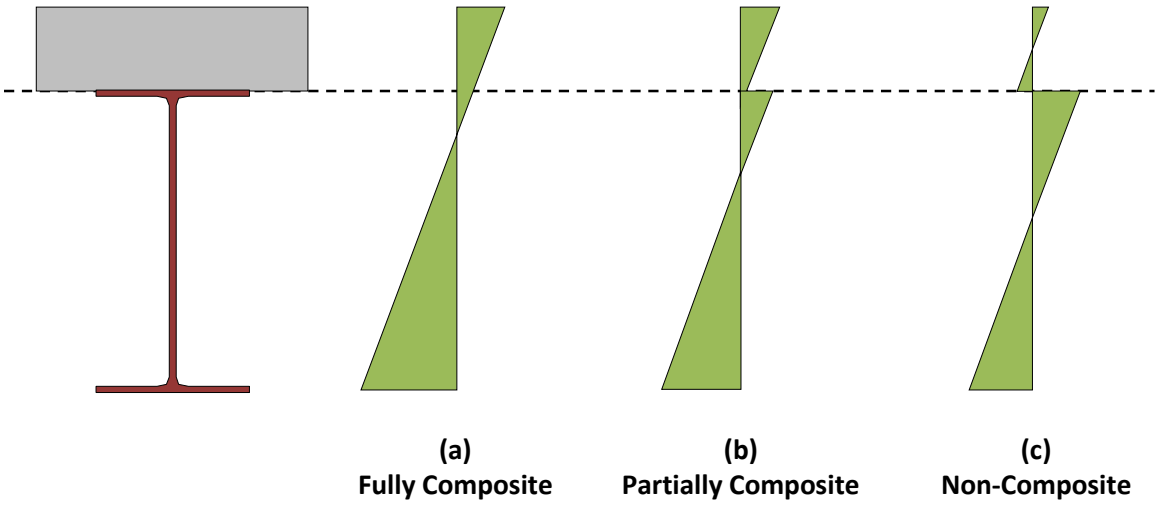

Figure 2-1: Strain Distribution in Fully, Partially, and Non-Composite Girders

2.2.2 Strength of Composite Girders

The maximum flexural strength of a compact, well-braced, fully or partially composite girder under positive moment is calculated using one of the assumed plastic stress distributions shown in Figure 2-2 (AISC 2010). For fully composite girders, the plastic neutral axis (PNA) can be located either in the concrete deck (a) or in the steel beam (b), while the plastic neutral axis in a partially composite girder will always be located in the steel section (c). At the plastic moment strength level, all portions of the steel beam

are assumed to be fully yielded in either tension or compression, depending on the location of the neutral axis. A compressive stress block with a resultant force equal to the horizontal interface shear force (C_f, defined in the next section) extends down from the top of the deck through a depth that satisfies force equilibrium. The deck is assumed to resist no tensile forces. The flexural capacity is determined by the summation of moments in this stress distribution. Several experimental studies have confirmed that this results in a lower-bound and generally quite accurate estimate of the actual strength of fully and partially composite girders (Culver and Coston 1961, Slutter and Driscoll 1963, Chapman and Balakrishnan 1964).

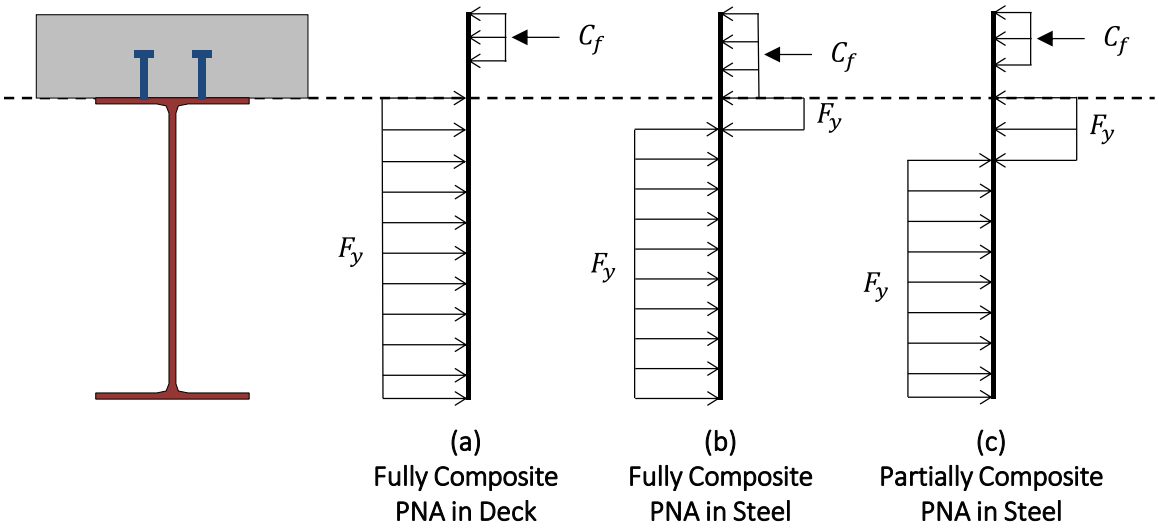

Figure 2-2: Plastic Stress Distributions in Composite Girders

Interface Shear Force

At the plastic moment strength level in a fully composite girder, the maximum horizontal interface shear force (C_f) that is transferred by the shear connection is the smaller of the maximum axial forces that can be developed above and below the interface, or in the deck and in the steel, respectively. The maximum compressive force that can be developed in the deck is usually assumed to take the form of the Whitney stress block, which is comprised of a uniform stress distribution of 85% of the compressive strength over the entire cross-sectional area of the deck. This conservatively ignores the deck reinforcement in compression. For composite girders under negative moment, the maximum tensile force in the deck is typically taken as the full yield strength of the

longitudinal reinforcement, ignoring the concrete in tension. The maximum compressive or tensile force that can be developed in the steel beam is the maximum plastic force if all fibers are yielded. In the case of negative moment, where a significant depth of the steel beam is in compression, this assumes that the section is compact and sufficiently braced so that no premature local or lateral-torsional buckling will occur.

For partially composite girders, the maximum interface shear force that can be transferred is controlled by the shear connectors, and is thus lower than the maximum forces that can be developed in the deck and in the steel. The maximum horizontal interface shear force that can be transferred in a partially composite girder is the sum of the ultimate strengths of all shear connectors located between the points of zero and maximum moment in a span. Thus, the horizontal interface shear force (C_f) is:

For positive moment regions:

$$C_f = min\begin{cases} 0.85\, f_c'\, A_c \\ \left(A_s\, F_y\right)_{girder} \\ \Sigma Q_n \end{cases} \qquad \textbf{\textit{Equation 2-1}}$$

For negative moment regions:

$$C_f = min\begin{cases} \left(A_s\, F_y\right)_{rebar} \\ \left(A_s\, F_y\right)_{girder} \\ \Sigma Q_n \end{cases} \qquad \textbf{\textit{Equation 2-2}}$$

where A_s is the area of the steel section or of the longitudinal reinforcement having a yield strength of F_y, A_c is the area of the concrete deck within the effective width having a 28-day compressive strength of f_c', and ΣQ_n is the sum of the static shear strength of all shear connectors between the points of zero and maximum moment.

If the top expression in Equation 2-1 or Equation 2-2 is the smallest, the plastic neutral axis is located in the steel beam. If the middle expression is the smallest, the plastic neutral axis is in the deck. In both cases, however, the girder is considered to be fully composite. If the bottom expression is the smallest so that the shear connectors control the strength of the section, the neutral axis is in the steel beam, and the section is considered to be partially composite.

The value of the interface shear force is used to determine the required number of shear connectors (N_{full}) to be placed between points of zero and maximum moment for a fully composite girder:

$$N_{full} = \frac{C_f}{Q_n} \qquad \textbf{Equation 2-3}$$

where Q_n is the static shear strength of a single connector.

For partially composite girders, the composite ratio (η) is defined as the ratio between the number of shear connectors provided (N) and the number of connectors required to develop full-composite action. This composite ratio is often expressed as a percentage. A girder with a composite ratio less than unity (less than 100%) is partially composite, while a girder with a composite ratio equal to or greater than unity is fully composite:

$$\eta = \frac{N}{N_{full}} \qquad \textbf{Equation 2-4}$$

Efficiency of Partial-Composite Behavior

While a partially composite girder has a reduced flexural strength as compared to a fully composite girder, the relationship between composite ratio and strength is not linear. In fact, partial-composite action is efficient, as small composite ratios can provide significant strength increases. This is illustrated in Figure 2-3, which shows the ultimate load-carrying capacity of a 38-foot long simple span girder with a point load at midspan as a function of the composite ratio, which is referred to as the shear connection ratio in the figure. The geometry of this girder is equivalent to the large-scale tests discussed in Section 2.3.2 (Kwon et al. 2007).

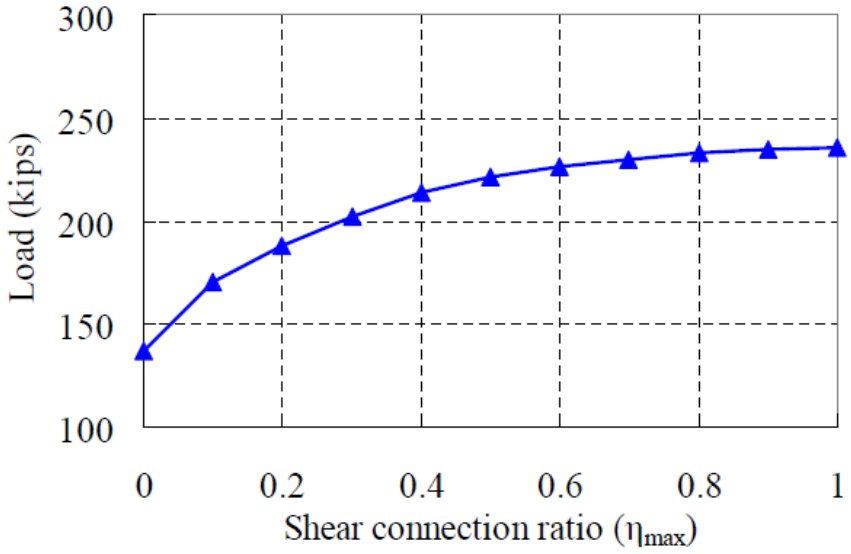

Figure 2-3: Effect of Shear Connection Ratio on Strength (Kwon et al. 2007)

Because of the efficiency of partial-composite action, many building structures are designed economically using partially composite girders. However, in bridge design, the fatigue strength of conventional welded shear studs tends to control the design, rather than the static strength requirements. Fatigue design usually requires enough shear connectors for fully composite action to develop in a bridge. The Association of American State Highway and Transportation Officials (AASHTO) bridge design specifications, discussed in Section 2.5.1, do not currently allow for partial-composite action for this reason (AASHTO 2010).

2.2.3 Stiffness of Composite Girders

The moment of inertia of a fully composite girder with negligible interface slip is computed by statics as the transformed moment of inertia of the composite cross section. However, the interface slip present in partially composite girders reduces the effective stiffness of the section. The American Institute for Steel Construction (AISC) *Commentary to the Specification for Structural Steel Buildings* provides an equation to estimate the effective moment of inertia (I_{eff}) of a partially composite girder for the purposes of calculating deflections (AISC 2010):

$$I_{eff} = I_s + \sqrt{\eta}\,(I_{tr} - I_s) \qquad \textbf{Equation 2-5}$$

where I_s and I_{tr} are the moments of inertia of the steel section and of the fully composite uncracked transformed section, respectively. The effective elastic section modulus (S_{eff}) can be estimated in the same manner to approximate the extreme fiber stresses in a partially composite section. These equations are based on empirical elastic testing of partially and fully composite girders in positive flexure (Grant et al. 1977). Note that the elastic modulus of steel should be used with these values of moment of inertia to obtain the flexural stiffness of the transformed composite or partially composite section.

The effective section properties calculated from Equation 2-5 are actually fictitious values that represent the overall behavior of the girder. They are intended for use to approximate deformations and stresses in design, rather than to describe the actual behavior of a partially composite cross section. The actual behavior is complex because plane sections do not remain plane due to the significant amount of interface slip. This is discussed further in Chapter 6. Partial-composite elastic beam theory that directly includes the effects of interface slip has been developed by several researchers, most notably Newmark et al. (1951) and Proctor (1963). More recent work by Seracino et al. (2004, 2006) has revisited the concepts of partially composite behavior with applications to composite bridge girders.

2.3 POST-INSTALLED SHEAR CONNECTORS

Creating composite action in existing non-composite bridges has been investigated previously in only a few studies prior to an extensive investigation conducted at the University of Texas at Austin over the past decade. This section summarizes the research conducted elsewhere regarding the development of post-installed shear connectors as well as the work that has been done at the University of Texas at Austin to date.

2.3.1 Types of Post-Installed Connectors Developed Previously

Klaiber et al. (1983) performed static pushout and girder tests on two types of post-installed connectors, shown in Figure 2-4. Before insertion, the shaft of the epoxied bolt connector (see Figure 2-4(b)) was coated in a concrete-steel epoxy to fill voids and create a solid bond between the connector and the deck. Both post-installed connectors exhibited higher ultimate strengths than conventional welded studs of the same diameter, and the double-nutted connector, which was simpler to install, was successfully used in the field.

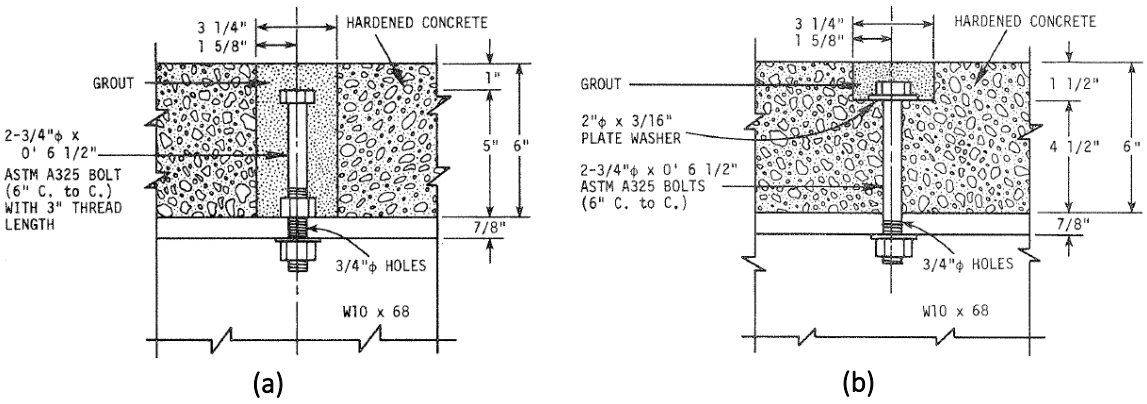

Figure 2-4: Post-Installed Connectors Tested by Klaiber et al. (1983) – (a) Double-nutted Connector and (b) Epoxied Bolt Connector

Dionne et al. (1997) investigated the use of post-installed shear connectors by conducting small-scale direct-shear static and fatigue tests on seven different types of mechanical anchors and three types of epoxied anchors. They suggested that the anchors that combined both mechanical and epoxied connections, shown in Figure 2-5, were most efficient in resisting slip and providing the necessary strength and ductility.

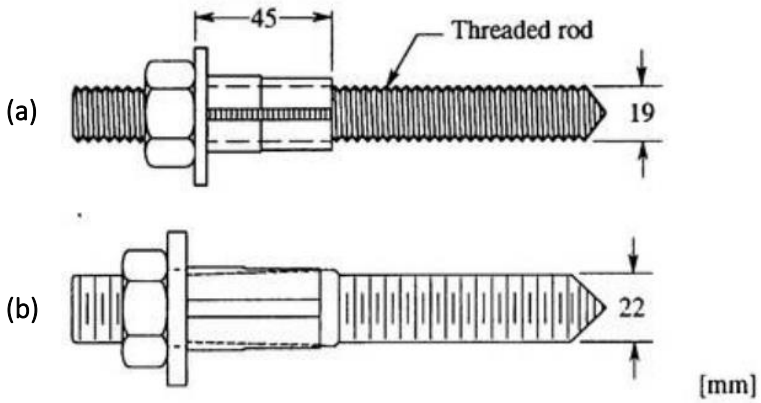

Figure 2-5: Post-Installed Connectors Recommended by Dionne et al. (1997) – (a) Mechano-chemical Anchor with Abutment Sleeve and (b) Mechano-chemical Anchor with Inverted Conical Sleeve

Coiled spring pins have also been used as post-installed shear connectors. Buckby et al. (1997) conducted small-scale static and fatigue pushout testing on these connectors, as shown in Figure 2-6, which were used to improve the fatigue life of an already composite box girder bridge in Canada.

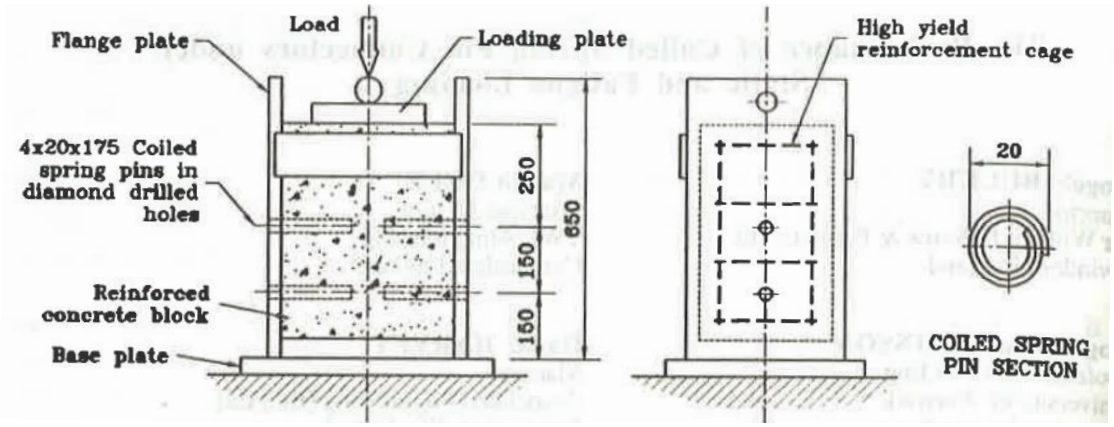

Figure 2-6: Coiled Spring Pin Connectors in Pushout Tests by Buckby et al. (1997)

2.3.2 Previous Research at the University of Texas at Austin

Research on post-installed shear connectors funded by the Texas Department of Transportation has been ongoing at The University of Texas at Austin for the past decade. This began with a laboratory-based research project focused on developing post-installed connectors with good static and fatigue performance to increase the strength of simply supported bridge girders (Kwon et al. 2007). This research was then implemented in the field to strengthen an existing non-composite bridge with simply supported spans near San Antonio, Texas (Kwon et al. 2009). A second laboratory-based project was conducted to extend this strengthening concept to continuous bridges by using both post-installed connectors and inelastic moment redistribution, a portion of which is described in detail in this dissertation (Kreitman et al. 2015). Finally, a design for strengthening an existing bridge in East Texas was completed using post-installed shear connectors and inelastic moment redistribution (Kreitman et al. 2016). This strengthening design is presented in detail as a design example in Appendix D.

This research ultimately recommends the use of the three connectors shown in Figure 2-7 for strengthening positive moment regions of bridges. Throughout all testing, high-strength threaded rods (ASTM A193 B7) and structural bolts (ASTM A325) with diameters of 3/4 or 7/8 inch were used for the connectors. Table 2-1 summarizes the theses and dissertations that contain additional details on this research, and the following sections present the key findings from these studies. Emphasis is placed on the behavior of the adhesive anchor, which is the easiest to install and was the focus of the research described in this dissertation.

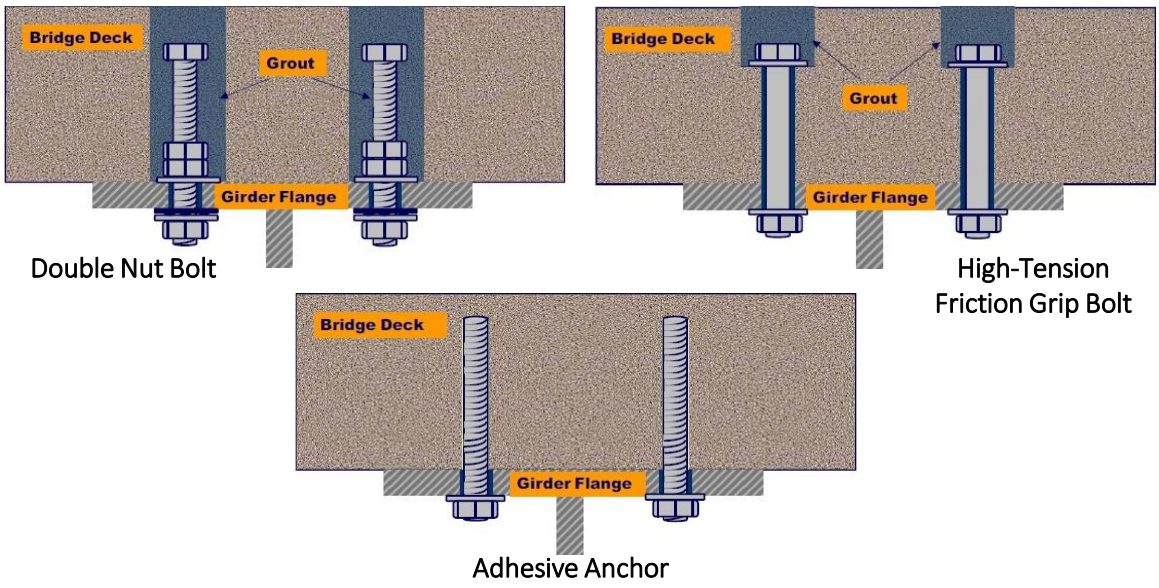

Figure 2-7: Post-Installed Connectors Recommended by Researchers at the University of Texas at Austin (Kwon et al. 2009)

Table 2-1: Additional Theses and Dissertations Describing Research Involving Post-Installed Shear Connectors at the University of Texas at Austin

Reference	Primary Contents
Hungerford (2004)	Small-scale static tests on six types of post-installed connectors (3/4-inch)
Schaap (2004)	Small-scale static tests on five other types of post-installed connectors (3/4-inch)
Kayir (2006)	Small-scale static and fatigue tests on five types of post-installed connectors tested by Hungerford and Schaap that exhibited good static behavior (3/4-inch)
Kwon (2008)	Small-scale static and fatigue tests on three types of post-installed connectors, large-scale static tests on simply supported girders strengthened with three types of connectors (7/8-inch), development of design provisions for simply supported bridges
Patel (2013)	Small-scale fatigue tests on adhesive anchors (7/8-inch), analytical work on fatigue behavior of partially composite simply supported bridge girders
Ghiami Azad (2016)	Large-scale fatigue tests on continuous girders strengthened with adhesive anchors (7/8-inch), analytical work on fatigue behavior of partially composite continuous bridge girders

Small-Scale Static and Fatigue Testing

In total, 11 different types of post-installed shear connectors were tested under static loads, and five of these connectors were also tested under fatigue loads. Additionally, cast-in-place welded studs were tested for comparison. These tests were all conducted on single connectors using a direct-shear test setup, which is designed to subject the connector to primarily shear force, minimizing any bending or prying tendencies that may be present in the more conventional push-out test. One of the direct-shear test setups used in these studies is shown in Figure 2-8.

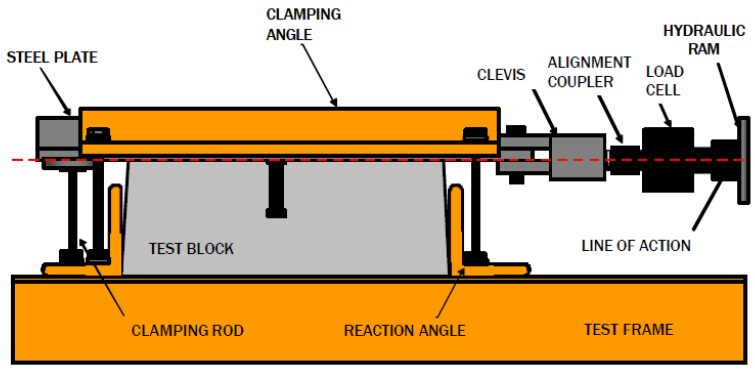

Figure 2-8: Sample Direct-Shear Test Setup (Kayir 2006)

For the three connectors shown in Figure 2-7, the following equation was recommended for the ultimate static strength of a single connector (Q_n):

$$Q_n = 0.5 A_{sc} F_u \qquad \textbf{Equation 2-6}$$

where A_{sc} is the cross-sectional area of the connector, taken as 80% of the gross area for connectors with threads in the shear plane, and F_u is the ultimate tensile strength of the connector material.

The results from all fatigue testing on adhesive anchors, including both 3/4- and 7/8-inch diameter connectors, are graphed in Figure 2-9. The top graph presents the data in the conventional terms of the stress range applied to the connector during testing. The significantly improved fatigue strength over welded shear studs is apparent in this graph, indicating the possibility for partial-composite design. However, over the course of this research, it became apparent that the interface slip in partially composite girders is also important, and that the connector slip may actually provide a better correlation with fatigue

life than does the connector stress. The bottom graph presents the same data with the vertical axis representing the connector slip range, rather than the stress range. Fewer data points are shown on this graph because slip was measured during only one portion of this testing.

Fatigue testing of large-scale girders strengthened with post-installed adhesive anchor shear connectors yielded even better fatigue strengths than observed in the small-scale testing. The results of these large-scale tests are summarized briefly in Chapter 5 and is discussed in detail by Ghiami Azad (2016).

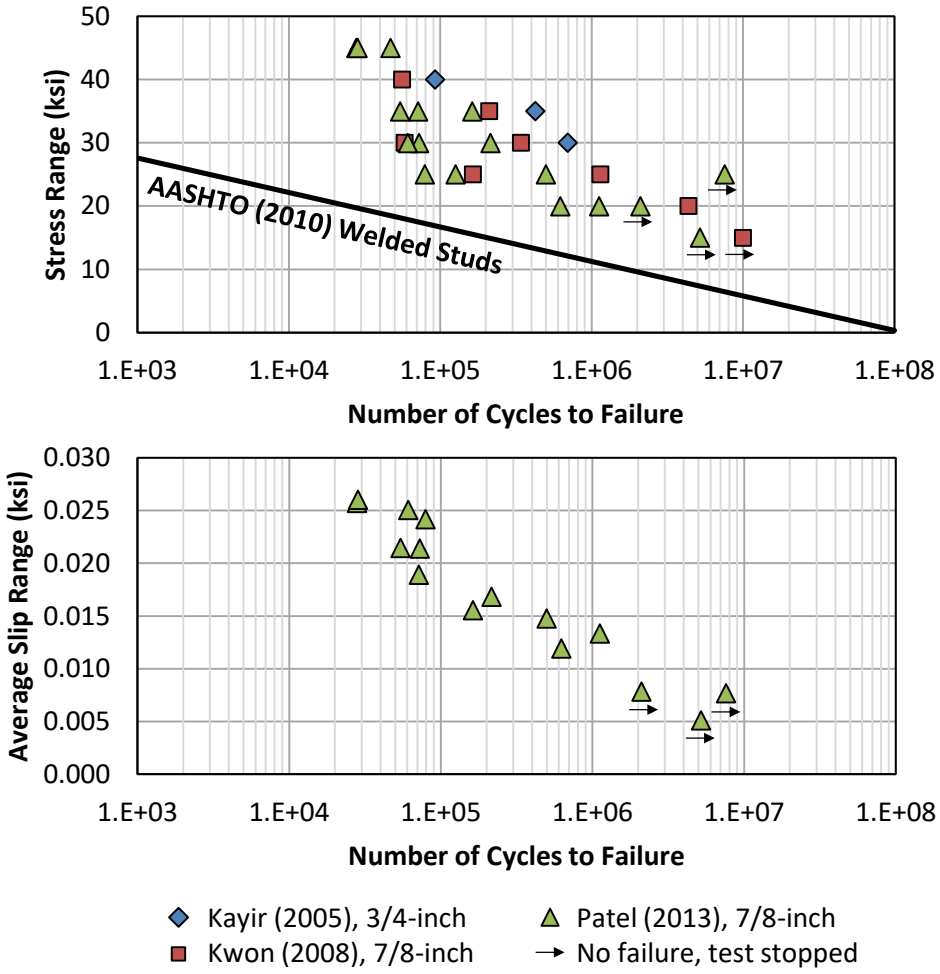

Figure 2-9: Results from Small-Scale Fatigue Testing of Adhesive Anchor Connectors – (a) Stress-based Approach and (b) Slip-based Approach

Large-Scale Girder Testing

The large-scale testing conducted by Kwon (2008) consisted of 38-foot simple span girders loaded monotonically to failure by a point load at midspan. The geometry of the specimens and a photograph of the setup is shown in Figure 2-10. After conducting one test on a non-composite girder, three additional girders were tested after strengthening with each of the three types of post-installed connectors shown in Figure 2-7. Eight pairs of connectors were installed at a uniform spacing on either side of the point load, giving the girders a composite ratio of 30%. A fifth beam was tested, also at a composite ratio of 30%, using adhesive anchor connectors concentrated near the ends of the beam to reduce the slip demand on the connectors. The results from this large-scale testing on the non-composite girder and the two adhesive anchor specimens are summarized in the load-deflection graph of Figure 2-10. The dashed black lines indicate the expected load-deflection curve for non-composite and 30% composite girders using simple plastic analysis. The ultimate strengths agree well with the simple plastic analysis, and the ductility of the specimen strengthened with adhesive anchor connectors concentrated near the ends of the girder was significantly greater than that of the specimen with uniform connector spacing.

The large-scale testing conducted on continuous girders strengthened with post-installed shear connectors is described in detail in Chapter 4, Chapter 5, and Chapter 6 of this dissertation.

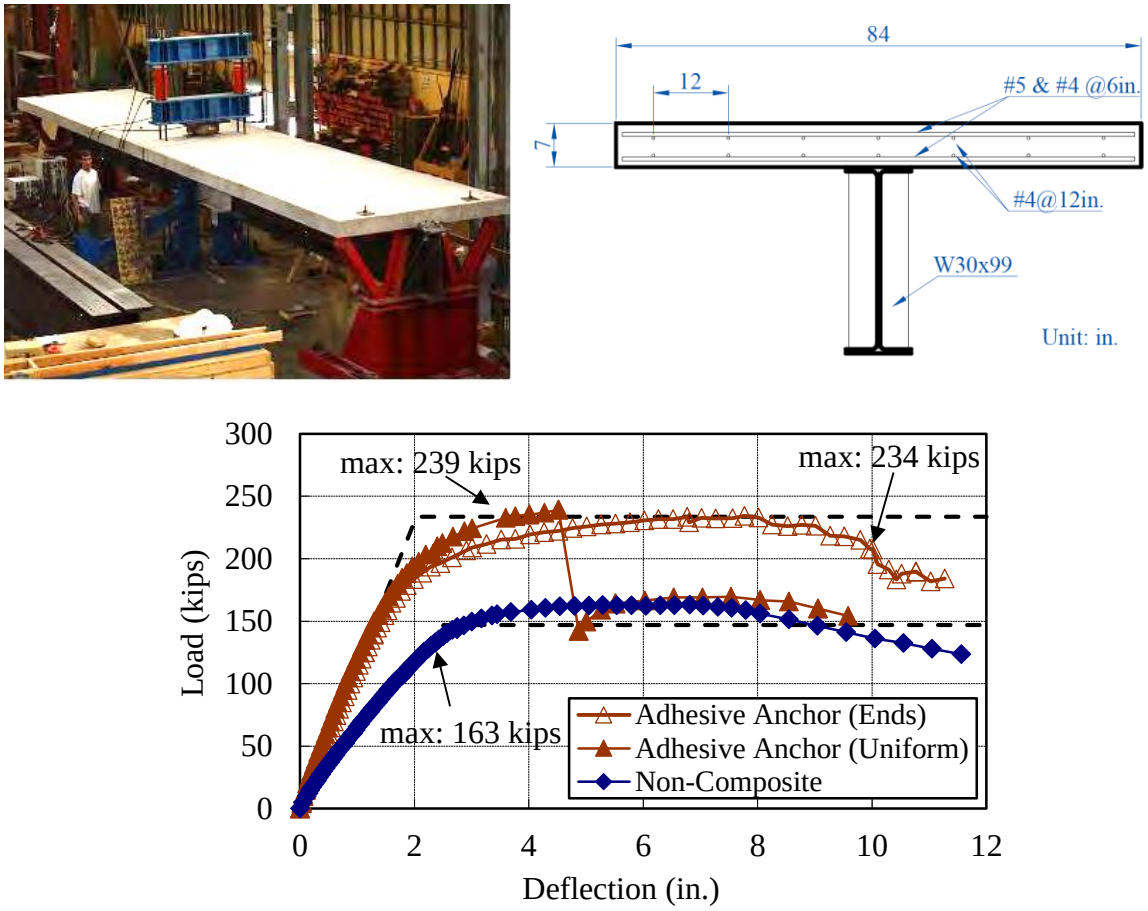

Figure 2-10: Test Setup and Results from Large-Scale Testing of Simply Supported Girders Strengthened with Post-Installed Shear Connectors (Kwon 2008)

Implementation

A strengthening scheme was designed and implemented on a simply supported three-span bridge near San Antonio, Texas, which was originally constructed in 1950. Each simply supported span was strengthened with one of the three different types of post-installed connectors from Figure 2-7. A composite ratio of 50% was used for the spans containing high-tension friction-grip bolt and double-nut bolt connectors, while significantly more adhesive anchor connectors were used due to uncertainties in the fatigue performance at the time. The connectors were concentrated near the ends of each simple span with a 12-inch longitudinal spacing.

Live load tests were carried out before and after the connectors were installed using dump trucks filled with gravel. Deflections were measured during the tests to evaluate the

increase in stiffness of the bridge response before and after connector installation. Additionally, strain gages were installed at select locations to monitor the neutral axis depth, which is an indicator of the amount of composite behavior. Although it was not possible to conduct strength testing, it was concluded that the post-installed connectors were effective in developing a significant amount of composite action under service-level loads.

A strengthening design was also conducted for a continuous three-span bridge in East Texas, which was originally constructed in 1943 and widened in 1961. The details of this design are discussed in the sample calculations provided in Appendix D. For further details, refer to Kreitman et al. (2016).

2.4 Moment Redistribution and Shakedown

Using inelastic procedures to design new steel bridges can result in a reduction of member sizes, particularly by eliminating the need for cover plates or multiple flange transitions in the negative moment regions over the piers. The AASHTO bridge design specifications have included some form of inelastic design procedures since 1973, including the allowance of inelastic moment redistribution from interior pier sections (Barth et al. 2004). When evaluating and strengthening existing bridges, accounting for the ductile, post-yielding behavior of steel by performing an inelastic analysis can be advantageous to minimize the amount of rehabilitation that is needed. Significant increases in load-carrying capacity can be obtained by simply recognizing the strength and ductility of steel beyond the elastic limit. However, yielding of a bridge under repeated large truck loads could lead to an undesirable accumulation of permanent deflections in a structure over time. This section describes the phenomenon of shakedown, which addresses this type of behavior.

2.4.1 Shakedown Behavior

Shakedown is the appropriate limit state to consider for a statically indeterminate structure subjected to repeated cycles of a load pattern that causes yielding. For continuous bridges, yielding can often be allowed at the interior pier sections so that excess moments are redistributed to the adjacent span regions. The main concern with this type of behavior is that the inelastic rotations sustained in the steel beams at the piers may increase with every cycle of load. Eventually, this may create serviceability problems if deflections

increase without bound. However, if the magnitude of the large loads crossing the bridge is high enough to cause yielding at the piers but not too high, the bridge will "shake down" after one or more cycles of load, and all future loads of equal or lesser magnitude will be resisted elastically. This is accomplished by the formation of residual moments in the continuous girders, as a result of the permanent inelastic rotations at the interior piers. These residual moments counteract the moments from the applied traffic loads and thus delay additional yielding during future cycles of load, preventing additional inelastic rotations. Note that a structure must be statically indeterminate to be able to carry residual moments and exhibit this behavior. For loads that are higher than this "shakedown limit load," the inelastic rotations will continue to increase with additional cycles, leading to "incremental collapse," under eventual excessive deformations. In this case, the residual moments are not capable of counteracting the moments from the applied loads to an extent that would prevent yielding and inelastic rotation from occurring at all sections along the girder during future cycles. Figure 2-11 illustrates the general behavior of shakedown (a) and incremental collapse (b).

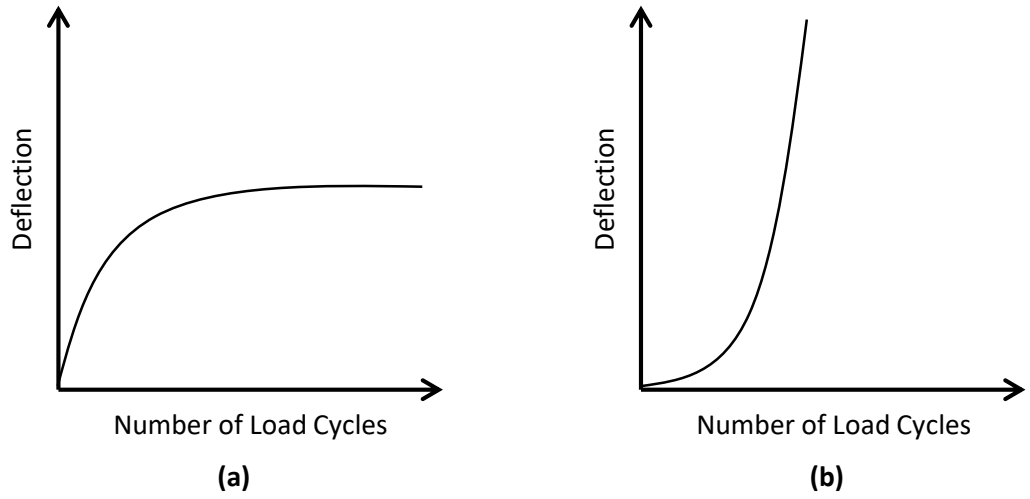

Figure 2-11: Illustration of (a) Shakedown Behavior and (b) Incremental Collapse Behavior

Note that shakedown is not the same as low-cycle fatigue, also called "alternating plasticity", in which fracture occurs as a result of a loading cycle that causes alternating yielding in tension and compression (ASCE-WRC 1971). Instead, the shakedown limit state refers to progressively increasing plastic rotations and permanent deformations

associated with repeated yielding in either tension or compression, but not both, at particular sections. For this reason, the shakedown limit state is often referred to as "deflection stability."

Illustrative Example

A simple example showing the shakedown behavior of a propped cantilever beam with a moving point load is presented here. This example has been adopted from Fukumoto and Yoshida (1969). Figure 2-12 depicts the response of a beam to two cycles of a point load moving from left to right across the beam, and Figure 2-13 shows the different deflected shapes as the point load moves across the beam. The following analysis makes a few simplifying assumptions. First, yielding is assumed to occur instantaneously through the entire cross section when the moment reaches the plastic moment. No yielding is considered before the plastic moment has been reached. Second, the material is assumed to be elastic-perfectly plastic such that no strain hardening occurs. Thus, the plastic moment is the maximum moment that can be carried by the section. These two assumptions are commonly referred to as "plastic hinge" behavior. Finally, it is assumed that the positive and negative plastic moment capacities are equal in magnitude ($\pm M_p$).

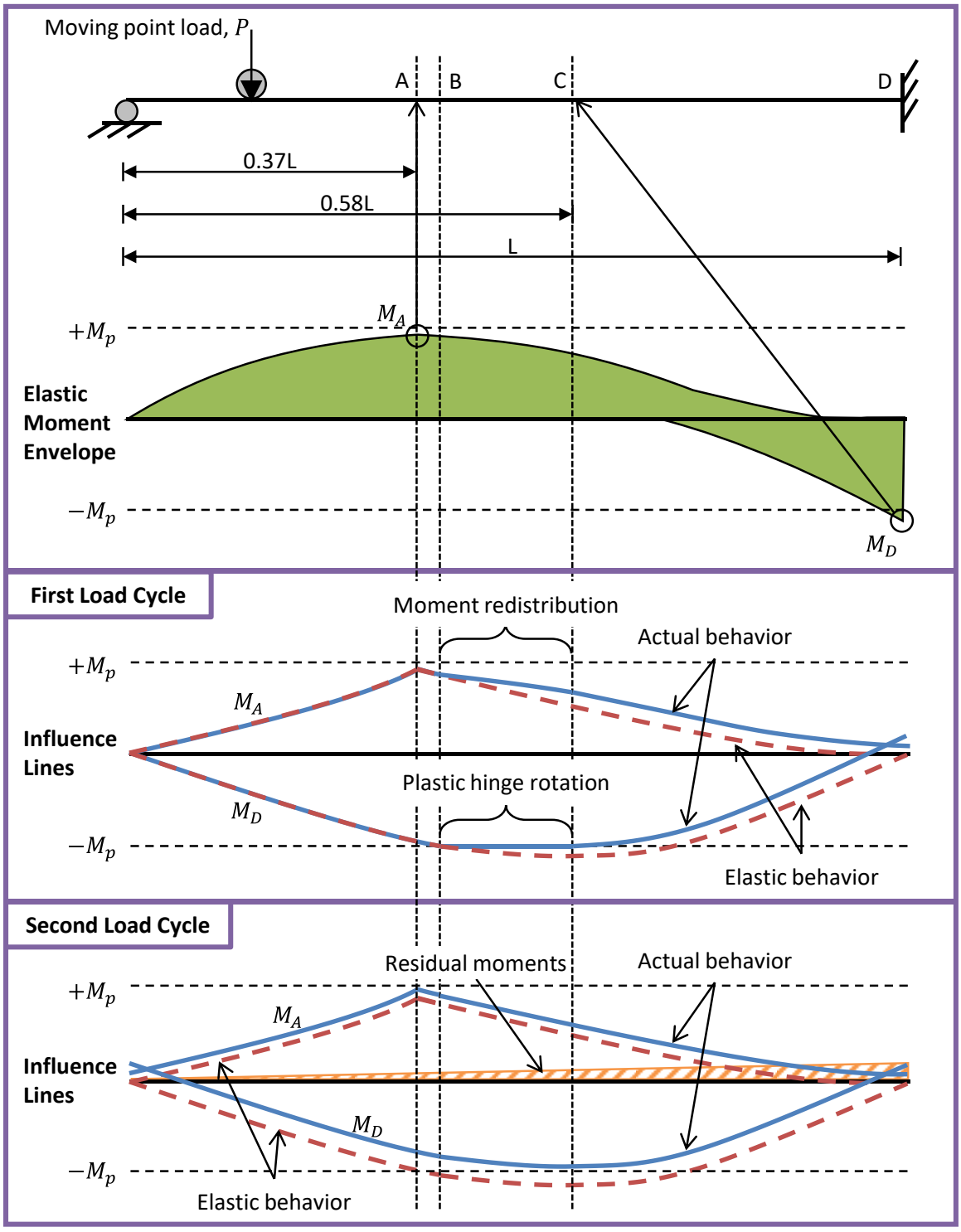

Figure 2-12: Shakedown of a Propped Cantilever with Moving Point Load – Moment Variation during the First Two Cycles

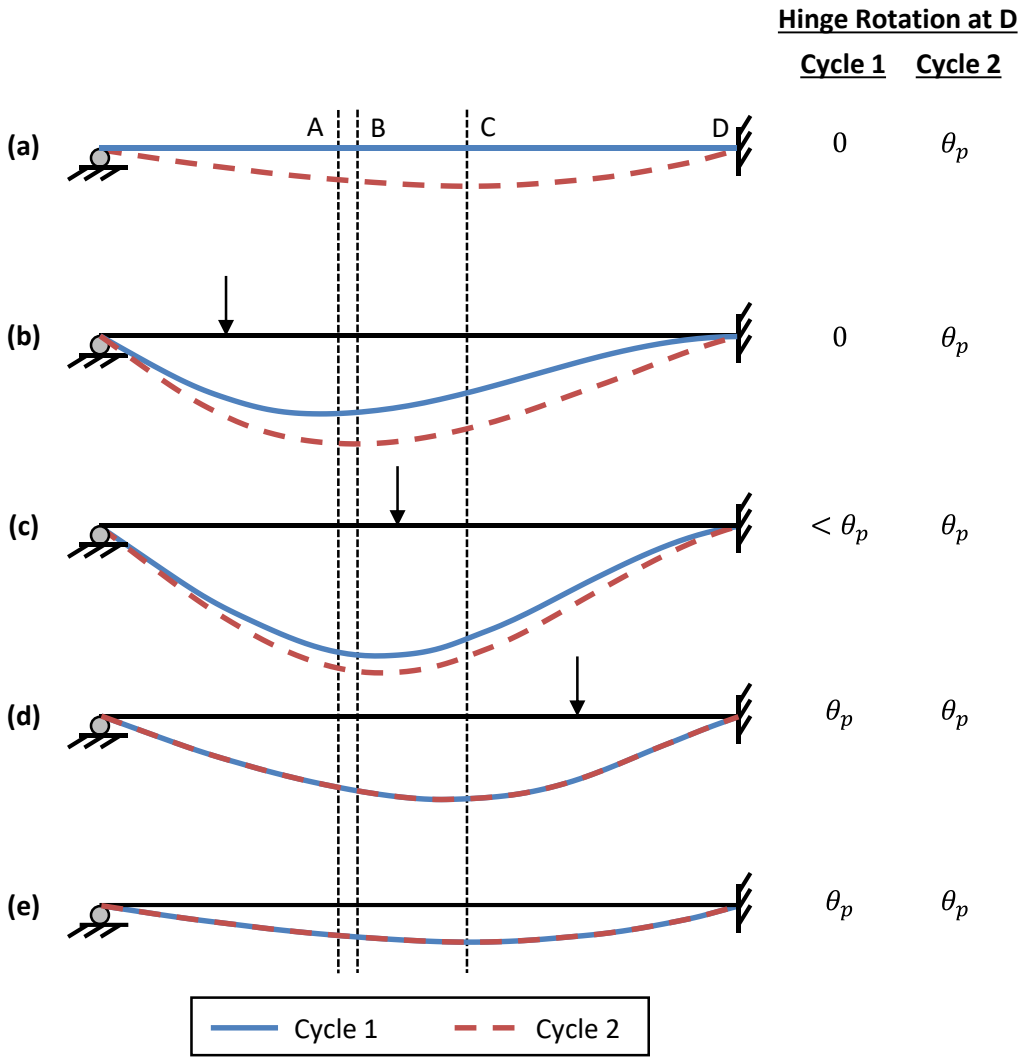

Figure 2-13: Shakedown of a Propped Cantilever with Moving Point Load – Deflected Shapes during the First Two Cycles

The elastic moment envelope in the top frame of Figure 2-12 represents the maximum positive and negative moment induced at each section along the beam as the load moves across the beam. The maximum positive moment in the beam occurs at point A when the load is also located at point A. The maximum negative moment occurs at the fixed end, or point D, when the load is located near midspan at point C. For a constant magnitude of load moving across the beam, the moment at D is larger than the moment at A, indicating that a plastic hinge will form at D at a lower load than it will at A. For the

purposes of this example, the magnitude of the applied load is greater than the load required to form a plastic hinge at D but smaller than the shakedown limit load.

The bottom two frames in Figure 2-12 show the influence lines for the moment at points A and D for the first and second loading cycles. An influence line plots the variation of a particular force quantity at a single section of the beam as a function of the position of the moving load on the beam. The elastic influence lines are shown as dashed lines, while the solid lines trace the actual influence lines for the inelastic behavior. These actual influence lines differ from the elastic lines during the first cycle because yielding occurs at point D and moments are redistributed to the remaining portions of the beam. This redistribution alters the moment at both points A and D, as well as at every other location along the beam.

Figure 2-13 shows the deflected shapes as the point load moves along the beam during the first and second loading cycles. The solid lines indicate the behavior during the first cycle while the dashed lines indicate the behavior during the second cycle.

As the load moves from left to right across the beam during the first cycle, the initial behavior is fully elastic, so that the solid and dashed lines in Figure 2-12 coincide. When the load reaches point A, the maximum positive moment is attained, but this moment has not exceeded the plastic capacity. Thus, as the load moves further to the right, the beam continues to respond elastically. However, once the load reaches point B, the moment at point D is equal to the plastic moment, and a plastic hinge forms at point D. At this point in the analysis, the section at D cannot carry any additional moment. However, as the load continues to move to the right between points B and C, the elastic moment demand at point D increases. Because the section cannot resist the additional demand, the excess moments are redistributed away from point D and out into the span. The result of this can be seen in the influence line for the moment at point A, which increases in magnitude as compared to the elastic influence line as the load moves to the right of point B. As the load continues to move to the right of point B, the plastic hinge at point D rotates freely, as indicated in Figure 2-13 (c).

The maximum negative elastic moment demand at the fixed end occurs when the load reaches point C. After the load moves past this location, point D begins to unload elastically because the moment demand is now decreasing at that location. Plastic deformation and moment redistribution cease, and the beam responds elastically as the load moves off the right end of the beam. However, once the load has been completely removed from the beam, residual moments remain in the system as a result of the permanent rotation

of the plastic hinge at point D (θ_p), which prevents the beam from returning to its original straight configuration, as shown in Figure 2-13 (e). Because only the reaction forces can act on the beam in the unloaded state, the residual moment diagram must have a triangular shape, as shown in the bottom frame of Figure 2-12 shaded with diagonal lines.

Because of the residual moments present in the system before the start of the second cycle, the initial moment at points A and D in the bottom frame of Figure 2-12 are not equal to zero as they were at the start of the first cycle. After this initial offset however, the trend of the elastic influence line is followed as the moving load transverses the entire length of the beam. Since the moments at points A and D do not exceed the plastic moment capacity for any location of the point load, no additional yielding or moment redistribution occurs. This is indicated in Figure 2-12 by the actual influence lines remaining within the bounds of the capacities. Thus, the residual moments that remain in the beam when the load moves off of the right end are unchanged from the first cycle. Additionally, the permanent inelastic rotation at point D (θ_p) remains unchanged as the load moves across the beam during the second cycle, as indicated in Figure 2-13. All future cycles of the same or lesser load will result in the same behavior as shown for the second load cycle, and no additional yielding or inelastic rotations will occur. In other words, this beam has "shaken down" for the particular magnitude of applied load.

Although the stabilization occurs after only a single cycle in this case, a more complex structure may take more than one loading cycle to shake down. If at any point during the second cycle in this example had the moment demand exceeded the plastic moment capacity at any location along the beam, additional plastic rotation and moment redistribution would have occurred in that location. This would have resulted in a different residual moment distribution at the end of the second cycle, which would then be the starting point for the third cycle. Several cycles may be necessary before a state of shakedown is reached, especially in a structure with more than two possible hinge locations

It may also be the case that the structure undergoes plastic rotation during every cycle and never comes to the stable condition shown in the second load cycle of Figure 2-12 and Figure 2-13. As additional cycles of load are applied, incremental collapse would eventually occur, as an increasing amount of permanent inelastic deformation accumulates with additional cycles. Any load causing this type of behavior is greater than the shakedown limit load and is associated with incremental collapse.

2.4.2 Shakedown Theorems

Shakedown was first recognized in Germany in the 1920s in statically indeterminate trusses (Grüning 1926). Much of the early theoretical work was completed in Europe during the following decade. The first mathematical representation of shakedown behavior was given by Bleich (1932) for a truss with one degree of static indeterminacy. Melan (1936) extended the mathematical framework for structures with more than one degree of indeterminacy. Since the mid-1900s, general theorems of shakedown and different methods of computing the shakedown load for beams and frames have been developed. There are three theorems which determine whether or not a structure will shake down (Neal 1977). These are the lower-bound, upper-bound, and uniqueness theorems, which are analogous to the well-known theorems regarding plastic limit loads for structures under static loading cases.

The lower-bound theorem requires the satisfaction of equilibrium and yield conditions. This theorem states that if a set of statically admissible residual moments exists such that the sum of those residual moments and the elastic moments from a particular applied loading pattern does not produce moments exceeding the plastic moment capacity anywhere along the beam, that applied load must be less than or equal to the shakedown limit load. Thus, all loading conditions satisfying the lower-bound theorem will result in a structure that will shake down to elastic behavior after some number of cycles.

The upper-bound theorem requires the determination of a plastic mechanism that satisfies compatibility of deformations. The theorem states that the applied load required to form this mechanism must be greater than or equal to the shakedown limit load. Thus, all loading conditions leading to all possible plastic mechanisms are greater than or equal to the shakedown limit load and will result in incremental collapse for all cases except for the true shakedown limit load. The true shakedown limit load is the smallest load resulting from all possible mechanisms.

The uniqueness theorem simply states that only the exact and unique shakedown limit load can satisfy both the lower- and upper-bound theorems.

The upper-bound theorem often provides an easy method to compute the shakedown load for a particular loading pattern for simple structures. However, concepts based on the lower-bound theorem are often used to develop simple design procedures for complex structures. This is the case for the AASHTO provisions for inelastic moment redistribution, which are discussed in Section 2.5.2.

An example of using both the upper- and lower-bound methods to calculate the shakedown load is given in the following sections for the same propped cantilever beam with a single moving point load from the previous example. For both examples, the assumptions that the section remains elastic up to a moment of M_p, that the material is elastic-perfectly plastic with no strain hardening, and that the positive and negative plastic moments are equivalent ($\pm M_p$) remain in effect. Refer to Figure 2-14 and Figure 2-15 for diagrams and calculations for the upper- and lower-bound theorem examples, respectively.

Upper-Bound Theorem Example

To calculate the shakedown load using the upper-bound theorem, a virtual work approach is used. First, the elastic moment envelope is computed. This is shown in the top frame of Figure 2-14 and is identical to that shown in the top frame of Figure 2-12. The maximum positive and negative moments occur at points A and D, respectively. These points will be the locations of the plastic hinges in the shakedown mechanism, which is shown in the middle frame of the figure. Because this is a simple structure, the controlling mechanism for shakedown is easily determined, as it must be the case that hinges form at the locations of the maximum positive and negative moments. For more complex structures, several mechanisms may need to be considered to arrive at the correct shakedown load. If the incorrect mechanism is chosen, the computed load will be greater than the correct shakedown limit load for the structure.

Once the moment envelope and mechanism are known, the internal and external virtual work are computed. These calculations are summarized in the bottom frame of Figure 2-14. The internal virtual work is the product of the plastic moment and the plastic hinge rotation at each hinge location. These values are added together to get the total internal virtual work ($\delta W_{internal}$). The external virtual work is the product of the moment from the elastic moment envelope and the plastic hinge rotation at each hinge location. These values are added together to get the total external virtual work ($\delta W_{external}$).

The shakedown load is calculated by equating the total internal and external virtual work. For the propped cantilever in this example, the shakedown load is equal to $5.59\ M_p/L$. For comparison, the load that causes the first hinge to form at the fixed end is $5.21\ M_p/L$ and the minimum static plastic collapse load is $5.83\ M_p/L$, occurring when the load is located a distance of $0.41\ L$ away from the pinned support (Fukumoto & Yoshida 1969).

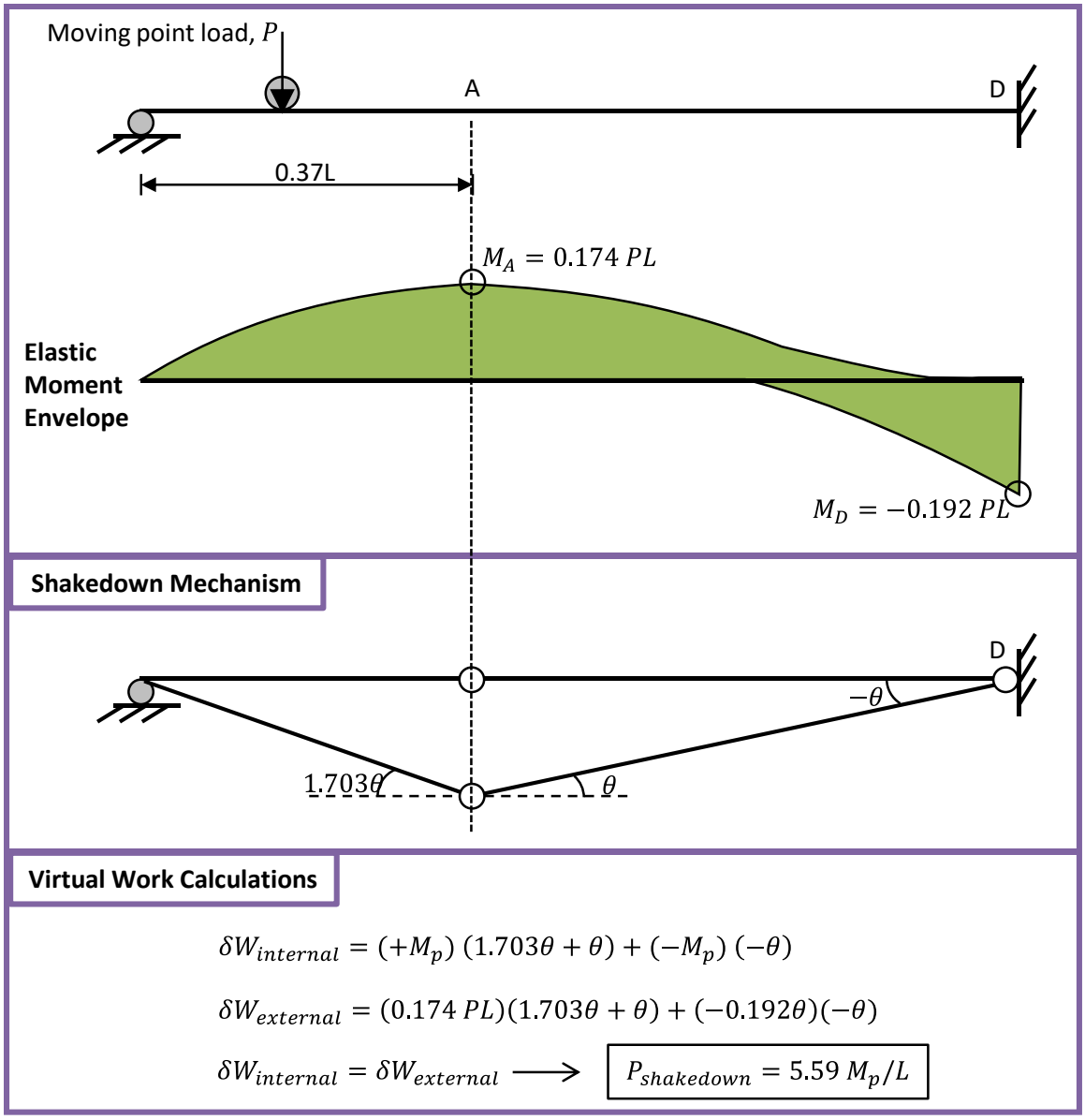

Figure 2-14: Upper-Bound Method Example

Lower-Bound Theorem Example

The first step in computing the shakedown load using the lower-bound method is to determine the elastic moment envelope for the applied load, which is shown in the upper frame of Figure 2-15 and is identical to the previous examples. The critical locations for positive and negative bending are points A and D, respectively, as in the previous two examples. Next, a distribution of residual moments must be chosen that satisfies

equilibrium in the unloaded structure. This distribution of residual moments is shown in the middle frame of Figure 2-15 in a general sense, such that the residual reaction forces ($R_{residual}$) are equal and opposite, resulting in a linearly varying moment diagram with a maximum residual moment at D.

To satisfy the requirements of the lower-bound theorem, total moment, or the summation of the elastic moment and the residual moment, must not exceed the capacity at any location. The bottom frame of Figure 2-15 provides calculations for the maximum load that can be applied to satisfy this requirement at both points A and D for different values of the residual reaction force. The controlling maximum calculated load, shown in bold for each case, will be less than or equal to the correct shakedown load ($5.59\ M_p/L$), which is achieved when a residual reaction force is chosen such that the maximum applied loads to remain below the capacity at both A and D converge to the same value.

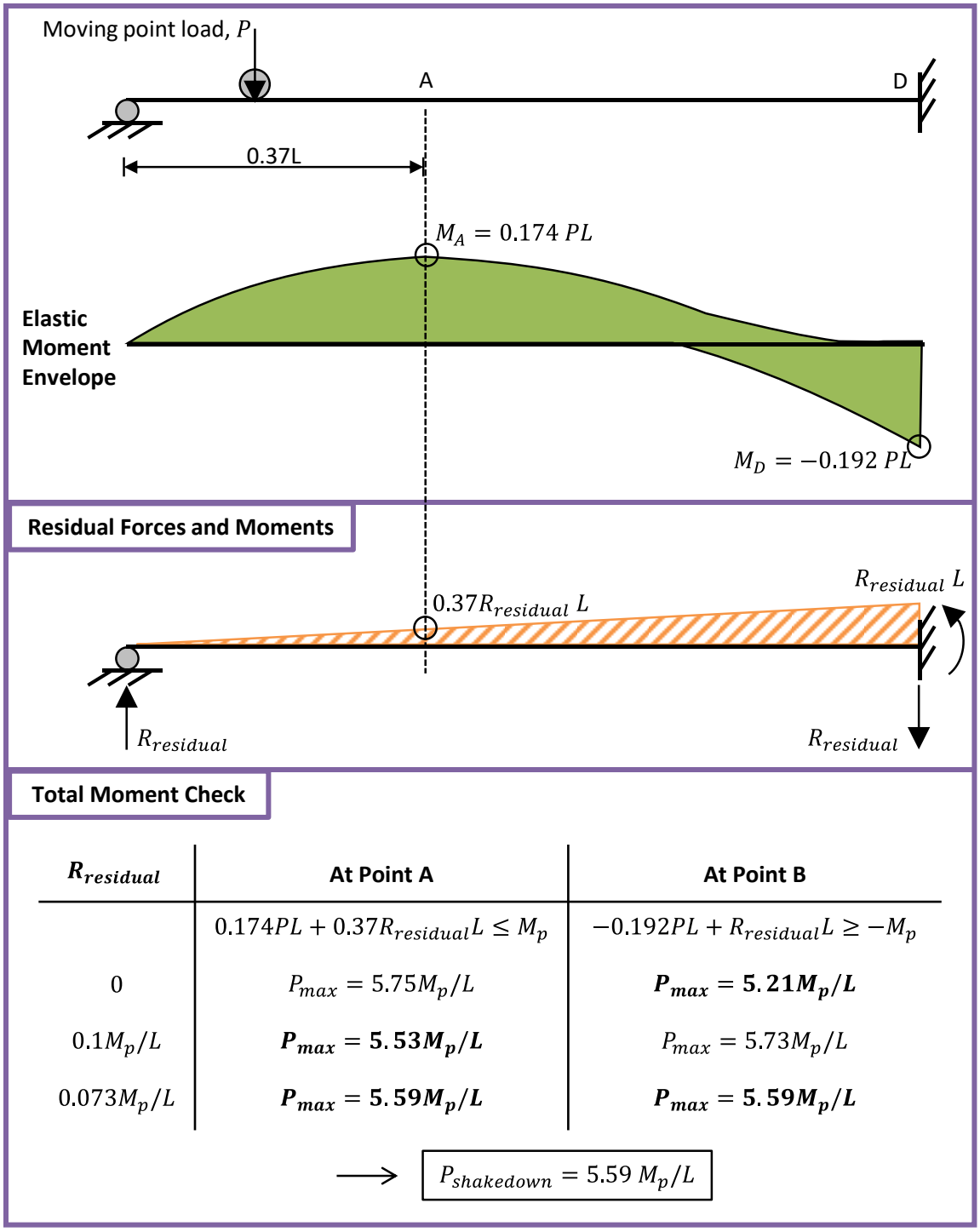

$R_{residual}$	At Point A	At Point B
	$0.174PL + 0.37R_{residual}L \leq M_p$	$-0.192PL + R_{residual}L \geq -M_p$
0	$P_{max} = 5.75M_p/L$	$\boldsymbol{P_{max} = 5.21M_p/L}$
$0.1M_p/L$	$\boldsymbol{P_{max} = 5.53M_p/L}$	$P_{max} = 5.73M_p/L$
$0.073M_p/L$	$\boldsymbol{P_{max} = 5.59M_p/L}$	$\boldsymbol{P_{max} = 5.59M_p/L}$

$\longrightarrow$ $P_{shakedown} = 5.59\ M_p/L$

Figure 2-15: Lower-Bound Method Example

2.4.3 Previous Research on Shakedown of Steel and Composite Girders

The majority of experimental testing completed in the area of shakedown has been conducted on bare steel beams, not on composite members. Small-scale tests were conducted by Klöppel (1936), Massonnet (1953), Gozum (1954), Sherbourne (1963), Fukumoto and Yoshida (1969), and Eyre and Galambos (1970), who all observed that the predicted shakedown loads were conservative, possibly due to strain hardening of the steel, which was typically ignored in the predictions.

Larger-scale shakedown testing for bridge structures began in the 1970s and 1980s under the direction of the American Iron and Steel Institute (AISI) (Grubb & Carskaddan 1979, Carskaddan 1980, Grubb & Carskaddan 1981). Following some initial theoretical studies, the experimental research was focused primarily on the effects of slenderness and moment gradient on the inelastic moment-rotation behavior of composite I-girders. However, with the exception of one test consisting of an actual steel-concrete composite girder, the experiments were conducted on singly symmetric steel-only I-sections with larger top flanges than bottom flanges to represent a composite section in negative bending that engages the reinforcing bars in the deck. This research led to the development and publication of an AASHTO guide specification for "Alternate Load Factor Design" (ALFD), also known as autostress design, which detailed an iterative inelastic analysis procedure to incorporate yielding and moment redistribution into bridge design, but was restricted to steel sections with compact flanges and webs (AASHTO 1986).

Design using the ALFD guide specification was verified by tests on composite bridges and bridge models. Roeder and Eltvik (1985) conducted load tests on a new bridge designed using ALFD up to load levels that caused yielding and inelastic moment redistribution. Good behavior was observed throughout the test, and less permanent deformation and deck cracking was observed than predicted. Moore and Grubb (1990) tested a ⅖-scale model of a two-span, three-girder, composite bridge designed using ALFD provisions, with the exception that the girders had noncompact webs. This model bridge performed well under AASHTO specified design service loads, overloads, and maximum loads, deeming ALFD an appropriate design method for sections with noncompact webs. Similar good behavior under AASHTO-defined limit states was observed by Weber (1994) after testing of a ½-scale model of a three-span, fully composite, single bridge girder comprised of a compact steel beam designed according to the ALFD specifications.

However, a few other experimental studies indicated that composite girders may not actually achieve shakedown under repeated large loads. Bergson (1994) conducted shakedown testing on a ⅓-scale model of a three-span, four-girder bridge that was initially designed and constructed for the purposes of elastic testing. Results from this test indicate a loss in composite action at loads near the predicted shakedown load, although extensive cracking was observed in the under-designed deck at large loads. Flemming (1994) applied an actual moving load using a bogie that was rolled across a ½-scale model of a two-span, five-girder bridge to investigate the shakedown behavior of partially composite girders. One of the spans of the bridge was constructed as 80% composite, while the other span was only 50% composite. The deflections generally did not stabilize during shakedown testing, and degradation in the composite strength was observed with additional cycles at larger loads. Similar behavior was observed by Thirugnanasundralingam (1991) during testing conducted on two-span, fully composite girders under a moving load applied using a "rocker beam" which had a curved bottom flange so that as it rotated, the point of load application moved along the test specimen. The tests indicated that the experimental shakedown load was significantly lower than the theoretical value, as measured slips and deflections did not stabilize. It is useful to note here that these specimens showing poor shakedown behavior in these three studies were no more than ½-scale models and had deck thicknesses not exceeding 4 inches. It is possible that the unrealistic deck design may have contributed to the observed poor behavior.

2.5 Applicable AASHTO Design Provisions

The following sections summarize the applicable design provisions from the AASHTO *LRFD Bridge Design Specifications* (AASHTO 2010). This includes both the procedures to design welded stud shear connectors and for inelastic moment redistribution.

2.5.1 Shear Connector Design

The provisions for the design of welded stud shear connectors in composite I-girder bridges are given in Section 6.10.10 of the LRFD specifications. The design starts with the fatigue provisions, because that limit state usually governs the number of connectors required, and then a strength check is performed. Partially composite design is not allowed in these specifications, primarily because the demands of the fatigue provisions usually result in fully composite girders.

Fatigue Design

The pitch (p), or longitudinal spacing, of the shear connectors is determined using the following equation (AASHTO LRFD Equation 6.10.10.1.2-1):

$$p = \frac{n\,Z_r}{v} \qquad \textbf{Equation 2-7}$$

where n is the number of connectors placed transversely in the cross section, Z_r is the fatigue resistance of a single connector, and v is the elastic shear flow at the steel-concrete interface. The fatigue resistance depends on the single-lane average daily truck traffic ($(ADDT)_{SL}$), which also determines which of the two fatigue load combinations is used for design. For $(ADTT)_{SL}$ values exceeding 960 trucks per day, the Fatigue I load combination is used to design for infinite fatigue life. Otherwise, the Fatigue II load combination is used to design for a finite fatigue life for a particular number of truck passages (N) over an assumed 75-year design life. The only difference between the two load combinations is the live load factor, which is 1.50 for infinite life for Fatigue I and 0.75 for finite life for Fatigue II. The fatigue shear resistance (Z_r) for infinite and finite life are given in the following equations.

For infinite life and the Fatigue I load combination (AASHTO LRFD Equation 6.10.10.2-1):

$$Z_r = 5.5d^2 \qquad \textbf{Equation 2-8}$$

For finite life and the Fatigue II load combination (combination of AASHTO LRFD Equations 6.10.10.2-2 and 6.10.10.2-3; 6.6.1.2.5-3):

$$Z_r = (34.5 - 4.28\,log(N))d^2 \qquad \textbf{Equation 2-9}$$

$$N = (365)(75)n(ADTT_{SL}) \qquad \textbf{Equation 2-10}$$

where d is the diameter of the shear connector and n is the number of stress cycles on the connector for a single truck passage. For continuous bridges with span lengths greater than 40 feet, n is taken as 1.0 for all connectors located more than one-tenth of the span length away from an interior support. For connectors located within one-tenth of the span length from an interior support, n is taken as 1.5.

The shear flow is calculated as (AASHTO LRFD Equation 6.10.10.1.2-3):

$$v = \frac{V_f \, Q}{I} \qquad \textbf{Equation 2-11}$$

where V_f is the range of vertical shear force at a particular section due to fatigue loading, Q is the first moment of the transformed area of the concrete deck, and I is the transformed moment of inertia of the composite cross section. This procedure inherently assumes that any slip at the interface is negligible so that the section is effectively fully composite.

Strength Design

For strength limit states, the number of connectors required is determined through plastic analysis of the cross-section, as discussed in Section 2.2.2. The minimum number of connectors (N) to be provided between the points of zero and maximum moment is (AASHTO Equation 6.10.10.4.1-2):

$$N = \frac{P_n}{Q_n} \qquad \textbf{Equation 2-12}$$

where P_n is the total longitudinal shear force in the deck at the point of maximum moment, and Q_n is the factored ultimate shear strength of a single connector, as defined in the specification. Note that P_n is equivalent to the variable C_f defined in Section 2.2.2. However, since partial-composite design is not currently allowed by the specifications, the third line of Equation 2-1 and Equation 2-2 is not included.

Other Requirements

The minimum and maximum longitudinal spacing allowed for shear connectors are 6 and 24 inches, respectively. The connectors are expected to be distributed with equal spacing along the length of the girders. The minimum transverse spacing of connectors is 4 inches, while the minimum clear distance to the edge of the flange is specified as 1 inch. Each connector must penetrate at least 2 inches into the deck and must have a clear top cover of concrete of at least 2 inches.

2.5.2 Inelastic Moment Redistribution

The autostress design provisions that first appeared in the AASHTO ALFD guide specification document in the mid-1980s were introduced into the first edition of the

AASHTO LRFD bridge design specifications nearly a decade later (AASHTO 1994). These provisions from the ALFD specifications provided a more rigorous alternative to the 10% allowance of moment redistribution from the interior piers for compact, well-braced girders that had been in the provisions for 20 years (AASHTO 1973). However, autostress design was never widely used by bridge engineers because it required an iterative inelastic analysis and was limited to only compact steel sections (Barth et al. 2004).

By the third edition of the LRFD specifications, the 10% moment redistribution provision was removed from the code and replaced by a simple, rational approach to estimate the redistribution moments based on shakedown behavior (AASHTO 2004). Details regarding the development of these provisions are provided by Hartnagel (1997). These optional provisions, which remain essentially unchanged through the specifications current at the time of this report, are located in Appendix B6 of the AASHTO *LRFD Bridge Design Specifications* (AASHTO 2010). The steps, illustrated in Figure 2-16 for a symmetric three-span continuous girder, are as follows:

- Ensure that the interior pier section and bridge geometry abide by the specified requirements. In particular, the girders must be well-braced and have a compact compression flange. The web can be compact, noncompact, or slender to a certain extent, and bearing stiffeners are required. The bridge must not have horizontal curvature, and the supports cannot exceed a 10° skew angle, nor can the cross frames be staggered.
- Conduct an elastic analysis of the bridge girder for the load combination of interest. Moment redistribution is allowed for Service II and all Strength load combinations. Obtain the elastic moment envelope (M_e).
- Compute the effective plastic moment capacity (M_{pe}) at each interior pier. This effective capacity accounts for the slenderness of the section and ensures that an adequate amount of plastic rotation can be attained for moment redistribution to occur.
- If the magnitude of the elastic moment at an interior pier exceeds the effective capacity, the difference between the two is the amount of moment that needs to be redistributed. This "redistribution moment" at that pier (M_{rd}) is limited to 20% of the elastic moment at that location.
- Draw the redistribution moment diagram by connecting the computed redistribution moments at each pier with straight lines.

- Add the redistribution moment diagram to the elastic moment envelope, and check that the capacity is not exceeded at any other location along the girder.

Elastic Moment Envelope

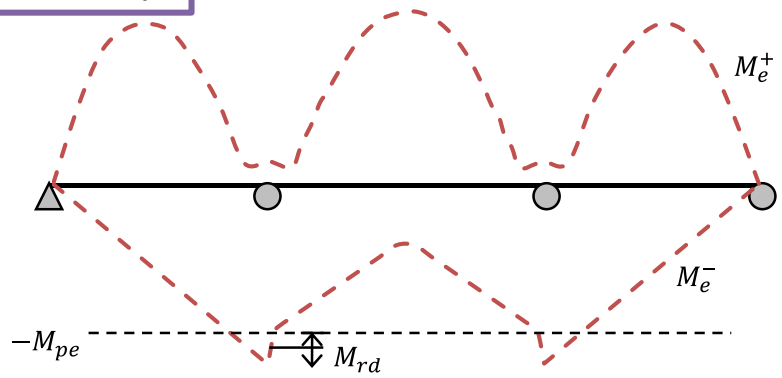

$$M_{pe} = \left(A - 2.3\frac{b_{fc}}{t_{fc}}\sqrt{\frac{F_{yc}}{E}} - 0.35\frac{D}{b_{fc}} + 0.39\frac{b_{fc}}{t_{fc}}\sqrt{\frac{F_{yc}}{E}\frac{D}{b_{fc}}} \right) M_n \leq M_n$$

A = Constant between 2.63 and 2.90, depending on section properties and limit state
E = elastic modulus

b_{fc} = width of compression flange
t_{fc} = thickness of compression flange
D = web depth
F_{yc} = yield stress of compression flange

$$M_{rd} = |M_e| - M_{pe} \leq 0.2M_e$$

Redistribution Moment Diagram

Resulting Moment Envelope

$$M_{total} = M_e + M_{rd}$$

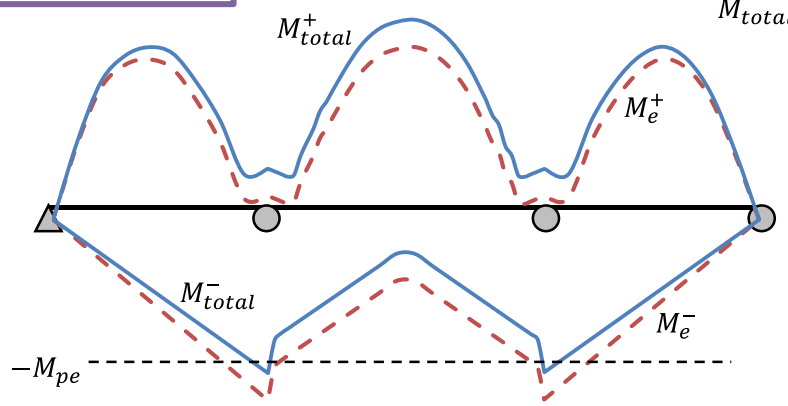

Figure 2-16: AASHTO Moment Redistribution Procedure

Note that this procedure is based on the lower-bound theorem, as it provides a simple method of determining a residual moment diagram that can be added to the elastic moments such that the capacity is not exceeded at any location along the girder. Thus, these redistribution moments are not necessarily representative of the actual residual moments expected to form in the structure.

2.6 SUMMARY

A comprehensive review of the relevant background information from the literature was presented in this chapter. This includes information regarding composite behavior, post-installed shear connectors, and inelastic moment redistribution. Additionally, applicable provisions from the AASHTO design specifications were discussed. These concepts were used to facilitate the research presented in the following chapters during the investigation into the behavior of continuous bridge girders strengthened with post-installed shear connectors and inelastic moment redistribution.

CHAPTER 3: PRELIMINARY BRIDGE STRENGTHENING STUDIES

3.1 OVERVIEW

Preliminary studies were conducted to evaluate the feasibility of the proposed approach to strengthen non-composite steel girder bridges with post-installed shear connectors and inelastic moment redistribution. These studies began by conducting a survey of existing Texas bridges that may be candidates for strengthening using this method. The bridges from this survey were then evaluated to assess the extent of strengthening that may be possible using this method. This chapter summarizes the process and results from these preliminary studies.

3.2 BRIDGE SURVEY

A survey of continuous non-composite steel I-girder bridges in Texas was conducted to determine the typical characteristics of bridges that may be candidates for strengthening with post-installed shear connectors and inelastic moment redistribution. The results from this survey formed the basis for the analytical and experiment work described in this dissertation. While detailed results of this survey are covered by Patel (2013), a summary is provided here.

Original design drawings and recent inspection reports from 36 continuous girder units from 25 bridges were studied. Most of these bridges were constructed between 1955 and 1965. Although a few of the surveyed bridges were constructed from plate girders with span lengths up to 270 feet, the focus of the survey was placed on the units consisting of rolled wide flange girders, which formed an overwhelming majority in the survey. The wide flange shapes vary from a 27WF94 to a 36WF194 for span lengths between 40 and 100 feet. Cover plates are welded to the top and bottom flanges to increase the flexural capacity at the interior supports for nearly all of the units studied. In some cases, similar cover plates are also located in the middle of the spans to improve the strength in positive bending.

Typical girder spacing ranges from 6.5 to 8.5 feet with three to eight girders in a typical cross section to accommodate two to six lanes of traffic. Approximately one-third of the bridges have skewed supports, while only a few have any horizontal curvature. The units studied are continuous over two to five spans and most are symmetric in both the longitudinal and transverse directions. The majority of the concrete decks are 6.5 inches

thick with average transverse and longitudinal reinforcement ratios of 0.9% and 0.5%, respectively.

Because only a few of the design drawings specified material requirements for each bridge, historic bridge design standards and material standards were consulted to determine the likely material properties of the steel beams, concrete deck, and reinforcing bars. The majority of the bridges were likely constructed using ASTM A7 steel, which has a minimum specified yield stress of 33 ksi, although a few bridges constructed after 1963 may have been built with ASTM A36 steel, having a yield stress of 36 ksi (AASHTO 2011). A design compressive strength of 3000 psi is assumed to have been used for the concrete deck, with the deck reinforcement having a likely yield stress of 40 ksi (THD 1951). The surveyed bridges are generally in good condition, with corrosion of the steel components and some cracking and spalling of the concrete decks and substructures being the most common issues noted during recent inspections.

3.3 CONCEPT STUDIES

Preliminary analyses were conducted on the 13 three-span continuous units from this survey to evaluate the feasibility and capabilities of strengthening with post-installed shear connectors and inelastic moment redistribution. To quantify the benefits gained from this strengthening, a load rating was conducted for each of the continuous units in the existing non-composite state as well as after strengthening.

3.3.1 Overview of Load Rating

Load rating provides a comparison of the load-carrying capacity of an existing bridge to the loads that are used in current design practices. This is a way to evaluate the safety and capacity of an existing bridge that was designed for different, usually smaller, loads.

Types of Load Rating and Limit States

The AASHTO *Manual for Bridge Evaluation* specifies procedures for conducting a load rating of an existing bridge using three methods: allowable stress rating, load factor rating, and load and resistance factor rating (AASHTO 2011). Load factor rating, based on the load factor design provisions from the most recent version of the AASHTO *Standard Specifications for Highway Bridges*, was chosen for the purposes of these studies to be

consistent with typical practices of the Texas Department of Transportation (AASHTO 2002).

A complete and thorough load rating considers flexure, shear, and axial forces at all locations in every member in the superstructure and substructure as well as the connections and any other details. The final reported load rating of a bridge is the smallest rating calculated in any component at any location along the bridge. However, for a particular type of bridge, the controlling sections and limit states can often be easily identified beforehand to simplify the process. For the continuous steel I-girder bridges considered in this study, the flexural capacity of the girders will usually control, especially if the girders are comprised of rolled sections. For built-up sections with stiffeners and thin webs, a load rating for shear should also be considered. Connections, such as girder splices, are not normally considered in the rating process but can be if necessary or desired. Since the bridges considered here are comprised of rolled sections and the welded girder splices carry low levels of moment, only the girder flexural behavior was considered in the load rating.

Load ratings for strength can be computed at both inventory and operating rating levels. The inventory rating is associated with load magnitudes used in the design of new bridges and makes use of the same load factors. Live loads equivalent to the inventory rating should be able to be resisted indefinitely throughout the life of the bridge, barring any fatigue or durability-related failures. The operating rating represents the maximum load the bridge is permitted to sustain. Repeated application of this large level of load to the bridge is not recommended (AASHTO 2011).

The limit states considered in these load ratings were Overload and Maximum Load, as defined by the AASHTO Standard specifications (AASHTO 2002). The Overload limit state restricts permanent inelastic deformations from heavy permit vehicles that may be occasionally allowed on the bridge (Hansell and Viest 1971). It corresponds to the Service II limit state in the LRFD specifications, and restricts the maximum stresses in the steel beam to 80% and 95% of the yield stress for non-composite and composite sections, respectively. Because the AASHTO specifications do not allow for partially composite design, it is unclear what limiting stress should be used for partially composite sections. However, a 95% limit has been chosen for this study due to the significant increase in stiffness for strengthened girders with even small composite ratios. When moment redistribution is considered from the interior supports, the stress limit at the Overload limit state is ignored in those regions. The Maximum Load limit state is associated with the

ultimate capacity of the bridge and corresponds to the Strength I limit state in the LRFD specifications when primarily considering gravity loads. Limit states involving serviceability, lateral loads, or other types of loads are generally not considered in load rating. The fatigue limit state can be investigated using provisions in the *Manual for Bridge Evaluation* if desired, but this was not done in this case (AASHTO 2011).

Load Rating Procedures

The first step in load rating is to conduct a structural analysis of the existing bridge using the live load corresponding to the chosen rating method. For the load factor rating conducted here, this was an HS 20 live load as defined in the AASHTO Standard specifications and summarized in Figure 3-1.

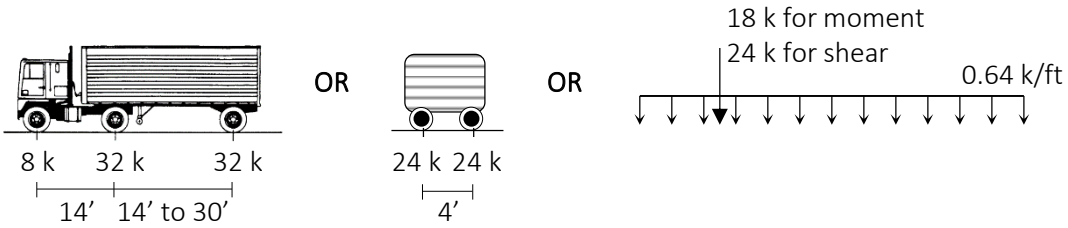

Figure 3-1: HS 20 Live Load (AASHTO 2002)

Next, the flexural capacities of the critical sections of the bridge are calculated. For load factor rating, the capacity is calculated using the design provisions in the AASHTO standard specifications. For a compact, sufficiently braced section in flexure, the capacity is taken as the plastic moment (M_p) for the Strength I limit state. For the Service II limit state, the capacity refers to the limits on the maximum stress in the steel beam. Actual or estimated in situ material properties should be used in the load rating calculations. Because this information was not readily available for these studies, the recommended material properties from the *Manual for Bridge Evaluation* were used, as discussed in Section 3.2 (AASHTO 2011).

The next step is to compute the rating factor at every critical section along the bridge for both the inventory and operating rating levels. This rating factor (RF) represents the fraction of the live load that the bridge can safely carry, and is defined as the ratio of the capacity available to resist live loads to the factored live load:

$$RF = \frac{C - A_1 D}{A_2 (L + I)} \qquad \textit{Equation 3-1}$$

where C is the capacity of the section, D is the dead load force effect, $(L + I)$ is the live load force effect including the impact factor or dynamic allowance, and A_1 and A_2 are load factors that depend on the type and level of the load rating. For load factor rating, A_1 is taken as 1.3 for both the inventory and operating levels, and A_2 is taken as 2.17 for the inventory rating and 1.3 for the operating rating. Because the only difference between the inventory and operating load rating calculations is the load factor on the live load (A_2), the two ratings will differ by a constant factor for all bridges. The operating rating will always be 1.67 times greater than the inventory rating. A bridge can adequately resist the full live load if all rating factors are greater than unity.

The final step in the rating procedure is to express the rating factor in terms of the live load. This is simply done by multiplying the rating factor by the magnitude of the HS load used in the structural analysis. For example, for the HS 20 load used here, the rating factor is multiplied by 20. The lowest inventory and operating load ratings from every section along the bridge are then chosen as the final load ratings for the bridge.

The load rating calculations for these concept studies were carried out using BAR7 (PennDOT 2010). This software, developed by the Pennsylvania Department of Transportation, analyzes a single girder line of a bridge using the provisions outlined in the *Manual for Bridge Evaluation*.

3.3.2 Load Rating Results

The 13 three-span bridges from the survey included in the concept studies were load rated before and after strengthening to evaluate the proposed strengthening method. Figure 3-2 shows a bar graph summarizing the results for existing and strengthened bridges. No moment redistribution was considered for the existing non-composite bridge girders. All girders were strengthened to a composite ratio of 30%, and the figure illustrates the variation in load rating for the strengthened girders both with and without consideration of moment redistribution.

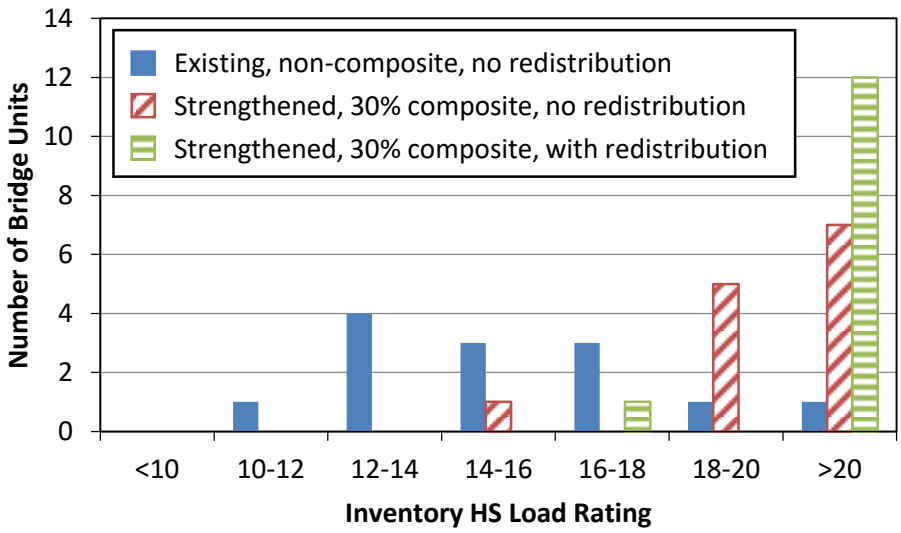

Figure 3-2: Load Rating Results

The existing bridges have inventory load ratings varying from HS 10.5 to HS 21.6, with 12 of the 13 bridges falling below the HS 20 target. The controlling load rating for all 13 of the existing bridges was the Overload limit state in one of the positive moment regions along the girders. This indicates that these bridges are good candidates for the proposed strengthening method, which is most effective in regions of the bridge dominated by positive bending. The Overload limit state is expected to control over the Maximum Load limit state for compact well-braced steel sections which can develop the full plastic moment capacity (Mertz 2004).

Without considering any moment redistribution, the strengthened bridges have inventory load ratings ranging from HS 15.0 to HS 23.9 with just over half of the strengthened bridges exceeding the HS 20 target. The controlling load rating for all of these girders is the Overload limit state in the negative moment regions, indicating that composite behavior has provided a significant strength gain in the positive moment regions. It also indicates that considering moment redistribution can further increase the load rating.

After strengthening to a composite ratio of 30% and allowing for moment redistribution, all but one of the 13 bridges have an inventory load rating exceeding HS 20. For most of the girders, the controlling load rating for this case is the Maximum Load limit state in negative moment regions, although a few bridges are controlled by the Overload limit state in positive bending. It is important to note here that the greatest contributor to

the increase in the load rating by considering moment redistribution is from the removal of the stress limits at the interior supports at the Overload limit state, so that the girder is allowed to reach the effective plastic moment at these locations . This leads to a large increase in the capacity at the Overload limit state, which often results in a significant increase in the load rating without actually requiring any moments to be redistributed. For all bridges in this study, the flexural capacity at an interior pier for the Overload limit state increases by 35% to 45% as the stress limit is removed in lieu of the effective plastic moment.

The only bridge that required moments to be redistributed in addition to this increase in capacity is the single bridge that remained below the HS 20 rating target. To reach an HS 20 inventory rating, this bridge must be strengthened to nearly fully composite in the positive moment regions with 13% of the elastic moment at the interior supports redistributed to the adjacent span regions at the Maximum Load limit state.

3.3.3 Summary

Thirteen three-span bridge units from the survey were investigated to evaluate the feasibility of the proposed strengthening method involving post-installed shear connectors and inelastic moment redistribution. The existing non-composite bridges were nearly all load rated below an HS 20 inventory level, which was chosen as the strengthening target for these studies. By adding post-installed shear connectors for a composite ratio of 30% and allowing for moment redistribution, all but one of the bridge units can be strengthened to an inventory load factor rating exceeding HS 20.

Overall, increases in the load rating of up to 70% were attained using a composite ratio of only 30% and minimal moment redistribution. These studies indicate that the proposed strengthening method is likely an efficient manner of strengthening continuous non-composite steel I-girder bridges.

CHAPTER 4: EXPERIMENTAL PROGRAM

4.1 OVERVIEW

A large-scale experimental program was developed to investigate the structural performance of continuous bridge girders strengthened with post-installed shear connectors and inelastic moment redistribution. Although the focus of this dissertation is on the behavior at the shakedown and ultimate strength limit states, the specimens were also tested under elastic and fatigue loading, as described by Ghiami Azad (2016). This chapter provides details of the single-girder specimens, the test setup, and the testing program. Results from these tests are discussed in Chapter 5 and Chapter 6.

4.2 SPECIMEN DESIGN

Two specimens were constructed to each represent a single girder line of a two-span continuous bridge. The first specimen had symmetric 42-foot long spans, while the second specimen had symmetric 52-foot spans. These span lengths are near full-scale, as 50-foot long exterior spans are common amongst the existing Texas bridges that were surveyed, as described in Chapter 3. Testing a single girder line conservatively eliminates interaction and load-sharing between adjacent girders and helps to simplify the interpretation of the results.

Although the specimens were designed to represent a typical bridge girder from the survey, it was difficult to replicate material properties from the mid-1900s due to lack of availability of older materials. Thus, instead of ASTM A7 steel, which has a specified minimum yield stress of 33 ksi, the steel beam was made of ASTM A992 steel, which has a minimum specified yield stress of 50 ksi. The design compressive strength for the concrete deck was 3 ksi, which is typical for existing bridges, although reinforcing bars with a nominal yield stress of 60 ksi were used in lieu of bars with a 40 ksi yield stress that are likely present in the existing bridges.

The two specimens were identical in cross section, as shown in Figure 4-1, and consisted of a W30x90 rolled wide flange section with a 6.5-inch thick, 6.5-foot wide concrete deck. This steel beam is lighter and more slender than any found in the bridge

---

Some content in this chapter has been previously published in the following article. This article was written primarily by the author of this dissertation with only minor contributions from the co-authors: Kreitman K, et al. (in press), 'Shakedown Behavior of a Continuous Steel Bridge Girder Strengthened with Post-Installed Shear Connectors', *Structures*, http://dx.doi.org/10.1016/j.istruc.2016.06.001

survey. Thus, it represents a conservative case for rolled steel shapes that could be found in bridge applications while preserving a realistic member depth. The deck dimensions are representative of the decks of the surveyed bridges, although the width is slightly smaller than the typical girder spacing (7 to 8 feet). The deck width was constrained by the geometry of the test setup and is not expected to have significantly affected the test results, because the strength of a partially composite girder is ultimately controlled by the strength of the shear connection, rather than that of the deck. The deck reinforcement was designed based on the findings from the bridge survey, and the reinforcement layout is shown in Figure 2-1. Pairs of adhesive anchors, shown in Figure 2-7, were used for shear connectors.

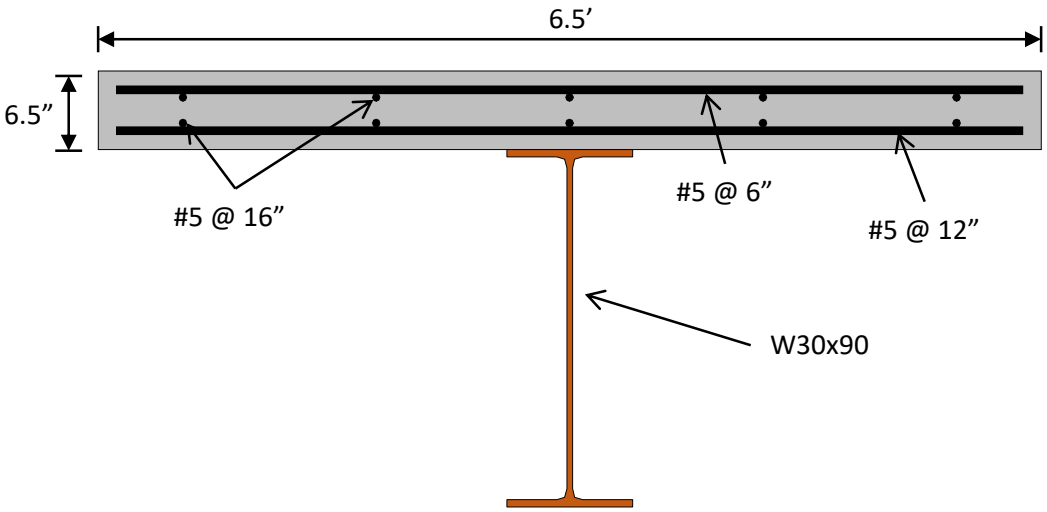

Figure 4-1: Cross Section View of Large-Scale Test Specimens

Elevation views of the two different girder specimens are shown in Figure 4-2 and Figure 4-3. The girders have a 12-inch overhang of the steel beam and a 6-inch overhang of the concrete deck from the centerline of the support on each end. Full-depth stiffeners were welded to each side of the web at the three support points to assist in bracing the beam during casting and to prevent localized failures at points of concentrated loads. A bolted splice in the steel beam was located at 7 feet from the interior support in the south span of both specimens. The splice was designed for 75% of the shear and moment capacity of the member, according to the AASHTO LRFD specifications (AASHTO 2010). This splice was provided to facilitate construction of the test specimen in the laboratory. Loads were applied to the girders in the four locations labeled A through D in the figures. The instrumentation layouts are also shown in the figures and are discussed in Section 4.5.

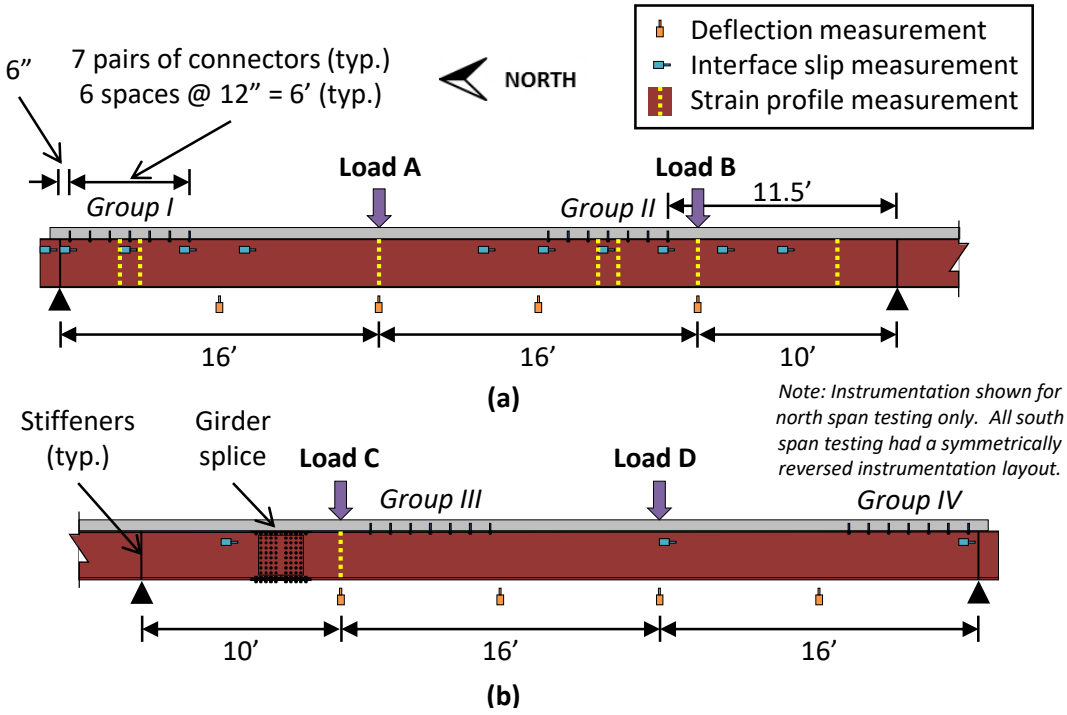

Figure 4-2: Elevation View of First Specimen – (a) North Span and (b) South Span

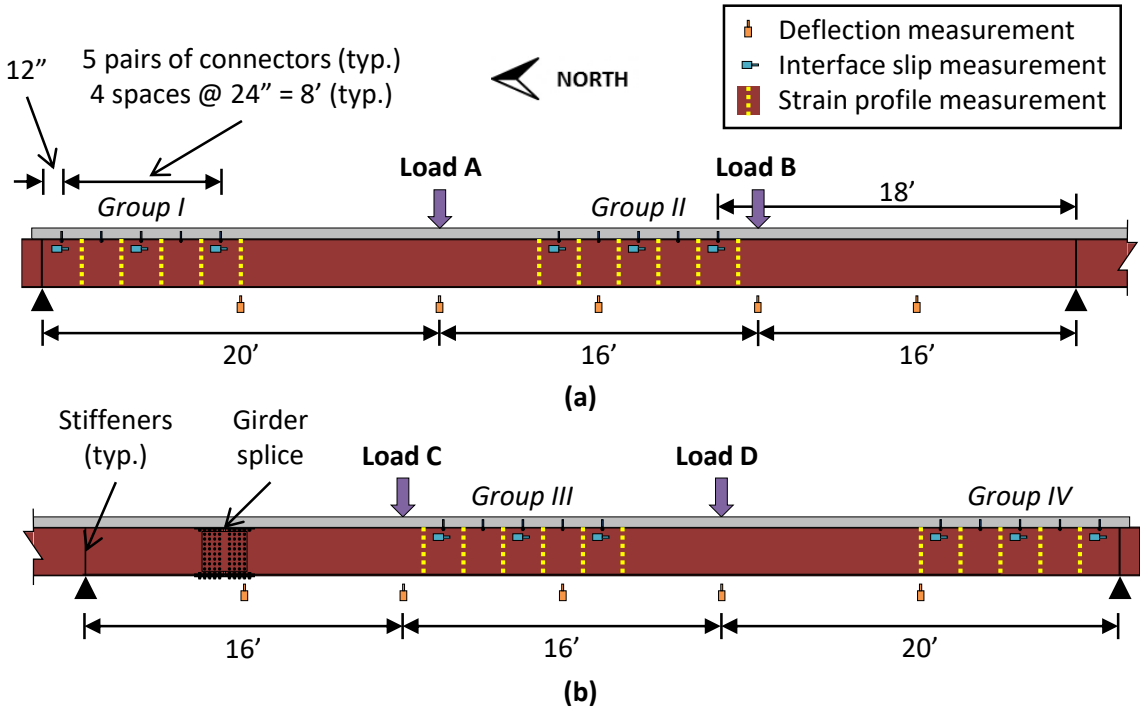

Figure 4-3: Elevation View of Second Specimen – (a) North Span and (b) South Span

To enhance the ductility of the specimens, the adhesive anchor shear connectors were concentrated in four groups near points of low moment demand, as indicated in Figure 4-2 and Figure 4-3. Groups I and II are located in the north span, while Groups III and IV are located symmetrically in the south span. The first specimen was designed to be nominally 30% composite so that each group contains 7 pairs of connectors. Thus, a total of 56 adhesive anchor shear connectors were installed along the entire length of the first specimen. The second specimen was designed as nominally 20% composite so that 5 pairs of connectors were installed in each group for a total of 40 connectors along the length of the girder. Transversely, the connectors were spaced approximately 6 inches apart on either side of the web. This essentially centered each connector on the protruding portion of the flange.

4.3 LABORATORY TEST SETUP

A test setup was constructed in the Ferguson Structural Engineering Laboratory to allow for an experimental program that would represent the effects of traffic loads on a bridge girder. Pictured in Figure 4-4 (a), the setup consisted of three support structures and four load frames that were positioned on the strong floor in the laboratory to accommodate the different geometry of the two specimens. The interior support (b) was designed to allow for essentially free rotation and longitudinal translation through means of a circular bar sandwiched between two flat plates. The two end supports (c) allowed for some restrained translation and rotation due to the flexibility of the slender W30x90 sections that served as the supports. Global rotation about the longitudinal axis was prevented by the V-shaped frames under the deck at the end supports (c). The bottom flange of the steel beam was braced laterally at 10- to 20-foot intervals using steel plates attached to short wide flange columns at each load frame (d,e). Sheets of polytetrafluoroethylene (PTFE) were used to reduce friction at all bracing locations. Hydraulic rams with capacities ranging from 200 to 500 kips were mounted on the load frames (d) and used to apply load to the top of the deck of the specimen. Load cells were placed at all load and support locations.

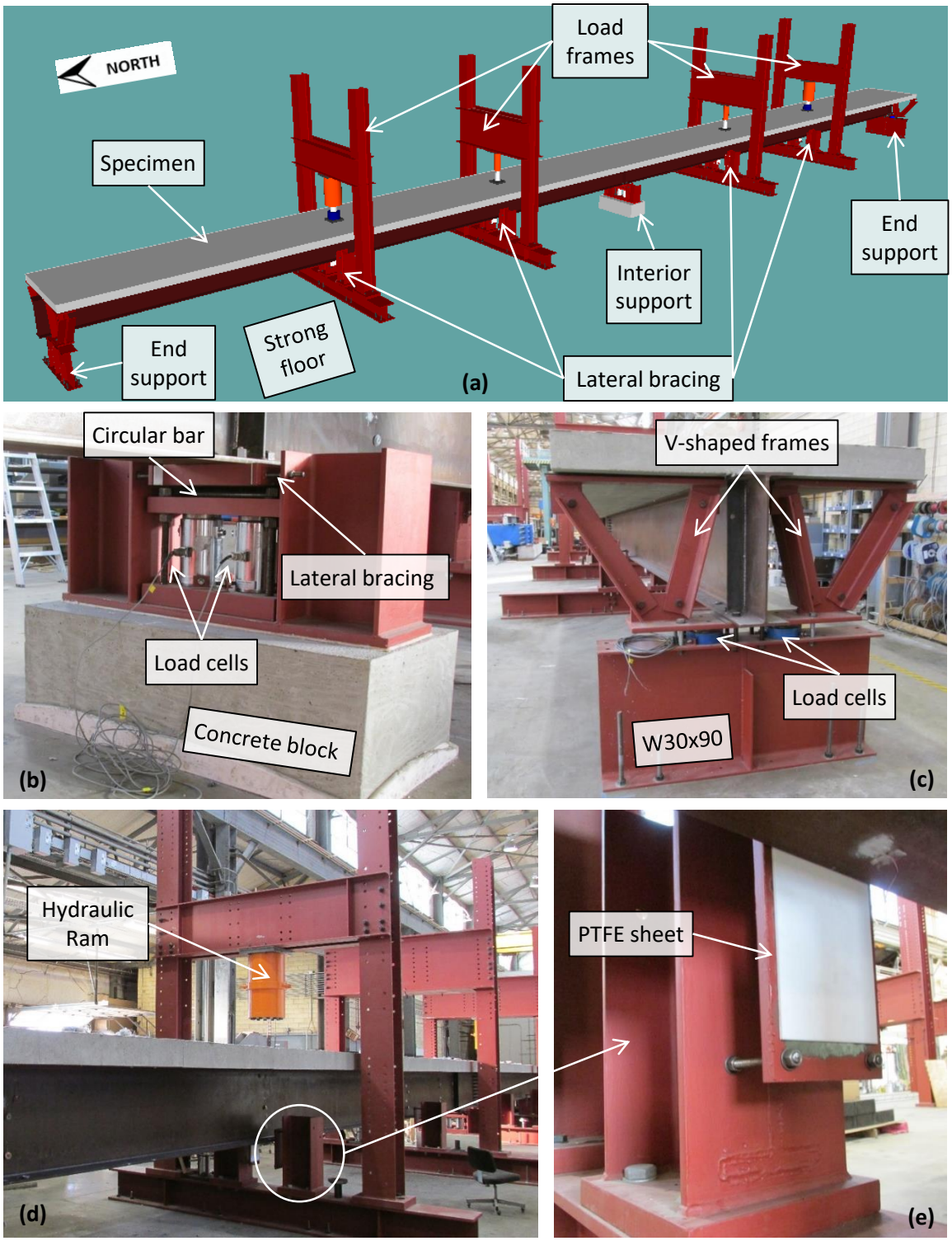

Figure 4-4: 3D Rendering and Photos of Test Setup – (a) Overall View, (b) Interior Support, (c) End Support, (d) Load Frame, and (e) Lateral Bracing

4.4 Specimen Construction

The specimens were constructed in several steps, as depicted in Figure 4-5. First, the steel beams were erected (a) and spliced together (b). Next, the deck formwork, which was constructed previously, was put in place (c). After laying and tying the mats of reinforcement (d), the deck was cast (e). The formwork was removed after approximately one week of curing.

Figure 4-5: Specimen Construction – (a) Steel Erection, (b) Splice Plates, (c) Deck Formwork, (d) Deck Reinforcement, and (e) Deck Casting

4.4.1 Connector Installation

The adhesive anchor shear connectors were installed after the deck was cast and cured, using the general procedure developed by Kwon et al. (2007). The connectors used in both of the specimens consisted of 7/8-inch diameter ASTM A193 B7 threaded rod with a corresponding structural nut and washer, and Hilti HIT-HY 200-R structural adhesive, as seen in Figure 4-6. The threaded rods were cut to approximately 6-3/4 inches long for a 4.5-inch embedment depth into the concrete deck. This resulted in a 2-inch top cover for the connectors as required by the AASHTO LRFD specifications (AASHTO 2010). Before installation, the cut rods were lightly cleaned and degreased to improve adhesion. The two-part adhesive was injected using the compatible Hilti HDM 500 manual dispenser and mixer.

Figure 4-6: Connector Supplies – (a) Threaded Rod and (b) Adhesive

The installation process is summarized in Figure 4-7. First, a 1-inch diameter hole was drilled through the top flange of the steel beam using a magnetic drill with an M2 HSS annular cutter (a). Care was taken to stop the drill as soon as possible after completing the cut in the flange as contact with the concrete tended to dull the cutter quickly. Next, a 15/16-inch diameter hole was drilled into the concrete deck to a depth of 4.5 inches, through the hole in the steel beam, using a rotary hammer drill (b). The hole was then cleaned as specified by the adhesive installation instructions (c). After using compressed air to clean the initial debris from the hole, an oversized round brush was inserted and removed twice using a twisting motion. Compressed air was used again to remove all debris from the hole. After cleaning, the adhesive was injected into the hole and the connector rod was inserted. The adhesive was viscous enough to not run downwards out

of the hole and to keep the threaded rod in place immediately after insertion. The rod did not need to be held in place while the adhesive cured. The threads below the underside of the top flange were wrapped with duct tape to prevent any adhesive from reaching that area. Excess adhesive was wiped off immediately with a rag. After allowing at least the specified one hour for the adhesive to cure, the tape was removed, and a washer and nut were placed on the threaded rod. The nut was then tightened to 125 ft-lb using a calibrated torque wrench, as specified by the adhesive installation instructions.

Figure 4-7: Connector Installation Process

4.4.2 Material Testing

To characterize the material strengths of the components of the specimen, several material tests were conducted on the steel beam, the deck concrete, the reinforcing bars, and the threaded rod comprising the connectors. The results from these tests are summarized in Table 4-1 and Table 4-2 for the two specimens. For the first specimen, the steel beams on either side of the splice were manufactured in different heats, and thus have slightly different material properties. The entire length of the second specimen was constructed of steel beams from the same heat as the south portion of the first specimen.

Table 4-1: Material Properties of the First Specimen

Material	Span	Yield Stress	Tensile, Compressive, or Shear Strength
Steel beam	North	Flange: 52.4 ksi Web: 54.7 ksi	Flange: 71.7 ksi Web: 72.3 ksi
	South	Flange: 56.3 ksi Web: 54.8 ksi	Flange: 76.0 ksi Web: 78.3 ksi
Concrete deck	Both	N/A	4.7 ksi
Rebar	Both	61.7 ksi	99.0 ksi
Connectors	Both	N/A	Tension: 134 ksi Shear: 87.7 ksi

Table 4-2: Material Properties of the Second Specimen

Material	Span	Yield Stress	Tensile, Compressive, or Shear Strength
Steel beam	Both	Flange: 56.3 ksi Web: 54.8 ksi	Flange: 76.0 ksi Web: 78.3 ksi
Concrete deck	Both	N/A	2.5 ksi
Rebar	Both	61.3 ksi	101 ksi
Connectors	Both	N/A	Tension: 134 ksi Shear: 87.7 ksi

The material properties of the steel beams were obtained by uniaxial tension testing of 8-inch long coupons that were produced from both the flange and web. The static yield

stress is reported in the table, as it is the most comparable to the slow load rates used in laboratory testing. With the exception of finite element modeling, in which different yield strengths were used for the web and the flange, all strength calculations presented or referenced in this dissertation were completed using the average yield stress from the two flange coupons.

The concrete material properties were determined by 28-day compression testing of 4-inch diameter, 8-inch tall cylinders that were cast from the deck concrete mix. To account for the two trucks of ready-mix concrete that were required to complete the total volume of the deck, the cylinders were made from a mixture of concrete from both trucks for the first specimen. For the second specimen, a separate set of cylinders were cast for each of the two trucks, and the strength reported in the table is an average of the two sets. Because testing of the specimen was conducted over a 6 to 9 month period after casting of the deck, cylinders were tested periodically during this time to get a measure of the concrete compressive strength throughout the testing program. However, no significant increase in the compressive strength was observed following the 28-day tests.

Tension testing of the deck reinforcement was conducted on short lengths of bars from the same heat as the reinforcement used in the deck of each specimen. The testing was conducted in a similar manner to the tension coupons of the steel beam, and the reported yield stress is the measured static yield stress during the test.

Shear and tension tests were conducted on the threaded rod used for the adhesive anchor shear connectors, and are discussed in more detail by Patel (2013).

4.5 INSTRUMENTATION

Both girders were instrumented to record the structural behavior during testing by measuring the applied loads and reaction forces, vertical deflections, interface slip, and longitudinal strain. Data from all of these sources were collected using an Agilent data acquisition system and LabVIEW software. Additionally, an optical motion tracking system (Optotrak Certus™) was used to continuously monitor the inelastic behavior during some phases of testing.

The layout of the instrumentation for each specimen is shown in the elevation views of Figure 4-2 and Figure 4-3. Deflections were measured at approximately evenly spaced locations along the length of the specimen at 8- to 10-foot intervals. The majority of the slip and strain measurements were concentrated in the vicinity of the post-installed shear

connectors to monitor the behavior of these specific regions. Note that for the first specimen, the instrumentation layout shown in the figure is for testing in the north span only. Testing in the south span was done using a symmetrically reversed instrumentation layout. The second specimen was tested using a consistent instrumentation layout throughout all phases of strength testing. Figure 4-8 shows photographs of the various types of instrumentation.

Figure 4-8: Photos of Instrumentation – (a) 500-kip Load Cell with Spherical Head, (b) 200-kip Load Cell with Load Button, (c) String Potentiometer, (d) Linear Potentiometer for Deflection, (e) Strain Gages, and (f) Linear Potentiometer for Slip

To measure the applied loads, 200- or 500-kip capacity load cells were placed between the piston of the hydraulic ram and a steel plate attached to the concrete deck using Hydro-Stone® gypsum cement. To minimize slight alignment errors, especially as the girder bends under load, spherical heads were placed on top of the 500-kip canister load cells, as shown in the figure (a). For the same purpose, a load button with a slightly curved bottom surface was threaded into the bottom of the 200-kip shear load cells, which were threaded directly into the piston of the ram (b). At all support locations, pairs of 100-kip (end supports) or 500-kip (interior support) load cells were sandwiched between steel plates to measure the reaction forces.

Vertical deflections were measured with either linear potentiometers with a 4-inch stroke (d) or string potentiometers with a 10- to 15-inch stroke (c). Interface slip was measured using linear potentiometers with a 2-inch stroke (f). These potentiometers were attached to the underside of the deck and measured the displacement of the deck relative to a small steel angle fixed to the underside of the top flange on the west side of the web. Analog dial gages with a 1-inch stroke were placed in a similar manner at a few locations on the east side of the web to provide redundancy in the measurements and to ensure that the slip values measured on both sides of the girder were the same. More than 250 strain gages with a 6-mm length were glued to the steel beam and deck reinforcement to monitor longitudinal strain in many locations (e). These gages were used to monitor the neutral axis depth, which indicates the amount of composite action, and to estimate the force carried by a pair of connectors.

To obtain an approximate measurement of the connector force and stress, sets of strain gages were placed through the depth of the steel beam on either side of a connector pair at a distance of one-half of the connector spacing from the connector location (see Figure 4-2 and Figure 4-3). From the measured strains, the curvature of the section was approximated, and the axial force in the steel beam was computed. The force carried by a connector pair was then estimated by taking the difference between the axial force in the steel beam on either side of the connectors. It was assumed that the two connectors in each pair shared the load equally and that any force transferred by friction is negligible. For the first specimen, only the middle connector in each group was instrumented with surrounding strain gages to estimate the connector force. For the second specimen, strain gages were used around all connectors for this purpose. Figure 4-9 shows the locations of the strain gages in a cross section surrounding the connectors for each specimen.

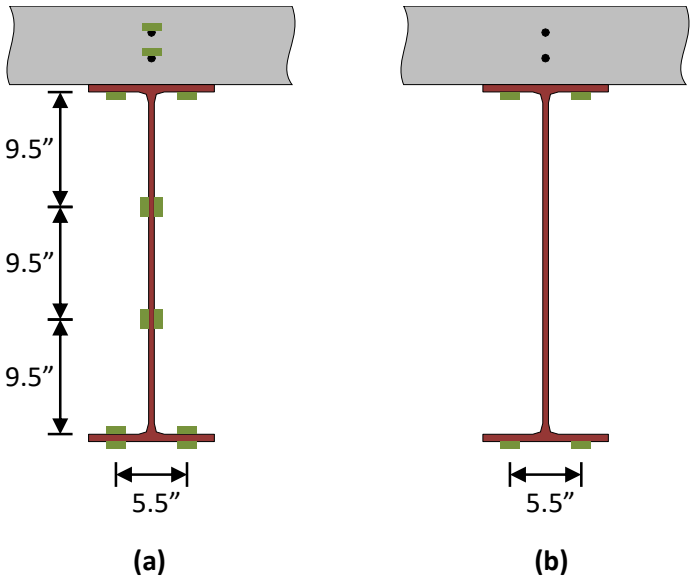

Figure 4-9: Cross Section Strain Gage Locations around Connectors for the (a) First Specimen and (b) Second Specimen

The optical motion tracking system was used to monitor the localized inelastic deformations in the steel beam during testing. This system is comprised of “markers,” which are attached to the specimen and emit rapid pulses of infrared light, and “position sensors,” which track the location of each marker in 3D space to an accuracy of 0.01 mm. A typical setup for this system is shown in Figure 4-10. For the first specimen, this system was used in all three critical locations at which yielding was expected, namely at the locations of Loads A and D as well as around the interior support. For the second specimen, only the regions near Load A and around the interior support were monitored using the optical system. Figure 4-11 shows the layout for the markers in the different locations for both specimens. All markers were placed on the west side of the girder. Post-processing of the data consisted primarily of computing longitudinal strains, rotations, curvatures, and neutral axis depths, and estimating the spread of the inelastic behavior along the length of the girder.

Figure 4-10: Typical Setup for Optical Motion Tracking System

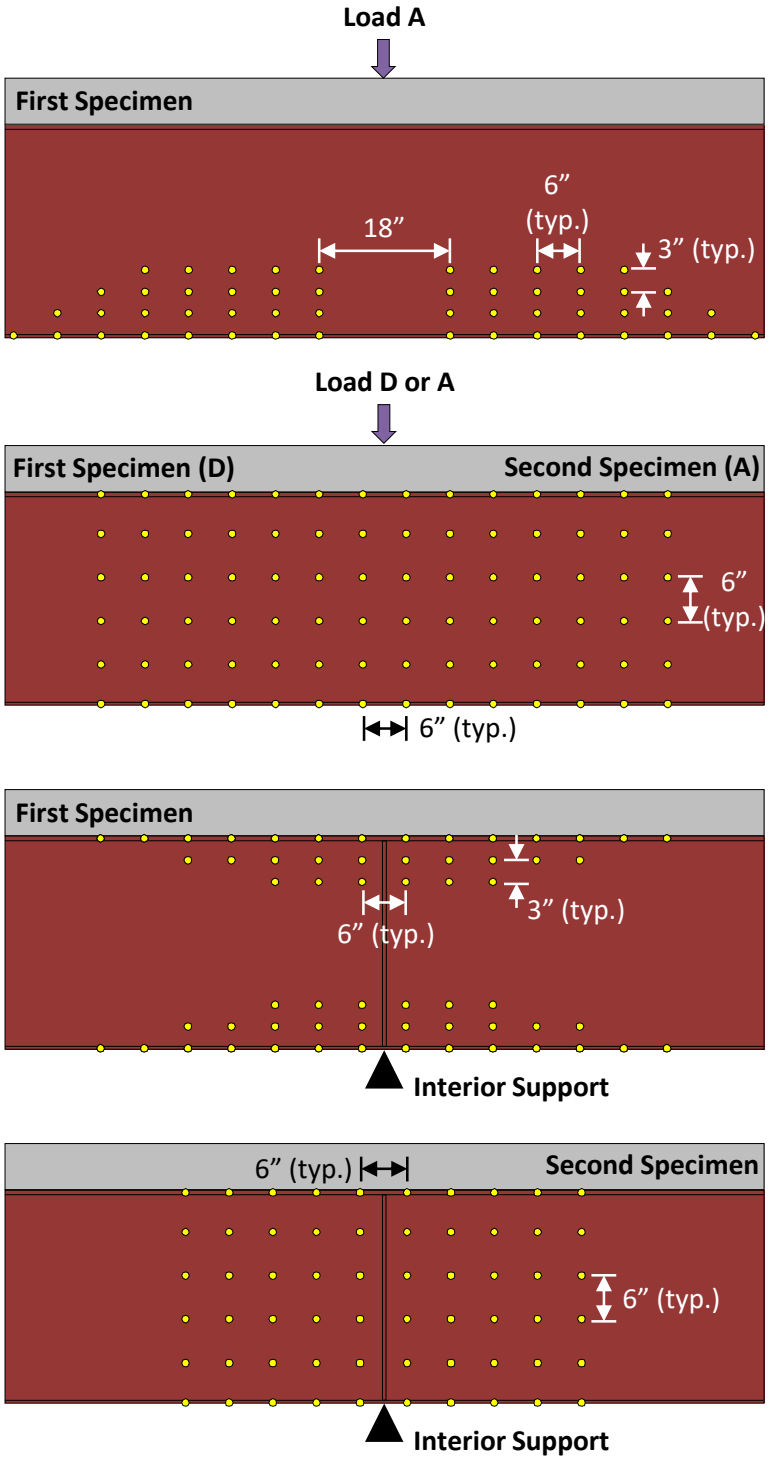

Figure 4-11: Marker Layout for Optical Motion Tracking System

In addition to the data recorded electronically, visual observations were made of the behavior during testing. This included observations of cracking in the concrete deck, yielding and local buckling in the steel beam, and fracture of the connectors. To better observe the inelastic behavior of the steel beam, a light coat of whitewash was applied on the east side of the steel beam at the locations at which yielding was expected, namely around the locations of Load A, Load D and the interior support.

4.6 TEST PROGRAM

Each girder specimen was subjected to several different types of loading over the course of approximately 6 months to simulate the various loads a bridge may be exposed to throughout its lifetime. This includes elastic-level loads, fatigue loads, large repeated loads representing the shakedown limit state, and monotonic loading to failure to determine the ultimate strength. The focus of this dissertation is on the inelastic behavior of the girders, namely on the testing conducted at the shakedown and ultimate strength limit states. Details from the elastic and fatigue tests are provided elsewhere (Ghiami Azad 2016), with important points summarized here.

Because of the difficulty of applying realistic bridge traffic loads in the laboratory, the effects of moving loads were simulated using cycles of strategically placed point loads at the four locations indicated in Figure 4-2 and Figure 4-3. For the first specimen, the two spans were generally tested separately, since applying load in one span put little demand on the shear connectors in the opposite span. Both spans of the second specimen were tested simultaneously, with the exception of the fatigue testing, to more accurately represent traffic flow along a bridge.

The following summarizes the eight phases of testing conducted on the first specimen, listed chronologically:

1. Elastic testing of the non-composite girder in the north span
2. Elastic testing of the composite girder in the north span
3. Shakedown testing in the north span
4. Fatigue testing in the south span
5. Fatigue testing in the north span
6. Shakedown testing in the south span
7. Ultimate strength testing in the south span
8. Ultimate strength testing in the north span

The following summarizes the five phases of testing conducted on the second specimen, listed chronologically:

1. Elastic testing of the non-composite girder in both spans
2. Elastic testing of the composite girder in both spans
3. Fatigue testing in the south span
4. Shakedown testing in both spans
5. Ultimate strength testing in both spans

4.6.1 Elastic Testing

Before installing the connectors, testing of the non-composite girder under small loads in the elastic range was conducted to break the natural bond at the interface between the bottom of the deck and the top flange of the steel beam. This is the expected condition of most existing non-composite bridges in the field. After installing the connectors, the same elastic testing was conducted on the strengthened girder to evaluate the increase in stiffness, which nearly doubled for both specimens. During the elastic testing phases, the maximum stress in the steel did not exceed 35% of the yield stress.

4.6.2 Fatigue Testing

Fatigue testing was conducted under the repeated application of Load A in the north span or Load D in the south span using a closed loop control system to automatically apply the loading cycles. The following sections provide only a brief summary of the test program for the fatigue testing in both specimens, as it is not the focus here.

First Specimen

A load range of 50 kips was chosen for the first fatigue test, which was conducted in the south span during the fourth phase of testing of the first specimen. This load caused connector slip ranges that were approximately equal to those expected under HL-93 fatigue loading, as defined in the AASHTO LRFD specifications, in strengthened bridges from the survey described in Chapter 3.

After excellent fatigue performance under a load range of 50 kips, it was decided to conduct the fatigue test in the north span of the first specimen under a larger load range of 75 kips. This represents a load that is 50% greater than an equivalent HL-93 fatigue truck, in terms of the slip demand placed on the shear connectors.

Second Specimen

A load range of 75 kips was again used for fatigue testing in the south span of the second specimen. Because of the longer span length and different connector layout in the girder, this further increased the maximum slip demand on the shear connectors to approximately 3 times that expected in a typical strengthened bridge under loading from an HL-93 fatigue truck.

4.6.3 Shakedown Testing

The phenomenon of shakedown was investigated by applying cycles of a load pattern which simulated the effects of a series of increasingly heavier trucks crossing a bridge. These load patterns are described in Figure 4-12 along with the corresponding moment diagrams for comparison to typical moment envelopes from a bridge live load. For the first specimen, the two spans were tested separately, so each cycle of the load pattern consisted of two load steps, each of which consisted of applying and then removing the load. Both spans of the second specimen were tested simultaneously, so three load steps comprised a single cycle of the load pattern.

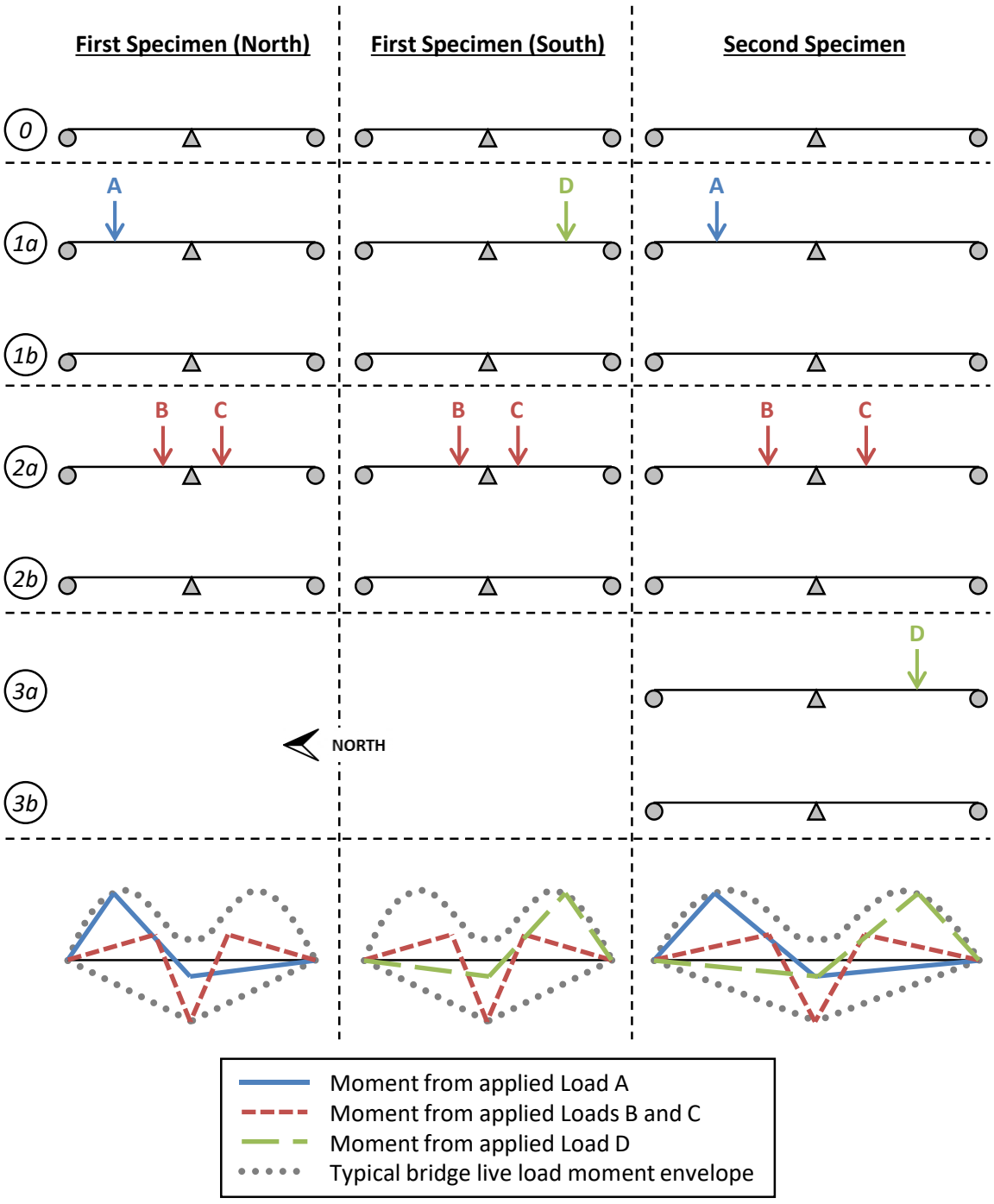

Figure 4-12: Load Patterns for Shakedown Testing

Cycles of the load pattern were applied repeatedly at the same level of load until the maximum deflection did not change significantly from one cycle to the next. At this

point, the girder was deemed to have "shaken down," or developed a set of residual moments which counteract the moments from the applied load to an extent that purely elastic behavior occurs for all future cycles of load at equal or lesser magnitude. Then, the magnitude of the load was increased, and the process was repeated. For testing purposes, shakedown was said to have occurred when the change in deflection did not exceed 0.01 inch between consecutive cycles. For the first specimen, this deflection was measured at the location of Load A for testing in the north span and at the location of Load D for testing in the south span. For the second specimen, in which the two spans were tested simultaneously, the deflection at both locations was required to abide by the criteria before shakedown was deemed to be achieved.

The relative magnitude of the loads that cause large positive moments (Load A and Load D) to the loads that cause large negative moments (Loads B and C) controls the amount of moment redistribution that must occur as the beam shakes down. The relative magnitudes of the loads were chosen to achieve approximately 20% moment redistribution from the interior pier sections for each specimen, which is the maximum amount of redistribution allowed by the AASHTO LRFD specifications (AASHTO 2010). For the first specimen, a ratio of approximately 0.87 was used between the magnitude of Load A or Load D and the magnitude of Loads B and C. This ratio was generally maintained throughout the test, especially at loads in the inelastic range. For the second specimen, this ratio was 1.0, because of the different span length and load locations.

Calculations for predicting the shakedown limit load for both specimens are given in Appendix A. Although moment redistribution of 20% was targeted, these calculations show that for the first specimen, the 0.87 load ratio actually results in moment redistribution of 22% in the north span and 25% in the south span. For the second specimen, the 1.0 load ratio actually results in moment redistribution of only 15%. These discrepancies are due to inconsistencies in defining the percentage of redistribution moments as well as the use of different stiffness distributions along the girder when determining the load ratio. As discussed in Chapter 7, because a continuous girder is statically indeterminate, the distribution of flexural stiffness along the length affects the elastic distribution of moments. In the early stages of research, the appropriate flexural stiffness distribution along a strengthened girder was unknown. Thus, the load ratio for the first specimen was chosen as an average of that from analyses at 20% redistribution using both the non-composite and composite stiffness, as described in Section 7.3. However, prior to testing of the second specimen, the parametric study described in

Chapter 7 had been completed, indicating that for the laboratory specimens, the distribution of flexural stiffness is close to that of the non-composite girder. Thus, the non-composite stiffness was used in the structural analysis which led to the choosing of the 1.0 load ratio for the second specimen. The prediction calculations in Appendix A use this non-composite stiffness for both specimens for consistency.

Approximately 100 cycles of load were applied during each of the three phases of shakedown testing over the course of several days. The loads were applied using pneumatic or electric hydraulic pumps, which were operated manually. For each loading and unloading step, data were recorded from all of the instrumentation at no less than five approximately equally spaced load intervals.

4.6.4 Ultimate Strength Testing

The final phases of testing for each specimen consisted of monotonic loading to connector failure to observe the ultimate strength of the girder as well as the post-peak load behavior. As shown in Figure 4-13, the two spans were tested separately for the first specimen, using Load A in the north span and Load D in the south span. Both Load A and Load D were applied to test the two spans simultaneously for the second specimen. Pneumatic or electric hydraulic pumps were used to manually apply the loads. In the elastic range, data were recorded at 5-kip load increments. Beyond the elastic range, data were recorded at deflection increments of 0.25 inch.

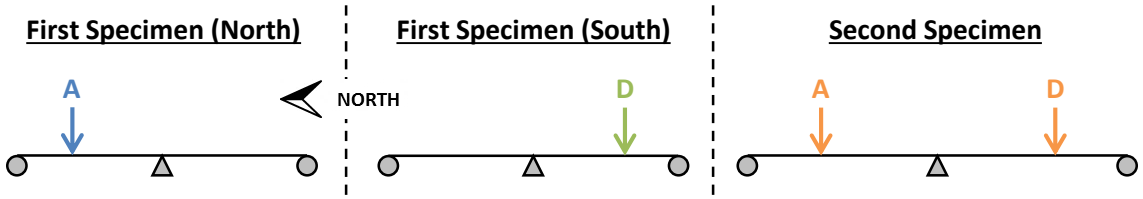

Figure 4-13: Load Patterns for Ultimate Strength Testing

4.7 SUMMARY

This chapter provided a summary of the experimental program that was developed and executed to investigate the structural performance of representative bridge girders strengthened with post-installed shear connectors. Two continuous two-span specimens were constructed and tested under fatigue, shakedown, and ultimate strength loading conditions. The results of this testing are discussed in Chapter 5 and Chapter 6.

CHAPTER 5: EXPERIMENTAL RESULTS

5.1 OVERVIEW

The results of the laboratory testing on the two strengthened girder specimens described in the previous chapter are presented and discussed in this chapter as well as in Chapter 6. First, a brief summary of the results of the fatigue testing is presented, followed by a detailed discussion of the load-deflection behavior, the inelastic behavior, the composite behavior, and the behavior of the shear connectors during the shakedown and ultimate strength phases of testing of both specimens. Chapter 6 further explores the inelastic behavior and moment redistribution during shakedown testing and some interesting features of the partial-composite behavior within the groups of shear connectors.

The predicted limit loads given in this chapter are based on simple plastic hinge analysis using the measured material properties, with calculations given in Appendix A. Note that all of the data presented in these chapters is solely from the superimposed loads applied during the experimental testing. The dead load is accounted for by a reduction in the predicted limit loads, as calculated in Appendix A. Generally, the dead load moments did not exceed 15% of the predicted moment capacity at any location along the girders.

5.2 FATIGUE TESTING

Although the results of the fatigue testing are presented in detail by Ghiami Azad (2016), a brief summary is provided here for both specimens for completeness.

First Specimen – South Span

The south span fatigue test was conducted at a load range equivalent to an HL-93 fatigue truck in terms of slip demand on the connectors. This test primarily loaded connectors that had not been subjected to any significant prior stress. After 2 million cycles of loading and no connector failures, the test was stopped. Insignificant changes in stiffness occurred in the partially composite girder over the course of the fatigue test, suggesting that little damage to the connectors had been sustained.

Some content in this chapter has been previously published in the following article. This article was written primarily by the author of this dissertation with only minor contributions from the co-authors: Kreitman K, et al. (in press), 'Shakedown Behavior of a Continuous Steel Bridge Girder Strengthened with Post-Installed Shear Connectors', *Structures*, http://dx.doi.org/10.1016/j.istruc.2016.06.001

First Specimen – North Span

The north span fatigue test was conducted at a load range 50% greater than that of an equivalent HL-93 fatigue truck. This test primarily loaded connectors that had been previously subjected to large stress demands from the shakedown testing. Over the course of the 330,000 cycles of loading applied during this phase of testing, a gradual loss of stiffness was observed in the girder. This was attributed to degradation of the adhesive surrounding the portion of the threaded rod of the connector that passes through the oversized hole drilled through the top flange of the steel beam. By the end of the test, essentially all of the adhesive had been degraded in this area in all of the connectors in the north span, leaving an approximate 1/8-inch "gap" region through which the connectors could slip without transferring any force, as shown in Figure 5-1. This resulted in essentially non-composite behavior under the applied fatigue loads.

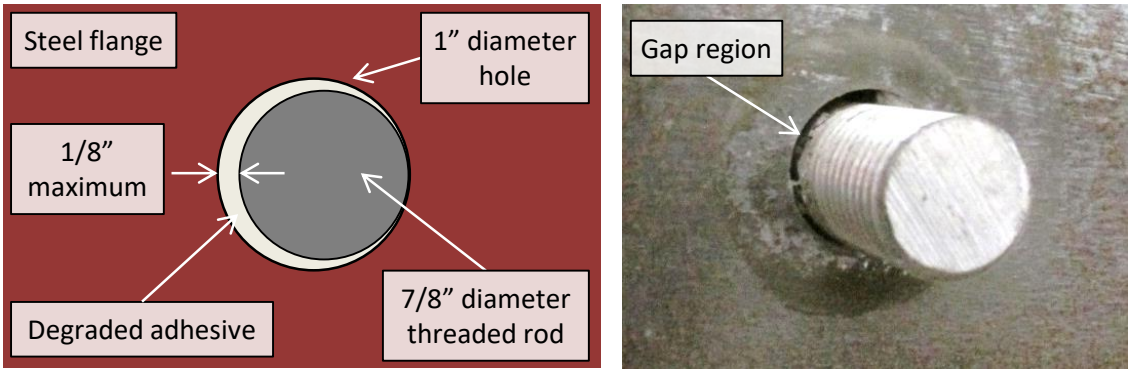

Figure 5-1: Adhesive Degradation during North Span Fatigue Test in First Specimen – (a) Schematic of Gap Formation and (b) Photograph of Typical Connector after Testing

Second Specimen – South Span

For the second specimen, fatigue testing was conducted only in the south span of at a load range predicted to cause maximum slip demand on the connectors of approximately 3 times that predicted by an HL-93 fatigue truck. This test was conducted for 1.7 million cycles of load and resulted in no shear connector failures. A small amount of adhesive degradation was observed corresponding to slight loss of stiffness of the girder, but not to the extent shown in Figure 5-1.

5.3 SHAKEDOWN TESTING

Two phases of shakedown testing were conducted on the first girder specimen, which considered the north and south spans separately. A single phase of shakedown testing was conducted along the entire length of the second girder specimen. The loading pattern followed for all three shakedown tests is described in Figure 4-12 and simulates the effects of increasingly heavier trucks crossing a bridge. This pattern causes alternating large positive bending moments at Load A in the north span or at Load D in the south span, and large negative bending moments at the interior support. As noted in Section 4.6.3, although both tests were designed such that shakedown was expected to occur at approximately 20% moment redistribution from the interior support, this predicted value was actually 22% to 25% for the first specimen and 15% for the second specimen due to discrepancies in the analysis technique.

Recall that shakedown was deemed to have been achieved when the change in deflection from one cycle to the next did not exceed 0.01 inch. Also, recall that when a statically indeterminate structure shakes down, it reaches a state in which the residual moments that have developed as a result of yielding at one or more location counteract the moments from the applied load to an extent that no additional yielding occurs in future cycles of the same or lower load.

5.3.1 Load-Deflection Behavior

First Specimen

The north span shakedown test of the first specimen was conducted prior to any fatigue testing, so that the connectors had not been subjected to any significant previous forces. The south span shakedown test took place after fatigue testing in both spans so that the connectors in this test had been previously subjected to 2 million cycles of fatigue loading. However, no significant deterioration of the composite behavior was observed during the south span fatigue test, and the prior fatigue loading seems to have had little to no influence on the results of the shakedown testing presented here.

A summary of the loading program for both phases of shakedown testing on the first specimen is given in Table 5-1. The number of cycles to achieve shakedown is noted in the table for each load level, along with the total residual deflection after all cycles at each load level. This residual deflection is representative of the extent of inelastic behavior that has occurred in the girder.

In this first specimen, shakedown was observed at load levels slightly beyond the predicted shakedown limit. Because the portion of the steel beam in the south span had a higher yield stress than that in the north span, the predicted shakedown limit loads are different for the two spans. The north span test was stopped at a load level of approximately 2.5% greater than the predicted limit to preserve the specimen for future phases of testing. Four additional cycles of load were applied at this load level, as well as at two lower load levels in the elastic range to demonstrate the repeatability of the behavior following shakedown at large loads. The south span test was continued to a load level of 9% greater than the predicted shakedown limit load. However, the test was stopped after one cycle at this load due to the onset of local buckling of the web of the steel beam at the interior support. Thus, shakedown was not observed at this load level. The largest load level at which shakedown was observed during the south span test was nearly 5% greater than the predicted limit.

Generally, the number of cycles required to achieve shakedown increased with increasing magnitude of the applied load. As more inelastic behavior occurs in both the critical positive and negative moment regions at larger loads, it takes more cycles of load for the residual moments to stabilize at a level that counteracts both the large positive and negative moment demands on the structure. However, less cycles were needed for the south span test than for the north span test, especially for loads beyond the predicted elastic limit. This is because during the south span test, only small amounts of additional yielding occurred from applying Loads B and C until large load levels were reached, as these loads were applied previously during the testing of the north span. Because the region around the interior support had already yielded during the north span test, essentially elastic behavior was observed in that region during testing of the south span until load levels nearing the predicted shakedown limit were reached.

Figure 5-2 plots the peak load-deflection behavior during the north and south span shakedown tests of the first specimen. The circular data points represent the magnitude of Load A or Load D and the deflection at the load point at the peak load of each cycle. Data for the load step consisting of Loads B and C are not shown in this figure. The solid and dashed lines show the full load-deflection behavior of single cycles of load, one at each of the predicted elastic and shakedown limits. Each of these individual cycles was essentially elastic, and the slope of the loading portion of each cycle did not change significantly throughout the test, indicating that there was little to no degradation in the composite behavior.

The accumulation of inelastic deformation can be seen graphically in the slight increases of deflection for consecutive cycles at the same level of load. At any given load level, the change in deflection from one cycle to the next generally decreased with increasing cycles until it fell below the shakedown criterion of 0.01 inch. This trend is further illustrated in Figure 5-3 for the load level at the predicted shakedown limit.

Table 5-1: Summary of Loading for Shakedown Testing of First Specimen

Load Magnitude (k)		**Number of Cycles to Shakedown**		**Net Residual Deflection at Load A or Load D (in)**		**Predicted Limit Loads**
A or D	B & C	North	South	North	South	
46	55	2	2	0.00	0.00	
70	85	2	2	0.01	0.00	
91	110	2	2	0.03	0.00	
108	130	2	3	0.06	0.00	
120	145	2	2	0.10	0.01	Elastic Limit
131	158	2	2	0.14	0.05	
140	160	3	3	0.17	0.06	
144	165	3	2	0.22	0.07	
148	170	4	3	0.25	0.09	
152	175	4	3	0.29	0.09	
157	180	5	3	0.35	0.11	
161	185	5	3	0.46	0.15	
165	190	6	3	0.54	0.18	
170	195	5	3	0.54	0.22	
174	200	7	4	0.65	0.25	
178	205	7	4	0.76	0.30	
183	210	8	7	0.91	0.39	
187	215	9	8	1.07	0.52	Shakedown Limit (N)
191	220	11 (15)*	10	1.23	0.67	Shakedown Limit (S)
200	230	--	14	--	1.14	
209	240	--	(1)†	--	1.44	
80	95	(4)‡	--	1.23	--	
140	160	(4)‡	--	1.23	--	
Total Cycles:		101	84			

*Shakedown achieved after 11 cycles; applied 4 additional cycles to investigate behavior

†Testing stopped after one cycle due to local buckling at interior support region

‡Additional cycles applied at lower elastic loads to investigate behavior

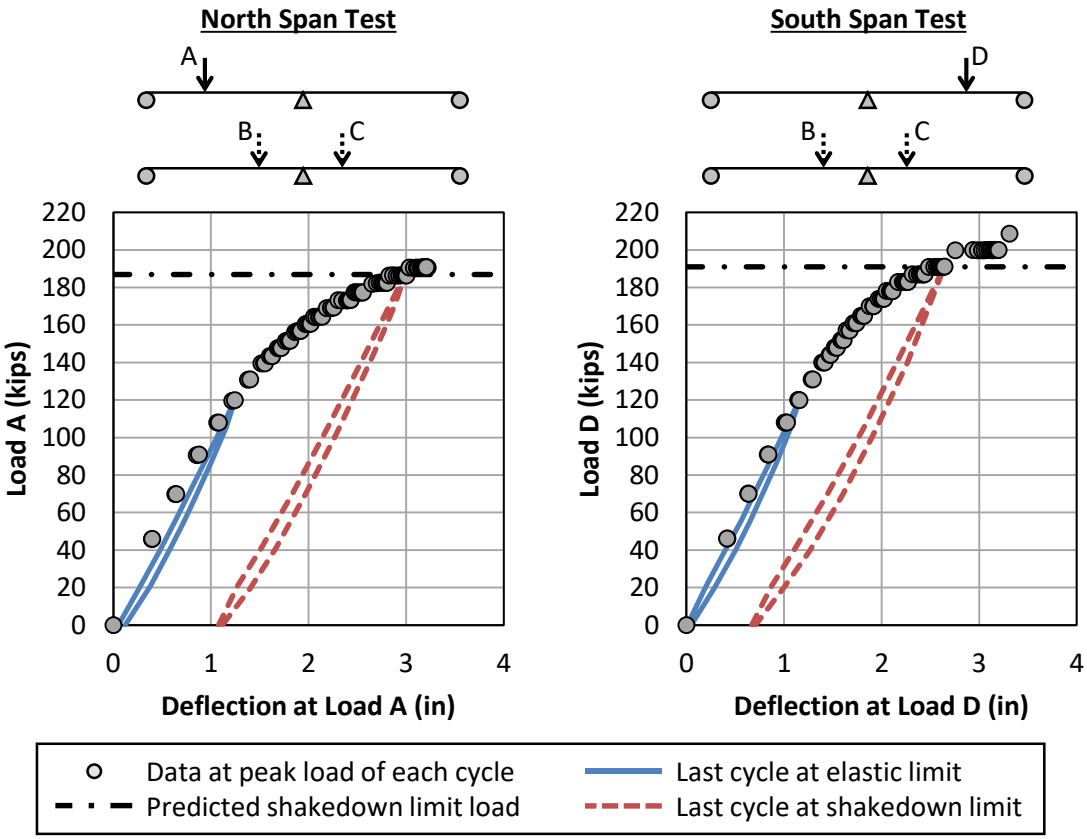

Figure 5-2: Peak Load-Deflection Behavior during Shakedown Testing of the First Specimen

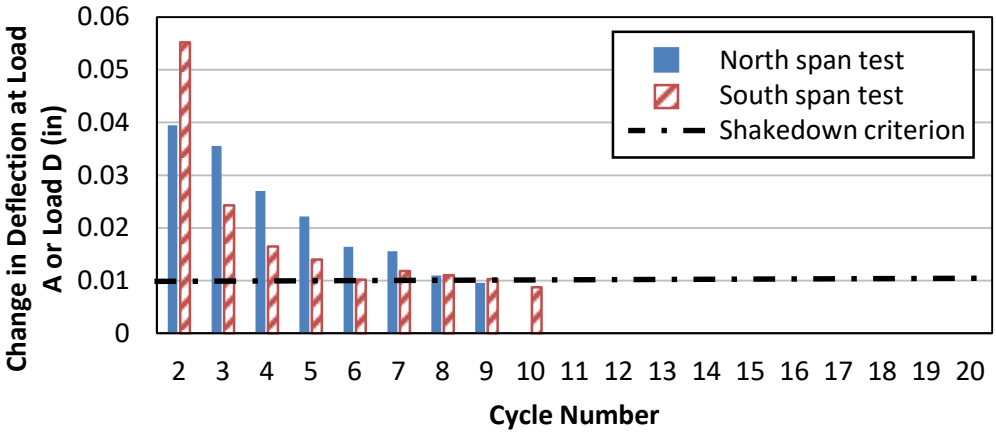

Figure 5-3: Change in Deflection between Consecutive Cycles during Shakedown Testing of the First Specimen – At the Shakedown Limit Load

Second Specimen

The shakedown test of the second specimen was conducted in both spans using all four loads. The connectors in the south span had been previously subjected to 1.7 million cycles of fatigue loading, which did not cause a significant amount of deterioration of the composite behavior. The connectors in the north span were installed just prior to this phase of shakedown testing and were not subjected to any significant previous forces.

Table 5-2, Figure 5-4, and Figure 5-5 summarize the loading program, plot the peak load-deflection behavior, and show the trends in the deflection change between cycles in the same manner as presented for the first specimen. While the general trends are similar, key points are discussed here for the second specimen.

The largest load level for which shakedown was observed in the second specimen was approximately 2.5% lower than the predicted shakedown limit. At the predicted shakedown limit, the test was stopped after 20 cycles because the deflection changes were not converging to a value below the 0.01-inch criterion, indicating that shakedown would not be observed at this level of load. This may be due to the excessively low nominal composite ratio of 20% that was used in this specimen. Three additional cycles of a lower level of load were again applied to confirm the repeatability of elastic behavior following the application of large repeated loads. As with the first specimen, more cycles were required to achieve shakedown and larger residual deflections were measured at larger load levels. However, it is difficult to make quantitative comparisons between the two specimens due to the different span lengths, load locations, and composite ratios, which required the use of a different applied load pattern and load ratio for shakedown testing.

Table 5-2: Summary of Loading for Shakedown Testing of Second Specimen

Magnitude of All Loads (k)	Number of Cycles to Shakedown	Net Residual Deflection at Load A or Load D (in)		Predicted Limit Loads
		North	South	
35	2	0.00	0.01	
50	3	-0.01	0.03	
65	3	-0.04	0.06	
75	5	-0.03	0.07	
85	4	0.01	0.08	
95	7	0.06	0.13	
100	3	0.09	0.16	Elastic Limit
105	6	0.12	0.19	
109	6	0.17	0.21	
114	6	0.24	0.28	
118	7	0.30	0.35	
123	6	0.40	0.43	
127	9	0.57	0.58	
132	12	0.75	0.72	
136	14	0.95	0.95	
141	17	1.30	1.35	
145	(20)*	1.57	1.49	Shakedown Limit
100	(3)†	1.57	1.52	
Total Cycles:	133			

*Shakedown not achieved at this load level, test stopped after 20 cycles

†Additional cycles applied at elastic limit to investigate behavior

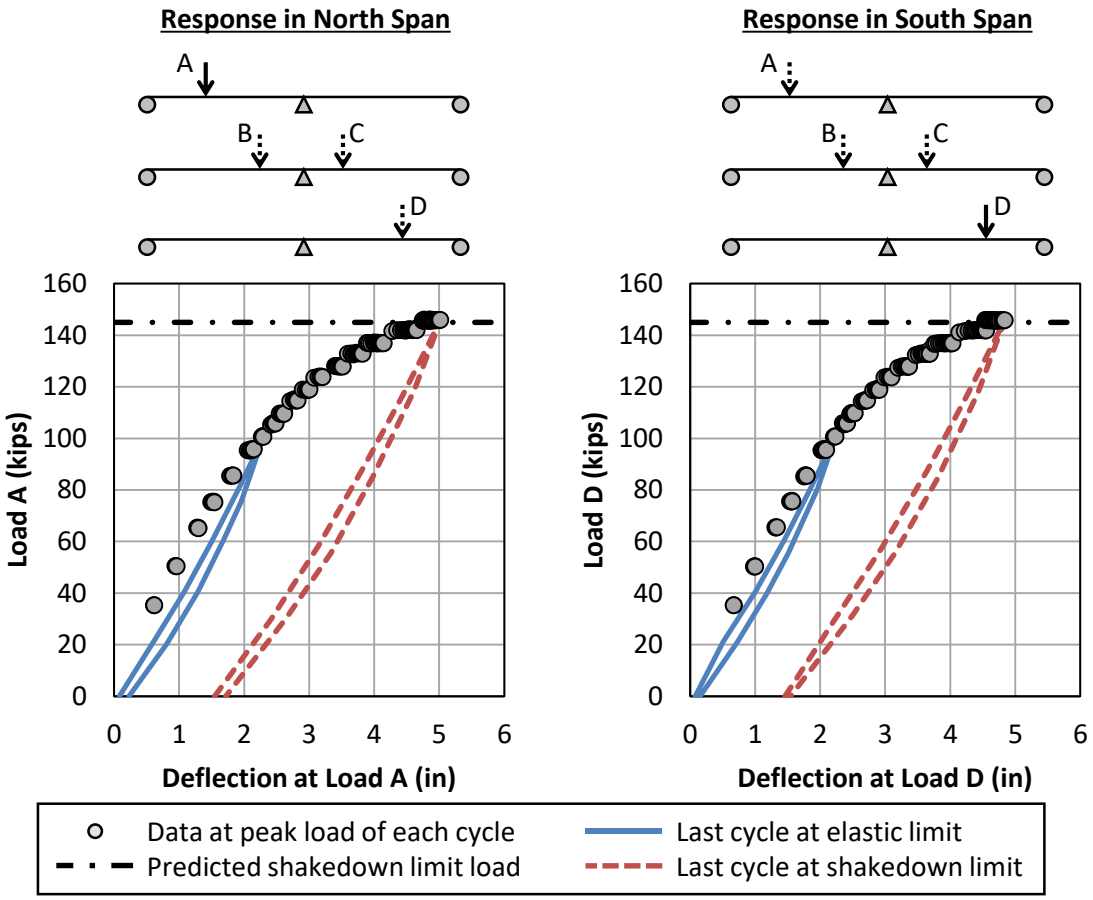

Figure 5-4: Peak Load-Deflection Behavior during Shakedown Testing of the Second Specimen

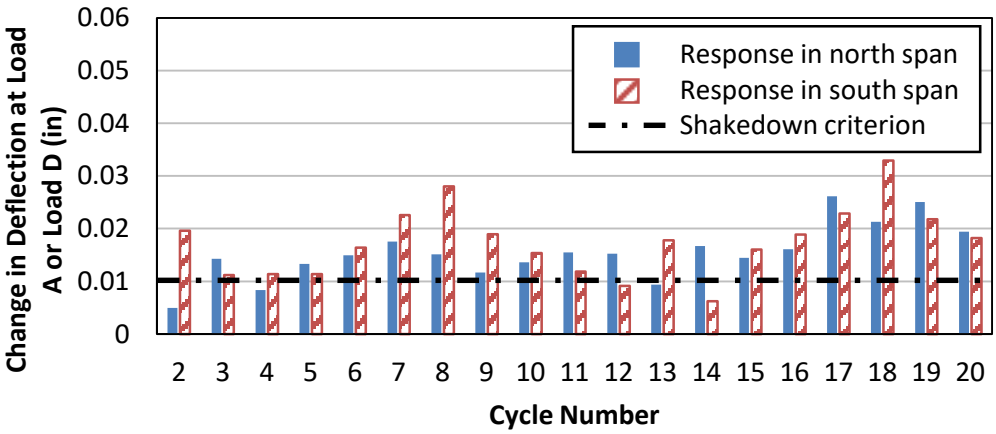

Figure 5-5: Change in Deflection between Consecutive Cycles during Shakedown Testing of the Second Specimen – At the Shakedown Limit Load

5.3.2 Inelastic Behavior

The extent of inelastic behavior in the girders was tracked by visually observing the pattern of yield lines formed in the steel beam and the cracks developed in the concrete deck during testing. Additionally, data from the optical motion tracking system, described in Section 4.5, were used to estimate the curvature at the interior support, where the majority of the inelastic behavior was expected to occur during shakedown testing.

Figure 5-6 shows photographs of the interior support region after the completion of all three phases of shakedown testing. To enhance the visibility of the yield lines, this portion of the steel beam was painted with whitewash prior to testing, so that the dark spots on the photographs indicate locations that had yielded. While the majority of the yielding appears to have occurred in the lower portion of the web where large concentrated forces entered the support structure, flexural yielding was also visible near the top of the web and on both flanges. The local buckling of the web that caused the termination of the south span shakedown test in the first specimen can be seen in just to the right side of the stiffener in the photograph. A similar pattern in the whitewash had begun to develop in the second specimen as well by the end of the shakedown testing, indicating the onset of local buckling.

The distribution of curvature along the region spanning 20 inches to either side of the center line of the interior support is also shown in Figure 5-6 for all three specimens. The plot shows the curvature distribution at the peak load for the predicted elastic and shakedown limits as well as at the maximum level of load applied beyond the shakedown limit. The predicted yield curvature is also plotted for comparison. This yield curvature was calculated by assuming that the neutral axis was located at mid-depth of the section, as expected for a non-composite section (see Section 5.3.3).

Generally, the curvature at the predicted elastic limit load was close to but did not exceed the predicted yield curvature at all locations. The exception to this occurred during testing of the south span of the first specimen. Because large levels of Loads B and C had already been applied during the north span test in the first specimen, a significant amount of residual curvature was present at this location prior to conducting the south span test. Thus, the curvature distribution at the predicted elastic limit load in the south span test is of similar shape as those at loads beyond the elastic limit. The curvature at the predicted shakedown limit load and at the maximum load applied increase from approximately the yield curvature on the outsides of the region to much larger values at the center line of the

support. Curvatures up to six times the predicted yield curvature were observed at large loads.

Figure 5-7 shows photographs of cracks developed in the concrete deck by the end of all three shakedown tests. In this figure and in all others showing deck cracking, the cracks have been marked with bold lines for emphasis. All cracks spanned the full width across the top of the deck. Upon removal of the formwork for the first specimen, three cracks formed under dead load. One of these cracks was located at the center line of the interior support, while the other two formed approximately 5 feet to either side of the support. These cracks extended through the full depth of the deck, indicating fully composite behavior due to the presence of the natural bond between the underside of the deck and top flange of the steel beam after casting. Dead load cracks did not form in the second specimen, and no deck cracking was observed during any of the phases of fatigue testing. During the shakedown phases of testing for both specimens, the bond had already been broken, so the cracks formed at this stage did not penetrate through the entire thickness of the deck, indicating non-composite behavior at this region.

The initiation of deck cracking during shakedown testing occurred at the interior support at a wide range of load levels between the two specimens. For the north span test of the first specimen, these cracks began to develop at a load level of approximately 90% of the predicted shakedown limit load. No additional cracks formed during the south span shakedown test of the first specimen, further confirming the minimal amount of inelastic behavior in that region during the test. However, for the second specimen, the first deck cracks at the interior support were observed at much lower loads, approximately 35% of the predicted limit load. This difference is likely due to the significantly lower concrete strength in the second specimen as well as the increased flexibility of the overall girder from the increased span length.

It is important to note that the deck cracking observed during these tests may be a concern for strengthened bridges in the field for durability reasons. Unfortunately, there is no simple method of predicting longitudinal flexural stresses in the deck over an interior support of a strengthened girder in which the span regions develop partial-composite action while the interior support regions remain non-composite. There is also no mention of deck stresses at interior supports in the moment redistribution provisions in Appendix B6 of the AASHTO LRFD specifications. If potential cracking of the deck is a concern for a particular application, the use of finite element models or another rational method of analysis may be necessary.

Although the majority of the inelastic behavior during the shakedown testing phases was expected to occur in the negative bending region at the interior support, some yielding of the steel beam and cracking of the deck were observed in the regions near Load A and Load D, which were subjected to large positive moments. This is noteworthy because analysis and design techniques based on simple plastic hinge analysis do not account for this behavior, as they assume that no inelasticity occurs prior to the development of the full plastic strength of the section. Figure 5-8 shows the typical development of a small amount of yield lines in the whitewash near these load points after the completion of shakedown testing. These yield lines were spread out to a maximum of 3 feet away from the load point and penetrated no more than one-third of the way into the bottom of the web. Further discussion of the extent of the inelastic behavior that occurred in positive bending in provided in Section 6.2.

A photograph showing the typical distribution of cracks in the underside of the deck by the end of shakedown testing is shown in Figure 5-9. These cracks were typically concentrated in a region no more than 18 inches to either side of the load point. For the first specimen, these deck cracks formed at the same time as those at the interior support, at approximately 90% of the predicted shakedown limit load in both spans. For the second specimen, no cracking was observed at the load points at any point during shakedown loading.

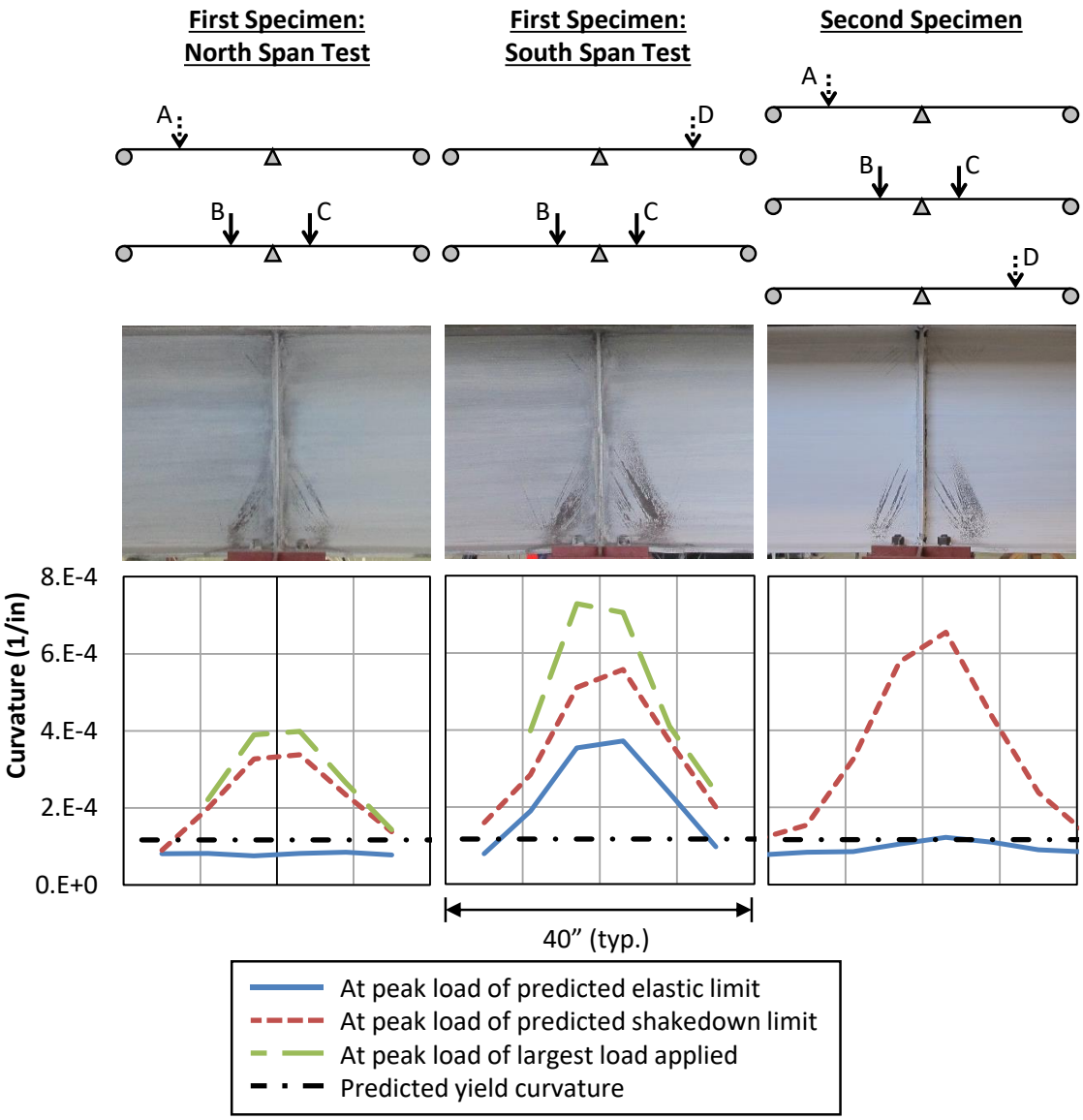

Figure 5-6: Photographs of Yield Lines in Whitewash after Shakedown Testing and Curvature Distribution during Shakedown Testing at the Interior Support

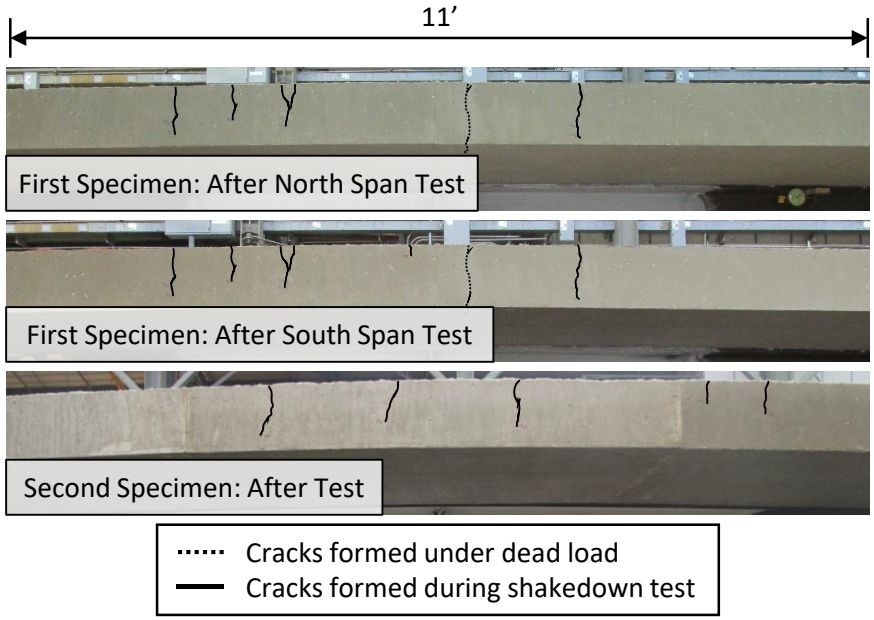

Figure 5-7: Photographs of Deck Cracks at Interior Support after Shakedown Testing

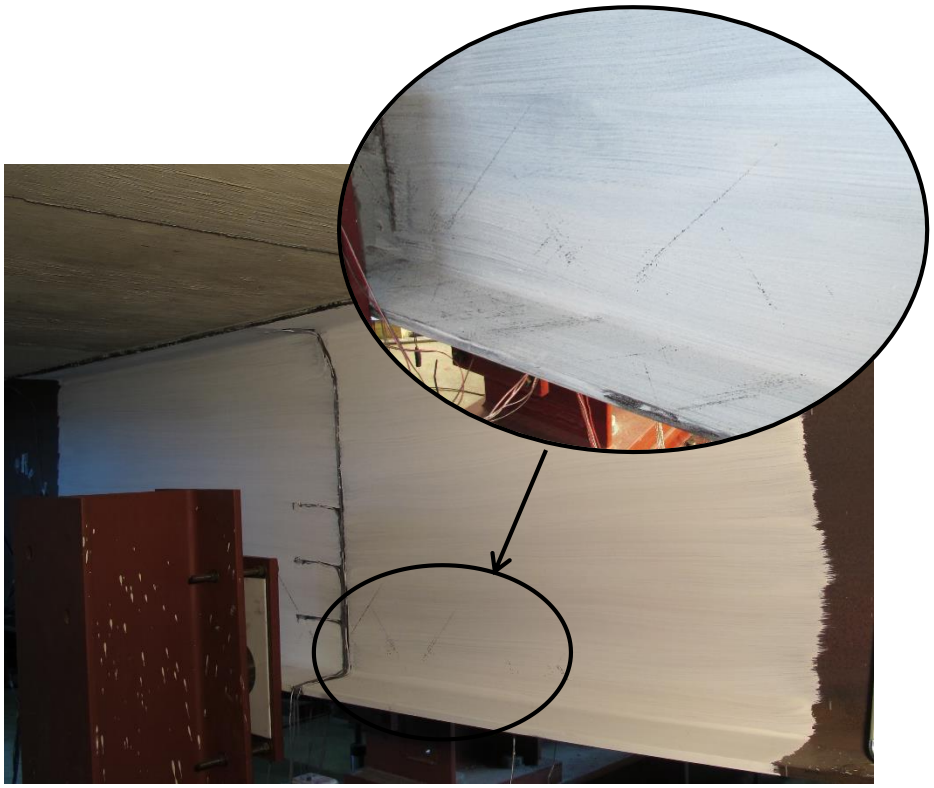

Figure 5-8: Photographs of Typical Yield Lines in Whitewash at Loads A and D after Shakedown Testing in Both Specimens

Figure 5-9: Photographs of Typical Deck Cracking at Load A or Load D after Shakedown Testing

5.3.3 Composite Behavior

The level of composite action can be evaluated by the location of the neutral axis within the depth of the steel section. For a doubly symmetric non-composite section, the neutral axis will be located at mid-depth of the steel beam for all levels of moment applied to the section. Any level of composite action with the concrete deck will raise the neutral axis above mid-depth. However, it is difficult to quantify the theoretical depth of the neutral axis in a partially composite girder because the presence of interface slip creates a complex strain distribution, as is discussed further in Section 6.3.3. Despite this, the plastic neutral axis can be easily calculated for any partially composite section, and will be used here as a comparison for the partially composite regions. However, note that this plastic neutral axis only truly applies as the cross section approaches its maximum strength.

The variation of the neutral axis locations at the peak load of each cycle is plotted in Figure 5-10 and Figure 5-11 for the first and second specimens, respectively. In each figure, the graph on the left shows the neutral axis location in regions dominated by positive bending at Load A and Load D, while the graph on the right shows the neutral axis location in the negative moment region around the interior support. The data on the graphs come from both strain gages and the optical system. Because the optical system is less accurate at measuring small strains, the data from that system is only plotted for load levels above the predicted elastic limit. The horizontal axis, which represents the applied load in all of

these graphs is normalized by the predicted shakedown limit load to facilitate comparison between the two specimens.

For both spans of the two specimens, the neutral axis in the partially composite regions near Load A and Load D was at or below the predicted plastic neutral axis location at all load levels. Generally, the neutral axis gradually and slightly dropped lower in the section from the start of the test to approximately 75% of the predicted shakedown load. As the load increased beyond that point, the neutral axis shifted back upwards in the section. The neutral axes were at approximately the same location in both specimens, despite the difference in the composite ratio, which results in a different predicted location of the plastic neutral axis. Further discussion of the variation in the partially composite neutral axis location at the locations of the connectors is given in Section 6.3.3.

At the interior support in both specimens, the neutral axis was located at or just above mid-depth of the steel beam, indicating that little to no composite action was developed at that location, as expected.

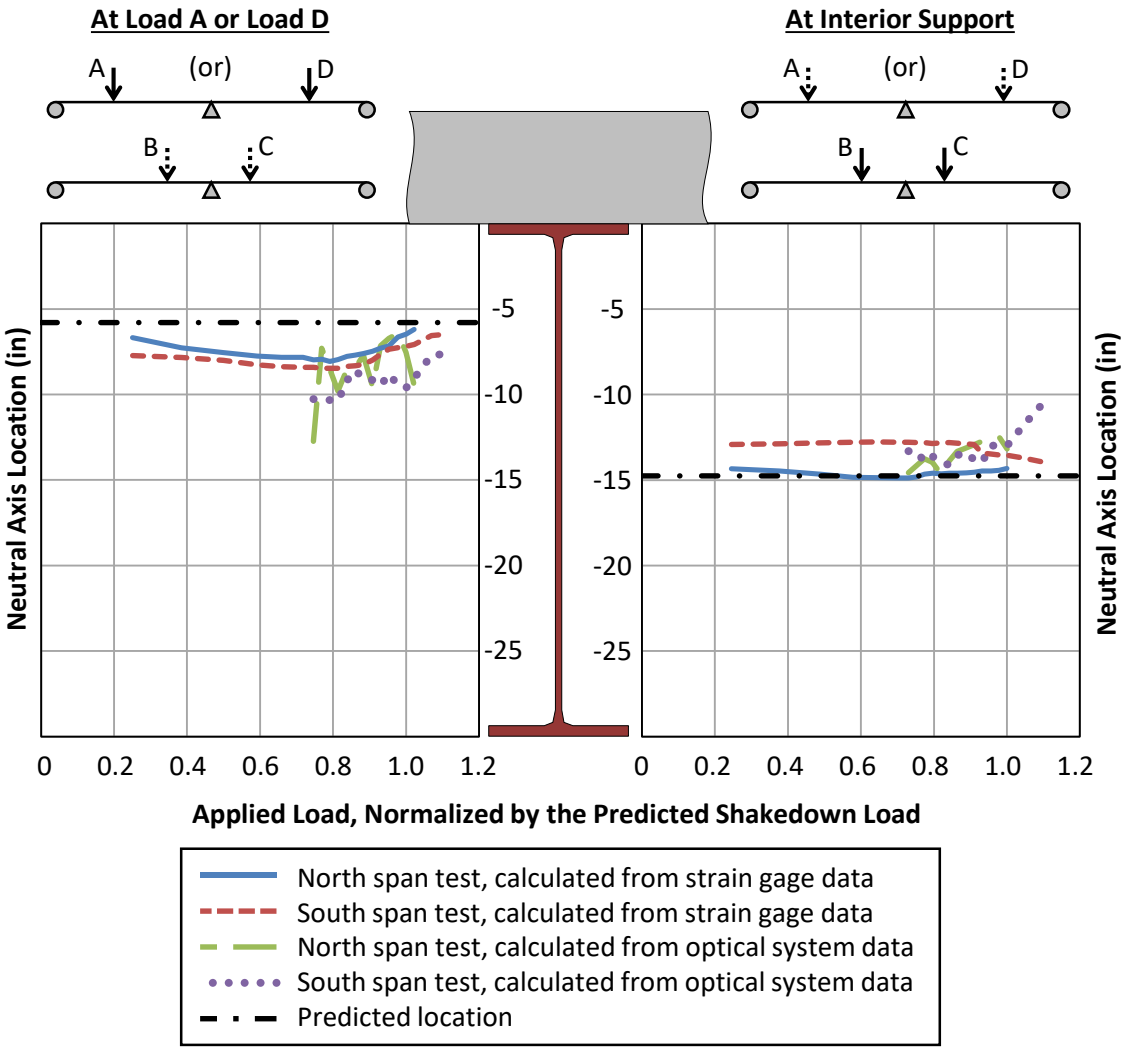

Figure 5-10: Neutral Axis Location during Shakedown Testing of the First Specimen

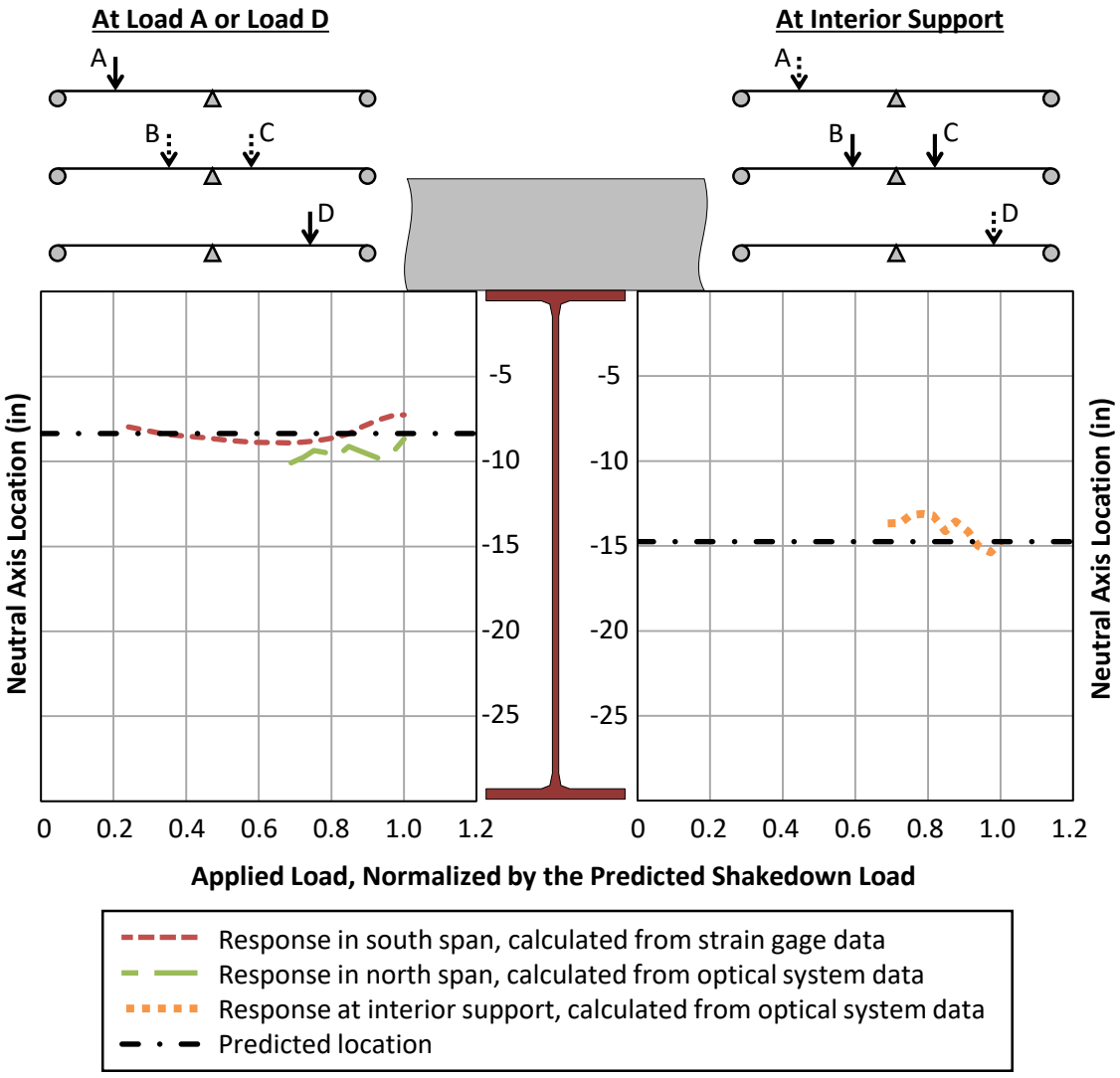

Figure 5-11: Neutral Axis Location during Shakedown Testing of the Second Specimen

5.3.4 Shear Connector Behavior

The force-slip behavior of the connectors was monitored during testing to assess the behavior of the shear connectors. In the first specimen, only the middle pair of connectors in each group was instrumented for both force and slip. For the second specimen, all connector pairs were instrumented for force and most were instrumented for slip. However, the results presented in this chapter are only for the middle connectors in each group, for which data was available for both specimens. A further look into the

distribution of force and slip between connectors in the same group is provided in Section 6.2.

The force-slip behavior for the middle connectors in each group is shown in the graphs of Figure 5-12 for a single cycle of Load A or Load D at both the predicted elastic and shakedown limit loads. In this figure, it was assumed that the pair of connectors in a cross section share the load equally, so that the force-slip behavior of a single connector could be plotted. Additionally, both the connector force and slip were taken as zero at the start of the shakedown test in the associated span on these graphs. For comparison, the design strength of a single connector is also plotted. The shape of the curves is similar for all connectors at both load levels, although the curve becomes more stretched horizontally at larger loads, indicating some softening of the shear connection as the tests progressed. Large discrepancies in the force values, particularly for the second specimen at the predicted shakedown limit load, are evident in the graph. It is likely that this is due to errors in the estimation of these force values, which were computed using the change in axial force in the steel beam from strain gage measurements on either side of the connector pair. Residual slip and force were present in all connectors at both load levels, with larger residual values at larger loads. However, the residual forces are not necessarily reliable quantities, because of the method used to estimate the force from strain gage measurements. Slight errors in the measurement of the small strains when the girder was unloaded may have significantly influenced the calculated force values. The residual slip was directly measured at the locations of the connectors during the test, and is thus a reliable value.

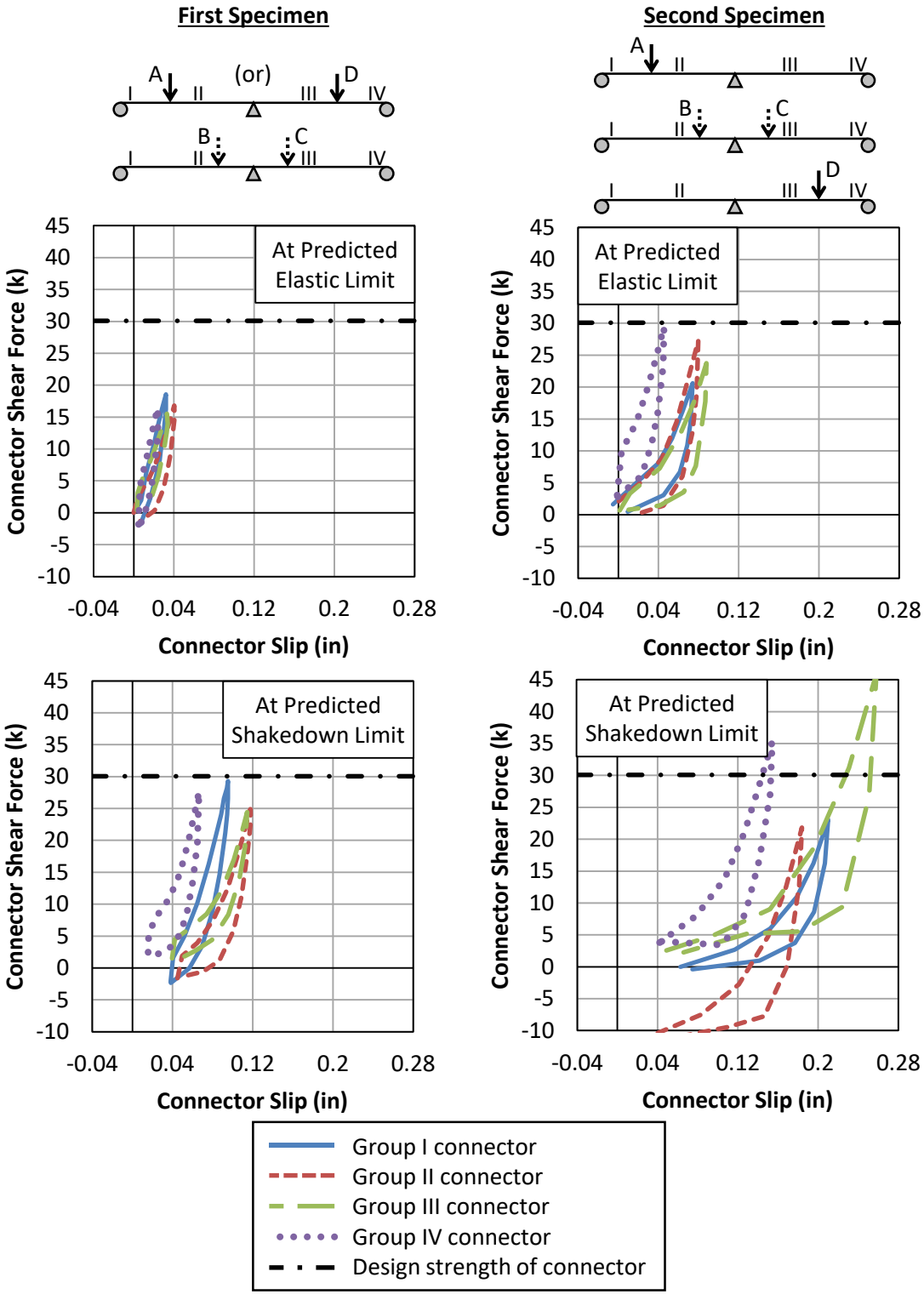

Figure 5-12: Force-Slip Behavior of Connectors during Shakedown Testing of Both Specimens

5.4 ULTIMATE STRENGTH TESTING

As with the shakedown testing, two phases of ultimate strength testing were conducted on the first girder specimen, which considered the north and south spans separately. A single phase of ultimate strength testing was conducted on the second specimen by loading both spans simultaneously. The loading pattern followed for all three ultimate strength tests is described in Figure 4-13 and primarily causes large positive moments at Load A and Load D, resulting in large demands on the connectors in each loaded span.

In both specimens, the ultimate strength testing was conducted after all other phases of testing were complete. By this time, all connectors had been subjected to large repeated loads during shakedown testing. Additionally, all connectors except for those in the north span of the second specimen had been subjected to previous fatigue loading. For most cases, the fatigue testing did not have a significant impact on the behavior of the partially composite girder. However, degradation of the adhesive between the threaded rod of the connectors and the top flange of the steel beam occurred during fatigue testing in the north span of the first specimen, as described in Figure 5-1. The effects of this degradation can be seen in the behavior during ultimate strength testing.

5.4.1 Load-Deflection Behavior

First Specimen

The load-deflection behavior during ultimate strength testing of the first specimen is shown in Figure 5-13. The deflection plotted in this graph is the total deflection since the start of all phases of testing. Thus, the initial deflection in each span represents the residual deflection from all prior testing. The predicted ultimate strength of the partially composite girder is also plotted on the graph for comparison. The plotted prediction is the average of that for both the north and south spans, which differ by approximately 10 kips due to slight differences in the yield stress of the steel.

Both spans exhibited essentially linear elastic behavior up to approximately the largest load applied during the shakedown testing. This was expected, because the girder had previously shaken down at these large levels of load, meaning that residual moments had already formed in the structure to offset the moments from the applied loads so that the response up to this point was elastic. However, the elastic stiffness in the north span was smaller than that in the south span. This is likely a result of the adhesive degradation

suffered by the connectors in the north span during fatigue testing, creating a gap region which softened the shear connection considerably.

Beyond the largest load applied during shakedown testing, the girder began to yield and lose stiffness, as reflected by the inelastic load-deflection behavior seen in the figure. The peak strength was reached in the north span at a load of 10% greater than the predicted ultimate strength and at a deflections of nearly 8 inches, or L/65. In the south span, the peak strength was reached at a load of 2% greater than the predicted ultimate strength and at a deflection of just over 6 inches, or L/85. At this point, all connectors in a single group in the tested span failed simultaneously. This failure was easily observed during testing, as it was accompanied by a loud noise. The connector failures occurred in Group I during the north span test and in Group III during the south span test. Because the test was run under deflection control, the failure of the connectors caused an approximately 30% drop in the load to a value close to the predicted non-composite strength.

Loading continued on both specimens following connector failure to observe the post-failure behavior. As the test was continued, both specimens rapidly picked up additional load, indicating that composite action was still present, even though half of the shear connectors had already failed in the tested span. This composite action may have been developed through a combination of friction at the interface and the remaining group of connectors in the tested span. Both tests were stopped at a deflection of nearly 9 inches, or L/55, when the maximum stroke of the hydraulic ram was reached. Unloading occurred nearly elastically for both specimens at a shallower slope than the initial elastic loading phase, because a significant amount of the composite stiffness was lost after connector failure.

The south span was reloaded the following day to continue the test after stacking thick steel plates on top of the deck to increase the effective stroke of the ram. Reloading occurred nearly elastically until the point of unloading was reached. Then the curve continued to follow the loading trend from the previous day until the maximum stroke of the ram was again reached at a deflection of approximately 14 inches, or L/35. Unloading was also nearly identical to the previous day. At this point, the test was stopped to prevent damage to the test setup.

When the deck was lifted off the steel beam during removal from the laboratory, it was noticed that four additional connectors had failed. These connectors were located in Group II in the north span. It is most likely that these connectors fractured during the

ultimate strength testing, based on the rough fracture surface, although it is unclear from the observations during testing and data collected when exactly these failures occurred.

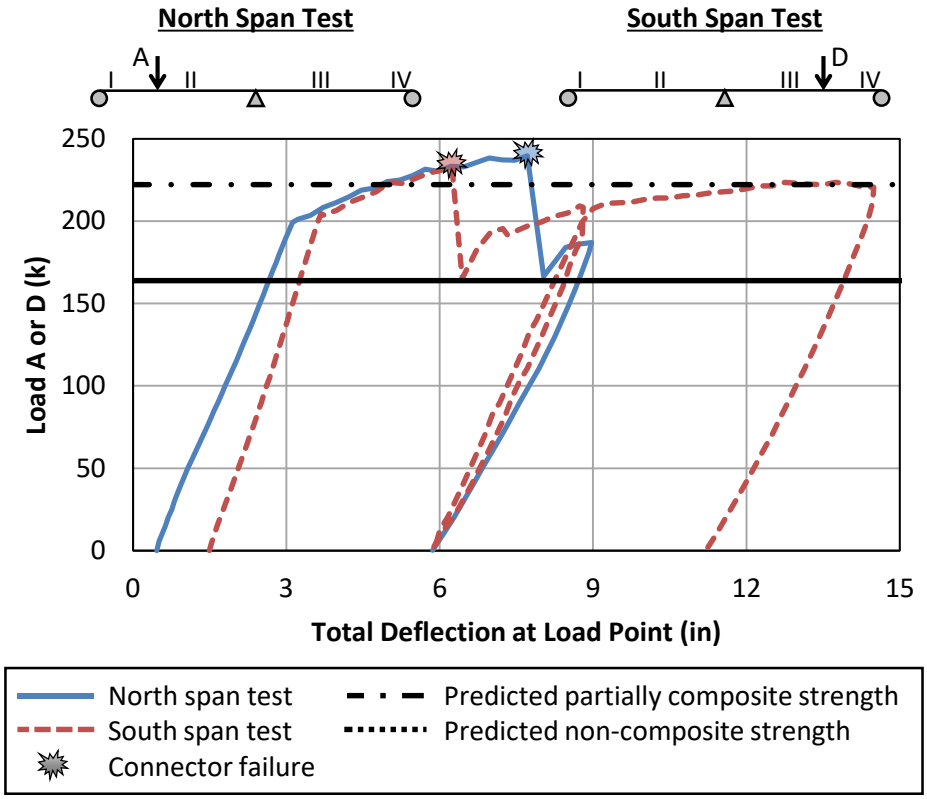

Figure 5-13: Load-Deflection Behavior during Ultimate Strength Testing of the First Specimen

Second Specimen

Prior to ultimate strength testing of the second specimen, it was determined that one of the connectors in Group III had already failed. Unfortunately, it was not possible to determine from the collected data whether this failure had occurred during the fatigue or shakedown testing phases. Although the majority of the fracture surface was rough, there were indications that a crack may have initiated in this connector during fatigue testing. Regardless, the loss of this connector did not seem to have any significant influence on the behavior during any subsequent phase of testing.

The second specimen followed similar load-deflection behavior as did the first, as shown in Figure 5-14. The elastic behavior of both spans was nearly identical, indicating

that fatigue testing, which only occurred in the south span, had no adverse effect on the elastic behavior. After reaching the maximum load applied during the shakedown testing, the load-deflection behavior entered the inelastic range, and the shear connection remained intact through a deflection of approximately 8 inches, or L/80. The peak load attained in both spans was nearly identical at approximately 10% larger than the predicted ultimate strength. Note that even though one of the connectors in Group III had failed prior to the test, both spans reached approximately the same peak load.

At this point, the shear connectors began to fail, although the failures did not occur simultaneously as they did in the first specimen. The majority of the connectors in Group III in the south span failed between a deflection of 8 and 8.5 inches, followed by the connectors in Group I in the north span between 8.5 and 9 inches. Each failure was accompanied by a loud noise and some loss in load-carrying capacity. However, it was difficult to determine the order in which the connectors failed based on visual observation, as many of them remained solidly adhered to the top flange of the girder even after the threaded rod had sheared at the interface (see Figure 5-24 for photographs of typical failed connectors). Additional discussion on the order of failure of the connectors in these groups is discussed in Section 6.3.1.

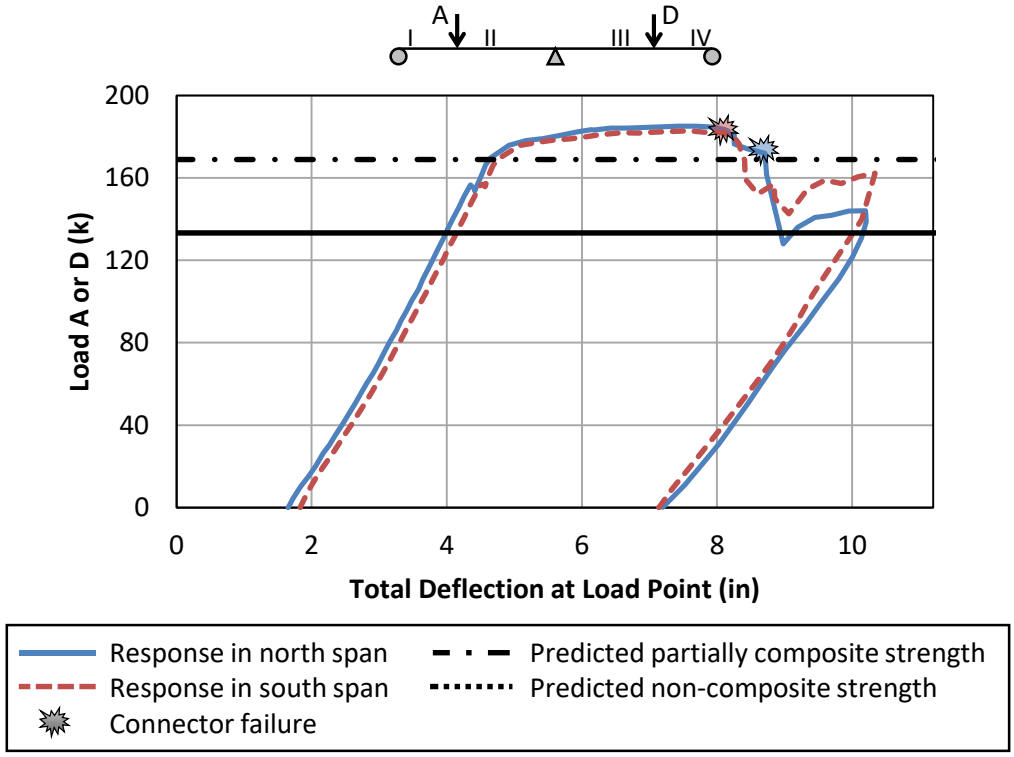

Figure 5-14: Load-Deflection Behavior during Ultimate Strength Testing of the Second Specimen

Both Specimens

Figure 5-15 provides photographs of the two unloaded specimens after the completion of the ultimate strength testing. The large residual deflections can be seen in the photographs, particularly in the south span of the first specimen. However, it is important to note that the specimens maintained a load-carrying capacity greater than at least the predicted non-composite limit load even after being pushed to large deflections during the ultimate strength testing. Despite some local buckling in the top flanges at the load points and in the bottom flange and web at the interior support, both specimens were still able to carry load exceeding the predicted non-composite strength up to deflections as large as L/35, indicating the significant ductility and inelastic strength of these girders.

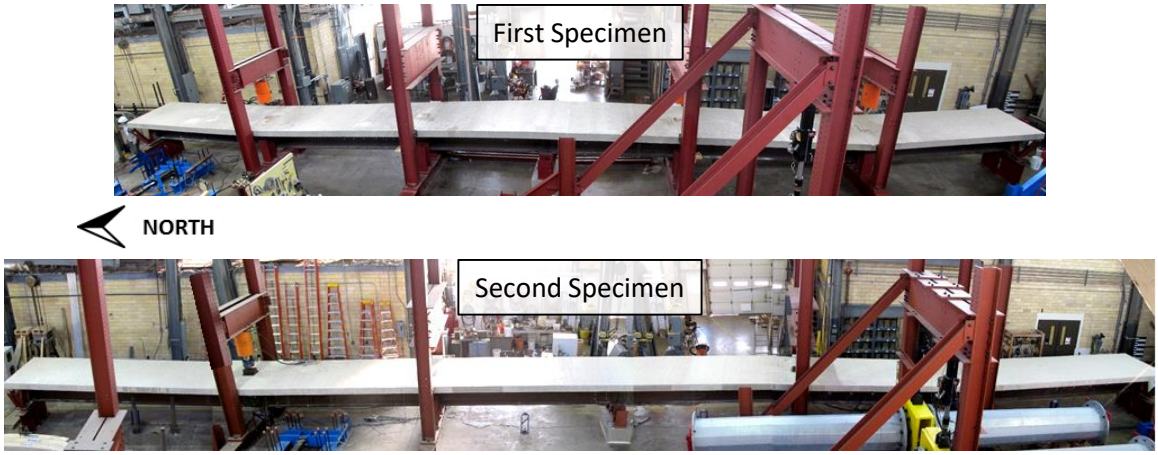

Figure 5-15: Photographs of Both Specimens after Ultimate Strength Testing

5.4.2 Inelastic Behavior

As with the shakedown testing, the extent of inelastic behavior was tracked throughout the ultimate strength testing at the load points and the interior support. This was done by visually observing the yield lines in the steel beam and cracking in the concrete deck, and by using the data recorded by the optical motion tracking system to estimate the strain distribution and curvature well into the inelastic range. Figure 5-16 shows the yield patterns in the steel beam at the interior support after all three ultimate strength tests. These patterns are similar to those observed after shakedown testing, but at a larger intensity. The majority of the yielding was again concentrated at the bottom of the web just over the interior support, where large concentrated reaction forces were resisted. Additional flexural yielding can be seen near the top of the web in the photographs. There was also significant yielding on both the top and bottom flanges. Significant amounts of local buckling in the web and bottom flange had developed in all three specimens by the end of the ultimate strength testing, just to the right side of the stiffener in the photos. This is depicted in Figure 5-17 for the second specimen. In this photo, the straight edge of the level and the shape of the buckle have been emphasized with solid and dotted yellow lines, respectively. Although this local buckling made it difficult to use the data from the optical system to estimate the curvature distribution at the interior support, the data indicates that there was only a small increase in this curvature during ultimate strength testing. This is to be expected, as the loading pattern primarily causes large positive moments at the load points and does not provide large negative bending demands at the interior support.

Figure 5-18 shows the cracking patterns that had developed in the deck by the end of all three ultimate strength tests. This figure differentiates between cracks formed under dead load, during shakedown testing, and during ultimate strength testing. All cracks spanned the full width across the deck, and were generally spaced at approximately 6 inches apart, which is equal to the spacing of the transverse reinforcement.

The yield line patterns in the positive moment regions near the load points after ultimate strength testing of both specimens are shown in Figure 5-19. Significant yielding in both flanges and through almost the entire depth of the web had occurred by the end of the ultimate strength testing, with the yielding spread over a distance of at least 4 feet to either side of the load point. Small amounts of local buckling occurred in the top flange and top portion of the web at points just slightly offset from the centerline of the load in each region. However, even under large deflections, these local buckles were small and did not have an adverse effect on the load-carrying capacity.

Figure 5-19 also shows the curvature distribution within a range of 50 inches around Load D in the first specimen and Load A in the second specimen, which were both instrumented with markers from the optical system during ultimate strength testing. The curvature distributions in the region around the load points are shown at the predicted ultimate strength limit, just before the first connector failure, and at large deflections well beyond failure of the connectors. The estimated yield curvature is plotted as well for comparison. This yield curvature was calculated based on the measured depth of the neutral axis at the predicted elastic limit load (see Section 5.4.3) As expected, the curvature increased with increasing deflection as the test progressed, with larger curvatures occurring closer to the load point. All curvatures were well into the inelastic range over the entire region shown on the plot, confirming that the yielding was widely spread in these partially composite regions.

Typical cracking of the underside of the concrete deck at the load points after ultimate strength testing is shown in Figure 5-20 (a), which differentiates between cracks formed during shakedown testing and those formed during ultimate strength testing. Additional cracks that developed during the ultimate strength testing phases were located a farther distance from the load point, at a typical spacing of approximately 6 inches, which again corresponds to the spacing of the transverse deck reinforcement. Some cracks that formed during the shakedown testing were also extended during the ultimate strength testing to span over the entire width of the underside of the deck.

Figure 5-20 (b) shows a photograph of the extensive deck cracking and crushing that occurred at Load D during the south span ultimate strength test of the first specimen at a deflection approaching 14 inches. This occurred just to the north side of the steel plate assembly through which the load was applied to the top of the deck. Significant crushing occurred above the top mat of reinforcement, while a very wide crack opened on the bottom side of the deck. This crack, along with the crushing on the top side, spanned over the full width of the deck.

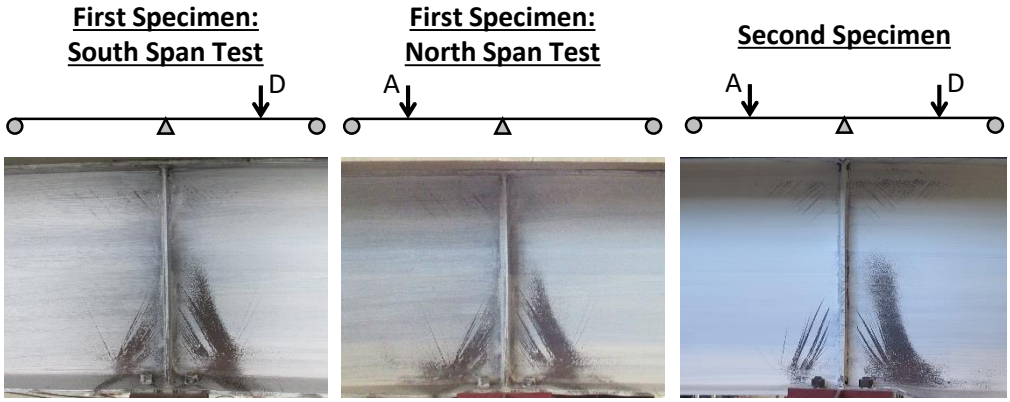

Figure 5-16: Photographs of Yield Lines in Whitewash after Ultimate Strength Testing at the Interior Support

(a) **(b)**

Figure 5-17: Photographs of Local Buckling at Interior Support after Ultimate Strength Testing of the Second Specimen – (a) Flange Buckling and (b) Web Buckling

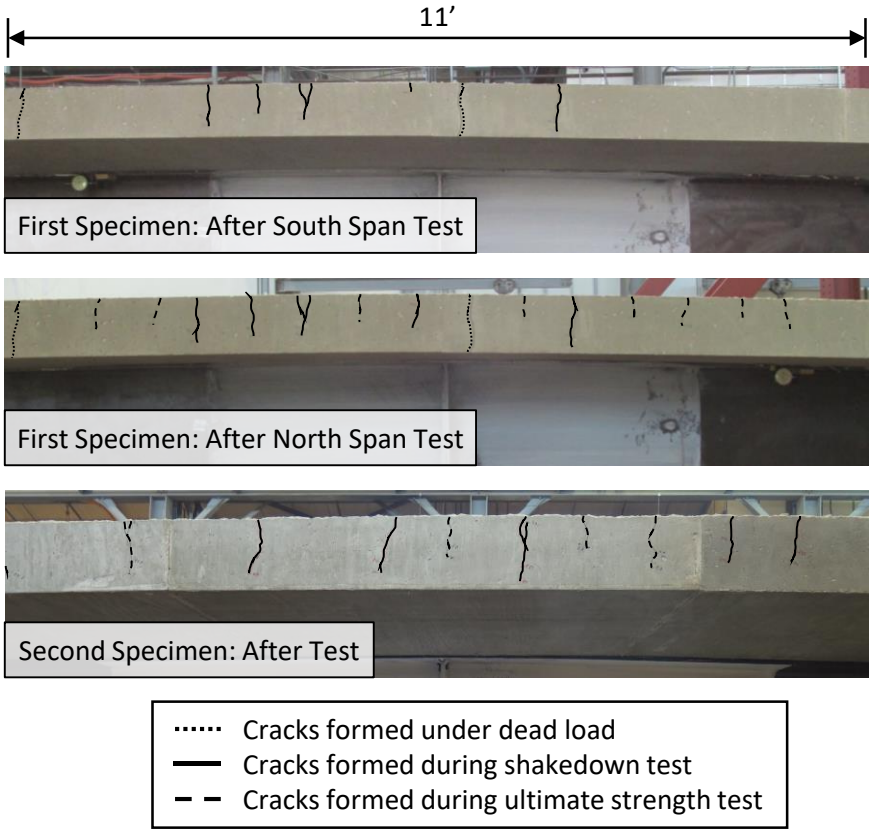

Figure 5-18: Photographs of Deck Cracking at Interior Support after Ultimate Strength Testing

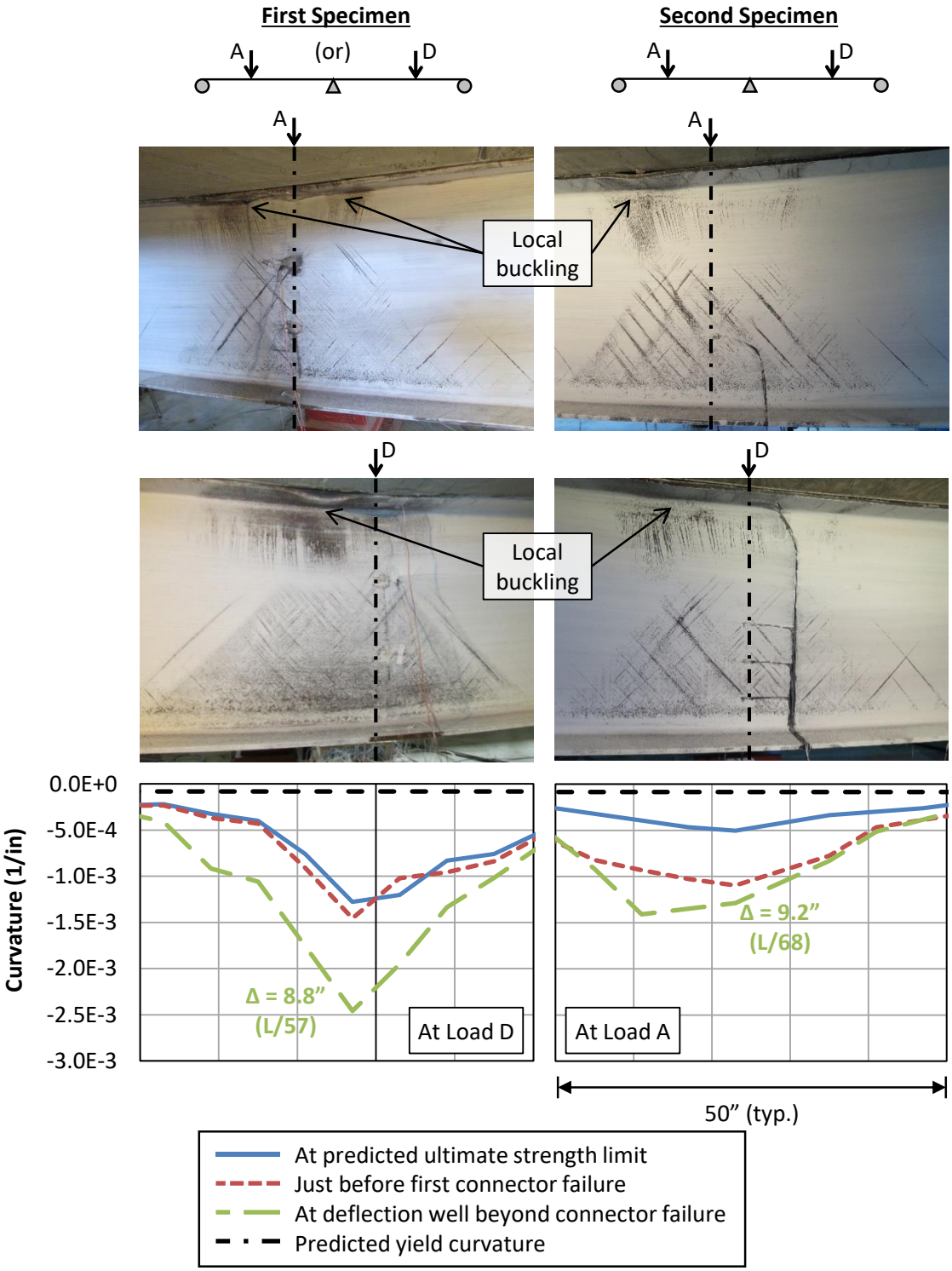

Figure 5-19: Photographs of Yield Lines in Whitewash after Ultimate Strength Testing and Curvature Distribution during Ultimate Strength Testing at Loads A and D

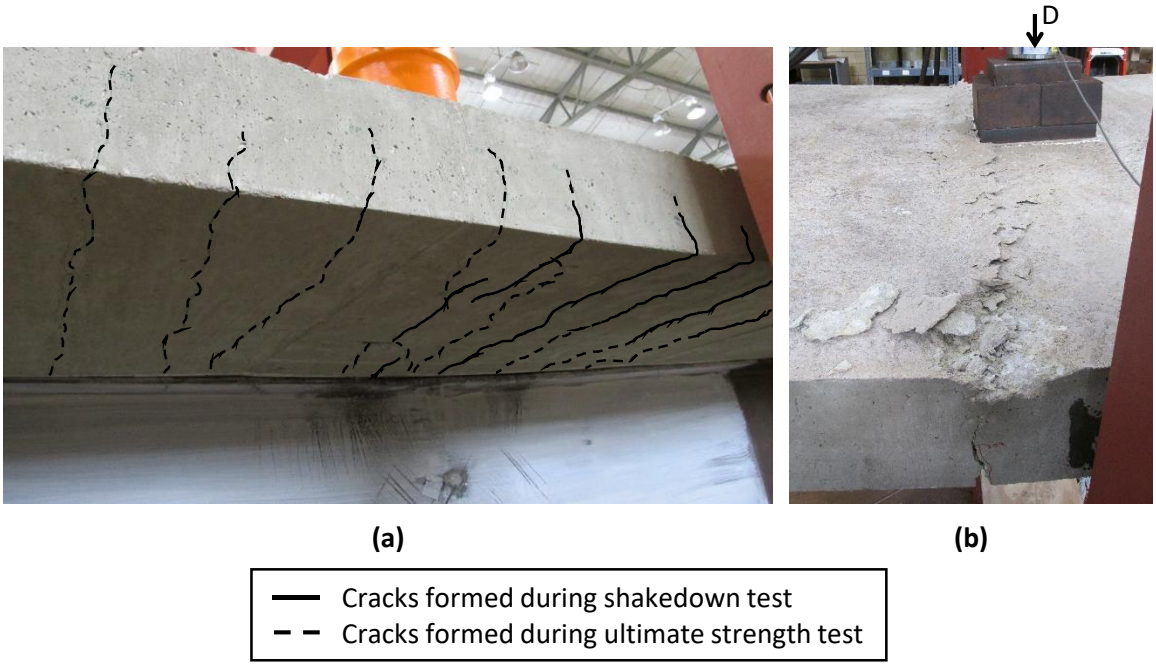

Figure 5-20: Photographs of Deck Cracking at Load A or Load D after Ultimate Strength Testing – (a) Typical Cracking of Underside of Deck and (b) Crushing of Deck at Load D during Ultimate Strength Testing of First Specimen in the South Span

5.4.3 Composite Behavior

In a similar manner as during the shakedown testing, the extent of composite behavior was monitored during the ultimate strength testing by the location of the neutral axis. Figure 5-21 and Figure 5-22 show the variation in this neutral axis location during the ultimate strength testing of the first and second specimen, respectively. The predicted neutral axis location is also plotted for comparison in the same manner as for the shakedown testing in Figure 5-10 and Figure 5-11.

The data on these plots was produced using both strain gages and the optical system. However, due to the localized nature of strain gage measurements, the data obtained at strains beyond the yield point proved to be unreliable for these calculations. On the other hand, data from the optical system is more reliable at larger strains. Thus, in the figures, the neutral axis locations determined using the strain gage data are only plotted within the elastic range, while those calculated from the optical system are plotted only in the inelastic range of the load-deflection curves shown in Figure 5-13 and Figure 5-14. Data from the optical system were not recorded nor were strain gages located in all regions of interest for

both specimens. Only the available data is plotted in the figures. For simplicity, these plots only include the loading portion of the tests. They do not show any unloading behavior.

At the location of Load A and Load D for both specimens, the neutral axis started fairly high in the section, near the predicted plastic neutral axis location, likely as a result of some friction at the interface. Once this friction was overcome, the neutral axis dropped lower in the section, before rising back towards the predicted location of the plastic neutral axis. At connector failure, the neutral axis immediately dropped approximately 2 inches in all cases, but remained well above mid-depth of the steel section, where the predicted neutral axis is located for a non-composite section. During the south span test of the first specimen, which was loaded to large deflections, the neutral axis continued to gradually fall lower in the section, approaching mid-depth at large deflections. This indicates that even after connector failure, some amount of composite action may have still been present in the girder.

At the interior support in both sections, the neutral axis again tended to start slightly above the predicted location before dropping down to just above mid-depth of the steel beam by the end of the elastic range. The neutral axis then remained at or just above the predicted location for the remainder of the test.

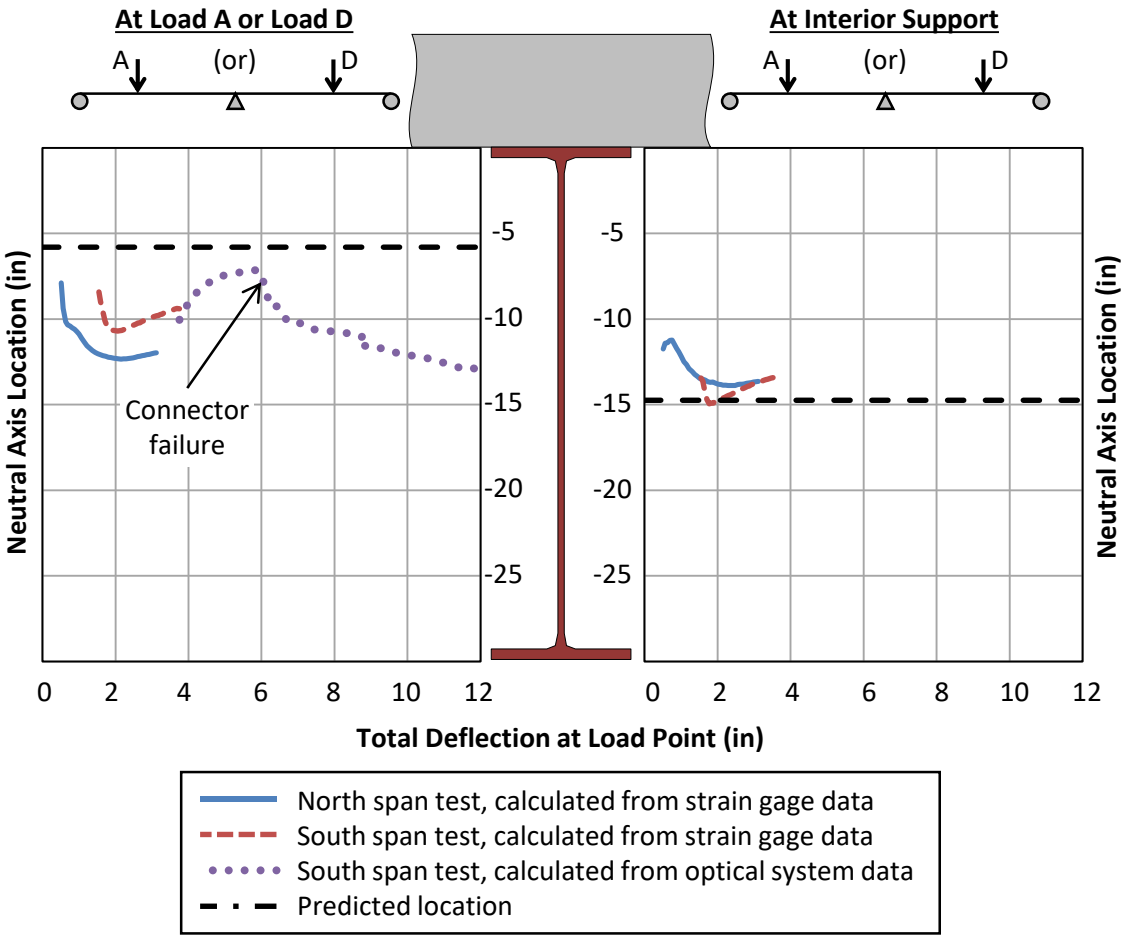

Figure 5-21: Neutral Axis Location during Ultimate Strength Testing of First Specimen

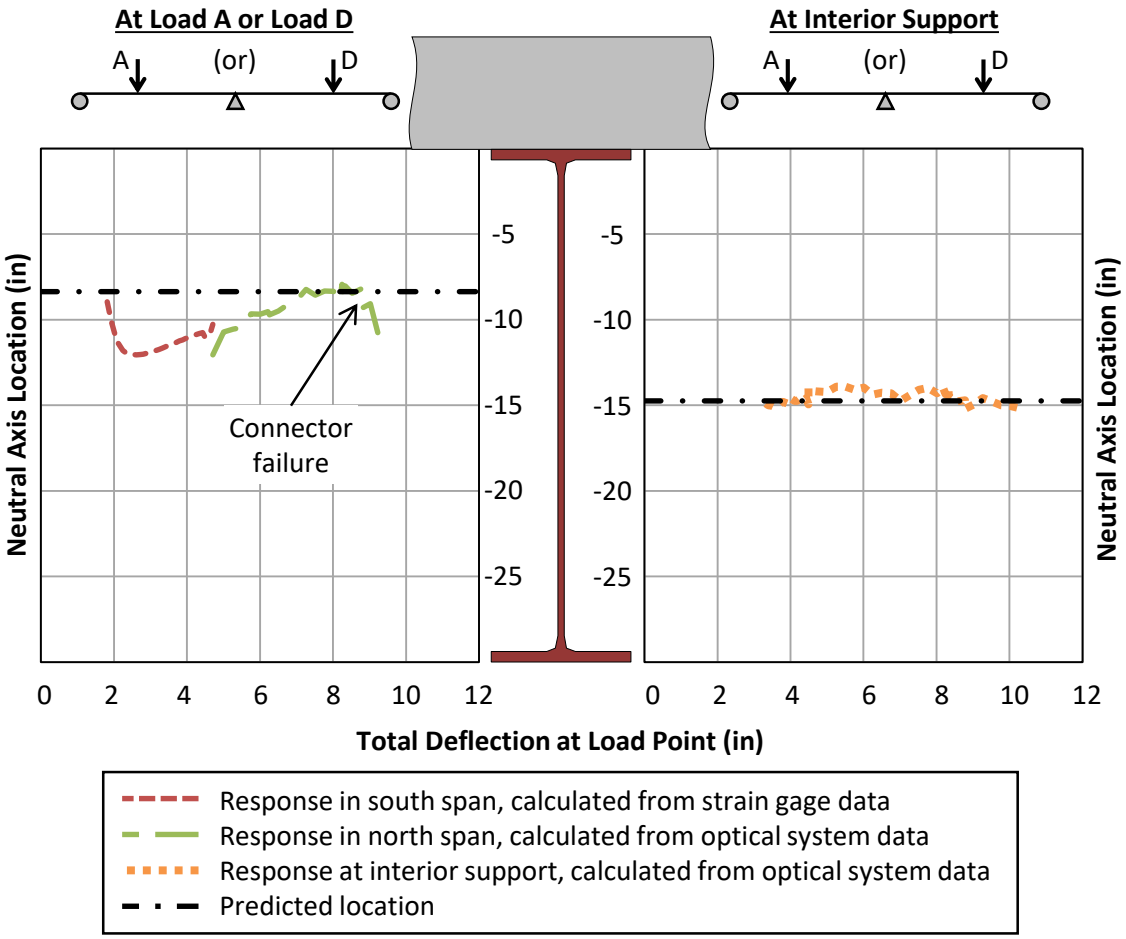

Figure 5-22: Neutral Axis Location during Ultimate Strength Testing of Second Specimen

5.4.4 Shear Connector Behavior

The force-slip behavior of the middle shear connectors in each group during the ultimate strength testing is shown for both specimens in Figure 5-23, which also notes the point of connector failure in both spans as well as the design strength for an individual connector. Recall that the connectors in Group I and Group III failed in both specimens, while the connectors in Group II and Group IV remained intact. Only the loading portions of the test are plotted in the figure, and the reloading of the south span of the first specimen is not included. As with the data from the shakedown testing shown in Figure 5-12, this figure plots the force-slip behavior of a single connector, assuming that the force is shared equally between the two connectors in a cross section.

Before discussing the results, it is important to note again here that the slip was directly measured on the specimen during testing, and thus provides reliable data. The force carried by the connectors was estimated using the change in axial force in the steel beam from one side of a pair of connectors to the other, as determined from strain gage data. Error in strain readings and the assumptions inherent in such an estimation make the force data less reliable than the slip data. Despite this, the trends seen in the plots for connector force are useful to help understand the overall behavior of the shear connection, both before and after connector failure.

There are significant differences between the force-slip behaviors of the connectors within each plot, especially during testing of the first specimen. One possible reason for these large discrepancies is that these plots only capture the behavior of one connector in each group. The distribution of load between connectors in a group is complex, and is discussed further in Section 6.3.1. However, the effects of the degraded adhesive in the north span connectors in the first specimen are evident in this data. The connectors in Group I were required to slip nearly 0.2 inch before carrying any load. This indicates that these connectors had to slip through the entire gap created by the loss of adhesive in the 1/8-inch oversized hole before coming into bearing on the opposite side of the hole to re-engage in composite action.

With the exception of the north span connectors in the first specimen, which had significant adhesive degradation, all of the connectors exceeded the design strength by 30 to 45% prior to failure. It is possible that the connectors that failed in the north span below the design strength reached the maximum slip capacity, which led to the fracture of those connectors. Despite this failure at a force level approximately 30% lower than the design strength, the girder was still able to carry a peak load well beyond the predicted ultimate strength. Additionally, although it was difficult to pinpoint the exact point of failure for each connector during testing of the second specimen, the failure points shown in the plot are the best estimate of when failure occurred based on the data and observations available. As discussed further in Section 6.3.1, it is likely that the middle connector in the north span was one of the last to fail in Group I, while the corresponding connector in the south span was one of the first to fail in Group III. During testing of the first specimen, all connectors in a group failed simultaneously.

After failure of a group of connectors in any span, the force in the intact connectors in the remaining group in that span dropped significantly, but not to zero. Although it is difficult to see in the plots, upon continued loading of the specimen, the force resisted by

these intact connectors increased with the same stiffness exhibited during the drop in the force, but never reached the maximum load attained prior to connector failure. This is another indication that some composite action continued to be developed in the specimen, even after half of the connectors in a span had failed, possibly as a result of friction at the interface and these intact connectors. This behavior was observed consistently during all of the ultimate strength testing conducted on both specimens, and is discussed in further detail in Section 6.3.1.

Figure 5-24 shows photographs of the failed connectors from both specimens and of the underside of the concrete deck in regions where the connectors failed and regions where they remained intact. In this figure, particular connectors are labeled to indicate their location within the specimen. The number denotes the distance in feet from the north end of the specimen, while the letter indicates whether the connector was located on the east or west side of the cross section. The majority of the connectors failed at the steel-concrete interface, as seen in the photographs at the top of the figure. The length of the portion of the threaded rod remaining above the nut and washer assembly in the failed connector was approximately equal to the flange thickness for nearly all failed connectors. Generally, little to no damage was observed in the concrete deck in the region immediately around all connectors, whether they failed or remained intact during testing.

However, seven connectors in the first specimen and one in the second specimen fractured at a depth of 1 to 1.5 inches into the concrete deck, as evidenced by the longer portion of the threaded rod above the nut and washer in the photographs. Three of these connectors in the first specimen were located in Group I and are shown in the top left photograph of the figure. The other four, not shown in the top left photograph, were located in Group II. All of these were in the north span and suffered near total degradation of the adhesive during fatigue testing. These connectors are assumed to have failed during ultimate strength testing, as no indication of prior failure was evident in the data. The single connector that fractured within the concrete deck in the second specimen did not have an extensive amount of adhesive degradation and is known to have failed prior to ultimate strength testing.

As seen in the photographs, the connectors that fractured within the concrete deck tended to exhibit permanent bending deformations. In the first specimen, significant amounts of crushing of the concrete deck occurred around these seven connectors, as shown by the dotted lines drawn around the breakout cones in the figure. Because the interface region is not visible during testing, it is difficult to determine causality in this

situation. It is unclear whether local concrete crushing occurred first, causing these connectors to fracture higher up within the deck, or if the connectors fractured within the deck first, but remained in place in the specimen for long enough to cause the concrete to crush before dislodging from the specimen. Additionally, some transverse cracking was observed between the connectors in Groups I and II in the first specimen, as marked by solid lines in the figure. No significant concrete crushing or cracking was observed on the underside of the concrete deck in the second specimen.

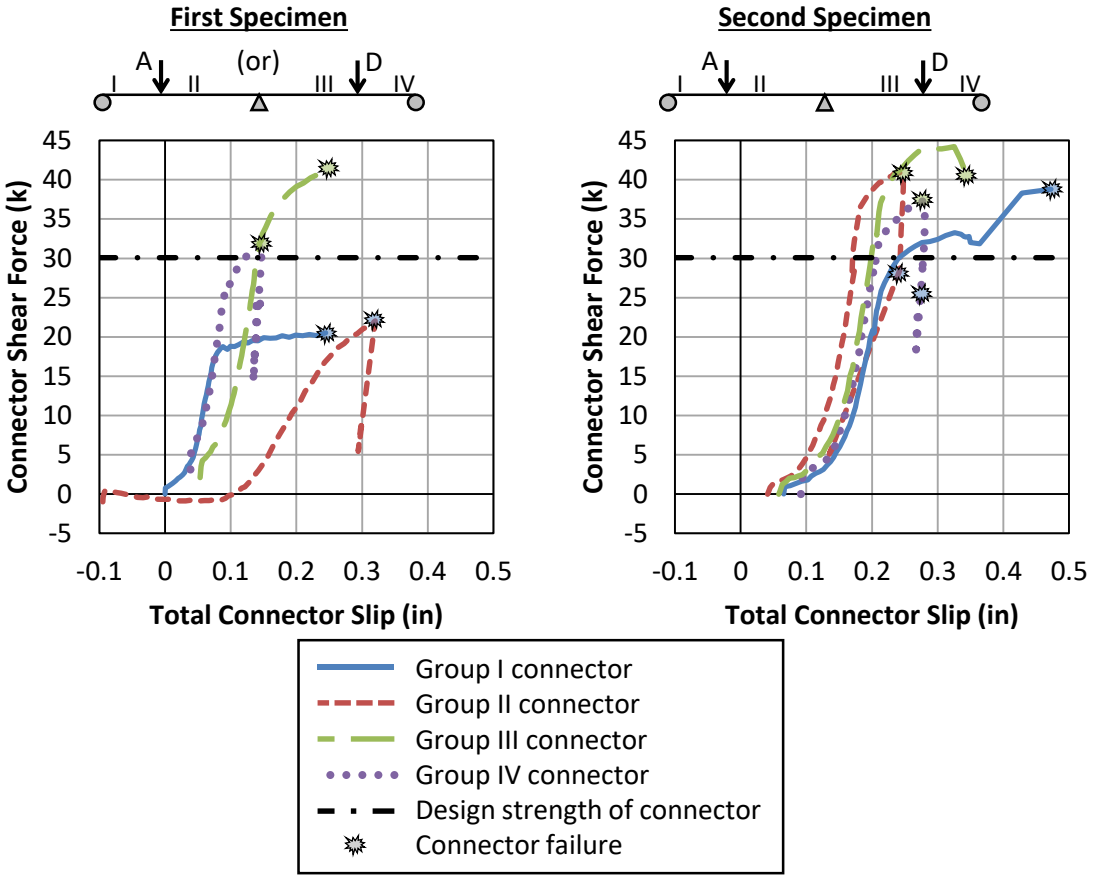

Figure 5-23: Force-Slip Behavior of Connectors during Ultimate Strength Testing of Both Specimens

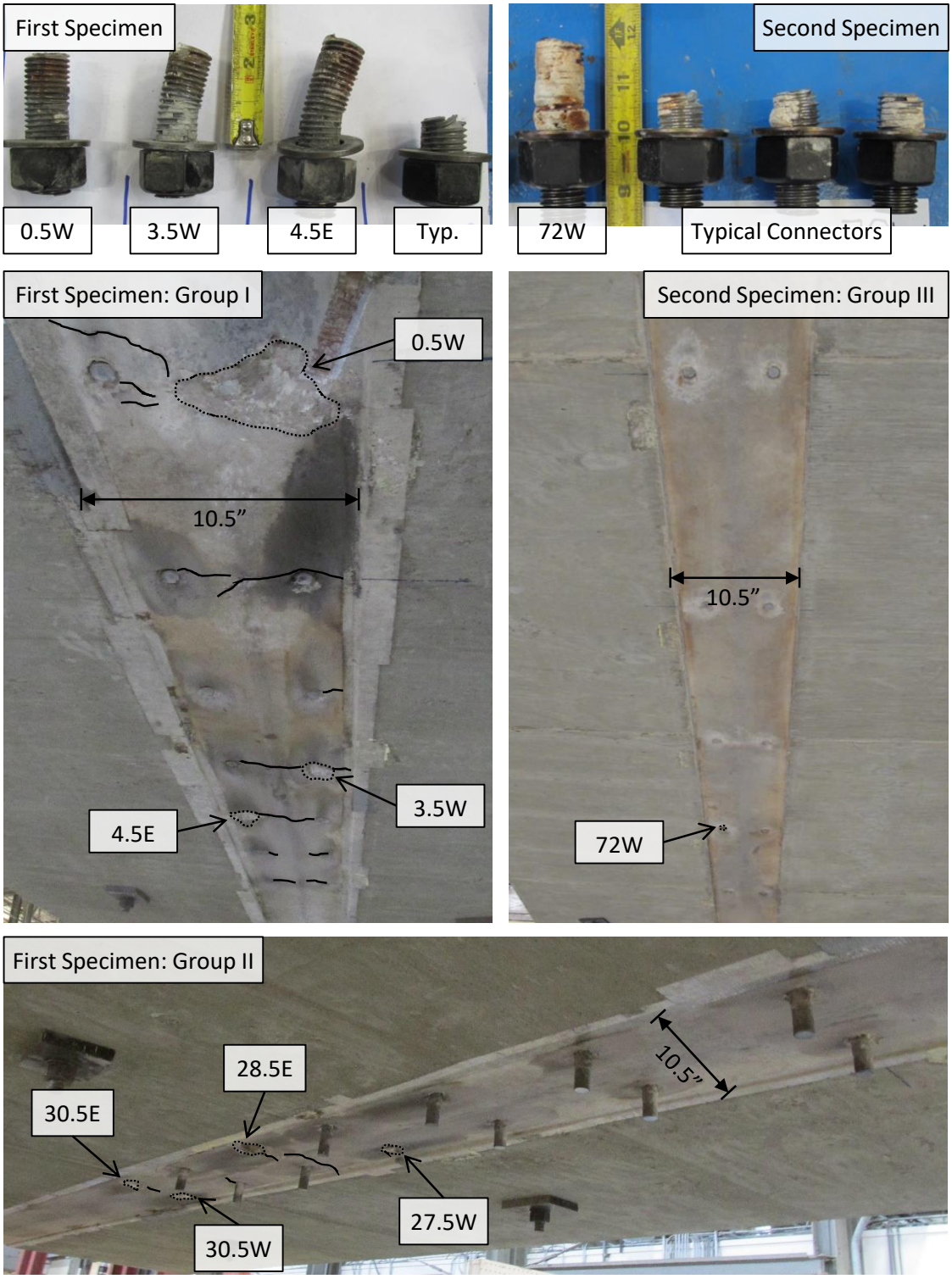

Figure 5-24: Photographs of Failed Connectors and Underside of Deck at Connector Regions after Ultimate Strength Testing of Both Specimens

5.5 SUMMARY

The results from laboratory testing of two large-scale two-span continuous bridge girders strengthened with post-installed adhesive anchor shear connectors were presented and discussed in this chapter. A further examination into particular details of the results is provided in Chapter 6. The two specimens, which were constructed with composite ratios of nominally 20% and 30%, exhibited excellent structural performance and resilient behavior throughout all phases of testing, which lasted nearly 6 months for each specimen. The predicted strength values were exceeded during fatigue, shakedown, and ultimate strength testing, and only one shear connector is known to have failed prior to the ultimate strength testing phases. This failure was only detected using ultrasonic testing, and was not obvious from any of the data collected during previous testing phases, indicating that the failure of a single connector did not adversely affect the behavior. Additionally, following connector failure in the ultimate strength testing phases, composite action was still able to develop, possibly as a result of friction at the steel-concrete interface and the remaining intact connectors. This allowed for the specimens to maintain load-carrying capacities well beyond the predicted strength of the non-composite girder to large deflections of up to L/35.

Generally, it does not seem that the fatigue loading had a significant influence on the strength of either specimen at both the shakedown and ultimate strength limit states. This was even true for connectors that had significant degradation of the adhesive between the threaded rod of the connector and the hole in the top flange of the steel beam, leaving essentially a 1/8-inch “gap” for the connector to slide in without resisting any force. In this case, enough slip occurred in the girder to re-engage the connectors in direct bearing with the steel flange, allowing for composite action to develop under large loads.

Overall, the results of this experimental program indicate that bridges strengthened with post-installed adhesive anchor shear connectors are expected to have good structural performance, even under large demands in the field that may require moment redistribution and significant ductility.

CHAPTER 6: FURTHER ANALYSIS OF EXPERIMENTAL RESULTS

6.1 OVERVIEW

This chapter provides further detailed analysis of the results from the experimental testing to give additional insight into the behavior of the specimens. An in-depth look into the inelastic behavior and plastic rotations sustained during the shakedown testing is discussed first, followed by the general trends in behavior within the shear connector groups.

6.2 INELASTIC BEHAVIOR DURING SHAKEDOWN LOADING

While the results presented in Chapter 5 were primarily associated with the behavior of the girder specimens under load, this section focuses on the "residual" data when the specimens were unloaded in between cycles of shakedown loading. When there are no externally applied loads on a statically indeterminate structure, any deformations and forces present in the system are derived solely from the permanent inelastic deformations that have previously occurred. Thus, the extent of inelastic behavior can be observed by interpreting this residual data and is quantified here by (1) the plastic rotation that developed at the critical locations, which is an indication of the ductility demand on the section, and (2) the amount of residual moment present in the unloaded state, which corresponds to the amount of moment redistribution that occurred under the applied load.

The plastic rotations were estimated using the data obtained through the optical system, which records the position of several "markers" which were fixed to the specimens in the gridded layouts shown in Figure 4-11. The rotation of each column of markers was calculated from this position data at each unloaded step. Any change in rotation along the length of a girder under no external load indicates permanent inelastic rotation at that location. The change in rotation from the columns of markers on opposite ends of each instrumented region was taken as the total plastic rotation in that region.

In theory, the residual moments present in the system can be determined from the residual reaction forces measured after the load was removed for each load step. However, evaluation of the data collected during testing led to the conclusion that these residual reaction forces were not reliable measurements, primarily because neither force nor moment equilibrium were satisfied at the unloaded state. This is likely because the residual reaction forces were small (less than 5 kips) in comparison to the capacity of the load cells

used to measure the forces. Thus, an alternate method of estimating the residual moments was developed using the residual deflections measured during testing, instead of the unreliable residual reaction forces. This deformation-based technique also provides an estimate of the plastic rotation, which can be compared to the rotations calculated from the optical system data.

Section 6.2.1 provides a description of this analysis technique, while Section 6.2.2 and Section 6.2.3 present the results regarding the plastic rotations and residual moments, respectively.

6.2.1 Method of Analysis

The technique developed to estimate the amount of moment redistribution from the residual deflected shape uses plastic hinges to represent the inelastic behavior at each critical section. The method is based on the assumption that the total residual deflection along the girder is the sum of the residual deflections caused by the rotation of each plastic hinge, shown in Figure 6-1. The permanent rotation of each plastic hinge causes residual moment to be present in the system in order to maintain zero deflection at the support locations. The shape of the residual moment diagram associated with a rotation of each hinge is also shown in the figure. For completeness, the equations derived for each deflected shape and for the associated residual moment at the interior support (M_{rd}) are provided in Appendix B.

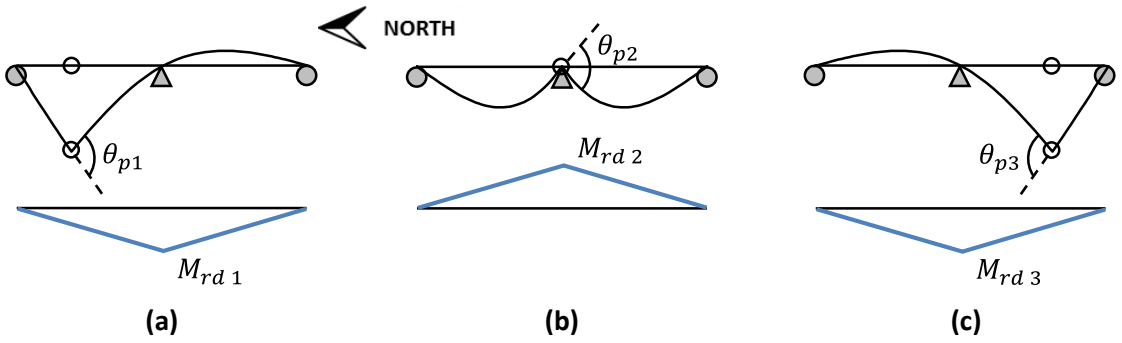

Figure 6-1: Deflected Shapes from Rotation of Plastic Hinges (a) at Load A in North Span, (b) at Interior Support, and (c) at Load D in South Span

The plastic hinge rotations were determined using a least squares fit, so that the deflections measured during testing most closely matched the analytically determined

deflected shape from the hinge rotations. A script in MATLAB was created to carry out the analysis, which was constrained so the rotations could not be less than zero (MathWorks 2015). Positive rotations were taken in the direction shown in Figure 6-1.

As seen in Appendix B, the equations describing the deflection due to the plastic rotation are entirely dependent on the geometry of the girder and are independent of the flexural stiffness (EI). However, the value of the redistribution moment is dependent on the stiffness, which can be difficult to quantify for partially composite girders with groups of shear connectors. Generally, for a statically indeterminate structure, the elastic distribution of moments is a function of the relative stiffness of different portions of a structure. Fortunately, as discussed in Section 7.3, the elastic distribution of moments expected for the non-composite girder will likely provide a good estimate for the partially composite girder. For the case of the experimental specimens, this is simply a constant stiffness over the entire length of the girder. However, the actual value of this stiffness to use in the analysis is unclear, as it depends on the level of partial-composite action.

Thus, to estimate the stiffness, a similar analysis was conducted using the measured deflections at the peak load of each cycle. In this case, the total deflection along the girder was assumed to be the sum of the elastic deflection caused by the applied load and the residual deflection caused by the rotation of each plastic hinge, shown in Figure 6-1. The plastic rotations calculated at the unloaded step immediately following each load step were used to determine the residual deflections at that load step. The remainder of the measured deflection under load was assumed to be due to purely elastic deformation.

The elastic deflected shape under the three different loading conditions used during the shakedown testing are shown in Figure 6-2, and the equations derived for these deflected shapes are provided in Appendix B. These equations assume that the flexural stiffness is constant along the full length of the girder. An estimate of the moment of inertia (I) at each load step was computed using a least squares best fit so that the measured deflections most closely matched the analytically determined deflected shape from the elastic deformation and the hinge rotations. This moment of inertia was then used to compute the residual moment at the unloaded steps using the equations in Appendix B associated with the plastic hinge rotations shown in Figure 6-1.

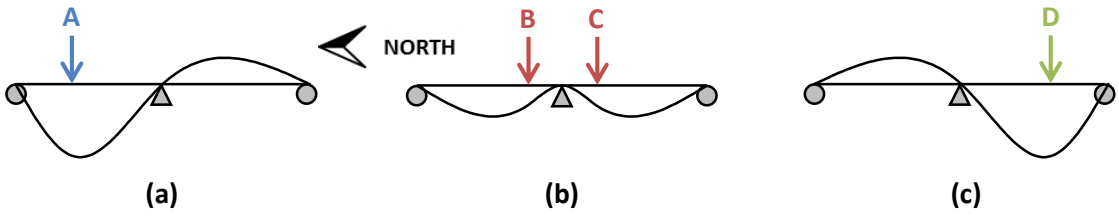

Figure 6-2: Elastic Deflected Shapes from Applied Load for (a) Load A in North Span, (b) Loads B and C in Both Spans, and (c) Load D in South Span

6.2.2 Plastic Rotations

The residual rotations calculated from the optical system data after the last cycle at the predicted shakedown limit load are shown in the following two figures. Figure 6-3 plots the variation in the residual rotation over the longitudinal distance near the critical locations around Load A and Load D for both specimens. Figure 6-4 plots the residual rotation variation around the interior support for both specimens. Note that for the second specimen, the optical system was only used at the location of Load A and at the interior support, and not at Load D. For the first specimen, the optical system was used in all three locations.

One key difference between the trends shown in the two figures is the slope of the rotation curves. Recall that under no external load, any change in rotation is primarily due to permanent plastic rotations. Throughout the majority of the instrumented regions at Load A and Load D in Figure 6-3, the slope of the rotation curves is fairly constant, with shallower slopes occurring farther away from the load point. This indicates that the plastic rotation is spread out over this entire region and likely extends slightly outside of the instrumented area. Conversely, at the interior support in Figure 6-4, there is a steep slope in the rotation curves close to the centerline of the support, but the curves quickly flatten out farther away from the support. This indicates that the plastic rotation is concentrated within a distance of approximately 10 inches from the support.

This observation is to be expected based on the section properties and the loading conditions. The shape factor (k), or the ratio of the plastic moment capacity to the yield moment, is larger for the partially composite section at Load A and Load D ($k = 1.24$ to 1.34) than for the non-composite section at the interior support ($k = 1.16$). These shape factors are calculated in Appendix A. As a comparison, the shape factor for the idealized case of a plastic hinge is 1.0. For higher shape factors, yielding will start to occur at the

extreme fibers of the cross section at relatively lower moments as compared to the plastic moment capacity. This means that sections that are farther away from the point of maximum moment will have already started to yield by the time the plastic capacity is reached at that point of maximum moment. Thus, inelasticity will ultimately be spread over a wider distance away from the point of maximum moment, as seen in Figure 6-3 at Load A and Load D. For smaller shape factors, sections that are fairly close to the point of maximum moment will remain fully elastic when the plastic moment capacity is reached at that point of maximum moment. This type of behavior is seen in Figure 6-4 at the interior support. In addition to the different shape factors, the relatively shallow and steep moment gradients at Load A and Load D and at the interior support, respectively, contribute to the plasticity spread within these regions (see Figure 4-13).

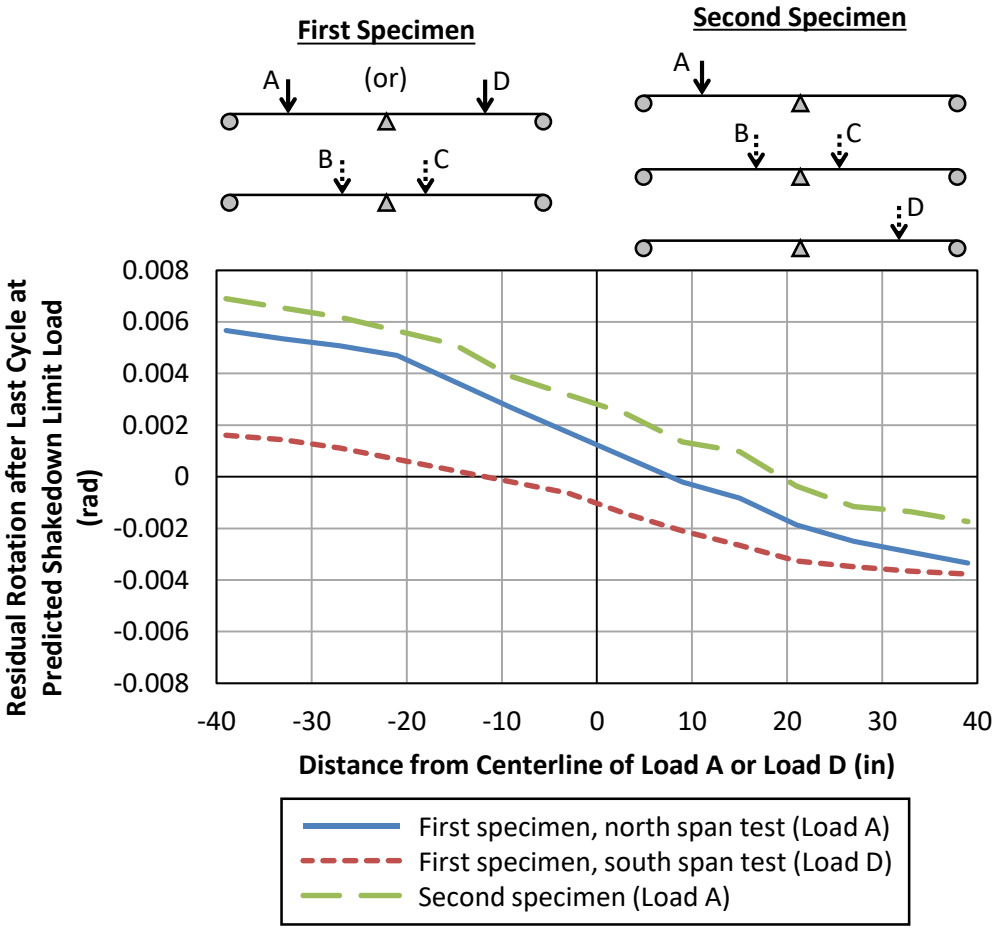

Figure 6-3: Residual Rotations in Positive Bending during Shakedown Testing of Both Specimens

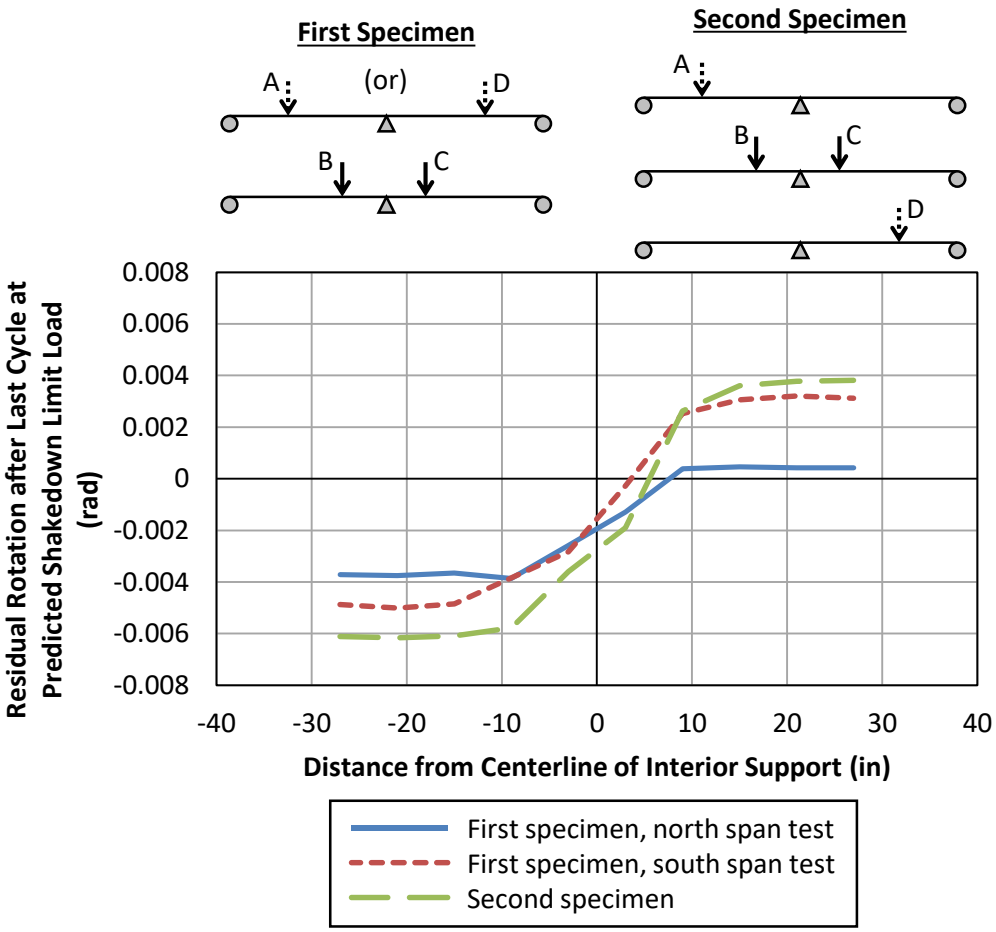

Figure 6-4: Residual Rotations in Negative Bending during Shakedown Testing of Both Specimens

The equivalent plastic hinge rotation at each critical location was estimated from the optical system data as the total change in rotation from one end of the instrumented region to the other. This is likely an accurate estimation at the interior support, because all of the inelastic behavior seems to be contained within the instrumented region, as indicated in Figure 6-4. However, this may underestimate the total plastic rotation around the locations of Load A and Load D because some inelasticity likely occurred slightly outside of the instrumented region, based on the trends shown in Figure 6-3.

In Figure 6-5 and Figure 6-6, this equivalent plastic hinge rotation is compared to the plastic hinge rotation determined using the analytical method described in the previous section at all unloaded steps for the first and second specimens, respectively. Generally, these two methods of calculating the plastic hinge rotation provided fairly similar values,

although the estimation based on the residual deflections tended to result in slightly higher values of plastic hinge rotation than did the data from the optical system. With the exception of the interior support location during south span testing of the first specimen, the trends in this data are nearly identical for all tests and all locations. Small amounts of plastic rotation begin developing at around half of the predicted shakedown limit load, and these rotations increased rapidly as the limit load is approached and exceeded. Recall that for the first specimen, the south span test was conducted after the north span test in which significant yielding occurred at the interior support. Thus, the plastic hinge rotation at the interior support at the start of the south span test is equivalent to the final rotation at that location during the north span test. No significant increase in the plastic hinge rotation at that interior support occurred until slightly below the predicted shakedown limit load. This is consistent with many of the observations made in Chapter 5.

For the first specimen, the total plastic hinge rotation varied between approximately 0.006 radians and 0.010 radians after shakedown was observed at the predicted limit load. For the north span test of the first specimen, the rotation at Load A was near the high end of that range while the rotation at the interior support was near the low end. The opposite was true for the south span test of the first specimen. Although shakedown was not observed in the second specimen at the predicted limit load, the plastic hinge rotations when the test was stopped varied between 0.009 radians and 0.012 radians at all three critical locations.

For comparison, the moment redistribution provisions in the *AASHTO LRFD Bridge Design Specifications* were developed to limit the plastic rotation at an interior support to a maximum of 0.009 radians at the Service II limit state and 0.03 radians at the Strength I limit state (AASHTO 2010). These limitations ensure that excessive deformations that may affect the serviceability of the bridge do not occur and that the cross section has adequate plastic rotation capacity so that the moment redistribution can happen without local buckling. The testing conducted here corresponds more closely to the Strength I limit state, which has a rotation limit of approximately twice the largest rotation that was observed experimentally. Note that within the specifications, these rotation limits apply only to the non-composite cross sections at the interior supports and not to the partially composite sections in the spans. While permanent inelastic deformations in the spans can contribute to excessive deflections and potential serviceability problems, local buckling is less of a concern because only a small portion of the steel section is subjected to compressive stresses.

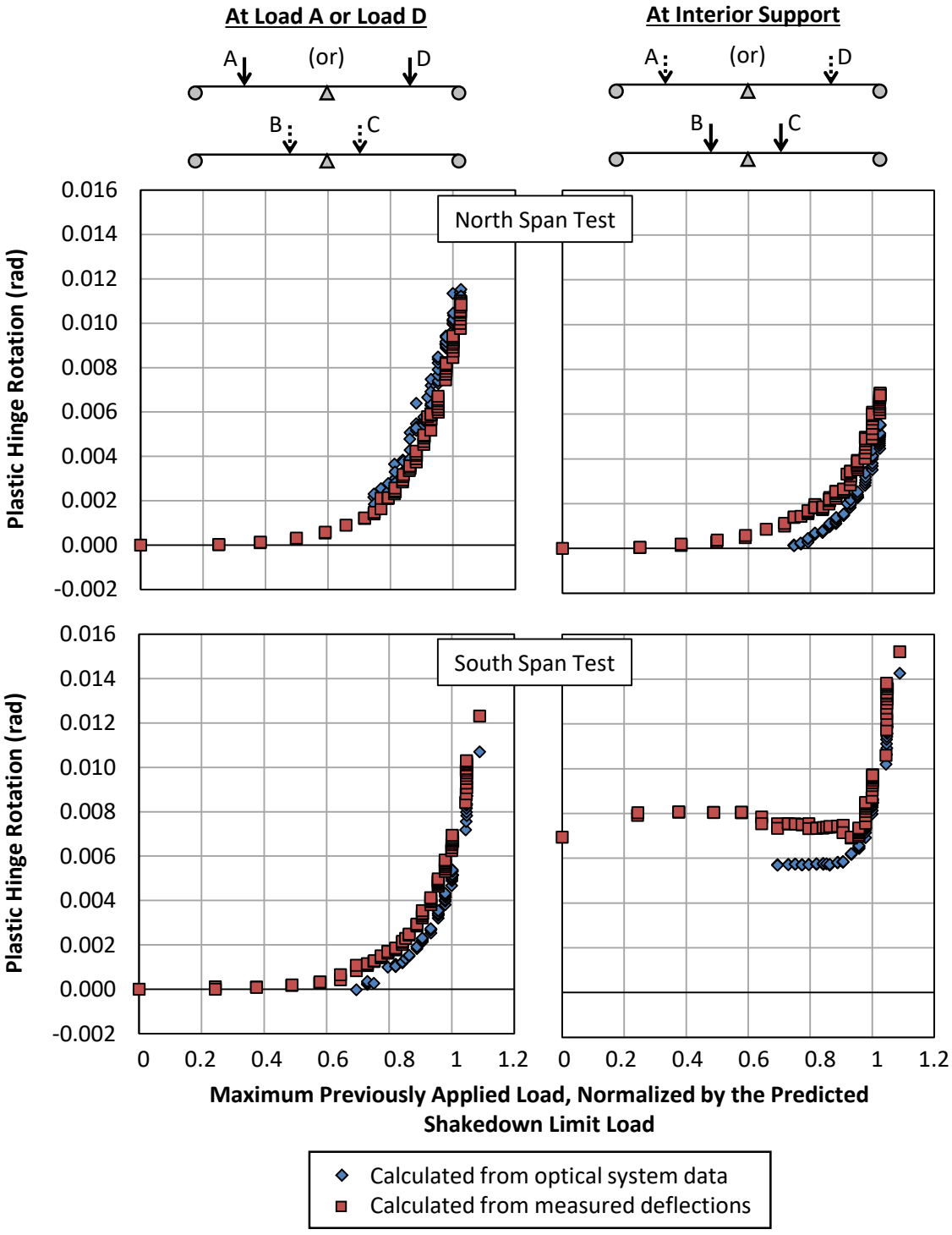

Figure 6-5: Plastic Hinge Rotation at Critical Locations during Shakedown Testing of First Specimen

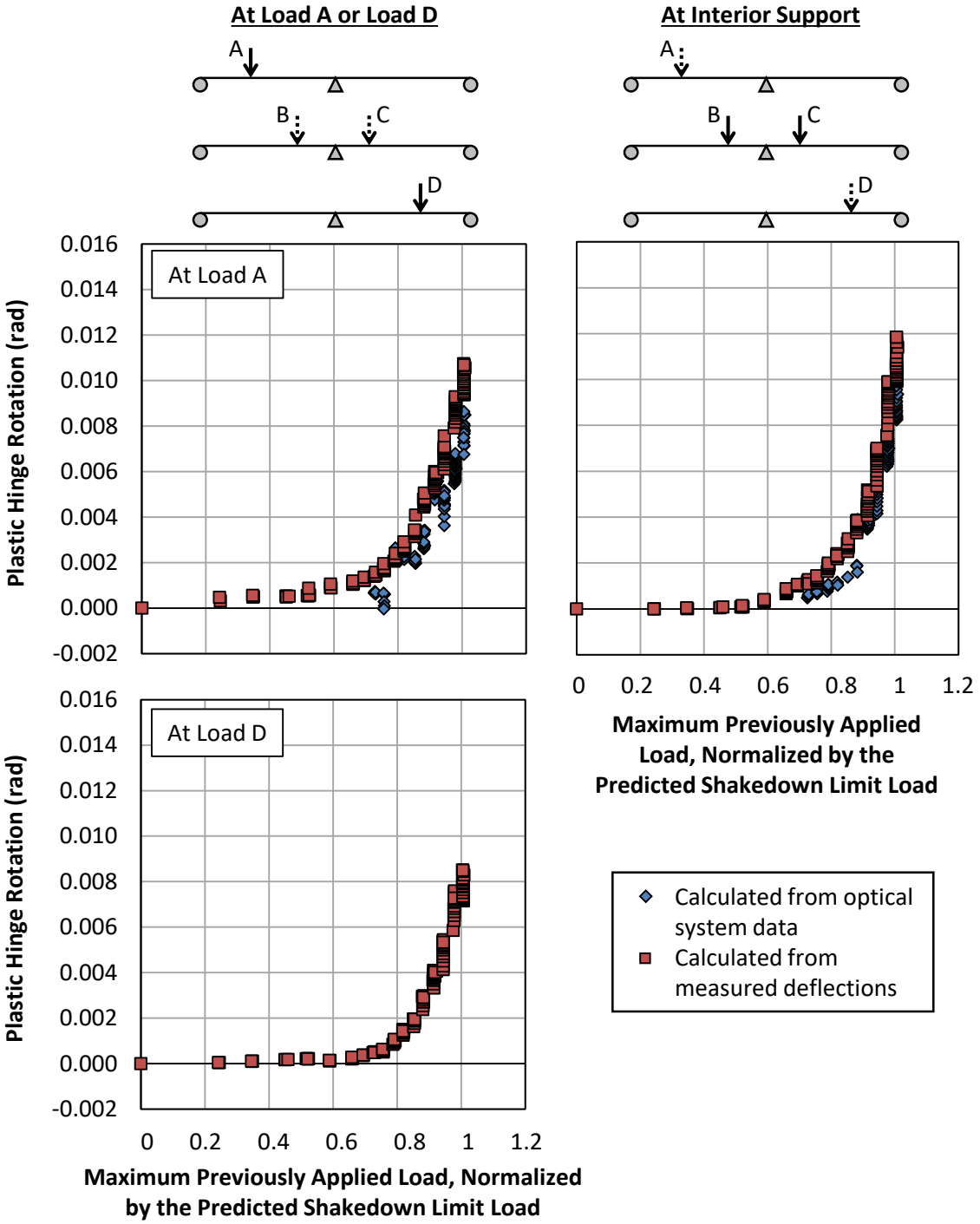

Figure 6-6: Plastic Hinge Rotation at Critical Locations during Shakedown Testing of Second Specimen

6.2.3 Residual Moment Results

As described in Section 6.2.1, the plastic hinge rotations computed at the unloaded state were used to determine the elastic portion of the response under the applied loads. An estimate of the moment of inertia was made based on this elastic behavior. The variation in this moment of inertia with the applied load for both specimens is shown in Figure 6-7. Note that for the second specimen, the moment of inertia values calculated for the individual load steps consisting of the application of Load A and Load D were similar and thus were averaged to obtain the data plotted in the figure. The figure also indicates the predicted effective moment of inertia for the partially composite section, calculated in Appendix A using Equation 2.5, as well as the moment of inertia for the non-composite section, which is simply that of the steel beam.

Generally, the moment of inertia under applied Load A or Load D is gradually reduced as the magnitude of the load increases. This might be a result of cracking occurring in the concrete deck or small losses in composite action. However, the load-deflection behavior of each cycle indicates that this has a negligible effect on the overall behavior (see Section 5.3.1). For the first specimen, the effective moment of inertia for the partially composite section provides a reasonably good prediction of the moment of inertia at low levels of loads, but over-predicts the observed value at larger loads. For the second specimen, the effective moment of inertia over-predicts the calculated value significantly at all loads. This might be because of the low composite ratio of this specimen, which falls just barely within the range of applicability of Equation 2.5.

For both specimens, the moment of inertia calculated under applied Loads B and C is significantly lower than that for Load A or Load D. This is likely because Loads B and C induce a moment diagram in which the point of maximum moment is closer to the interior support than any of the shear connectors. Thus, the connectors are ineffective in creating composite action under this type of load. However, the calculated values of the moment of inertia are still well above that predicted for the non-composite section, indicating that there may still be small benefits from composite action. For the first specimen, the moment of inertia under applied Loads B and C remains essentially constant through all levels of load. However, for the second specimen, this moment of inertia decreases slightly at low levels of load before leveling off to a relatively constant value at higher loads.

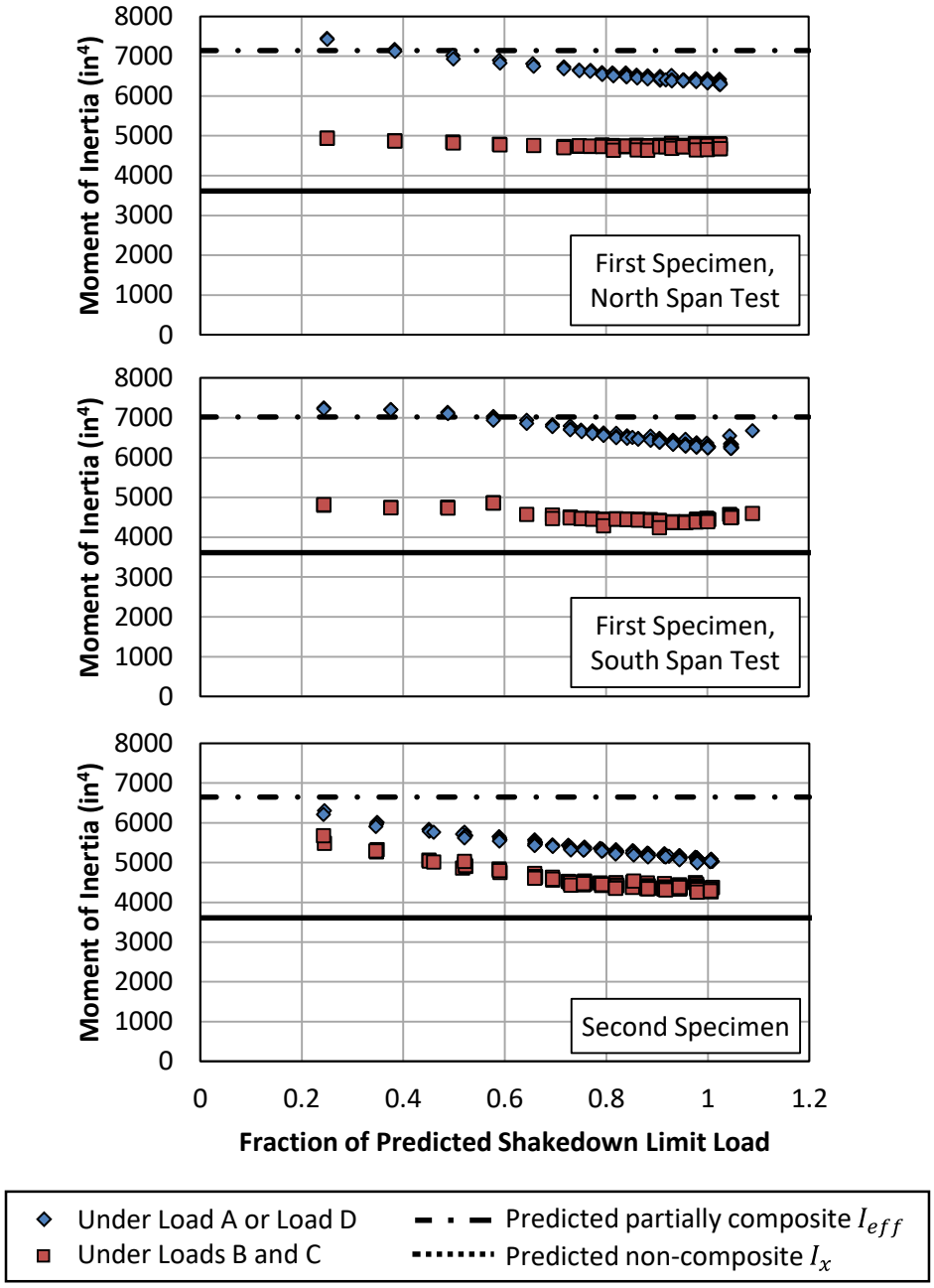

Figure 6-7: Variation in Estimated Moment of Inertia during Shakedown Testing of Both Specimens

Finally, the calculated values of the moment of inertia from Figure 6-7, along with the plastic hinge rotations from Figure 6-5 and Figure 6-6, were used to estimate the residual moments at each unloaded step, which directly indicate the amount of moment

that has been redistributed up to that point in the test. The maximum residual moment, which occurs at the interior support, is equivalent to the redistribution moment defined in the AASHTO LRFD specifications (M_{rd}). The equations derived to perform these calculations are provided in Appendix B. For each cycle of load, the moment of inertia under applied Load A or Load D was used in these calculations, rather than that under applied Loads B and C. This was done because the entire length of the girder is subjected to residual moments that are either all positive or all negative. Thus, the connectors are effective in creating composite action and the moment of inertia calculated under applied Load A or Load D is likely a better representation of the stiffness than that calculated under applied Loads B and C. The predicted redistribution moment at the shakedown limit load, calculated in Appendix A based on the AASHTO LRFD specifications, is also indicated on the graphs for each test.

The general trends seen in Figure 6-8 are similar to those seen in Figure 6-5 and Figure 6-6 because the redistribution moments are directly related to the amount of permanent inelastic deformation that has developed in the structure. Again, the trends observed during the south span test of the first specimen are consistent with the expected behavior because significant yielding had already occurred at the interior support during the north span test conducted beforehand.

At the shakedown limit load, the predicted redistribution moment exceeds the estimated redistribution moment for both specimens. Particularly, the predicted value exceeds the estimated experimental value observed during testing of the first specimen by more than 150%. For the second specimen, the predicted value exceeds the value estimated from the experimental data by only 30%. The over-prediction of this redistribution moment is to be expected because the AASHTO LRFD provisions for moment redistribution assume that yielding only occurs in negative bending at the interior supports, and that no yielding occurs in positive bending in the spans. As indicated in Figure 6-1, the redistribution moments from the plastic hinge rotation in the spans and at the interior support have opposite signs. Thus, some of the positive redistribution moment that results from plastic rotation at the interior support will be offset by the negative redistribution moment developed due to any yielding in the spans. Additionally, it is important to note that there were several assumptions that were made in calculating these estimated redistribution moments from the measured deflections that may introduce some error into the results.

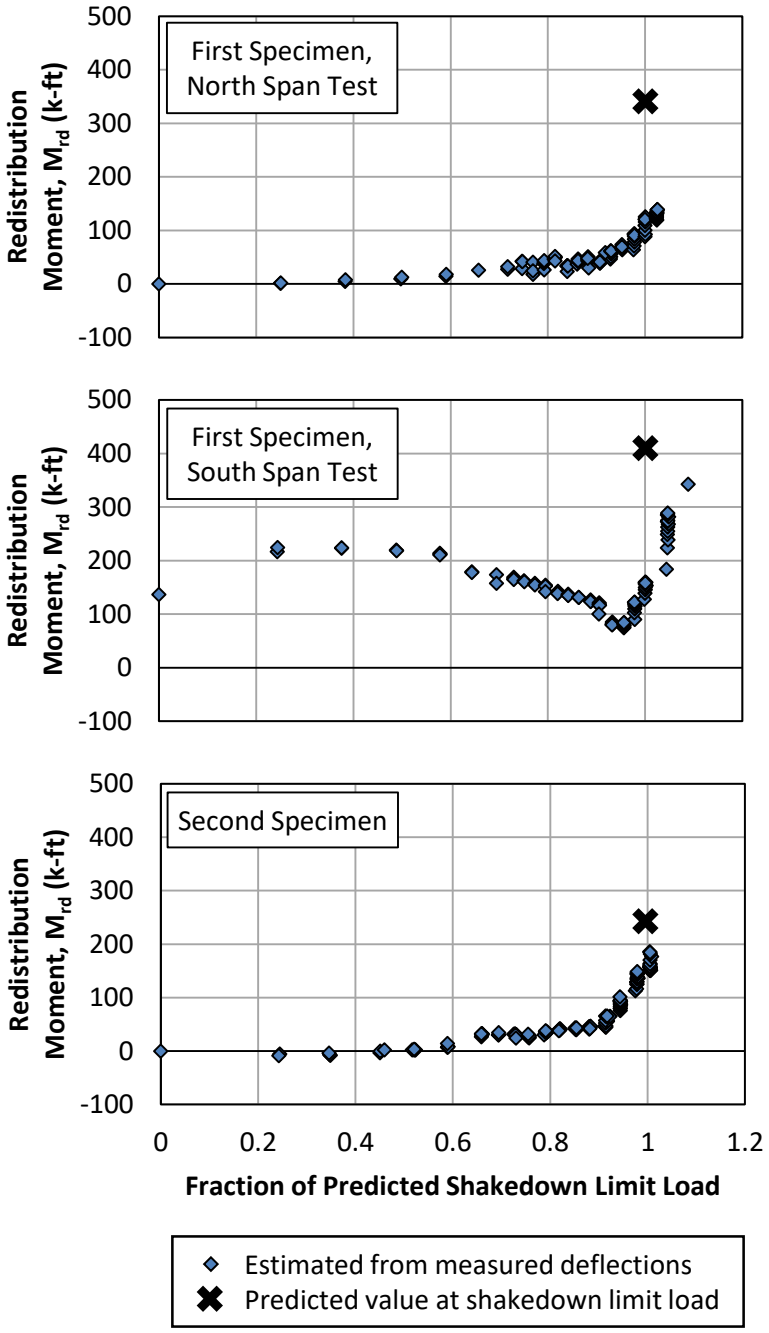

Figure 6-8: Variation in Estimated Redistribution Moment during Shakedown Testing of Both Specimens

6.2.4 Discussion of Inelastic Analysis

The analysis technique used here is largely limited to shakedown-type loading in which the structure is frequently loaded and unloaded, and each cycle of load, even well within the expected range of inelastic behavior, induced a nearly elastic response. This limitation comes from the challenges that arise in separating the elastic and inelastic portions of the response at any given point in the loading history. These challenges primarily stem from the difficulties in estimating the distribution of flexural stiffness, which affects the distribution of moments within a statically indeterminate structure. This can be particularly difficult for partially composite girders with shear connectors concentrated in groups, as discussed in Section 7.3. Thus, it was not feasible to apply this type of analysis to results from the ultimate strength tests due to the uncertainty in differentiating between the elastic and inelastic responses.

This more rigorous analysis technique not only provides additional information regarding the inelastic behavior but also highlights some of the assumptions that are commonly made in simple models, such as the upper- and lower-bound methods. One example of an assumption that is not aligned with the actual behavior is using a plastic hinge to represent the inelastic behavior. This is an assumption that is made in nearly every type of inelastic analysis short of detailed finite element modeling. The data from the optical system clearly show that flexural yielding of an I-shaped girder is spread over a finite length surrounding the location of maximum moment. However, as shown in the results here, using plastic hinges to model concentrated inelasticity provides a reasonable estimate of the overall behavior. Another example is the inherent assumption in the AASHTO LRFD moment redistribution provisions that yielding only happens in negative bending at the interior supports of continuous girders, so that all sections in the spans subjected to primarily positive moment demands remain elastic. As has been illustrated in the data presented here, a significant amount of inelastic behavior occurred in regions of both positive and negative bending during the testing of these two large-scale specimens.

However, despite these limitations of simple models to predict the observed inelastic behavior below the limit load, these models are still powerful tools for design and analysis, as long as the differences between the predicted and actual behavior are kept in mind.

6.3 BEHAVIOR WITHIN CONNECTOR GROUPS

In Chapter 5, the general force-slip behavior of the shear connectors during testing was presented for only the connector pair located at the middle of each group. This section explores the distribution of force and slip amongst all connectors in a group as well as the variation of cross-sectional behavior within a connector group. All of the results presented in this section are from both shakedown and ultimate strength testing of the second specimen because it was more fully instrumented to collect this data than was the first specimen (refer to Figure 4-3).

6.3.1 Connector Force

As discussed in Section 4.5, the force carried by the shear connectors was estimated by placing strain gages through the depth of the steel beam on either side of a connector pair. The change in the axial force in the steel beam, which was calculated from the strain readings, from one side of a connector pair to the other was assumed to be the horizontal interface shear force transferred between the steel beam and the concrete deck by that pair of connectors. Although this process ignores any force transfer that may occur through friction and tends to be sensitive to measurement errors in the strain values, the general trends shown by the results are useful to illustrate how the forces might be distributed within a group of connectors.

In this section, the data regarding the force in the connectors is first presented in terms of the sum of all of the shear connector forces in each group. This total connector force is a measure of the level of composite action in the girder, as it represents the compressive force developed in the concrete deck, which is equilibrated by an equal and opposite tensile force in the steel beam. The compressive force developed in the deck is the manner through which composite action actually occurs because it allows the concrete to participate in resisting positive flexural demands on the section. Following the discussion of the total force in a group, the distribution of force within a group of connectors is explored.

Total Connector Force in a Group

Figure 6-9 and Figure 6-10 plot the sum of all connector forces in each group during shakedown and ultimate strength testing, respectively. These total force values indicate that each connector carried on average a maximum of 30 to 35 kips of force during the

shakedown testing and 35 to 40 kips of force during the ultimate strength testing. This is slightly larger than the design strength of a single connector (30.1 kips, as computed in Appendix A). To simplify the plot in Figure 6-10, only the data from the loading portion of the ultimate strength testing is shown.

The sign convention used in the figures associates positive connector forces when, moving from north to south along the girder, compressive force is being transferred into the deck, increasing the axial tension in the steel beam. For example, the application of Load A induces a positive force in Group I and a negative force in Group II. Similarly, the application of Load D induces a positive force in Group III and negative force in Group IV. Because any downward load applied to a continuous girder induces negative moments at the interior support, which tends to put the concrete deck in tension, any compressive force developed in the deck under positive flexure in the spans must flow out of the deck prior to reaching the negative moment region around the interior support. Thus, the total force in the two groups in one span should be equal and opposite, as indicated in both figures for load cases involving Load A and Load D. In these load cases, the maximum positive moment is located between the connector groups in the loaded span so that a significant amount of compression is in the deck at this point of maximum positive moment.

However, a different trend is seen in Figure 6-9 under applied Loads B and C during shakedown testing. Theoretically, this load case should not engage any composite behavior because the point of maximum positive moment is located outside of both connector groups in each span. Thus, any compressive force developed in the deck between the connector groups would have been subsequently removed from the deck at the location of this maximum positive moment. However, as can be seen in the figure, a small amount of force is still developed, mostly in Group I and Group IV at the ends of the girder. Although an exact explanation for this is unclear based on the data collected, it is possible that the associated equilibrating interface shear force occurs through friction developed between the load point and the start of the negative moment region around the interior support.

Further evidence that the development of interface shear forces through friction may be possible is indicated in Figure 6-10 by the behavior of the intact connector groups (II and IV) after connector failure occurred in Group I and Group III. While the order of failure is discussed further in the next section, this figure indicates that there may be some force carried by the intact connector groups, particularly in Group IV, following complete connector failure in the other group in the span.

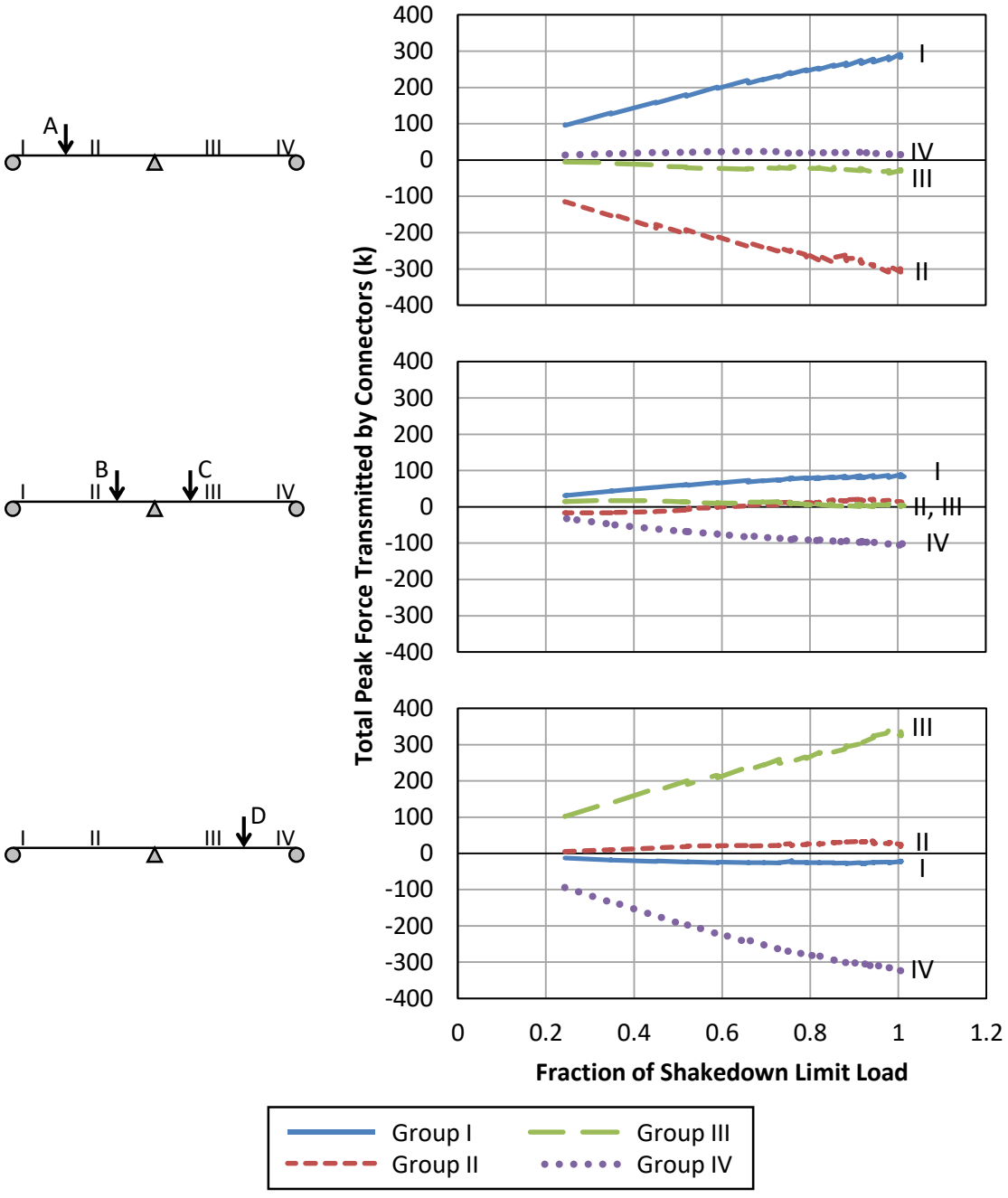

Figure 6-9: Total Force Transmitted into the Deck in Each Shear Connector Group during Shakedown Testing of the Second Specimen

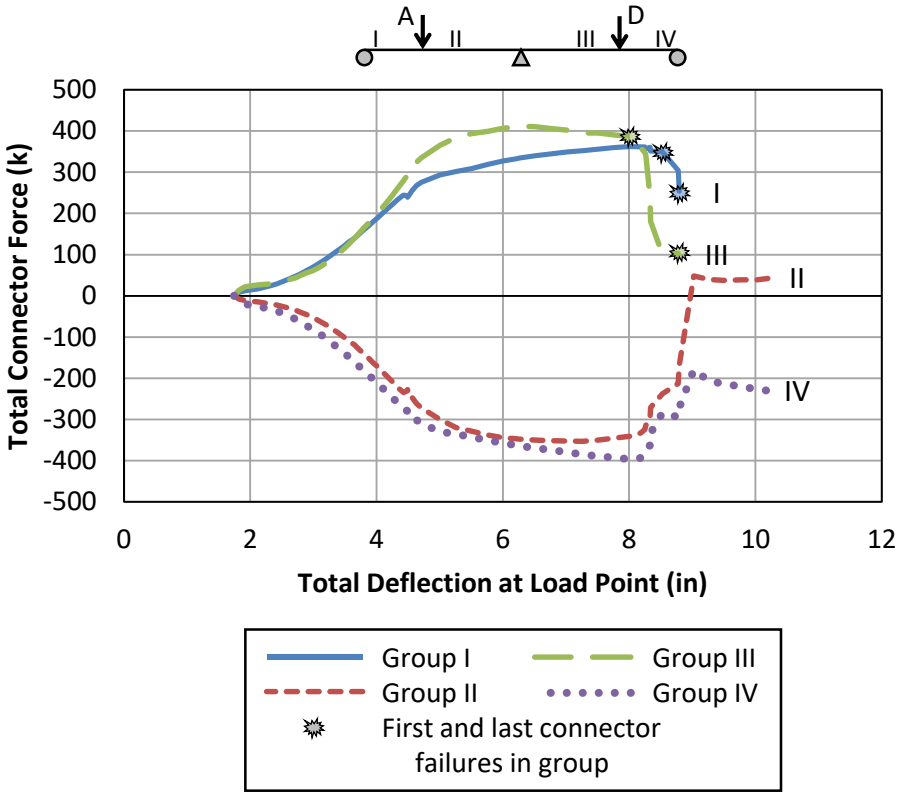

Figure 6-10: Total Force Transmitted into the Deck in Each Shear Connector Group during Ultimate Strength Testing of the Second Specimen

Distribution of Force within a Group

The variation of force in each pair of connectors is plotted in Figure 6-11 and Figure 6-12 for shakedown and ultimate strength testing, respectively. For the shakedown testing, results from only Group I and Group II in the north span are shown for the three different loading conditions. The behavior in Group III and Group IV was nearly identically symmetric to that in Figure 6-11, and is thus not shown here. Again, only the loading portion of the ultimate strength testing data is included in Figure 6-12.

During shakedown testing, a significant amount of force was carried in connectors in Group I and Group II only under applied Load A. This is to be expected, as the other two loading cases do not induce a maximum value of positive moment in the region between these connector groups. However, as with the total force data, there are indications that small amounts of connector force were induced during the other loading cases. Although the trends of approximately linearly increasing connector force with

applied load were reasonably consistent amongst all connectors in a group, the actual magnitude of that force varied considerably between connectors. There are not any significant trends of how or why this variation occurs, and it doesn't seem to be closely linked to the slip distribution within the connector groups, as discussed in the next section. It is possible that this variation is simply a result of the local conditions around each connector. Previous research has shown that during small-scale testing, the stiffness of individual shear connectors in the elastic range varied significantly, likely due to the quality of both the concrete in the immediate vicinity of the connector and of the adhesive layer around the connector (Patel 2013). Inconsistencies in the alignment and centering of each connector during installation might also play a role. This variation might also be in part due to slight errors in the strain measurements that were compounded through the force estimation process.

During ultimate strength testing, the trends in the estimated force are also similar between each pair of connectors in a group with fairly linear behavior in the elastic range followed by a softening of the connectors as the deflections increased. Again, a variation of the magnitude of the force is present between connectors, although this variation seems to be reasonably consistent with that observed in the shakedown testing. For example, in Group I, connector pair "e" consistently resists the highest load, while connector pair "a" generally resists the lowest level of load in both tests. Additionally, recall that one of the connectors in the pair at location "b" in Group III had failed at some point prior to ultimate strength testing. The force estimated to be carried by this single connector is significantly lower than all other single connectors. The exact reason for this is unclear, but it is possible that the asymmetry of the cross section with a single connector inhibits the effectiveness of the connector, or that the remaining connector was also damaged, but it was not detectable at the time.

The points on the plot in which connector failures were estimated to have occurred are also denoted in Figure 6-12 and listed in Table 6-1. It was not possible to exactly pinpoint the failure of each individual connector from audial and physical observations during testing. While failure of the connectors was accompanied by a loud noise, it was often difficult to determine from where the noise originated. The bottom portion of some connectors were easily removed from the specimen following failure, but several were held tightly in place after fracturing by the adhesive surrounding the connector in the top flange of the steel beam and had to be hammered out after testing was complete. Thus, these

estimates were made primarily using the trends in the connector force, supplemented by observations made during testing.

An interesting observation to note is that connector failures occurred at a wide range of estimated connector force. The values reported in Table 6-1 are for a single connector, assuming a pair of intact connectors shares the force equally. While some variability in the strength of a single connector is expected, this was likely exacerbated by the method used to estimate the force from strain measurements. Additionally, it is logical that the connectors in Group III would be the first to fail because one of these had already fractured prior to the start of the ultimate strength testing. However, the reason that the connectors in Group I failed rather than those in Group II is unclear from the force data. Although the data indicates that the most heavily loaded connector pair was in Group I (pair "e"), this was not the first connector pair to fail in the north span. Furthermore, the maximum total force developed in both groups was essentially equal. A better explanation for this is the slip demand on the connectors, as discussed in the next section.

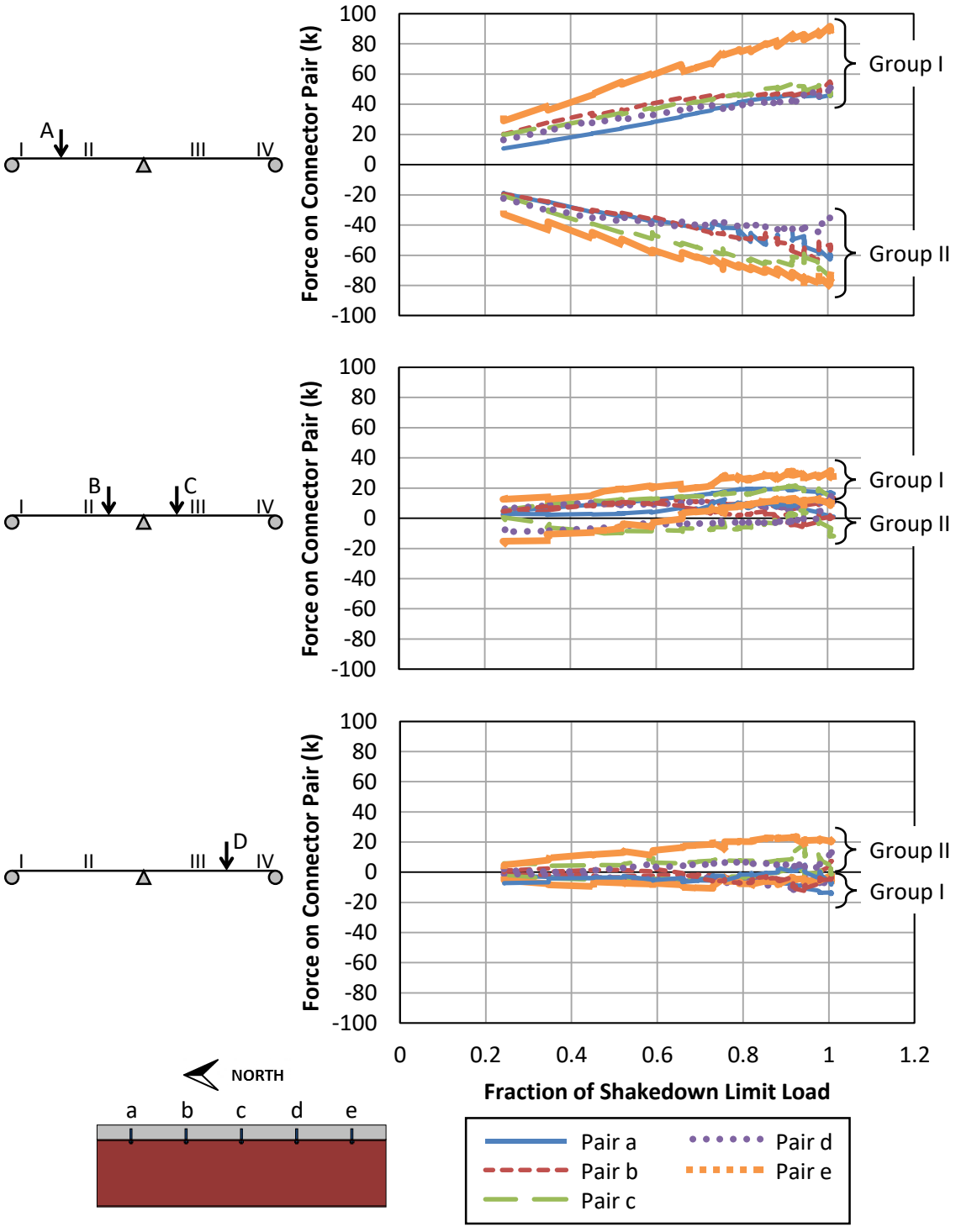

Figure 6-11: Typical Distribution of Force within Connector Groups during Shakedown Testing of the Second Specimen

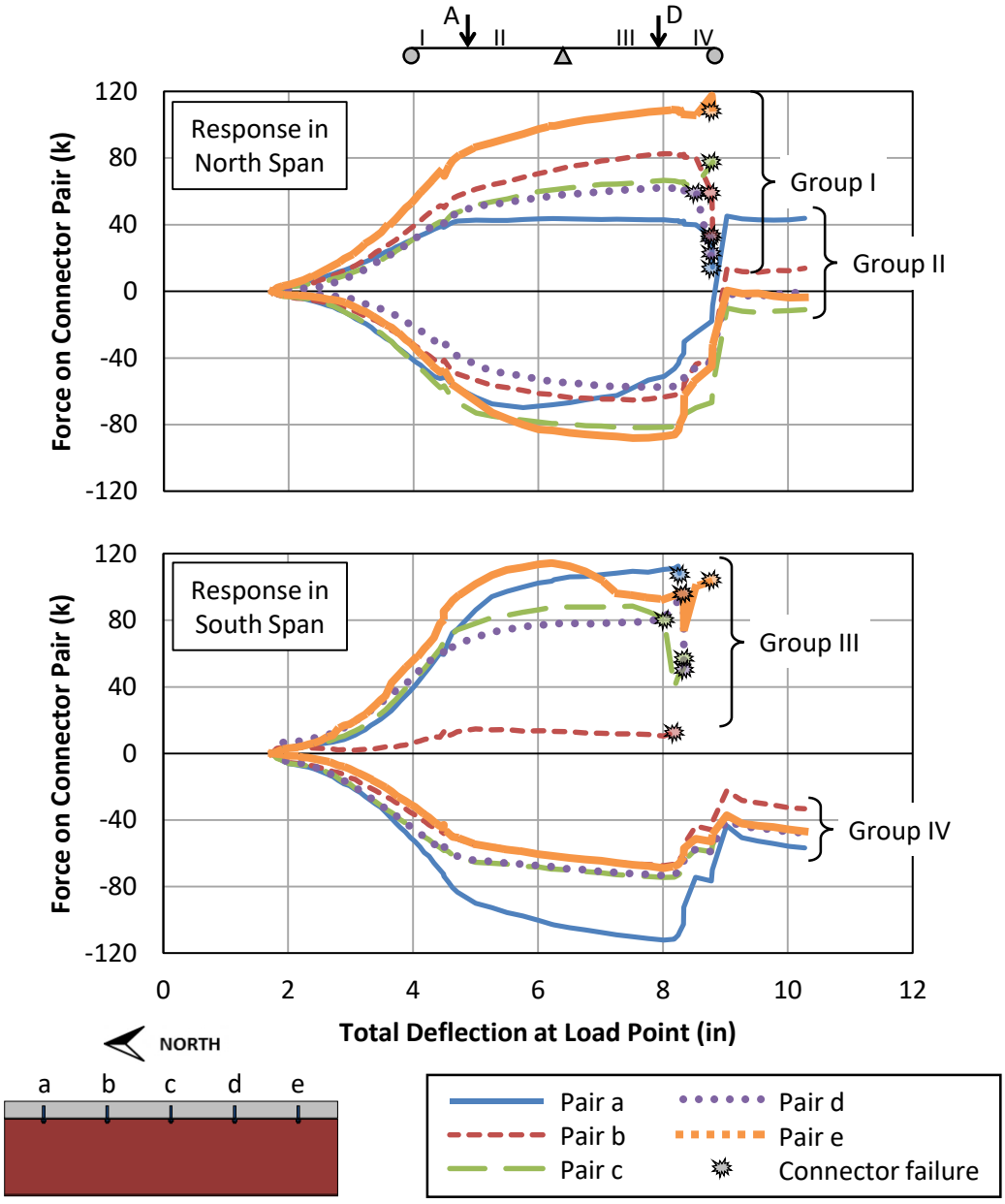

Figure 6-12: Distribution of Force within Connector Groups during Ultimate Strength Testing of the Second Specimen

Table 6-1: Estimated Order of Connector Failure during Ultimate Strength Testing of the Second Specimen

Group	Connector	Deflection (in)	Connector Force (k)	Connector Slip (in)
III	b (#1)	--	--	--
III	c (#1)	8.02	40.6	0.34
III	b (#2)	8.18	6.3	0.42
III	a (both)	8.26	54.1	0.50
III	d (#1)	8.33	47.5	0.39
III	e (#1)		47.7	0.36
III	c (#2)	8.34	27.9	0.45
III	d (#2)		25.5	0.43
I	d (#1)	8.53	30.0	0.36
I	a (#1)	8.78	16.2	0.44
I	b (#1)		29.3	0.43
III	e (#2)		51.7	0.50
I	a (#2)	8.79	7.3	0.49
I	b (#2)		17.0	0.48
I	c (both)		38.8	0.47
I	d (#2)		8.6	0.46
I	e (both)		55.1	0.45

6.3.2 Connector Slip

The interface slip within the groups of connectors was measured using linear potentiometers, as pictured in Figure 4-8. For the second specimen, these linear potentiometers were located at the first, middle, and last connectors in each group. Thus, a direct measure of connector slip was only made for three out of five pairs of connectors in every group. However, due to the compatibility requirements for deformations and the small longitudinal spacing of the connectors (24 inches), linearly interpolating between the measured values will likely provide a good estimate of the slip of the other two connectors in each group. Nevertheless, to simplify the graphs in this section, only the three connectors with linear potentiometers at the same location are shown.

The variation of slip between individual connectors in a group is plotted in Figure 6-13 and Figure 6-14 for shakedown and ultimate strength testing, respectively. As with the force data, results from only Group I and Group II in the north span are shown for the three different loading conditions used in the shakedown testing, because the behavior in Group III and Group IV was nearly identically symmetric. Also, only the loading portion of the ultimate strength testing is shown in Figure 6-14.

During both shakedown and ultimate strength testing, the slip measured in the exterior groups (I and IV) was nearly constant for all connectors in the group. However, the slip measured in the interior groups (II and III) increased significantly from the connector closest to midspan to the connector closest to the interior support.

As with the force data, the connectors in the north span underwent significant amounts of slip under the application of Load A. However, significant slips were also observed under applied Loads B and C, which is in contrast to the connector forces estimated for this loading case. This slip that occurs without the transfer of significant amounts of force indicates softening of the shear connector with increasing load. This softening is also evident in the nonlinear variation of slip with the applied load in comparison to the linear increase of connector force with load. Negligible amounts of slip occurred in the north span connectors under applied Load D until large load levels were reached.

During ultimate strength testing, the slip follows an approximately linear increase with deflection, with some slight deviations. In particular, at large deflections just prior to connector failure, the slip in the connectors in Group I began to increase at a rapid rate while the slip in the connectors in Group II began to level off. As mentioned previously, it is likely that the significantly larger slips that occurred in the Group I connectors, as can be seen in Figure 6-14, was the main reason that this was the group that failed in the north span. Note that the values of slip just prior to failure given in Table 6-1 for the connectors that were not directly instrumented to measure slip were linearly interpolated from the measurements at adjacent connectors.

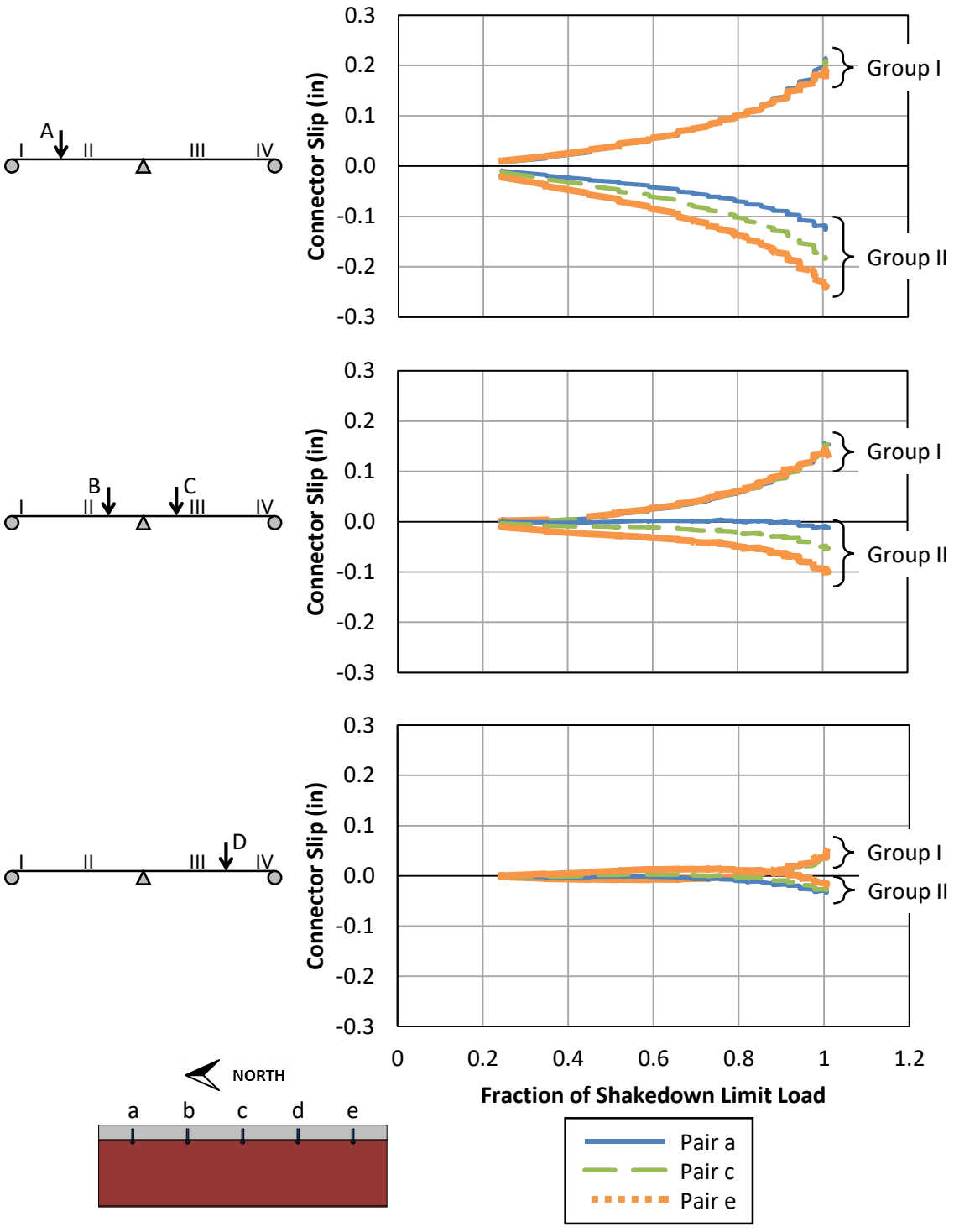

Figure 6-13: Typical Distribution of Slip within Connector Groups during Shakedown Testing of the Second Specimen

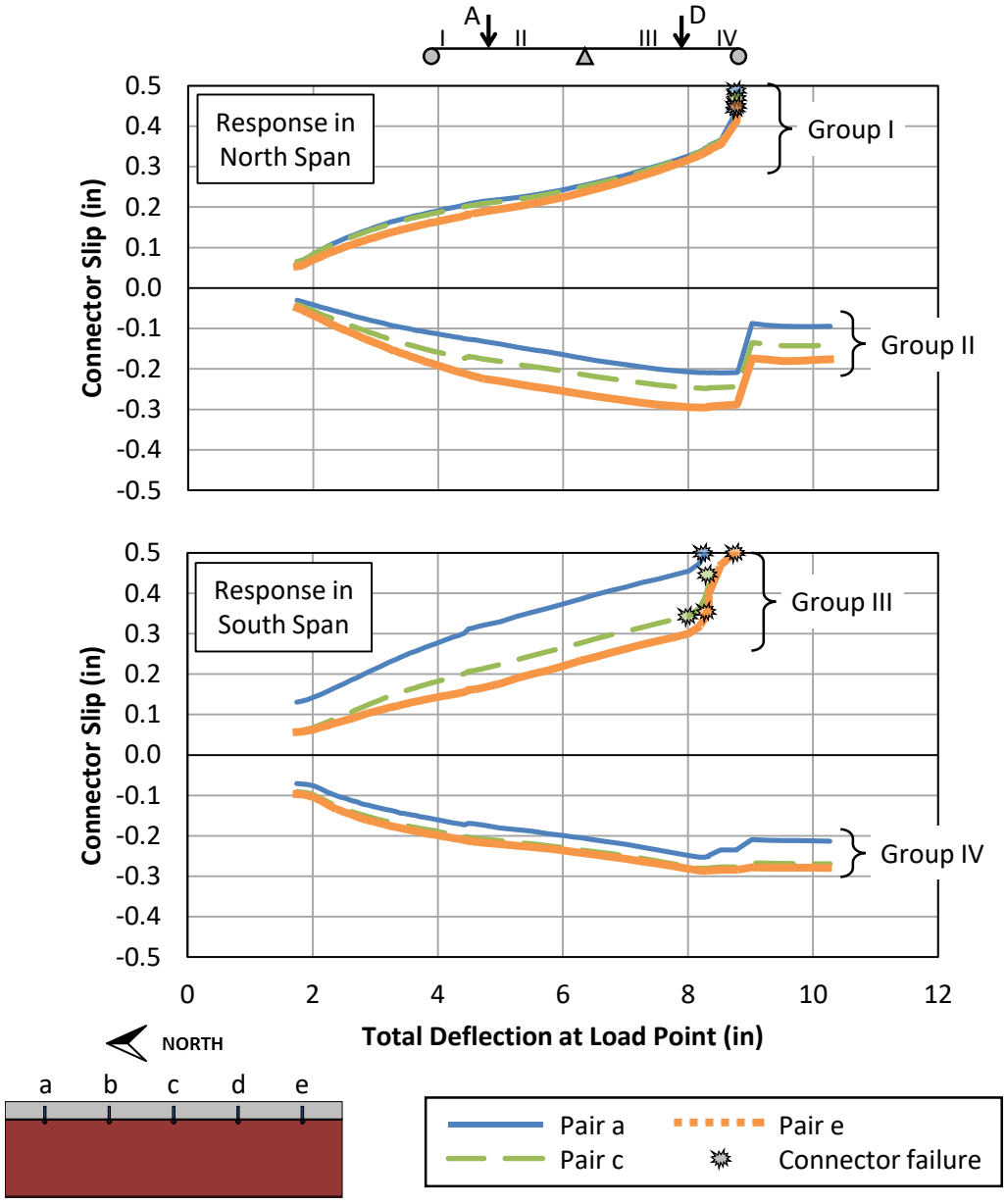

Figure 6-14: Distribution of Slip within Connector Groups during Ultimate Strength Testing of the Second Specimen

6.3.3 Cross-Sectional Behavior

Although the main purpose of installing strain gages through the depth of the steel beam throughout the connector groups was to estimate the connector force, noteworthy trends in the cross-sectional behavior within these groups were also apparent in the data.

To investigate this cross-sectional behavior, general features of a strain profile in a partially composite section is first discussed. Then, data showing the variation in the measured neutral axis location during the experimental testing is presented.

Strain Profiles

The left plot in Figure 6-15 shows the typical variation in strain profiles measured within a connector group. In the figure, tensile strains are taken as positive. This data was recorded during ultimate strength testing near the end of the linear elastic region for connectors in Group II. The plotted strains were directly measured in the steel beam, but were estimated in the concrete deck. The estimate of the deck strains was made using the assumptions that the slope of the strain profile is the same as that in the steel beam and that no net axial force is present in the girder. The interface strain discontinuity discussed in Section 2.2.1 that causes slip in partially composite girders is evident from the plot.

Because of this strain discontinuity, the section effectively has two different neutral axes, one of which corresponds to the strains in the steel beam and the other corresponding to the strains in the concrete deck. The right plot in Figure 6-15 illustrates the change in the location of these two neutral axes within the connector group. On the north end of the group (location "a"), the cross section is partially composite as the neutral axis in the steel beam is located above mid-depth while the neutral axis in the concrete deck is located below mid-depth. This indicates that there is a net tensile axial force in the steel which is counteracted by a net compressive axial force in the deck. Moving southward in the group, the neutral axis in the steel drops in the section while the neutral axis in the concrete rises. This indicates that the section is trending towards non-composite behavior, as compressive force is transferred from the deck back into the steel beam. At location "f" at the south end of the group, the neutral axes are located at approximately mid-depth in both the steel and concrete, as is expected for non-composite behavior.

An interesting feature of partially composite behavior is that the common assumption in beam theory that plane sections remain plane is violated by the slip that occurs at the interface. Thus, the moment (M) resisted by a cross section is not directly related to the curvature (ϕ) by the constant values of the elastic modulus (E) and moment of inertia (I) even for simple elastic behavior (i.e. $M \neq (EI)\phi$). In fact, the direct calculation of a single value of the moment of inertia of a partially composite section is not feasible because the cross-sectional response under a given moment depends on the

interface strain discontinuity at that section, which is related to the slip. Unfortunately, slip and strain discontinuity are variables that cannot be determined through cross-sectional analysis, and must be computed through a global analysis of the entire girder (Ghiami Azad 2016). The effective moment of inertia that can be calculated using Equation 2.5 is an empirically determined value that is useful for estimating the expected deflections for design purposes. The same is true for the effective section modulus that can be calculated using the same relationship.

To illustrate this behavior, consider that between locations "a" and "f" in the region shown in Figure 6-15, the moment from the applied loads decreases by approximately 85%. However, the curvature, measured as the slope of the strain profile, decreases by only 65%, indicating the nonlinear relationship between moment and curvature in partially composite sections.

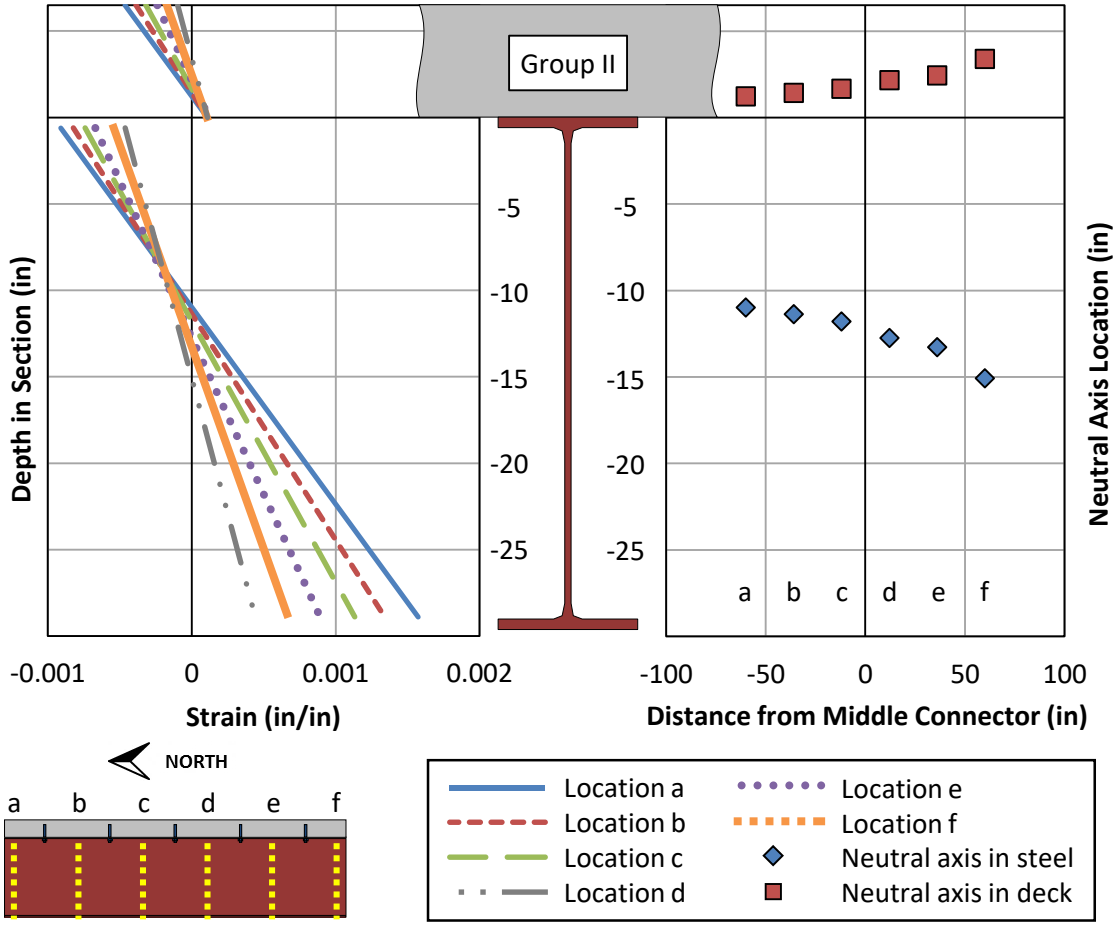

Figure 6-15: Typical Variation of Strain Profiles between Connector Pairs

Neutral Axis Locations

The variation in the location of the neutral axis in the steel beam is plotted in Figure 6-16 and Figure 6-17 for shakedown and ultimate strength testing, respectively. In both figures, the results from only Group I and Group II in the north span are shown because the behavior in Group III and Group IV was nearly identically symmetric. Note that to simplify the plots, only neutral axis locations that fell within the bounds of the steel section are shown. Additionally, only the loading portion of the ultimate strength testing data is shown in Figure 6-17. Note that the predicted location of the partially composite neutral axis plotted in both figures is actually the plastic neutral axis of the partially composite cross section. Because this applies only to sections subjected to large levels of moment, it does not provide a good estimate of the neutral axis location within the connector groups.

Significantly different neutral axis locations were observed between exterior (Group I) and interior (Group II) connector groups during both shakedown and ultimate strength testing. Additionally, there is less variation in the neutral axis location within Group I than within Group II. These discrepancies are primarily due to differences in the slip and the associated strain discontinuity, which significantly impact the strain profile as discussed in the previous section.

During shakedown testing, a general trend of the neutral axis moving lower in the section with increasing applied load was followed. The neutral axis location measured at most southerly location in Group II (location "f") remained fairly constantly at mid-depth under applied Load A, as would be expected for a non-composite section. However, for the other two load cases, the neutral axis at this location was slightly above mid-depth, indicating that some different effects of composite action may have been present in these cases as well, as was also evident in the connector force plots in Figure 6-9 and Figure 6-11. Note that no strain measurements were taken at the comparable location in Group I, as this would have been located at the centerline of the exterior support where theoretically no deformation would occur.

During ultimate strength testing, the neutral axis location in Group I tends to move upwards significantly with the measured deflection prior to connector failure. In Group II, much smaller rises in the neutral axis location occurred with increasing deflections. Immediately after the connectors in Group I failed, the neutral axis at all locations in this group dropped to approximately mid-depth of the steel beam, indicating non-composite behavior. In Group II, the neutral axis dropped, but remained above mid-depth of the steel

beam following connector failure. This is further indication that some composite action may be developed in the vicinity of the remaining intact connectors following connector failure in the span.

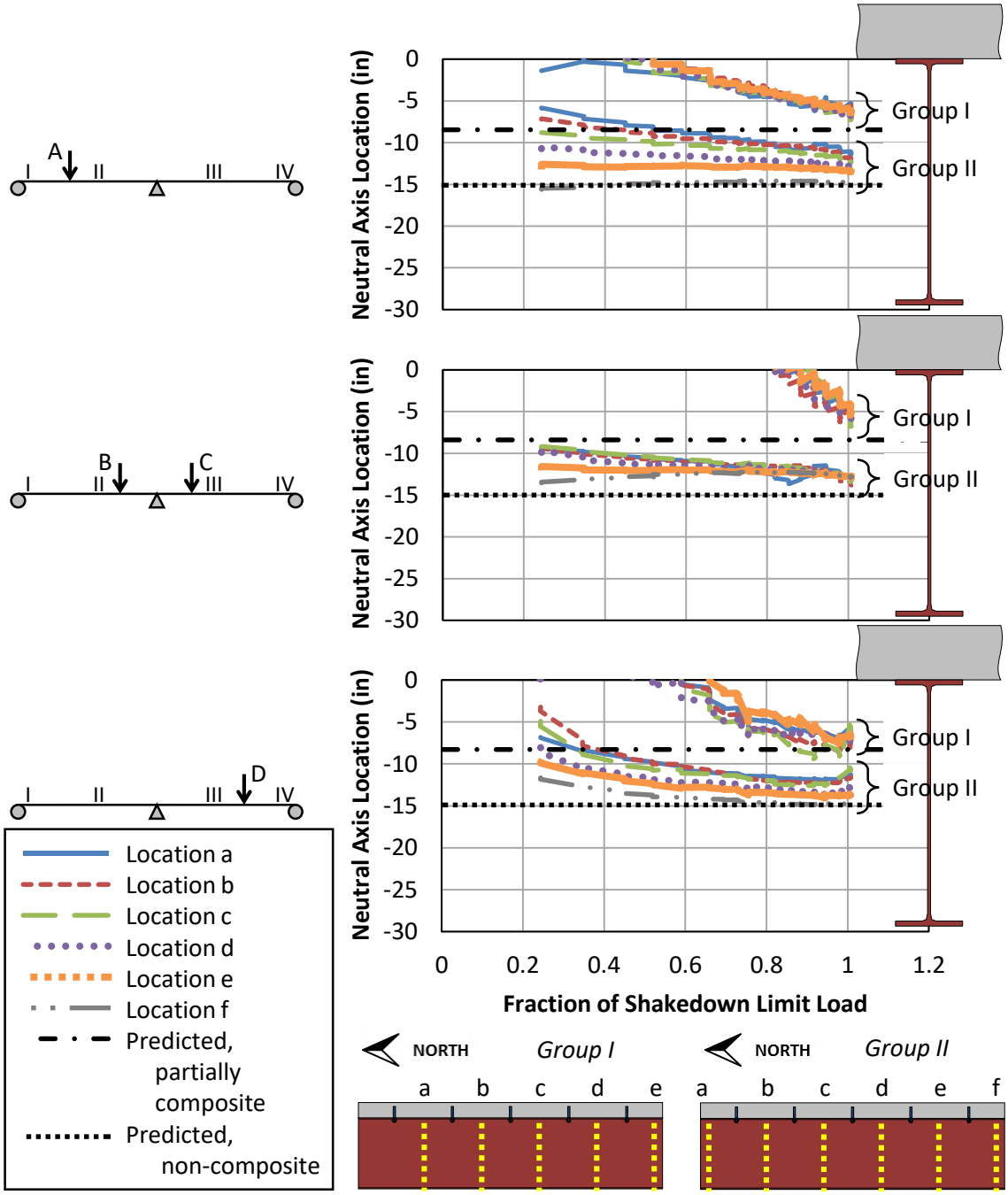

Figure 6-16: Typical Variation of Neutral Axis Location during Shakedown Testing of the Second Specimen

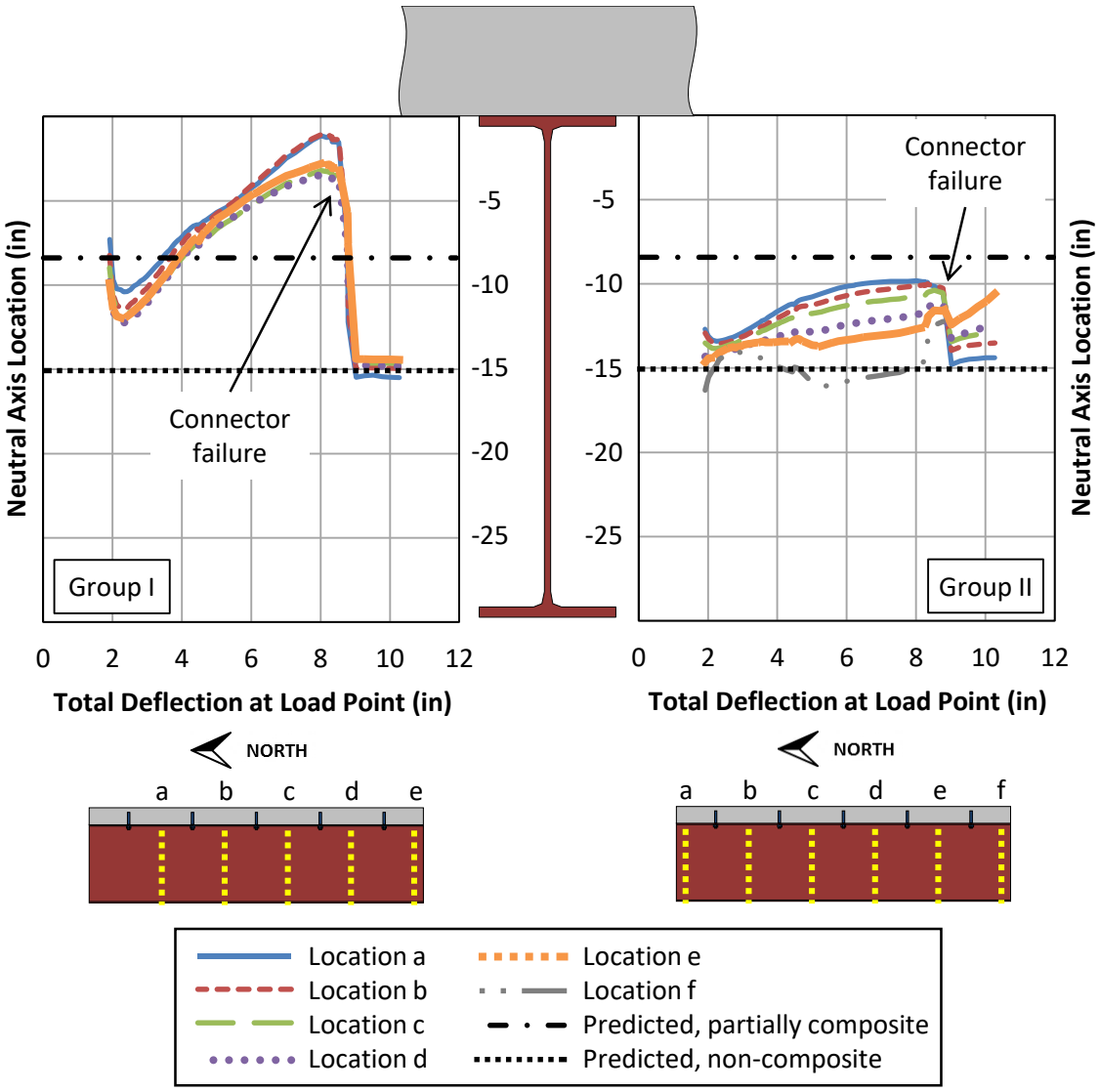

Figure 6-17: Typical Variation of Neutral Axis Location during Ultimate Strength Testing of the Second Specimen

6.4 SUMMARY

This chapter explored some additional features of the results from the experimental testing, beyond those presented in Chapter 5. The first portion of the chapter examined the inelastic behavior of both specimens during shakedown testing, while the second portion focused on the behavior within the groups of concentrated shear connectors during shakedown and ultimate strength testing of the second specimen.

The inelastic behavior during shakedown testing was investigated using two methods to estimate the plastic rotation that occurred at the critical locations. This also led to estimates of the variation of the moment of inertia and the redistribution moments that developed during testing. It was found that plastic rotations of up to 0.0122 radians and 0.0155 radians occurred in positive bending at the load points and in negative bending at the interior support, respectively. Additionally, the moment of inertia was found to decrease slightly with increasing loads, likely a result of cracking of the concrete deck and possibly also from slight losses in composite action. The estimated redistribution moments were significantly smaller than the predicted values, likely because of the assumptions made in the prediction calculations.

The investigation into the behavior within the groups of connectors included computing the total amount of force transmitted by the connector groups, comparing the distribution of connector force and slip within a group, and observing the cross-sectional behavior within a group. Based on the total force transmitted by each group of connectors, it was determined that the design strength of a single connector provides a conservative estimate of the actual strength provided. However, there was significant variation of the force estimated to be carried by each pair of connectors in a group, which is likely a result of the method in which these forces were calculated. It seems that the particular groups in which connector failure initiated were determined by the slip of the connectors, rather than the force. Finally, the complexities of the cross-sectional behavior for a partially composite section due to the interface slip were illustrated by the curvatures and neutral axis locations within a connector group.

CHAPTER 7: FINITE ELEMENT MODELING

7.1 OVERVIEW

Finite element models were developed using the general purpose finite element software ANSYS Mechanical (version 14.5) to further explore the behavior of continuous girders strengthened with post-installed shear connectors (ANSYS 2012). These models were utilized primarily for two different goals. First, elastic models were constructed to investigate the effects of post-installing shear connectors on the distribution of elastic moments in continuous girders. Second, models using inelastic materials were developed to predict the experimental behavior of the two girder specimens discussed in Chapter 4, Chapter 5, and Chapter 6.

Following a description of the techniques used for the modeling and analysis, this chapter describes the results of a parametric study on the elastic distribution of moments in a strengthened continuous girder. The results from modeling of the experimental testing are then presented, along with a discussion of the challenges encountered, especially in simulating repeated inelastic behavior of the concrete deck and shear connectors.

7.2 MODELING AND ANALYSIS TECHNIQUES

Models were constructed primarily for two- or three-span continuous girders and consisted of a single prismatic steel beam with a concrete deck, as shown in Figure 7-1. Post-installed shear connectors were added to create composite action. The following sections describe the details of the element types and material models used for the steel, concrete, and connectors. Additionally, boundary and loading conditions are discussed, along with analysis techniques. The results of the finite element simulations were validated using problems with known solutions, such as the limit state of plastic collapse under monotonic loading and shakedown behavior under repeated loading of continuous non-composite girders. Partially composite modeling techniques were validated against experimental data from the simply supported girder tests discussed in Section 2.3.2 (Kwon 2008).

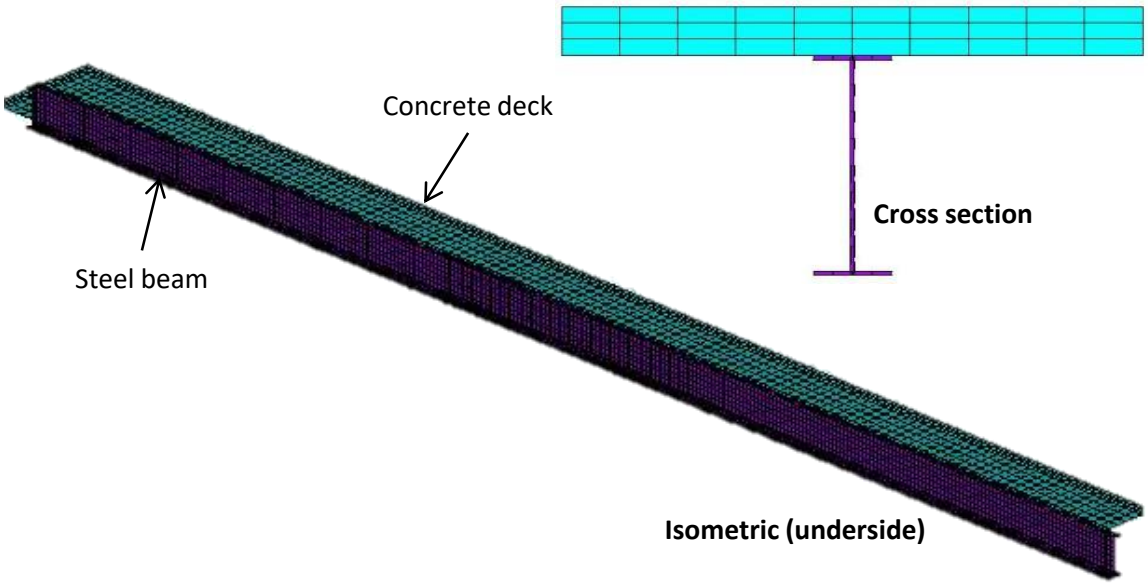

Figure 7-1: Typical Finite Element Model

7.2.1 Steel Beam

The steel beam was modeled using 4-node shell elements (SHELL181) with six degrees of freedom, or three translations and three rotations, at each node. This element, which has five integration points through the shell thickness, considers bending, membrane, and shear deformations, and is capable of attaining large strains and rotations in nonlinear applications. A full integration scheme with incompatible modes was used to improve accuracy in the bending-dominated analysis. A mesh size of 10-15% of the beam depth was used for both the web and for the flanges, with approximately square elements.

For elastic analyses, an elastic material model was used for the steel beam, using the elastic properties shown in Figure 7-2. For inelastic analyses, an elastic-perfectly plastic, bilinear kinematic hardening relationship was used for the material model for a uniaxial state of stress, with parameters as defined in Figure 7-2. The yield stress used in each model was taken as the measured yield stress from tensile coupons given in Table 4-1 and Table 4-2. A very small value, which was many orders of magnitude smaller than the elastic modulus, was used for the strain hardening modulus to achieve convergence. This relationship is a reasonable representation of the stress-strain behavior of steel for values of strain that do not exceed the onset of strain hardening. Yielding under multi-axial states of stress is based on the von Mises (J_2) yield criterion (von Mises 1913).

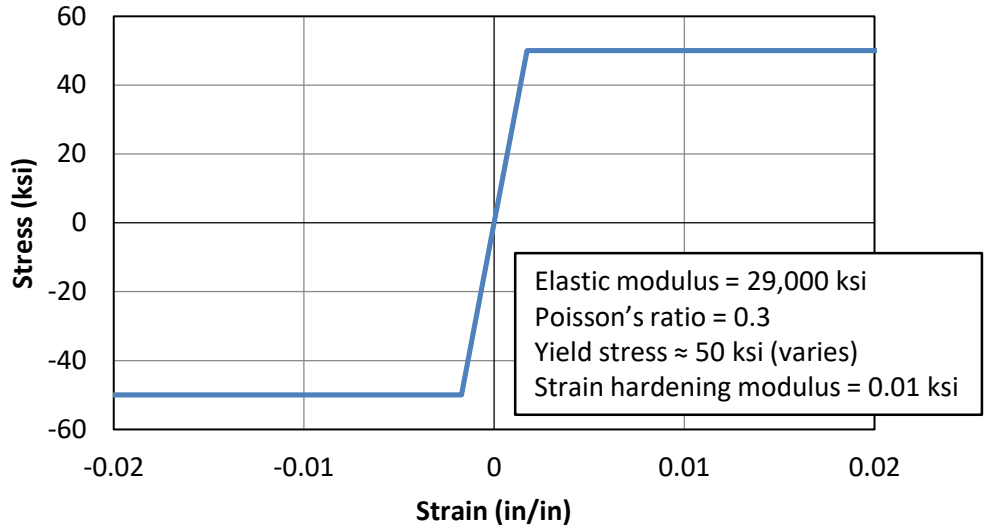

Figure 7-2: General Material Definition for Steel Beam

7.2.2 Concrete Deck

Eight-node solid elements with three translational degrees of freedom at each node were used to model the concrete deck. Generally, a mesh size of 5-10% of the deck width was used. The deck was divided into at least three elements through the thickness to provide accuracy under bending deformations. For elastic analyses, an elastic material model was used for the concrete deck. An elastic modulus of 3120 ksi was used to represent the stiffness of concrete with a nominal compressive strength of 3 ksi. A nominal Poisson's ratio of 0.2 was also used in all elastic and inelastic analyses.

For inelastic analyses, a variety of material models were used in attempts to attain convergence, accuracy, and computational efficiency for different loading conditions. However, it was ultimately decided to develop a "multilinear elastic" model to approximate the effects of the concrete deck in a more computationally efficient manner. The following two sections discuss the inelastic material models considered and the multilinear elastic material model that was developed for efficiency.

Inelastic Concrete Material Models

The following inelastic material models available in ANSYS were considered when modeling the behavior of the concrete deck:

1. The “cast iron plasticity” model, which is a metal plasticity model that allows for different hardening behavior in tension and compression. Although this model is well-suited for monotonic loading conditions, it provides a poor definition of the material behavior under repeated inelastic loading, because it represents cracking and crushing as ductile yielding through the accumulation of fictitious plastic strain.
2. The “concrete” model, which is a smeared cracking model based on the multi-axial state of stress that can be defined in conjunction with smeared reinforcement in three perpendicular directions. While this model better represents the actual inelastic behavior of the concrete material than does the cast iron plasticity model, localized damage due to stress concentrations in the vicinity of the shear connector elements resulted in poor convergence, especially during unloading steps.
3. The “microplane” model, which enforces uniaxial stress-strain laws on many planes oriented in different directions in an element. In a similar manner to the “concrete” model, this model provides a reasonable estimate of the actual behavior in the inelastic range, but was difficult to achieve convergence with, especially upon unloading.

Multilinear Elastic Material Model

It was ultimately realized that the large computational demand associated with the inelastic concrete material models could be significantly reduced by developing a simpler multilinear elastic material model to approximate the effects of the concrete deck without simulating any specific localized cracking. Large inelastic stresses and strains are not expected to occur in the concrete deck in partially composite girders, even at large loads, because the strength is controlled by the shear connectors. Consequently, using an elastic material model for the concrete is expected to be a reasonable approach. An exception to this is that large localized inelastic demands may occur in the concrete deck in the vicinity of the shear connectors. However, for the modeling approach used herein, the effects of any inelasticity in the concrete around the shear connectors on the local response of the connectors is included, in an approximate way, in the shear connector model described in the next section.

The multilinear elastic material model in ANSYS is defined by discrete stress-strain points, and the behavior must be the same in tension and compression. It is compatible with SOLID65 elements, which are capable of cracking, crushing, and plastic deformation, although none of these attributes were used. For simplicity, a bilinear, elastic-perfectly plastic model was chosen with a strain hardening modulus of many orders of magnitude smaller than the elastic modulus to promote convergence. Thus, the main parameters that are needed to define the model are the effective elastic stiffness and the effective maximum stress. To adequately simulate the contribution of the deck to the overall stiffness of the girder under low levels of load, the effective elastic stiffness was taken as equal to the elastic stiffness of the actual concrete in the deck. The effective maximum stress was determined so that the flexural capacity (M_p) of the effective deck is equal to that of the actual deck for a particular expected value of the axial load (P) in the deck at the ultimate strength of the section. This is illustrated in Figure 7-3, in which T is the plastic tensile force developed in the bottom mat of the deck reinforcement, f_c' is the compressive strength of the actual deck, and f_{ce}' is the maximum stress in the effective deck.

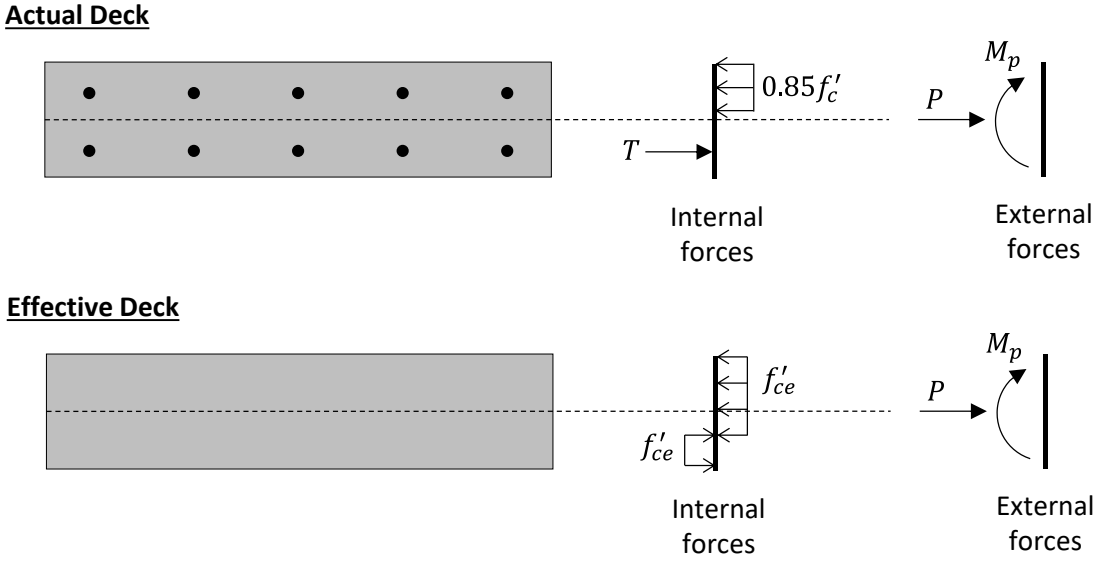

Figure 7-3: Equivalent Effective Deck Section for Multilinear Elastic Material Model

Note that the net axial force in the deck changes along the length of the girder as force is transferred between the steel beam and concrete deck through the shear connectors. However, for simplicity, the calculations for the effective deck were only done at the

location of maximum positive moment, and consistent material properties were used for the deck along the entire length of the girder. Because the deck only contributes a minimal amount of strength in the non-composite negative moment regions, there is only a small error introduced by this assumption. Figure 7-4 shows the multilinear elastic material models used to represent the behavior of the deck in the predictions for the experimental testing discussed in Section 7.4. This effective material model was validated against data from previous experimental testing of simply supported girders strengthened with post-installed shear connectors (Kwon 2008) and compared favorably to simulations using the cast iron, concrete and microplane material models.

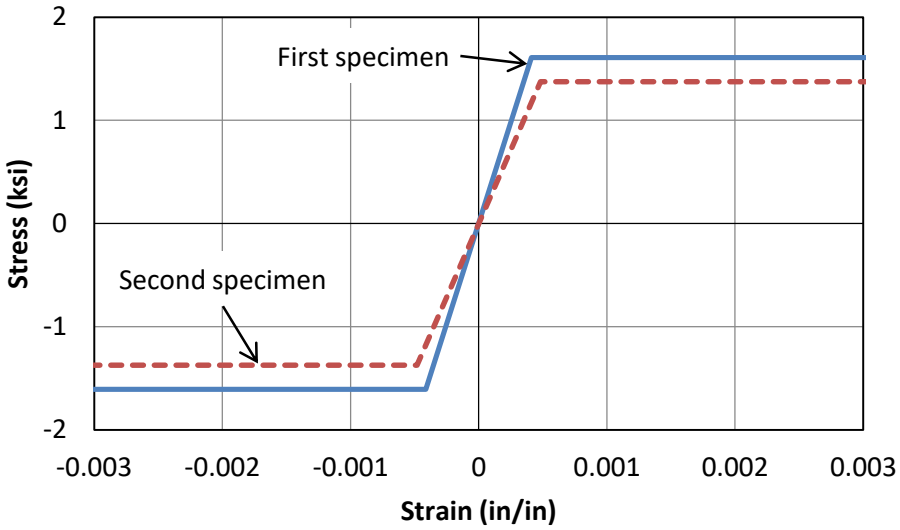

	Specimen 1	Specimen 2
Effective elastic stiffness (ksi)	3,910	2,850
Poisson's ratio	0.2	0.2
Effective compressive strength (ksi)	1.6	1.4

Figure 7-4: Sample Material Definition for Concrete Deck – Multilinear Elastic Material Model

7.2.3 Shear Connectors

The post-installed shear connectors were represented by nonlinear translational spring elements (COMBIN39). These are unidirectional longitudinal or torsional spring elements with a generalized, user-defined nonlinear force-deformation behavior.

Each connector was defined by two longitudinal spring elements: one in the longitudinal direction (parallel to the girder line) and one in the transverse direction (perpendicular to the girder line). These spring elements connected the centerline of the shell element representing the top flange of the steel beam to the underside of the solid elements of the concrete deck. Relative vertical displacement between the top flange of the girder and the deck was prevented using constraint equations, effectively eliminating any uplift of the deck in the model.

For elastic analyses, a stiffness of 900 kips per inch was used for these springs, based on observations during the small-scale fatigue testing conducted in an earlier phase of this research (Patel 2013). For inelastic analyses, the force-deformation behavior defined for these elements was based on small-scale static testing of single adhesive anchor connectors from previous research, and is shown in Figure 7-5 (Kwon 2008). Hysteretic behavior is modeled using the option to unload along a path parallel to the initial slope. If reloading occurs before the sign of the force in the element changes, the reloading path will follow the unloading path back to the original curve. However, if the sign of the force in the element does change before reloading occurs, the element does not retain knowledge of the loading history, and the reloading follows the original force-deformation curve that passes through the origin. Because the reversed loading behavior of adhesive anchor shear connectors in the inelastic range has not been adequately tested, it is unclear how accurate this spring element represents the behavior. However, the load-slip behavior from reversed load fatigue testing conducted by Patel (2013) indicates that this may be a reasonable approximation. These nonlinear spring elements have infinite ductility as defined here and are thus not able to simulate connector failure.

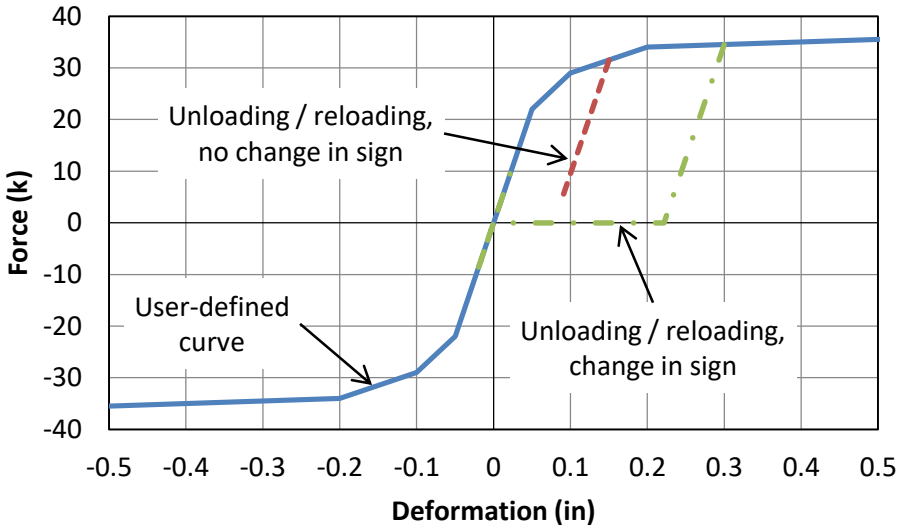

Figure 7-5: Force-Deformation Behavior of Shear Connector Springs

7.2.4 Boundary Conditions and Applied Loads

Exterior pinned supports of a continuous girder were modeled simply by defining a boundary condition of zero displacement in the vertical direction for a single node centered under the web on the bottom flange. Because these exterior supports were not generally associated with large reaction forces under the loading conditions used here, no problems occurred due to large stress concentrations at this localized boundary condition.

Interior pinned supports of a continuous girder were modeled by defining a boundary condition of zero displacement in the vertical direction for all of the nodes in the web of the steel beam, including those at the intersection of the web with the top and bottom flanges. Although this does not physically represent the conditions present in the experimental testing or typical conditions in a bridge girder, this boundary condition was chosen to spread out the large reaction forces associated with these interior pinned supports under the loading conditions used in the experimental testing without compromising the expected behavior due to inelastic rotations at these supports. This method of providing vertical support to the steel beam was observed to adequately represent the expected inelastic behavior under shakedown loading of a bare steel beam and was thus used in these models to provide a reasonable estimate of the behavior at these locations.

Translation in the longitudinal direction was prevented by defining a boundary condition of zero displacement at a single node at mid-depth of the web at the interior

support. Translation in the out-of-plane direction was prevented by defining a boundary condition of zero displacement at a single node at mid-depth of the web at each of the exterior supports. This also prevents global rotation about the vertical axis. Global rotation about the longitudinal and horizontal axes was prevented by placing elastic springs with small values of stiffness under the extreme edges of the concrete deck at both ends of the girder. These springs were comprised of COMBIN14 elements, which are longitudinal or torsional uniaxial spring-damper elements. The longitudinal option was chosen in the vertical direction, and a spring stiffness of 0.001 kip per inch was used.

Self-weight of the steel beam and concrete deck were not directly included in the model to simplify the loading process. This is because the self-weight is carried by the non-composite section, prior to installing the connectors, while the other loads are resisted by the partially composite section, after installing the connectors. Instead, the yield stress of the steel was reduced by an amount equal to the extreme fiber stress in the non-composite section under the self-weight only. This reduction was different for positive and negative bending regions for each girder and varied from 4 ksi to 10 ksi.

Concentrated loads were applied to the girder as pressure loads on 12-inch square by 1.5-inch thick plates. These are the dimensions of the plates used to apply load in the experimental testing. These plates were comprised of SOLID45 elements, which are general eight-node solid elements with many capabilities that were not used here. A simple elastic material model for steel was used for these plates, which were placed at the loading points on top of the concrete deck to avoid the direct application of concentrated forces to the deck.

While the majority of the models were run under load control, simulations of the experimental testing at the ultimate strength limit state were conducted under deflection control. This was done by specifying a vertical deflection at the center of the loading plates.

7.2.5 Analysis Procedure

All simulations were conducted as nonlinear static analyses, with the only nonlinearities coming from the material models. ANSYS uses a Newton-Raphson iterative method for seeking equilibrium solutions during a simulation. The geometry was considered to be linear for all analyses. The sparse direct solver was used for all analyses,

and automatic time stepping was used to determine the magnitude of change for each iteration.

7.3 Elastic Distribution of Moments in Partially Composite Girders

It is common practice when evaluating or load rating existing bridge girders to carry out the structural analysis using line elements that represent a single girder. Conducting this type of structural analysis on a continuous, statically indeterminate system requires an estimation of how the flexural stiffness is distributed along the girder. Changes in the distribution of stiffness affect the elastic distribution of moments, with stiffer portions of the structure attracting larger moments.

For non-composite girders, the flexural stiffness at each location along the girder can be simply defined as the product of the moment of inertia of the cross section of the steel beam and the elastic modulus of steel. Additionally, for fully composite girders, the transformed moment of inertia of the composite cross section can be used to define the flexural stiffness at any location along the girder in the same manner. However, the moment of inertia of a partially composite cross section is difficult to define because plane sections do not remain plane due to the slip that occurs at the steel-concrete interface, as discussed in Section 6.3.3. An effective moment of inertia for a partially composite girder can be estimated using Equation 2-5, but it is unclear the extent to which that this moment of inertia is applicable along the length of a continuous girder. The behavior becomes even more complex when the connectors are concentrated in groups, rather than distributed uniformly along the girder. Thus, it is difficult to define the appropriate flexural stiffness parameters to be used when conducting a line element structural analysis of a strengthened girder.

To better understand this behavior, a parametric finite element study was undertaken to investigate the effects of post-installing shear connectors on the elastic distribution of moments in strengthened girders. The main objective of this study was to make recommendations regarding how to conduct a structural analysis to design and evaluate girders strengthened with post-installed shear connectors. These studies included both 3D finite element modeling in ANSYS and line element modeling in RISA-2D (RISA 2002). In the 3D models, the connectors are discretely represented in a layout recommended by the design provisions given in Chapter 8. In the line element models, the effects of post-installing connectors are represented by using different values of flexural

stiffness at different locations along the girder. In these models, the elastic modulus for the steel-concrete section was taken as the elastic modulus of steel (29,000 ksi), and the moment of inertia was varied to represent different values of flexural stiffness.

7.3.1 Description of Models for Parametric Study

Three different girder geometries were chosen from the bridge survey discussed in Section 3.2 with different exterior-to-interior span ratios, as shown in Table 7-1. Although the interior span of Girder A is longer than the exterior spans, this girder represents geometries with effectively equivalent span lengths, because the moment envelope under bridge live load creates approximately equal maximum moments in all spans. Girders B and C represent bridge girders with relatively short and long interior spans, respectively.

The composite ratio was varied independently in the interior and exterior spans at the values indicated in Table 7-2, representing the range of non-composite to fully composite. Figure 7-6 shows the connector layout used in all 3D FEA models. Each line element analysis was conducted once using the stiffness distribution of the non-composite girder and once using a distribution in which the stiffness of the positive moment regions was taken as that of the composite section (I_{eff}), calculated using Equation 2-5, while the stiffness of the negative moment regions was taken as that of the non-composite section, or the steel beam only (I_s). This is illustrated in Figure 7-7. The dead load inflection points were used to locate the transition between the positive and negative moment regions in these analyses. In cases where a span has a composite ratio of zero, the stiffness in the positive moment region was taken as the stiffness of the non-composite section ($I_{eff} = I_s$).

Concentrated loads of 100 kips were applied to each girder in all analyses in configurations that cause large positive moments in the exterior span (case I), large negative moments at the interior supports (case II), and large positive moments in the interior span (case III). The locations of these loads are indicated in Figure 7-8. The 100-kip load magnitude was an arbitrary choice, since the analyses were conducted under fully elastic conditions, but maintaining a consistent value of load enabled direct comparison of the results from each analysis.

The concrete deck was considered uncracked along the entire length of the girder in the 3D FEA model. This is consistent with the recommendations given in Section 4.5.2.2 the *LRFD Bridge Design Specifications* (AASHTO 2010). The elastic stiffness of the deck was computed using a concrete compressive strength of 3 ksi.

Table 7-1: Girder Geometry for Parametric Study

Girder	Span Length (ft)		Steel Shape	Deck Dimensions (in)	
	Exterior	Interior		Width	Thickness
A	70	90	W36x150	96	6.5
B	50	50	W30x116	96	6.5
C	60	100	W36x150	104	6.5

Table 7-2: Post-Installed Shear Connectors for Parametric Study

Girder	Number of Connectors per Group			
	$\eta = 0$	$\eta \approx 0.3$	$\eta \approx 0.6$	$\eta \approx 1.0$
A	0	16	32	52
B	0	12	24	40
C	0	16	32	52

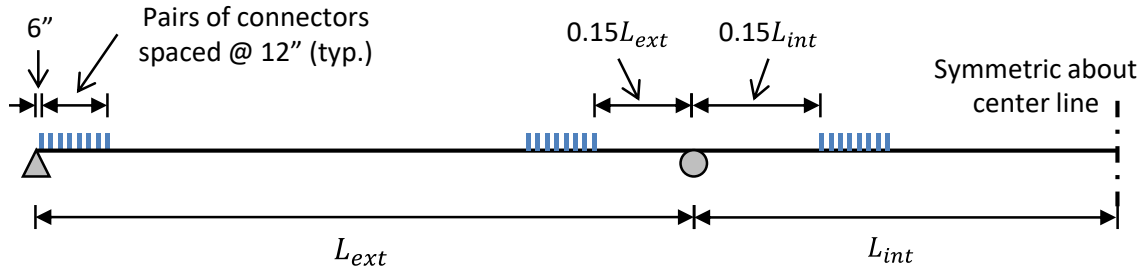

Figure 7-6: Connector Layout for 3D FEA Models in Parametric Study

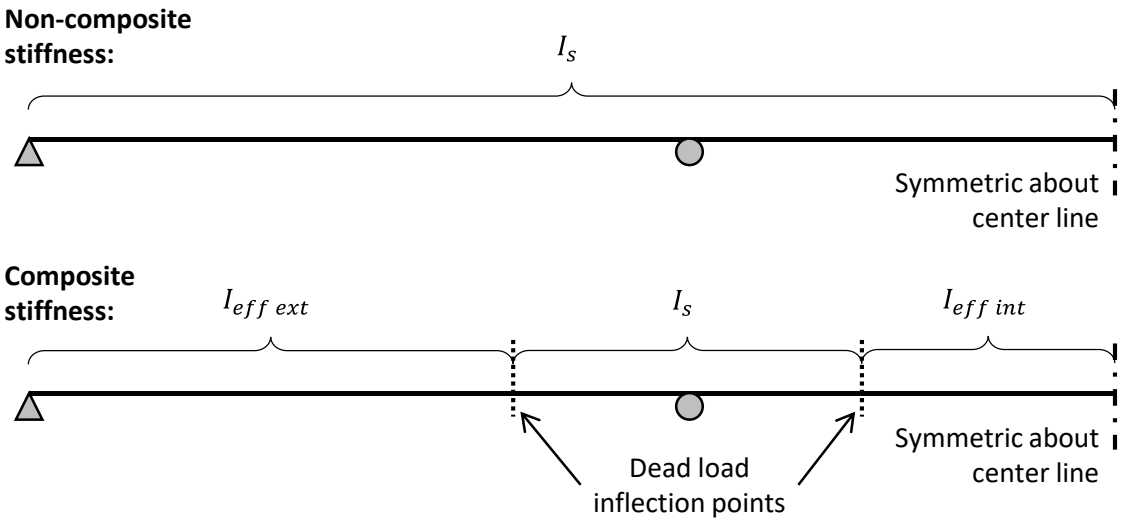

Figure 7-7: Stiffness Distributions for Line Element Models in Parametric Study

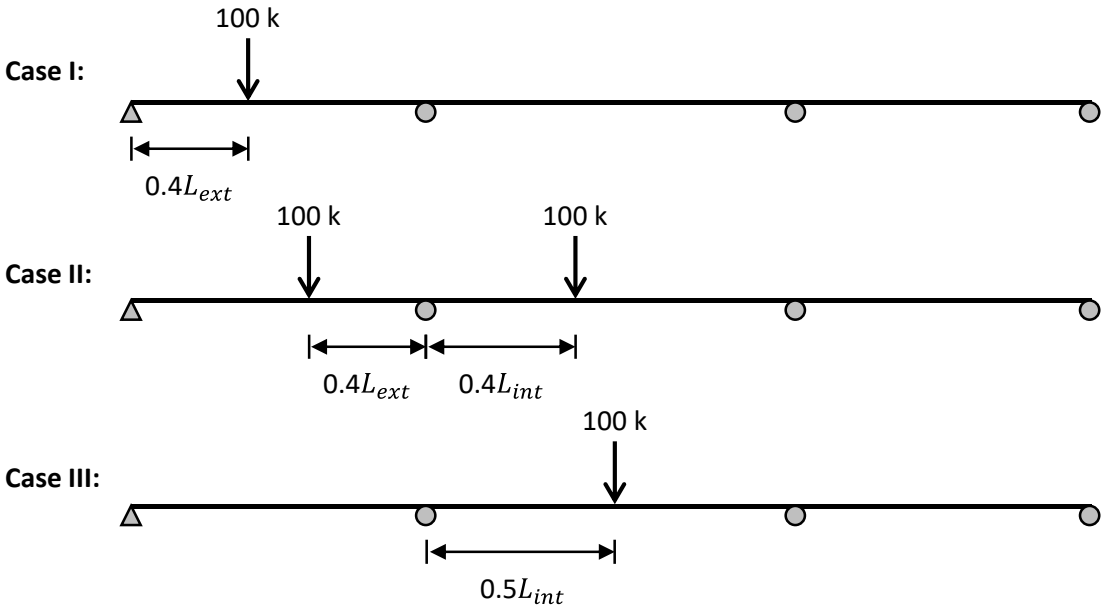

Figure 7-8: Loading Cases for Parametric Study

7.3.2 Results from Parametric Study

For each of Girders A, B, and C, a total of 48 different analyses were run in ANSYS using varying combinations of composite ratios in the interior and exterior spans under the three different cases of loading. The same 48 analyses were also carried out in RISA using

each of the two stiffness distributions shown in Figure 7-7. The reaction forces from each analysis were used to draw a bending moment diagram and determine the peak moment for each case. The peak moment is of most interest because it will often control the load rating of a girder. For loading Cases I and III, the peak moment was taken as the positive moment at the point of the applied load, in the exterior or interior span, respectively. For loading Case II, the peak moment was taken as the negative moment at the interior support.

The peak moments from all analyses of the strengthened girder were compared to that of the non-composite girder to evaluate the effects of post-installing shear connectors on the elastic distribution of moments. Figure 7-9 shows a bar graph indicating the difference in the peak moments between each line element analysis and the corresponding 3D FEA model for Girder A. The horizontal axis of this figure indicates the different combinations of composite ratios in the exterior and interior spans. The percent difference was calculated using the FEA model as a baseline, as this model was assumed to provide the most accurate moments for design. A positive percentage in the graph indicates that the peak moment from the line element analysis was greater than that obtained from the FEA model, and vice versa. The blue and red bars represent the line element analyses conducted using the non-composite and composite stiffness distributions, respectively. The composite ratios for the exterior and interior spans in each analysis are denoted at the bottom of the figure.

Note that while only the results from Girder A are presented here, similar results were obtained from Girders B and C. Bar graphs indicating the results from these two girders are shown in Figure C-2 and Figure C-3 in Appendix C.

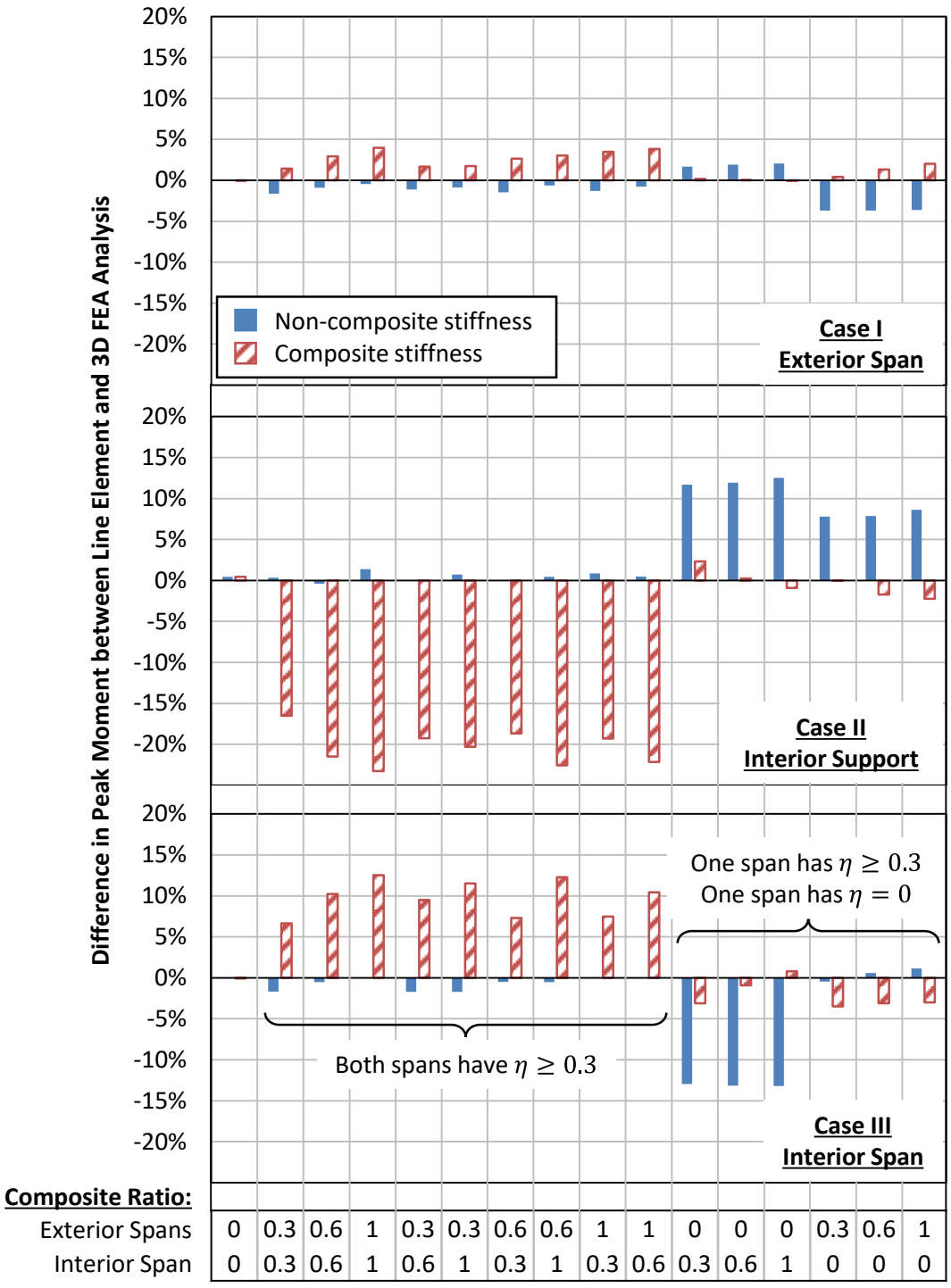

Figure 7-9: Comparison of Peak Moments from 2D and 3D Analyses for Non-Composite and Strengthened Girder A

The graphs indicate that the peak moment in the exterior span (loading Case I) is not particularly sensitive to the stiffness distribution. For all combinations of composite ratios in the exterior and interior spans, the difference in the peak moment between the line element analysis and the 3D FEA model is below 5%, regardless of the stiffness distribution used in the line element analysis. This is likely because the flexibility of the pinned end of the exterior span prevents significant stiffening of the entire span from any composite action developed through post-installing shear connectors.

However, larger differences can occur in the peak moment determined through 3D FEA modeling and line element analysis at both the interior support and the interior span. As can be seen in the figure, the trends for a strengthened girder can be categorized in two distinct groups. The first group includes all cases in which both the exterior and interior spans have a composite ratio of at least 0.3. For all combinations of composite ratios in the exterior and interior spans that fall into this category, the peak moment in the line element analysis is estimated to within 2% of that from the 3D FEA model using the non-composite stiffness distribution. Differences in the peak moment of more than 20% can occur if the composite stiffness distribution is used for these analyses. The second group includes all cases in which one span has a composite ratio of at least 0.3 while the other is not strengthened and thus has a composite ratio of zero. In these cases, the peak moment in the line element analysis was no more than 4% different than that from the 3D FEA model when the composite stiffness distribution is used. Up to a 15% difference in the peak moment can occur if the non-composite stiffness distribution is used in this case.

Although the reasons for these trends are not perfectly clear, it seems that when all spans have a composite ratio of at least 0.3, this leads to a significant stiffening effect along the entire length of the girder, rather than distinctly stiffening the positive moment regions without modifying the behavior of the negative moment regions. Thus, for these cases, the non-composite stiffness distribution, which does not distinguish between positive and negative moment regions, provides a better estimate for the elastic distribution of moments than does the composite stiffness distribution, which has discretely different stiffness in positive and negative moment regions. However, when some but not all spans have a composite ratio of at least 0.3 while the remaining spans have a composite ratio of zero, significant stiffening seems to occur only in positive moment regions with little effect on the behavior in the negative moment regions. For these cases, the discretely varying composite stiffness distribution provides a better estimate of the elastic distribution of moments than does the non-composite stiffness distribution.

7.3.3 Analysis Recommendations

These results indicate that for girders in which all spans are strengthened with post-installed shear connectors, the non-composite stiffness distribution can be used in a line element analysis to determine the flexural demand for a strengthening design. This is convenient because it does not require a separate structural analysis for the existing and strengthened structures. However, if only some of the spans are strengthened with post-installed connectors, it is likely that using the non-composite stiffness distribution will lead to significant errors in the design moments. Thus, it is recommended to conduct a separate structural analysis for the strengthened structure using the effective composite stiffness (I_{eff}) in spans that will be strengthened and the non-composite stiffness in spans in which no shear connectors will be added.

7.4 Inelastic Behavior of Strengthened Girders

Finite element modeling in ANSYS was also used to predict the results of the experimental testing of the two large-scale girder specimens. Although similar simulations were run prior to the testing to aid in the design of the specimens and the test program, the results presented here are from analyses conducted after the experimental testing was complete, which follow the exact same loading program as used in the testing. The modeling techniques and parameters were not changed to provide a better match with the experimental data. Instead, the procedures described in Section 7.2 that had previously been developed and validated using simple problems and previous experimental results were used in these predictions with no alterations.

Modeling repeated inelasticity of strengthened girders at the shakedown limit state presented some challenges. Generally, it was difficult to maintain computational efficiency and attain convergence at each load step while also simulating reasonably accurate behavior of the individual elements and materials. This was found to be particularly challenging for the concrete deck, which was ultimately modeled as a multilinear elastic material, which simulated the effect of the deck on the overall behavior of the girder to promote convergence and efficiency, as discussed in Section 7.2.2. Additionally, some uncertainty arises in the load-slip behavior of the nonlinear spring elements used to represent the shear connectors, as discussed in Section 7.2.3. However, due to the lack of experimental data regarding the behavior of adhesive anchor connectors, the extent of this

uncertainty is unclear. These nonlinear spring elements also have unlimited ductility and thus were not able to simulate connector failure, as is evident in the results presented here.

The figures in this section provide graphs that compare the data obtained during the experimental testing and the computational modeling in ANSYS. Figure 7-10 shows a comparison of the load-deflection behavior for both specimens during shakedown loading. Overall, a good match is seen between the experimental and computational results in the peak load-deflection behavior during shakedown loading. Slightly larger deflections tended to occur during the experimental testing than in the computational models at loads beyond first yield. However, under large load levels during the south span loading of the first specimen, the computational deflections increase beyond those observed experimentally.

Additionally, significantly fewer cycles were required to achieve shakedown for the computational modeling than for the experimental testing. This is illustrated in Figure 7-11, which shows the change in peak deflection from one cycle to the next at the predicted shakedown limit load in the north span of the first specimen. Seven cycles were required to achieve shakedown during the experimental testing, while only three cycles were required in the computational model.

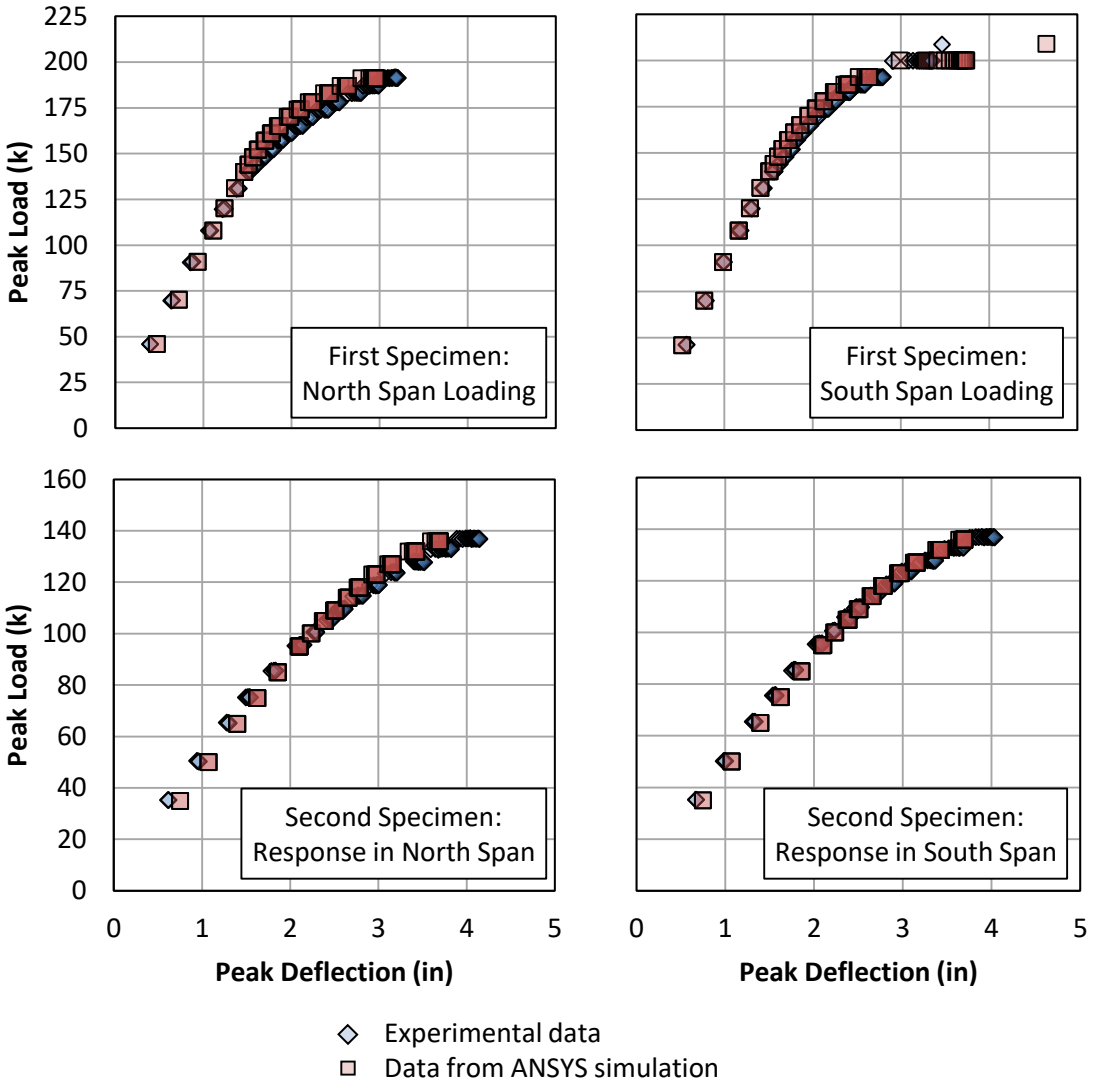

Figure 7-10: Comparison of Experimental and Computational Load-Deflection Behavior during Shakedown Loading

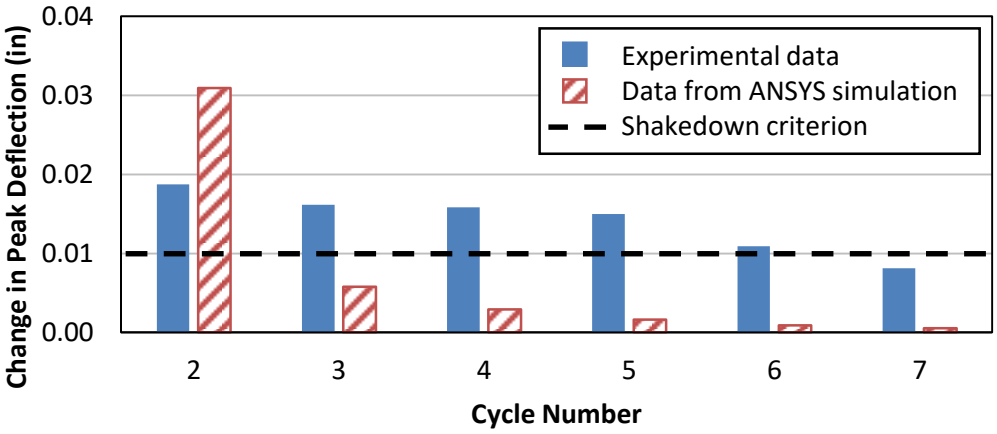

Figure 7-11: Comparison of Experimental and Computational Deflection Change at the Shakedown Limit Load during North Span Loading of the First Specimen

Figure 7-12 shows a comparison of the load-deflection behavior for both specimens during ultimate strength loading. The overall behavior is similar between the experimental and computational data. One key difference is that the initial deflection, which represents the residual deflection from prior loading, differs between the two cases. Additionally, connector failure is not captured in the computational model. However, the elastic stiffness during loading is nearly identical between the experimental and computational results, with the exception of the north span loading in the first specimen. Recall from Section 5.2 that degradation of the adhesive between the threaded rod of the connector and the hole in the top flange of the steel beam occurred after fatigue testing under a load 50% greater than a typical bridge fatigue load. This effectively reduced the stiffness of the girder as the connectors could slip through a "gap" region from one side of the oversized hole to the other without carrying any force, as illustrated in Figure 5-1. The unloading and reloading stiffness is also lower for the experimental testing than for the computational modeling because the unloading and reloading occurred after failure of a portion of the connectors, which is not simulated in the ANSYS model.

Despite the lack of connector fracture in the computational simulations, the difference in the peak load attained both experimentally and computationally did not exceed 6%, even under large deflections during the loading of the south span of the first girder.

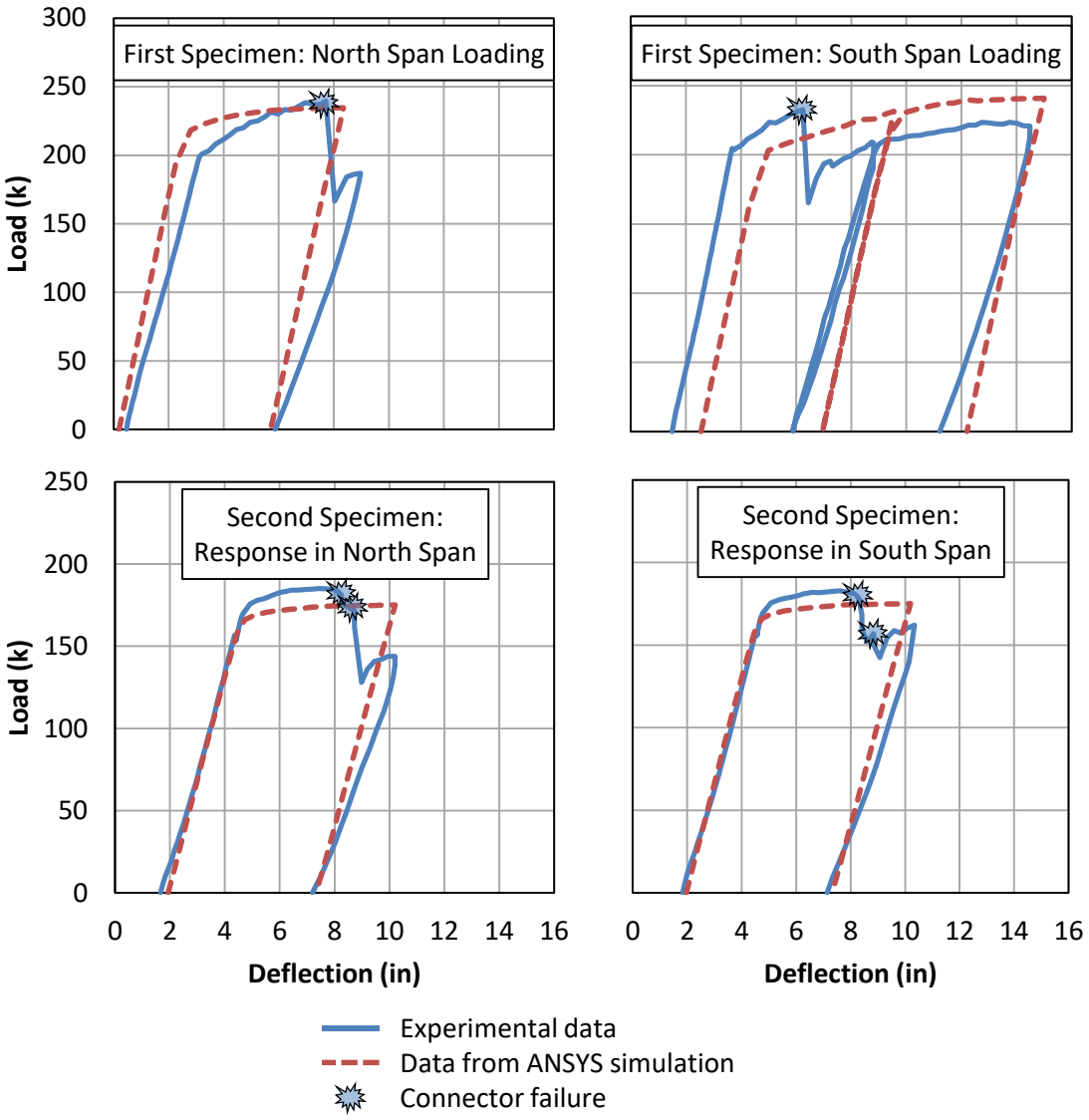

Figure 7-12: Comparison of Experimental and Computational Load-Deflection Behavior during Ultimate Strength Loading

Comparisons of typical connector behavior are given in the following two figures for both the shakedown and ultimate strength loading cases. Figure 7-13 illustrates examples of poor (a) and good (b) computational representations of the experimental shear connector behavior during shakedown loading in the north span of the first specimen. Generally, good correlations in the behavior occurred when no force reversal occurred in the connector during the computational simulation. Poor correlations in the behavior occurred when reversal of the connector force caused the connector slip to return to zero,

regardless of the force-slip history of the element, as discussed in Section 7.2.3. Figure 7-14 illustrates examples of intact (a) and failed (b) connectors during ultimate strength loading in the south span of the first specimen. This figure highlights the key discrepancies in the behavior between the experimental and computational results when unloading and reloading the connector as well as the lack of connector failure in the computational model.

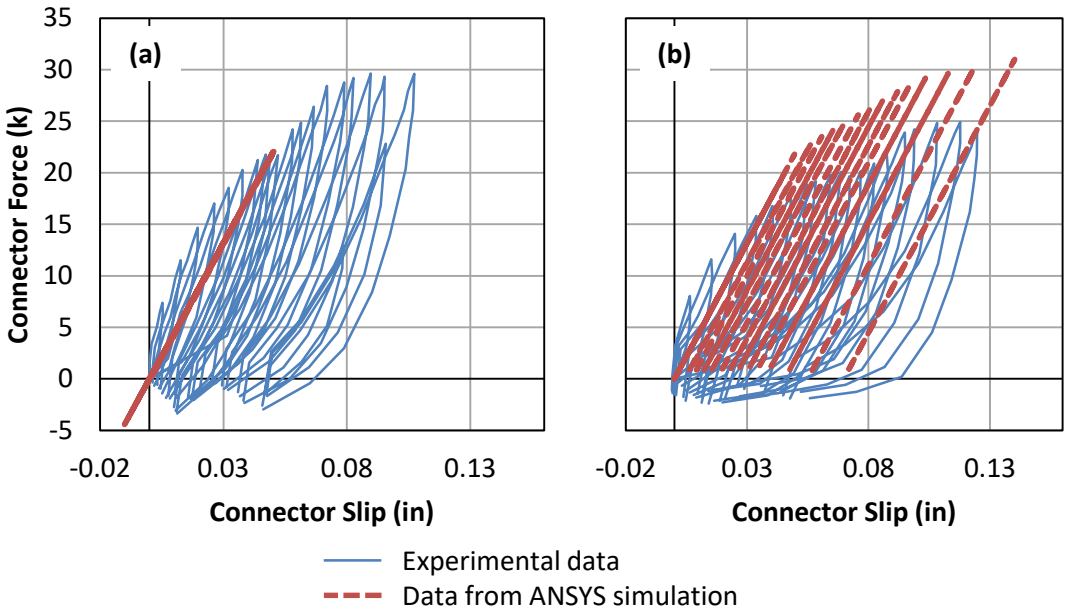

Figure 7-13: Comparison of Experimental and Computational Connector Behavior during Shakedown Loading – (a) Poor Representation of Behavior due to Force Reversal, and (b) Good Representation of Behavior with No Force Reversal

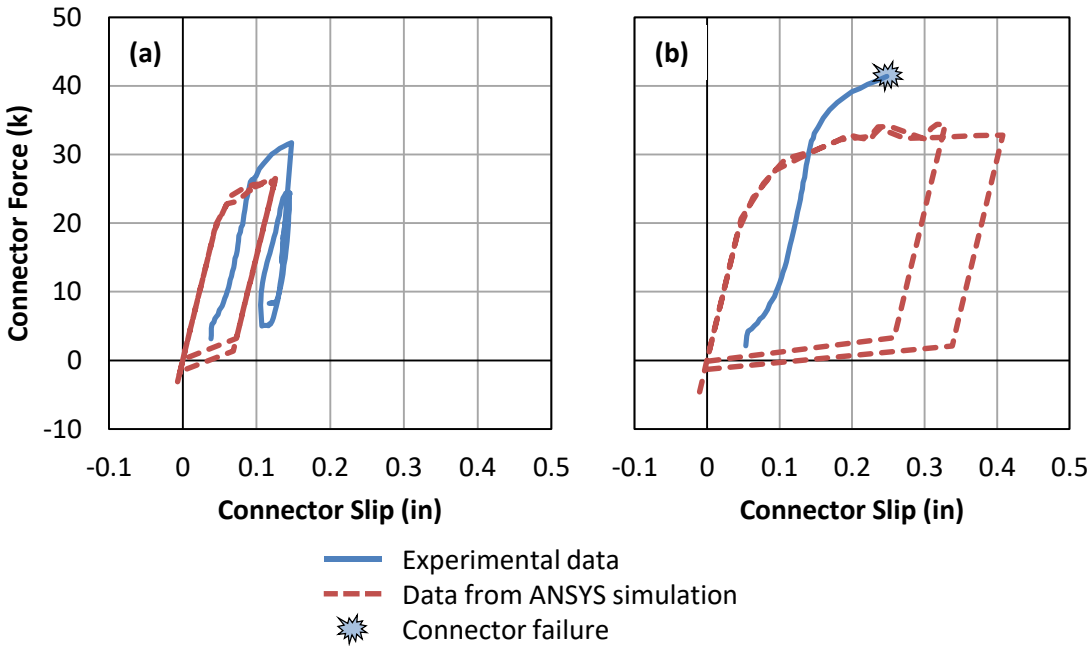

Figure 7-14: Comparison of Experimental and Computational Connector Behavior during Ultimate Strength Loading – (a) Typical Intact Connector, and (b) Typical Failed Connector

Despite the discrepancies in the shear connector behavior and the approximations made in the material model of the concrete deck, the overall experimental behavior of the two girder specimens was predicted well by the finite element simulations. Improvements in the accuracy of this model may be gained through the following suggestions:

- Replace the nonlinear spring elements with longitudinal truss elements for modeling of the shear connectors. This will provide more flexibility in the force-slip behavior defined for the connectors by allowing for the use of a variety of inelastic material models available in ANSYS, which are capable of maintaining knowledge of the load history regardless of whether or not the force is reversed. However, note that additional experimental data on the inelastic behavior of adhesive anchor shear connectors under reversed loading conditions is needed to better define this material model.
- Incorporate one or more additional types of spring and/or truss elements in series to represent the shear connectors. This could allow the simulation of connector fracture at a critical connector force or slip. Additionally, this could allow for modeling of a "gap" region caused by adhesive degradation.

- Continue exploring the use of inelastic material models for the concrete deck to attain both convergence and acceptable levels of computational efficiency.

7.5 SUMMARY

Finite element modeling was conducted using ANSYS to simulate continuous bridge girders strengthened with post-installed shear connectors. The modeling and analysis techniques used were validated using simple examples and a limited amount of experimental testing conducted previously. The models were used both to investigate the effects of post-installing shear connectors on the elastic distribution of moments in a continuous girder and to predict the behavior of the experimental testing.

From the parametric study conducted regarding the elastic behavior of strengthened girders, it was concluded that post-installing shear connectors in concentrated groups does not seems to have a significant effect on the elastic distribution of moments in many cases. In particular, if all of the spans have a composite ratio of at least 0.3, the peak moment in the partially composite strengthened girder can be estimated with less than 5% error by the elastic moment distribution of the non-composite girder. However, if one or more spans remain non-composite while others are strengthened to a composite ratio greater than 0.3, the composite stiffness distribution indicated in Figure 7-7 provides significantly more accuracy in the elastic distribution of moments.

The computational simulations of the experimental testing yielded comparable overall results under both shakedown and ultimate strength loading. This occurred despite the fact that some approximations were made in the computational model that differ from the physical properties of the system. These approximations include (1) the use of a multilinear elastic material model that represents the effects of the concrete deck on the overall behavior of the girder without explicitly modeling localized damage, (2) the force-slip model used for the connectors that unrealistically returns to zero slip when the force changes sign, and (3) a boundary condition that provides vertical support to all nodes through the web of the girder at the centerline of the interior supports to minimize local inelastic deformations from large concentrated reaction forces. The good comparability observed between the computational modeling and experimental testing indicate that the model is likely not sensitive to these approximations, although further study would be necessary to confirm this. Additionally, further work could be done to improve the computational model to minimize or eliminate these approximations.

CHAPTER 8: DESIGN APPROACH AND RECOMMENDATIONS

8.1 Overview

Recommendations for designing a strengthening scheme for existing non-composite continuous steel I-girder bridges were developed based on the preliminary strengthening studies, experimental testing, and finite element modeling, as described in earlier chapters of this dissertation. These recommendations and a general design procedure are summarized in this chapter, along with recommendations for installation of adhesive anchor shear connectors. A detailed design example with sample calculations is provided in Appendix D.

8.2 Recommended Strengthening Design Procedure

The recommended design procedure for strengthening existing bridges with post-installed shear connectors and moment redistribution is summarized in Figure 8-1. This procedure was developed considering primarily the flexural strength of the bridge girders and the fatigue strength of the post-installed shear connectors. Girder shear strength and the behavior of other bridge components are not explicitly included here, but should be checked as needed.

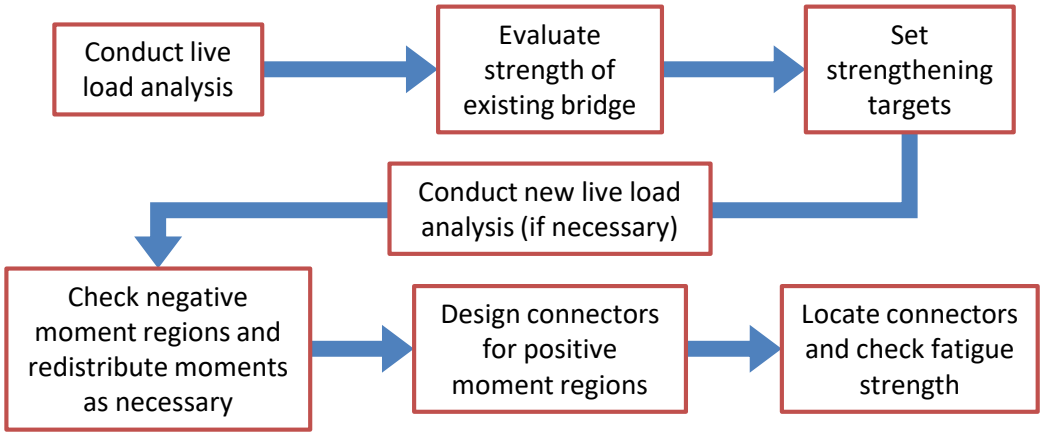

Figure 8-1: Design Procedure

8.2.1 Conduct Live Load Analysis

The first step that should be taken is to conduct a structural analysis on the bridge under the live load that will be used to evaluate the existing bridge. This loading pattern

can be chosen to meet the needs of a particular bridge or situation, allowing for flexibility in the procedure for a variety of cases. In this research project, an AASHTO HS 20 load was used to be consistent with the Load Factor Design and Rating methods from the *Standard Specifications for Highway Bridges* (AASHTO 2002).

The moving load analysis can be conducted in any manner desired by the designer. As described in Section 7.3, a simple line element analysis using the non-composite flexural stiffness adequately represents the distribution of forces along the length of the girder in both the non-composite existing bridge as well as the partially composite strengthened bridge, assuming post-installed shear connectors are used in all spans. The appropriate distribution factors should be applied for interior and exterior girders. This type of simple analysis works well for straight girder bridges with a fairly symmetric span layout.

A more rigorous live load analysis can be conducted using software with 3D modeling capabilities, such as SAP2000, which can explicitly model the steel beams, concrete deck, and shear connectors (CSI 2011). This type of analysis may be particularly useful for bridges with complex geometries. However, it requires an initial guess of the number and layout of the shear connectors to be made, leading to an iterative design procedure. It is recommended to run separate analyses for the non-composite existing bridge and for the partially composite strengthened bridge, because the moment envelopes may vary based on the location of the shear connectors. This may be especially true for asymmetric span layouts or if the composite ratio varies greatly along the length of the strengthened bridge. In any 3D model, it is recommended that each adhesive anchor shear connector be represented as a linear elastic spring with a stiffness of 900 kips per inch. Alternatively, a pair of connectors in the same cross section can be combined into a single spring with a stiffness of 1800 kips per inch.

8.2.2 Evaluate Existing Bridge

Using the results from the live load analysis, the strength of the existing bridge can be determined by conducting a load rating. For the purposes of this research, the Load Factor Rating method was used, as specified in the *Manual for Bridge Evaluation* (AASHTO 2011). The limit states of Overload and Maximum Load were both considered in the load rating process. The Overload limit state prevents excessive permanent deformations of the bridge under typical levels of load and corresponds to the Service II

limit state in the *LRFD Bridge Design Specifications* (AASHTO 2010). The Maximum Load limit state is a reflection of the maximum carrying capacity of the bridge and corresponds to the Strength I limit state in the LRFD specifications when only considering gravity loads.

Fatigue was not considered in the evaluation of existing bridges during this research, but can be if desired. The *Manual for Bridge Evaluation* provides guidelines on evaluating the remaining fatigue life for critical details of existing bridges (AASHTO 2011). Recently proposed revisions to these guidelines are available through research conducted by the National Cooperative Highway Research Program (NCHRP 2012).

8.2.3 Set Targets for Strengthened Bridge

Once the existing bridge has been evaluated, targets for the strength and remaining life of the strengthened bridge should be established before beginning the strengthening design process. These targets can be chosen to accommodate any particular case, but it is recommended that both strength limit states for the girders and fatigue limit states for the post-installed shear connectors are considered. For fatigue of the post-installed shear connectors, a projected average daily truck traffic in a single lane ($(ADTT)_{SL}$) of the bridge over the expected remaining life should be estimated.

Throughout the majority of the research discussed here, a strengthening target of attaining an inventory load rating of HS 20 was chosen as an upper bound of the strengthening requirements that a bridge owner might consider. A bridge with an inventory rating of HS 20 has a load-carrying capacity meeting the design requirements for a new bridge designed with the Load Factor Design method from the most recent edition of the AASHTO Standard specifications. For fatigue, no specific strengthening targets were consistently used, as this will vary depending on the desired remaining bridge life and the projected truck traffic over that life for the particular bridge of interest.

8.2.4 Conduct Additional Live Load Analysis (If Necessary)

If the target strength live load is of the same type as the live load used in the analysis of the existing bridge, there is often no need to conduct additional analysis. As shown in Section 7.3, post-installing groups of shear connectors near the ends of the positive moment regions to develop partially composite action does not significantly change the elastic distribution of moments within a continuous girder in many cases. This is true for straight

girders with reasonably symmetric span layouts that require post-installed shear connectors in all spans. For other cases, more rigorous modeling may be necessary.

However, if the target strength live load is of a different type than the live load used in the analysis of the existing bridge, a new live load analysis must be conducted prior to beginning the strengthening design. For example, this would be the case if the non-composite bridge was evaluated using an HS 20 live load, but the strengthening target is an HL-93 live load.

8.2.5 Check Negative Moment Regions and Redistribute Moments

To begin the design of the strengthened bridge, the first step is to check the negative moment regions around the interior piers. If the capacity of the existing non-composite girder exceeds the demand from the moment envelope at all pier locations, the negative moment regions can be deemed acceptable in terms of strength, and the design can proceed to the positive moment regions.

Otherwise, if the demand from the moment envelope at any of the interior pier locations exceeds the capacity of the existing non-composite girder, inelastic moment redistribution is required. It is recommended that the provisions of Appendix B6 of the AASHTO LRFD specifications be used for moment redistribution. These provisions require that the bridge is straight with no more than a 10° skew, and that the interior pier sections are well-braced, meet slenderness limits, and have bearing stiffeners. Based on the results from the bridge survey, these provisions are generally already satisfied in most existing bridges with the exception of the support skew angle limit, the bearing stiffener requirement, and often the lateral bracing requirements. In many cases, bearing stiffeners and/or additional lateral bracing will need to be added to the bridge as part of the strengthening process. These requirements ensure that the interior pier sections have adequate inelastic rotation capacity for moment redistribution to occur.

The provisions also limit the amount of moment redistribution to 20% of the elastic moment, a requirement that does not seem to be restrictive for strengthening the surveyed bridges. This limitation prevents serviceability problems from arising due to excessive permanent deflections caused by the inelastic deformations at the interior piers and prevents local buckling from occurring at the interior supports due to excessive inelastic rotational demands. By following the procedure outlined in the specifications, the "redistribution moment diagram" can be drawn, as detailed in Section 2.5.2. These

redistribution moments are then added to the design moment envelope for the remainder of the design. Note that inelastic moment redistribution can occur at both the Overload and Maximum Load limit states, although the capacities and moment envelopes will be different between the two cases. This process is illustrated in detail in the design example provided in Appendix D.

8.2.6 Design Connectors for Positive Moment Regions

The next step in the design is focused on strengthening the positive moment regions near the middle of the spans by adding shear connectors and creating composite action. To begin this process, the required strength in these regions is determined from the design moment envelope, including the redistribution moments if applicable. Simple plastic cross-sectional analysis is then used to determine the number of connectors needed to attain the required strength, as described in Section 1.2.2 and illustrated in Appendix D. The following equation was recommended by Kwon et al. (2009) for the design strength of a single post-installed shear connector (Q_n):

$$Q_n = 0.5 A_{sc} F_u \qquad \textit{Equation 8-1}$$

where A_{sc} is the effective shear area of the connector, taken as 80% of the nominal area for the threaded rod adhesive anchor connectors, and F_u is the specified nominal tensile strength of the connector material.

Note that the maximum strength of a fully composite girder is controlled by the properties of the steel beam and concrete deck, rather than the shear connectors. If the required strength in any of the positive moment regions exceeds the strength of the fully composite cross-section, adding more shear connectors will not result in any further strength gain. Along with the 20% limit on moment redistribution, the strength of the fully composite section places an upper limit on the potential strength increase that can be achieved for a particular bridge.

8.2.7 Locate Connectors along Bridge

After the strength design is complete, the connectors must be laid out along the girders before the fatigue limit state can be checked. The following recommendations for connector layout, illustrated in Figure 8-2, are made based on parametric studies conducted by Ghiami Azad (2016):

- Connectors should be placed in pairs, with one on either side of the web at every location. It is recommended that general AASHTO requirements regarding clear cover, edge distance, and minimum transverse spacing are followed. A transverse spacing of approximately 6 inches was used in all laboratory testing for beams with 10- to 11-inch wide flanges.
- It is recommended that connectors are concentrated near points of zero or low moment, rather than distributed uniformly through the positive moment regions, to improve the ductility of the strengthened girders.
- A longitudinal spacing of approximately 12 inches is recommended between pairs of concentrated connectors. However, analysis indicates that the behavior is not significantly affected by slight changes in spacing, provided that the connectors are still effectively concentrated near points of low moment. All laboratory testing was conducted with 12- or 24-inch spacing. Choosing a connector spacing that is a multiple of the transverse rebar spacing will help avoid bars during construction.
- At the ends of continuous units, the connector group should be located as close as possible to the end of the steel beam. It is recommended to take this distance as one-half of the longitudinal spacing of the connectors. The minimum longitudinal distance from the centerline of the support to the first connector pair used in the laboratory testing was 6 inches.
- The most efficient location for the interior connector groups is typically when the connector closest to the interior support is located approximately 15% of the span length away from that support. For high composite ratios or large connector spacing, the group should be moved closer to the interior support. However, it is not recommended that the connector closest to the interior support is located closer than 10% of the span length from that support, as this significantly increases the fatigue demand on the connectors, based on the AASHTO LRFD specifications.
- Constructability and accessibility in the field should be considered when choosing a connector layout. If possible, the site should be visited to identify potential problems that may arise during connector installation. The use of a rebar locator is highly recommended to slightly modify the layout to avoid reinforcing bars in the deck during construction.

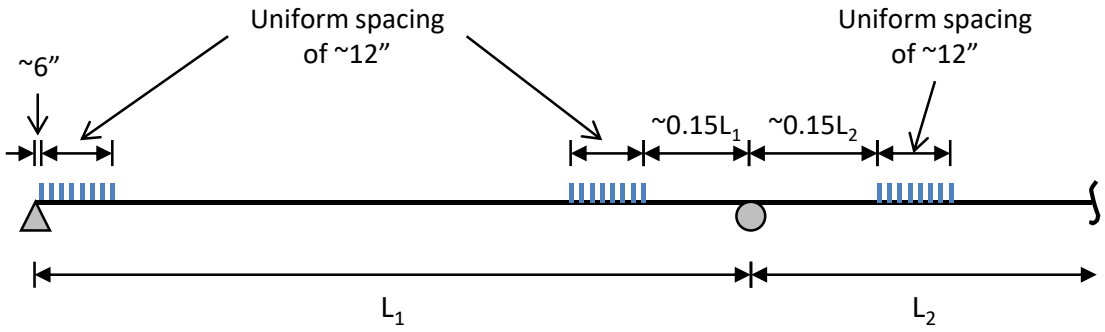

Figure 8-2: Recommended Connector Layout

8.2.8 Check Fatigue Strength of Connectors

Once a connector layout has been chosen, an analysis is conducted under fatigue loading, and the connectors are checked at the fatigue limit state. The following fatigue design provisions for post-installed adhesive anchor shear connectors have been recommended based on recent testing of adhesive anchor shear connectors (Kreitman et al. 2016). The provisions follow a parallel format to the general fatigue design provisions in Section 6.6 of the AASHTO LRFD specifications, rather than the shear stud provisions in Section 6.10.10.

To determine which load combination is used for design, a limiting value of the average annual daily truck traffic in a single lane ($(ADTT)_{SL\ limit}$) is calculated based on the expected remaining bridge life in years (Y):

$$(ADTT)_{SL\ limit} = \frac{8{,}700{,}000}{Y} \qquad \textbf{Equation 8-2}$$

The above equation was determined by equating the fatigue resistances of the adhesive anchor for finite and infinite life, given in the following equations, accounting for the different load factors in the two load combinations, and corresponds to the values in Table 6.6.1.2.3-2 of the AASHTO LRFD specifications. This limit assumes that the number of stress cycles per truck passage (n) is equal to one, and should be divided by the value of n, as defined later in this section, if this is not the case.

If the predicted average annual daily truck traffic in a single lane ($(ADTT)_{SL}$) over the expected remaining bridge life in years (Y) is greater than the limit given in Equation 8-2, the Fatigue I load combination is used to design for infinite fatigue life. In this case, the nominal fatigue resistance ($(\Delta F)_n$) is defined in Equation 8-3:

$$(\Delta F)_n = (\Delta F)_{TH} = 15\ ksi$$ ***Equation 8-3***

If the $(ADTT)_{SL}$ is less than the limit given in Equation 8-2, the Fatigue II load combination is used to design for finite fatigue life over a computed number of stress cycles (N), defined by Equation 8-4. Note that the Fatigue II load combination will control in essentially every situation, as Equation 8-2 generates very high limiting $(ADTT)_{SL}$ values that are unlikely to be exceeded. In this case, the nominal fatigue resistance ($(\Delta F)_n$) is defined in Equation 8-5:

$$N = (365)(Y)(n)(ADTT)_{SL}$$ ***Equation 8-4***

$$(\Delta F)_n = \left(\frac{A}{N}\right)^{\frac{1}{m}}$$ ***Equation 8-5***

where $A = 4.24\ x\ 10^{15}\ ksi^7$ and $m = 7$. For continuous bridges with span lengths greater than 40 feet, the number of cycles per truck passage (n) is taken as 1.0 for connectors located more than one-tenth of the span length away from an interior support. For connectors located within one-tenth of the span length from an interior support, n is taken as 1.5. Note that the exponent in the equation for the Fatigue II load combination has been modified from 1/3 in the current AASHTO LRFD specifications to 1/7 for post-installed adhesive anchor shear connectors.

The nominal fatigue resistances were derived from small-scale direct-shear testing done on 3/4- and 7/8-inch diameter connectors (Kayir 2006, Kwon 2008, Patel 2013). Caution should be used in applying these design equations to connectors outside of this range. The fatigue analysis should be conducted using a procedure that explicitly considers the slip at the steel-concrete interface in partially composite girders, which can significantly reduce the force demand on the connectors. This procedure is discussed in detail by Ghiami Azad (2016).

8.3 Recommended Connector Installation Procedure

The adhesive anchor shear connectors are recommended to be comprised of 7/8-inch diameter ASTM A193 B7 threaded rods. A two-part structural adhesive (Hilti HIT-HY 150-MAX or 200-R) was used in all of the experimental testing. The connectors are

installed with the following procedure, illustrated in Figure 8-3, which is nearly identical to that used in the laboratory specimens:

1. Drill a 1-inch diameter hole through the top flange of the steel beam at the connector location (a). This can be done using a portable drill with a magnetic base.
2. Through the hole in the flange, drill a 15/16-inch diameter hole into the concrete deck to the desired depth (b). This can be done using a rotary hammer drill. A 2-inch cover to the top of the concrete deck was maintained in all laboratory testing, leaving an embedment depth of 4.5 inches into the deck.
3. Clean the hole with a wire brush and compressed air, as specified by the adhesive installation procedures (c).
4. Inject the adhesive into the hole using the appropriate dispenser (d). Take care that the hole is filled from the top down so that no air bubbles are present. The Hilti adhesive was viscous enough to not run downwards out of the hole after injection.
5. Place the threaded rod into the hole using a twisting motion so the adhesive fills the threads (e). The Hilti adhesive was able to hold the connector in place immediately after installation and has a 9-minute working time at 70°F.
6. Allow the adhesive to cure. The Hilti adhesive has a 1-hour cure time at 70°F.
7. Tighten the nut to the torque specified by the adhesive (f). The Hilti adhesive specifies a torque of 125 foot-pounds for 7/8-inch diameter rods.
8. Strike the exposed threads below the nut with a grinder. Although it is unlikely to occur, this will prevent any nuts that inadvertently loosen over time from potentially falling onto traffic or pedestrians passing under the bridge.

Figure 8-3: Connector Installation

Generally, this procedure follows the installation process recommended by the Hilti adhesive product with a few exceptions, namely the use of a 15/16-inch diameter hole in the deck instead of the prescribed 1-inch diameter. Due to the slightly enlarged head of the hammer drill bits, a 1-inch bit does not fit through the 1-inch diameter hole in the top

flange. To minimize the oversized hole in the flange, a 15/16-inch diameter bit was used for the hole into the deck.

8.4 SUMMARY

A design procedure for strengthening existing non-composite continuous steel I-girder bridges was presented in this chapter along with the recommended installation procedure for post-installed adhesive anchor shear connectors. Appendix D contains a detailed design example which illustrates the application of this design procedure to strengthening a non-composite bridge.

CHAPTER 9: SUMMARY AND CONCLUSIONS

9.1 SUMMARY

The behavior of continuous non-composite bridge girders strengthened with post-installed adhesive anchor shear connectors and inelastic moment redistribution was studied. The primary objectives were to explore the feasibility of this strengthening method, to evaluate the performance of strengthened girders, and to develop design recommendations for implementing such strengthening measures in existing non-composite bridges. A variety of theoretical, experimental, and computational tasks were completed as part of this investigation.

Following a review of the relevant literature, preliminary studies were carried out to assess the effectiveness of this strengthening method. A survey of 25 non-composite steel I-girder bridges in the state of Texas was conducted to determine typical characteristics of bridges that may be candidates for this type of strengthening. Thirteen of these bridges were load rated both before and after strengthening to assess the feasibility and effectiveness of the strengthening. These studies indicated that the proposed strengthening method is likely an efficient method of increasing the load rating of such bridges.

Next, large-scale testing was conducted on a representative bridge girder strengthened with post-installed shear connectors. While this dissertation focused on the experimental behavior at strength limit states, including under large repeated loads requiring moment redistribution and under monotonic loading to failure, the comprehensive testing program also included elastic and fatigue loading phases, which are discussed elsewhere (Ghiami Azad 2016). Excellent performance was observed throughout all phases of testing, with the specimens exceeding the predicted strength at all limit states.

Finite element models were also constructed to explore the elastic and inelastic response of strengthened girders. These models were used to develop recommendations for conducting simplified structural analysis on line girder elements under elastic-level loads. Prior to conducting the experimental testing, these models were also used to predict the behavior during that testing. However, this was difficult to accomplish accurately due to the complexities of modeling repeated inelastic behavior of concrete and the shear connectors.

Finally, a design approach was recommended for strengthening existing continuous non-composite steel I-girder bridges, along with recommended procedures for installing adhesive anchor shear connectors. A detailed design example is presented in Appendix D.

9.2 CONCLUSIONS

The findings of this research indicate that strengthening continuous non-composite steel girder bridges with post-installed shear connectors and inelastic moment redistribution is a feasible and efficient method of extending the useful service life of a bridge. Additionally, although not discussed in detail in this dissertation, the application of 2 million cycles of fatigue loading did not adversely affect the strength of the post-installed connectors. The following points summarize the major conclusions from this research:

- Many existing non-composite steel girder bridges in Texas have a significantly lower load-carrying capacity than is required by current design standards. Strengthening of these bridges may be necessary or desired to maintain safety or to avoid load-posting.
- Significant strength gains can be achieved by post-installing shear connectors and allowing for moment redistribution in continuous bridges. Most of the surveyed bridges require a composite ratio not exceeding 30% and only small amounts of moment redistribution to reach a load-carrying capacity exceeding that required by current design standards. Increases in load rating of up to 70% may be attained.
- Experimental testing of large-scale strengthened girders indicated resilient structural performance under elastic, fatigue, and strength loading, even at composite ratios below 30%. Shakedown behavior was observed at loads up to 5% beyond the predicted shakedown limit load, and the ultimate strength of the specimens exceeded that predicted by simple plastic analysis. However, it was noted that simple plastic analysis does not adequately predict the inelastic behavior that occurs prior to reaching the limit load.
- Post-installing shear connectors in groups near the ends of the positive moment regions in each span, as is recommended here, often does not significantly change the distribution of flexural stiffness along the length of the girder. Thus, the results from a simple line element structural analysis conducted using the

stiffness distribution of a non-composite girder can generally be used to approximate the expected distribution of moments in a partially composite strengthened girder. This applies only to cases in which all spans are strengthened with post-installed shear connectors, and may provide inaccurate results under other conditions.

- Finite element analysis of continuous girders strengthened with post-installed shear connectors provided reasonably similar results to the experimental testing. However, efficiently modeling the behavior of the concrete deck and the shear connectors under repeated loads in the inelastic range can be challenging.

9.3 Recommendations for Future Research

The following recommendations are made for future research conducted on strengthening existing non-composite steel girder bridge with post-installed shear connectors:

- Additional research is needed regarding the necessity of bearing stiffeners and the required spacing of lateral bracing around the interior supports of continuous steel girder bridges for inelastic moment redistribution. These features may not be present in older bridges, but are required by the moment redistribution provisions in Appendix B6 of the AASHTO LRFD specifications, which are recommended for use in conjunction with the strengthening design procedure discussed in Chapter 8. The addition of bearing stiffeners and new cross frames as part of a strengthening project increases the cost, and based on this research, the circumstances under which these features are actually needed are unclear.
- Expanding the scope of this research to a wider range of bridge geometries is needed for applicability of these strengthening procedures to an increased number of older bridges. This research focused on straight bridges with no skew or low skew angles, which is also a requirement to use the moment redistribution provisions in the AASHTO LRFD specifications. Additional research is needed to examine the feasibility and design requirements for strengthening curved and heavily skewed bridges with post-installed shear connectors and inelastic moment redistribution.

- Additional work is needed to develop efficient and accurate finite element modeling techniques for post-installed adhesive anchor shear connectors in partially composite girders. In particular, better modeling approaches are needed to simulate the interaction between a shear connector and the surrounding concrete, especially under repeated or reversed loading where there is accumulated damage in the vicinity of the connector. Additionally, the development of a technique to model the gap that may develop due to the degradation of the adhesive between the threaded rod of the connector and the hole in the top flange of the steel beam is needed.
- Conducting a long-term field monitoring program of a strengthened bridge is needed to assess the durability of adhesive anchor shear connectors and evaluate the permanent deformations associated with any moment redistribution that may occur over time.

The following recommendations are made for future research conducted on the general behavior and the design of shear connectors in composite bridge girders:

- Research that focuses on reconciling the different observed behavior of shear connectors in small-scale, simple tests and large-scale girder tests is needed to better understand the complexities of composite behavior. These differences are observed both under fatigue loading and under monotonic loading to failure. With a better understanding of this behavior, an improved small-scale shear connector test may be developed that is more representative of the actual loading and deformation environment for a shear connector in an actual girder.
- Extending the concepts developed in this research to conventional welded shear studs would be useful to promote improvements in the current design procedures for composite girders. A number of issues examined during the course of this research may have useful implications for improving the design of new composite bridges using welded shear studs and for using new methods to evaluate existing composite bridges constructed with welded shear studs.
- Additional research is needed to investigate the use of high-strength threaded rods as shear connectors that are installed without welding in new composite bridges. This may lead to the use of a much smaller number of shear connectors than is currently required when using welded shear studs.

APPENDIX A: EXPERIMENTAL PREDICTIONS

A.1 OVERVIEW

This appendix contains calculations for the predicted strengths and behavior of the girder specimens in the experimental testing described in Chapter 4 and Chapter 5. These calculations are presented separately for the north span of the first specimen, the south span of the first specimen, and both spans of the second specimen. The two spans of the first specimen have different steel yield strengths, and thus the predictions differ slightly. Additionally, the two specimens have different span lengths, so different predictions are made for each. However, the geometric properties of the cross section are identical for all spans in both specimens and are summarized in Table A-1.

Table A-1: Section Properties for Both Specimens

Flange width (b_f, in)	10.4
Flange thickness (t_f, in)	0.61
Flange area (A_f, in^2)	6.34
Total depth (d, in)	29.5
Web thickness (t_w, in)	0.47
Area (A_s, in^2)	26.3
Moment of inertia (I_x, in^4)	3610
Elastic section modulus (S_x, in^3)	245
Plastic section modulus (Z_x, in^3)	283
Deck width (b_{deck}, in)	78
Deck thickness (t_{deck}, in)	6.5
Deck area (A_{deck}, in^2)	507
Deck moment of inertia (I_{deck}, in^4)	1790

Additionally, the properties and strength of the shear connectors are consistent among both spans of the two specimens. The design strength of the 7/8-inch diameter (d_{sc}) connectors is calculated using Equation 8.1 as follows. In the calculation, A_{sc} is the effective cross-sectional area of the connector, which is taken as 80% of the gross area because the connector is threaded. Note that the nominal ultimate tensile strength of the

connectors is used in this calculation ($F_{u\,sc} = 125\ ksi$) rather than the measured tensile strength of the threaded rod because of the empirical nature of the design equation:

$$A_{sc} = 0.8\frac{\pi\ {d_{sc}}^2}{4} = 0.8\left(\frac{\pi\left(\frac{7}{8}in\right)^2}{4}\right) = 0.481\ in^2$$

$$Q_n = 0.5\ A_{sc}\ F_{u\,sc} = 0.5(0.481\ in^2)(125\ ksi) = 30.1\ kips$$

A.2 First Specimen – North Span

The material properties for the north span of the first specimen are given in Table A-2.

Table A-2: Material Properties for the North Span of the First Specimen

Steel yield stress in positive moment regions ($F_{y\,span}$, ksi)	52.4
Steel yield stress in negative moment regions ($F_{y\,pier}$, ksi)	52.4
Elastic modulus of steel beams (E_s, ksi)	29000
Compressive strength of concrete (f'_c, ksi)	4.7
Elastic modulus of concrete (E_c, ksi)	3910

A.2.1 Properties of Non-Composite Section at Interior Support

Yield Moment

The yield moment of the section in negative bending at the interior support is calculated using the properties of the steel beam only:

$$M_{y\,pier} = S_x\ F_{y\,pier} = (245\ ksi)(52.4\ ksi)\left(\frac{1\ ft}{12\ in}\right) = 1070\ k.ft$$

Moment Capacity and Shape Factor

The specimen was designed to have adequate lateral bracing to prevent lateral-torsional buckling, and the W30x90 shape is compact. Thus, the moment capacity of the section in negative bending at the interior support is the plastic moment of the steel section. The "shape factor" (k_{pier}) of the section is defined as the ratio of the plastic moment to the yield moment:

$$M_{p\ pier} = Z_x\ F_{y\ pier} = (283\ ksi)(52.4\ ksi)\left(\frac{1\ ft}{12\ in}\right) = 1240\ k.ft$$

$$k_{pier} = \frac{M_{p\ pier}}{M_{y\ pier}} = \frac{1240\ k.ft}{1070\ k.ft} = 1.16$$

Neutral Axis

The neutral axis for a doubly symmetric non-composite section at all levels of load in the elastic and inelastic range is expected to be located at mid-depth of the web.

A.2.2 Properties of Partially Composite Section in the Span

Elastic Properties and Yield Moment

The effective moment of inertia (I_{eff}) and effective elastic section modulus (S_{eff}) of a partially composite section can be estimated using Equation 2.5. This equation interpolates between the properties of the non-composite section (I_x and S_x) and the fully composite transformed section (I_{tr} and S_{tr}). To compute the properties of the full-composite section, the elastic neutral axis of the fully composite transformed section ($y_{NA\ tr}$) must be located below the steel-concrete interface. In the following calculations, n is the short term modular ratio:

$$n = \frac{E_s}{E_c} = \frac{29000\ ksi}{3910\ ksi} = 7.42$$

$$y_{NA\,tr} = \frac{A_s\left(\frac{d}{2}\right) - \frac{A_{deck}}{n}\left(\frac{t_{deck}}{2}\right)}{A_s + \frac{A_{deck}}{n}}$$
$$= \frac{(26.3\ in^2)\left(\frac{29.5\ in}{2}\right) - \frac{(507\ in^2)}{7.42}\left(\frac{6.5\ in}{2}\right)}{(26.3\ in) + \frac{(507\ in^2)}{7.42}} = 1.75\ in$$

$$I_{tr} = I_x + A_s\left(\frac{d}{2} - y_{NA\,tr}\right)^2 + \frac{I_{deck}}{n} + \frac{A_{deck}}{n}\left(\frac{t_{deck}}{2} + y_{NA\,tr}\right)^2$$
$$= 3610\ in^4 + (26.3\ in^2)\left(\frac{29.5\ in}{2} - 1.75\ in\right)^2$$
$$+ \frac{(1790\ in^4)}{7.42} + \frac{(507\ in^2)}{7.42}\left(\frac{6.5\ in}{2} + 1.75\ in\right)^2$$
$$= 10000\ in^4$$

$$S_{tr} = \frac{I_{tr}}{d - y_{NA\,tr}} = \frac{10000\ in^4}{(29.5\ in) - (1.75\ in)} = 361\ in^3$$

Additionally, the composite ratio (η) of the section must be calculated, which is equal to the ratio of the number of connectors provided (N) to the number of connectors required for fully composite action (N_{FC}), which is calculated based on the maximum interface shear that can be developed in the fully composite section ($C_{f\,FC}$). In this case, there are 7 pairs of connectors in each group, so $N = 14$:

$$C_{f\,FC} = min\begin{cases}0.85f_c' A_{deck} \\ A_s F_y\end{cases} = min\begin{cases}0.85(4.7\ ksi)(507\ in^2) \\ (26.3\ in^2)(52.4\ ksi)\end{cases} = min\begin{cases}2030\ k \\ 1380\ k\end{cases}$$
$$= 1380\ k$$

$$N_{FC} = \frac{C_{f\,FC}}{Q_n} = \frac{1380\ k}{30.1\ k} = 45.8$$

$$\eta = \frac{N}{N_{FC}} = \frac{14}{45.8} = 0.306$$

The effective elastic section properties for the partially composite section can now be calculated using Equation 2.5. To calculate the section modulus, simply replace the moment of inertia terms with the corresponding section modulus terms. The yield moment is also computed using the effective section modulus:

$$I_{eff} = I_x + \sqrt{\eta}(I_{tr} - I_x)$$
$$= (3610\ in^4) + \sqrt{0.306}\big((10000\ in^4) - (3610\ in^4)\big)$$
$$= 7140\ in^4$$

$$S_{eff} = S_x + \sqrt{\eta}(S_{tr} - S_x) = (245\ in^3) + \sqrt{0.306}\big((361\ in^3) - (245\ in^3)\big)$$
$$= 309\ in^3$$

$$M_{y\ span} = S_{eff}F_{y\ span} = (309\ in^3)(52.4\ ksi)\left(\frac{1\ ft}{12\ in}\right) = 1350\ k.ft$$

Moment Capacity and Shape Factor

The moment capacity of a partially composite section is calculated following the procedure for simple plastic cross section analysis described in Section 2.2.2. The interface shear (C_f) is calculated as follows. For a partially composite section, the third term in the equation, which represents the strength of the shear connection, will always control:

$$C_f = min\begin{Bmatrix} 0.85f_c'A_{deck} \\ A_sF_{y\_span} \\ N\ Q_n \end{Bmatrix} = min\begin{Bmatrix} 0.85(4.7\ ksi)(507\ in^2) \\ (26.3\ in^2)(52.4\ ksi) \\ (14)(30.1\ k) \end{Bmatrix} = min\begin{Bmatrix} 2030\ k \\ 1380\ k \\ 421\ k \end{Bmatrix}$$
$$= 421\ k$$

Because the section is partially composite, the plastic neutral axis will always be located in the steel beam, either in the top flange or in the web. If the plastic neutral axis is in the web of the steel beam, the net plastic force in the top and bottom flanges will cancel out, since the section is doubly symmetric. Thus, the plastic neutral axis can only be in the web of the steel beam if the maximum plastic force that can be developed in the web ($P_{y\ web}$) is greater than the compressive force in the slab, or the interface shear. Otherwise, the plastic neutral axis is located in the top flange of the steel beam:

$$P_{y\,web} = A_{web}F_{y\_span} = \left(A_s - 2A_f\right)F_{y\_span}$$
$$= (26.3\ in^2 - 2(6.34\ in^2))(52.4\ ksi) = 714\ k$$

$$714\ k > 421\ k \ \rightarrow\ P_{y\,web} > C_f \ \rightarrow\ Plastic\ neutral\ axis\ is\ in\ the\ web$$

The stress distribution at the plastic moment capacity is shown in Figure A-1. Force resultants, which act at mid-height of the corresponding stress block, are indicated by filled arrowheads and bold labels. For simplicity, an equivalent stress distribution, shown in the far right portion of the figure, will be used for the calculations. In this equivalent stress distribution, the top half of the steel is shown under the yield stress in compression, while the bottom half of the steel is subjected to the yield stress in tension. This stress distribution creates two equal force resultants that form a force couple with the same magnitude as the plastic moment of the steel section ($M_{p\ steel}$). The portion of the steel above mid-depth of the beam and below the plastic neutral axis is also under a tensile stress of twice the yield stress. The unknown distance z represents the height of the web above mid-depth of the steel section but below the plastic neutral axis. Since the interface shear (C_f) is no longer controlled by the plastic force in the deck, only the top portion of the deck is assumed to be under compressive stress. The depth of the concrete compression block is denoted as a.

$$a = \frac{C_f}{0.85f_c' b_{eff}} = \frac{421\ k}{0.85(4.7\ ksi)(78\ in)} = 1.35\ in$$

$$T_s = zt_w\left(2F_{y\_span}\right) = (z)(0.470\ in)\left(2(52.4\ ksi)\right) = \left(49.3\frac{k}{in}\right)(z)$$

$$M_{p\ steel} = Z_x F_{y\_span} = (283\ in^3)(52.4\ ksi) = 14800\ k.in$$

$$\Sigma F = 0 \ \rightarrow\ T_s - C_f = 0 \ \rightarrow\ \left(49.3\frac{k}{in}\right)(z) - 421\ k = 0 \ \rightarrow\ z = 8.55\ in$$

$$M_{p\,span} = \Sigma M_{interface} = T_s\left(\frac{d}{2} - \frac{z}{2}\right) + C_f\left(t_{deck} - \frac{a}{2}\right) + M_{p\,steel}$$
$$= \left(\left(49.3\frac{k}{in}\right)(8.55\ in)\right)\left(\frac{(29.5\ in)}{2} - \frac{(8.55\ in)}{2}\right)$$
$$+ (421\ k)\left(6.5\ in - \frac{1.35\ in}{2}\right) + 14800\ k.in$$
$$= (21700\ k.in)\left(\frac{1\ ft}{12\ in}\right) = 1810\ k.ft$$

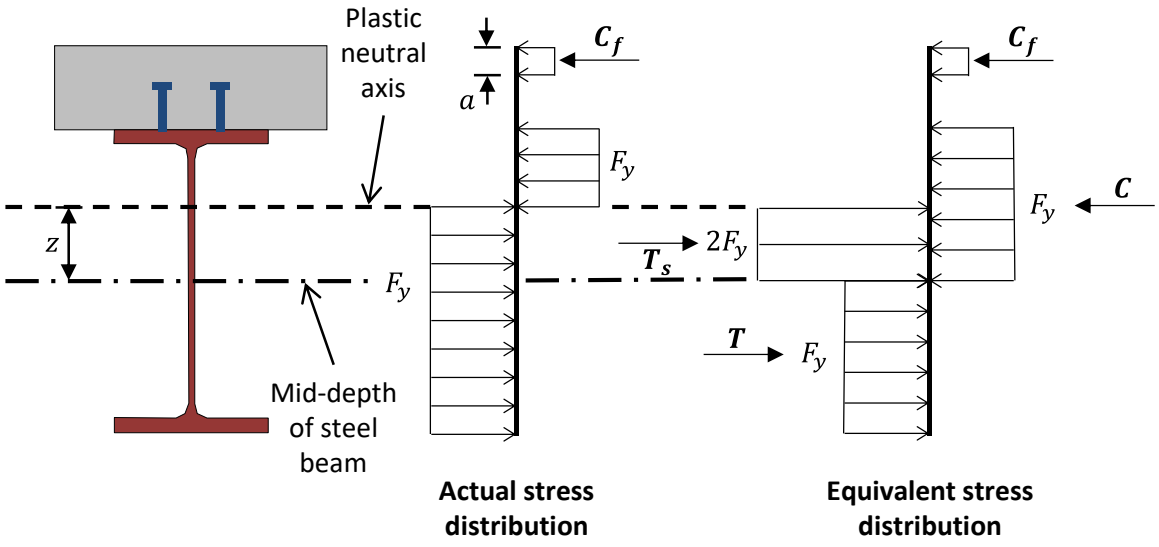

Figure A-1: Stress Distribution at Plastic Moment of Partially Composite Section with Neutral Axis in the Web of the Steel Beam

The shape factor (k_{span}) is determined in the same manner as for the non-composite section at the interior support:

$$k_{span} = \frac{M_{p\,span}}{M_{y\,span}} = \frac{1810\ k.ft}{1350\ k.ft} = 1.34$$

Neutral Axis

For a partially composite section, the location of the neutral axis in a cross section is difficult to define because plane sections do not remain plane due to the slip that occurs at the interface. In fact, the distribution of slip over the entire length of the girder must be

calculated first to locate the neutral axis for a particular cross section, which will vary depending on the location of the cross section along the length of the girder as well as the flexural demand on the section. However, the location of the neutral axis at the plastic moment is simple to define using the stress distribution in Figure A-1. In this case, the plastic neutral axis is 8.55 inches above mid-depth of the web, or 6.20 inches below the steel-concrete interface. This is the value that is plotted as the "predicted location" in Figure 5-10 and Figure 5-21 for comparison to the experimental data.

A.2.3 Dead Load Analysis

When predicting the strength under the applied loads in the experimental testing, the effects of the dead load must be considered. The dead load is calculated as the sum of the self-weight of the steel beam ($W_s = 90\ lb/ft$) and the weight of the concrete deck ($W_c = 150\ lb/ft^3$):

$$DL = W_s + W_c\, A_{deck} = \left(90\frac{lb}{ft}\right) + \left(150\frac{lb}{ft^3}\right)(507\ in^2)\left(\frac{1\ ft}{12\ in}\right)^2$$
$$= \left(618\ \frac{lb}{in}\right)\left(\frac{1\ k}{1000\ lb}\right) = 0.618\frac{k}{ft}$$

The moments resulting from this dead load are shown in Figure A-2. The critical locations are at Load A and at the interior support. The dead load moments at these two locations are denoted DL_{span} and DL_{pier}, respectively:

$$DL_{span} = 76.6\ k.ft \qquad DL_{pier} = -136\ k.ft$$

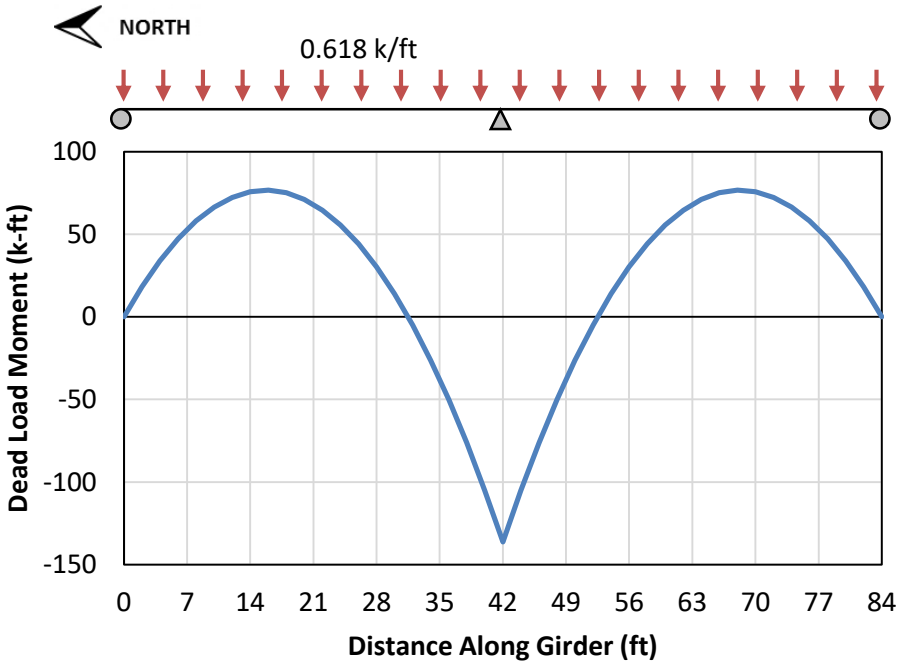

Figure A-2: Dead Load Moments for First Specimen

A.2.4 Predictions under Shakedown Loading

For the first specimen, a load ratio of 0.87 was used between Load A and each of Loads B and C. The associated moment diagrams under unit loads $0.87P$ and P are shown in Figure A-3.

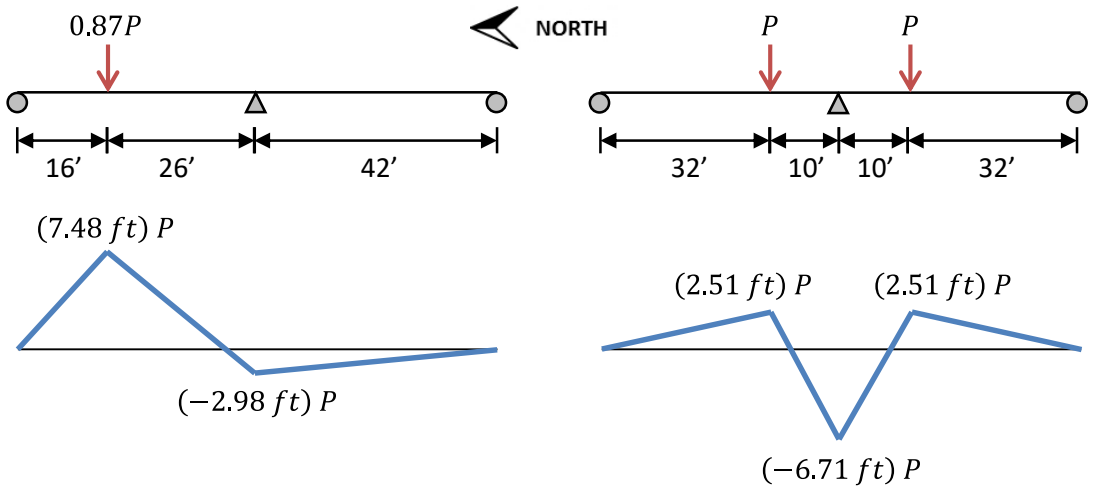

Figure A-3: Load Pattern and Moment Diagrams for Shakedown Testing of the North Span of the First Specimen

Elastic Limit Load

First yield in the specimen under the loading pattern shown in Figure A-3 can occur either at the location of Load A in positive bending or at the interior support in negative bending. The following calculates the load (P_y) that causes first yield to occur at both locations:

$$At\ Load\ A:\ \ (7.48\ ft)\ P_y + DL_{span} = M_{y\ span} \ \rightarrow\ P_y = \frac{M_{y\ span} - DL_{span}}{7.48\ ft}$$
$$= \frac{1350\ k.ft - 76.6\ k.ft}{7.48\ ft} = 170\ k$$

$$At\ Interior\ Support:\ \ (-6.71\ ft)\ P_y + DL_{pier} = -M_{y\ pier}$$
$$\rightarrow\ \ P_y = \frac{M_{y\ pier} + DL_{pier}}{6.71\ ft} = \frac{1070\ k.ft - 136\ k.ft}{6.71\ ft}$$
$$= 139\ k$$

The smaller of these two values for P_y controls, indicating that first yield is predicted to occur at the interior support at a load of $P_{B,C\ EL\ limit} = 139\ k$. For the purposes of presenting the results in Chapter 5, this was rounded to the closest load level used in the testing, or $P_{B,C\ EL\ limit} = 145\ k$.

Shakedown Limit Load

Predicting the shakedown limit load is done using the upper-bound method described in Section 2.4.2. The only possible mechanism for this loading pattern is shown in Figure A-4.

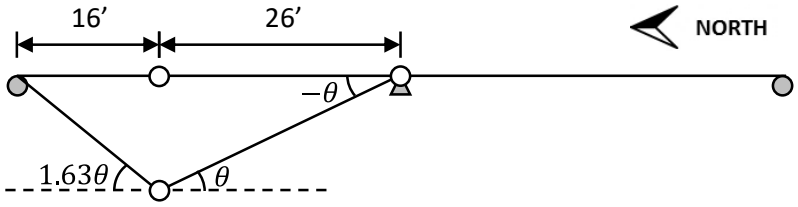

Figure A-4: Shakedown Mechanism for the North Span of the First Specimen

The internal and external virtual work are calculated as follows. The predicted shakedown limit load is then computed based on equilibrium of the virtual work:

$$\begin{aligned}\delta W_{internal} &= (M_{p\ span} - DL_{span})(1.63\theta + \theta) \\ &\quad + \left(-M_{p\ pier} - DL_{pier}\right)(-\theta) \\ &= (1810\ k.ft - 76.6\ k.ft)(2.63\theta) \\ &\quad + (-1240\ k.ft - (-136\ k.ft)\ )(-\theta) = (5660\ k.ft)(\theta)\end{aligned}$$

$$\begin{aligned}\delta W_{external} &= \left((7.48\ ft)\ P\right)(1.63\theta + \theta) + \left((-6.71\ ft)\ P\right)(-\theta) \\ &= \left((26.4\ ft)\ P\right)(\theta)\end{aligned}$$

$$\begin{aligned}\delta W_{internal} = \delta W_{external} \quad &\rightarrow \quad (5660\ k.ft)(\theta) = \left((26.4\ ft)\ P_{SD}\right)(\theta) \\ &\rightarrow \quad P_{SD} = 215\ k\end{aligned}$$

$$P_{A\ SD\ limit} = 0.87P = 0.87(215\ k) = 187\ k$$

$$P_{B,C\ SD\ limit} = P = 215\ k$$

The amount of moment redistribution is commonly quantified as the percentage of the redistribution moment (M_{rd}) to the total elastic moment at the interior pier (M_{el}). The

redistribution moment is simply the amount by which the elastic moment exceeds the moment capacity at the interior pier.

$$M_{el} = (-6.71\ ft)P_{B,C\ SD\ limit} + DL_{pier} = (-6.71\ ft)(215\ k) - 136\ k.ft$$
$$= -1580\ k.ft$$

$$M_{rd} = |M_{el}| - M_{p\ pier} = |-1580\ k.ft| - 1240\ k.ft = 340\ k.ft$$

$$\frac{M_{rd}}{|M_{el}|} = \frac{340\ k.ft}{|-1580\ k.ft|} = 22\%$$

While the specimens and loading procedure were originally designed to target 20% moment redistribution, the load ratio was chosen prior to conducting both the material testing and the parametric study discussed in Section 7.3 regarding the elastic distribution of moments in a strengthened girder. Thus, different assumptions were originally made in determining the load ratio to use for testing than are used in this appendix to calculate the predicted behavior. For this reason, the actual amount of moment redistribution is not exactly equal to the initial 20% target.

A.2.5 Predictions under Ultimate Strength Loading

Ultimate strength testing was conducted in the north span of the first specimen under the application of only Load A. The associated moment diagram under a unit load P is shown in Figure A-5.

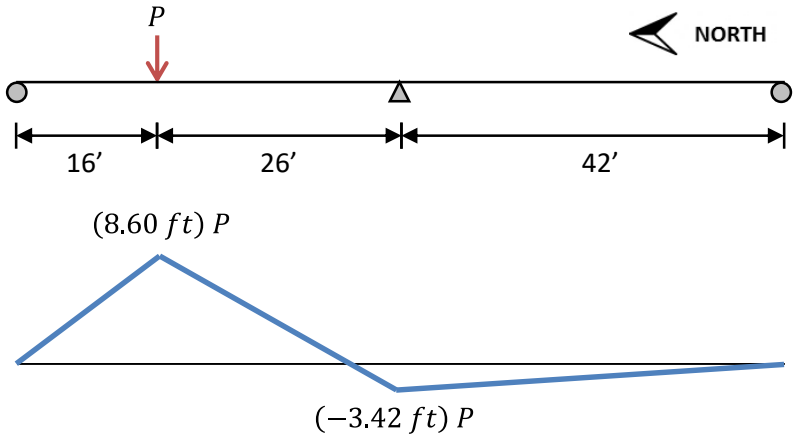

Figure A-5: Ultimate Strength Loading for the North Span of the First Specimen

Predicting the plastic limit load is done using the upper-bound method, also called the kinematic method, for static loading. This is based on similar principles of virtual work used in the upper-bound method for predicting the shakedown limit load, and more details can be found elsewhere (Neal 1977). The only possible mechanism for this applied load is shown in Figure A-6 and is identical to that for shakedown loading.

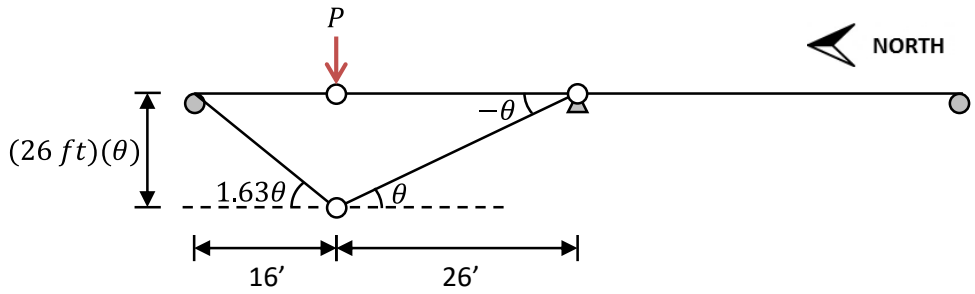

Figure A-6: Ultimate Strength Mechanism for the North Span of the First Specimen

The internal and external virtual work are calculated as follows. The predicted plastic limit load (P_{ULT}) at the ultimate strength limit state is then computed based on equilibrium of the virtual work:

$$\delta W_{internal} = (M_{p\ span} - DL_{span})(1.63\theta + \theta)$$
$$+ \left(-M_{p\ pier} - DL_{pier}\right)(-\theta)$$
$$= (1810\ k.ft - 76.6\ k.ft)(2.63\theta)$$
$$+ (-1240\ k.ft - (-136\ k.ft)\ )(-\theta) = (5650\ k.ft)(\theta)$$

$$\delta W_{external} = (26\ ft)(\theta)(P)$$

$$\delta W_{internal} = \delta W_{external} \quad \rightarrow \quad (5650\ k.ft)(\theta) = (26\ ft)(\theta)(P_{ULT})$$
$$\rightarrow \quad P_{ULT} = 217\ k$$

A.3 First Specimen – South Span

The material properties for the south span of the first specimen are given in Table A-3.

Table A-3: Material Properties for the South Span of the First Specimen

Steel yield stress in positive moment regions ($F_{y\ span}$, ksi)	56.3
Steel yield stress in negative moment regions ($F_{y\ pier}$, ksi)	52.4
Elastic modulus of steel beams (E_s, ksi)	29000
Compressive strength of concrete (f'_c, ksi)	4.7
Elastic modulus of concrete (E_c, ksi)	3910

A.3.1 Properties of Non-Composite Section at Interior Support

Yield Moment

The yield moment of the section in negative bending at the interior support are identical to that calculated for the north span because it is the same section:

$$M_{y\_pier} = S_x\ F_{y\ pier} = (245\ ksi)(52.4\ ksi)\left(\frac{1\ ft}{12\ in}\right) = 1070\ k.ft$$

Moment Capacity and Shape Factor

The moment capacity of the section in negative bending at the interior support and the shape factor are identical to that calculated for the north span because it is the same section:

$$M_{p\_pier} = Z_x \, F_{y\,pier} = (283\ ksi)(52.4\ ksi)\left(\frac{1\ ft}{12\ in}\right) = 1240\ k.ft$$

$$k_{pier} = \frac{M_{p\,pier}}{M_{y\,pier}} = \frac{1070\ k.ft}{1240\ k.ft} = 1.16$$

Neutral Axis

As with the north span, the neutral axis for a doubly symmetric non-composite section at all levels of load in the elastic and inelastic range is expected to be located at mid-depth of the web.

A.3.2 Properties of Partially Composite Section in the Span

Elastic Properties and Yield Moment

The elastic properties and yield moment of this partially composite section is calculated in the same manner as for the north span. Again, there are 7 pairs of connectors, so $N = 14$. The calculations for the fully composite transformed section are identical to that of the north span and thus are not repeated here. The stress distribution at the plastic moment capacity is identical to that shown in Figure A-1:

$$C_{f\,FC} = min\begin{Bmatrix} 0.85 f_c' A_{deck} \\ A_s F_y \end{Bmatrix} = min\begin{Bmatrix} 0.85(4.7\ ksi)(507\ in^2) \\ (26.3\ in^2)(56.3\ ksi) \end{Bmatrix} = min\begin{Bmatrix} 2030\ k \\ 1480\ k \end{Bmatrix}$$
$$= 1480\ k$$

$$N_{FC} = \frac{C_{f\,FC}}{Q_n} = \frac{1480\ k}{30.1\ k} = 49.2$$

$$\eta = \frac{N}{N_{FC}} = \frac{14}{49.2} = 0.285$$

$$I_{eff} = I_x + \sqrt{\eta}(I_{tr} - I_x)$$
$$= (3610\ in^4) + \sqrt{0.285}\big((10000\ in^4) - (3610\ in^4)\big)$$
$$= 7020\ in^4$$

$$S_{eff} = S_x + \sqrt{\eta}(S_{tr} - S_x) = (245\ in^3) + \sqrt{0.285}\big((361\ in^3) - (245\ in^3)\big)$$
$$= 307\ in^3$$

$$M_{y\ span} = S_{eff}F_{y\ span} = (307\ in^3)(56.3\ ksi)\left(\frac{1\ ft}{12\ in}\right) = 1440\ k.ft$$

Moment Capacity and Shape Factor

The moment capacity and shape factor of a partially composite section is calculated in the same manner as for the north span:

$$C_f = min\begin{Bmatrix} 0.85f_c'A_{deck} \\ A_sF_{y\_span} \\ N\ Q_n \end{Bmatrix} = min\begin{Bmatrix} 0.85(4.7\ ksi)(507\ in^2) \\ (26.3\ in^2)(56.3\ ksi) \\ (14)(30.1\ k) \end{Bmatrix} = min\begin{Bmatrix} 2030\ k \\ 1480\ k \\ 421\ k \end{Bmatrix}$$
$$= 421\ k$$

$$P_{y\ web} = A_{web}F_{y\_span} = \big(A_s - 2A_f\big)F_{y\_span}$$
$$= (26.3\ in^2 - 2(6.34\ in^2))(56.3\ ksi) = 767\ k$$

$$767\ k > 421\ k \ \rightarrow\ P_{y\ web} > C_f \ \rightarrow\ Plastic\ neutral\ axis\ is\ in\ the\ web$$

$$a = \frac{C_f}{0.85f_c'b_{eff}} = \frac{421\ k}{0.85(4.7\ ksi)(78\ in)} = 1.35\ in$$

$$T_s = zt_w\left(2F_{y\_span}\right) = (z)(0.470\ in)\left(2(56.3\ ksi)\right) = \left(52.9\frac{k}{in}\right)(z)$$

$$M_{p\ steel} = Z_x F_{y\_span} = (283\ in^3)(56.3\ ksi) = 15900\ k.in$$

$$\Sigma F = 0 \ \rightarrow \ T_s - C_f = 0 \ \rightarrow \ \left(52.9\frac{k}{in}\right)(z) - 421\ k = 0 \ \rightarrow \ z = 7.96\ in$$

$$\begin{aligned} M_{p\ span} = \Sigma M_{interface} &= T_s\left(\frac{d}{2} - \frac{z}{2}\right) + C_f\left(t_{deck} - \frac{a}{2}\right) + M_{p\ steel} \\ &= \left(\left(52.9\frac{k}{in}\right)(7.96\ in)\right)\left(\frac{(29.5\ in)}{2} - \frac{(7.96\ in)}{2}\right) \\ &+ (421\ k)\left(6.5\ in - \frac{1.35\ in}{2}\right) + 15900\ k.in \\ &= (22900\ k.in)\left(\frac{1\ ft}{12\ in}\right) = 1910\ k.ft \end{aligned}$$

$$k_{span} = \frac{M_{p\ span}}{M_{y\ span}} = \frac{1910\ k.ft}{1440\ k.ft} = 1.33$$

Neutral Axis

As discussed previously for the north span, locating the neutral axis in a partially composite cross section is difficult, because plane sections do not remain plane due to the interface slip. Thus, the location of the neutral axis at the plastic moment is plotted as the "predicted location" in Figure 5-10 and Figure 5-21 for comparison to the experimental data. For this case, the plastic neutral axis was calculated to be 7.96 inches above mid-depth of the web, or 6.79 inches below the interface.

A.3.3 Dead Load Analysis

Because the geometry of the girder specimen is symmetrical across the interior support, the dead load is identical to that for the north span, as shown in Figure A-2:

$$DL_{span} = 76.6\ k.ft \qquad DL_{pier} = -136\ k.ft$$

A.3.4 Predictions under Shakedown Loading

As with the north span, a load ratio of 0.87 was used between Load D and each of Loads B and C. The associated moment diagrams under unit loads $0.87P$ and P are shown in Figure A-7. These are identical to those for the north span loading, but are mirrored across the interior support

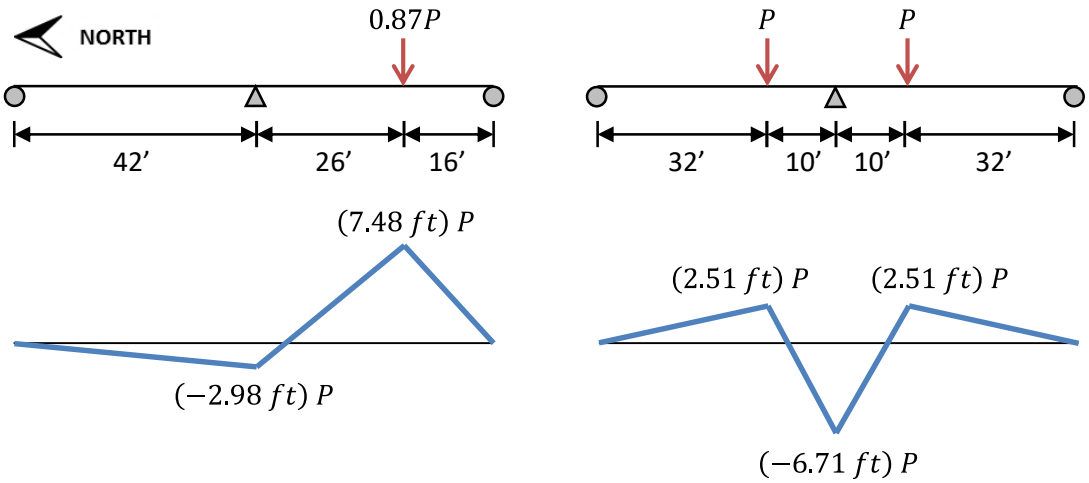

Figure A-7: Load Pattern and Moment Diagrams for Shakedown Testing of the South Span of the First Specimen

Elastic Limit Load

For the north span loading, first yield was calculated to occur at the interior support. Because the only difference between the north and south spans of the first specimen is that the yield strength of the steel in the positive moment regions of the south span is slightly larger than that of the north span, the interior support will control again for the south span loading. Thus:

$$P_y = P_{B,C\ EL\ limit} = 139\ k$$

Again, this value was rounded to the closest load level used in the testing, or $P_{B,C\ EL\ limit} = 145\ k$ for comparison to the load levels applied to the specimen during testing.

Shakedown Limit Load

Predicting the shakedown limit load and calculating the actual amount of moment redistribution are done in the same manner as for the north span. The only possible mechanism for this loading pattern is shown in Figure A-8. This mechanism is identical to that for the north span, but mirrored across the interior support:

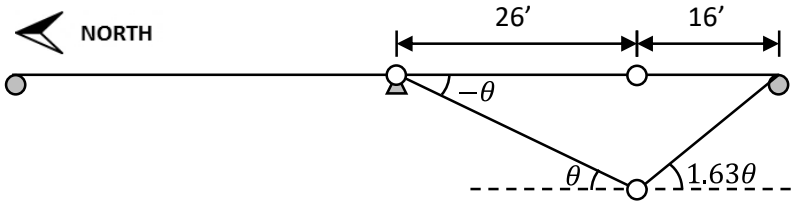

Figure A-8: Shakedown Mechanism for the South Span of the First Specimen

$$\delta W_{internal} = (M_{p\ span} - DL_{span})(1.63\theta + \theta) + \left(-M_{p\ pier} - DL_{pier}\right)(-\theta) = (1910\ k.ft - 76.6\ k.ft)(2.63\theta) + (-1240\ k.ft - (-136\ k.ft)\ )(-\theta) = (5930\ k.ft)(\theta)$$

$$\delta W_{external} = \left((7.48\ ft)\ P\right)(1.63\theta + \theta) + \left((-6.71\ ft)\ P\right)(-\theta) = \left((26.4\ ft)\ P\right)(\theta)$$

$$\delta W_{internal} = \delta W_{external} \quad \rightarrow \quad (5930\ k.ft)(\theta) = \left((26.4\ ft)\ P_{SD}\right)(\theta) \rightarrow \quad P_{SD} = 225\ k$$

$$P_{D\ SD\ limit} = 0.87P = 0.87(215\ k) = 195\ k$$

$$P_{B,C\ SD\ limit} = P = 225\ k$$

$$M_{el} = (-6.71\ ft)P_{B,C\ SD\ limit} + DL_{pier} = (-6.71\ ft)(225\ k) - 136\ k.ft = -1650\ k.ft$$

$$M_{rd} = |M_{el}| - M_{p\,pier} = |-1650\ k.ft| - 1240\ k.ft = 410\ k.ft$$

$$\frac{M_{rd}}{|M_{el}|} = \frac{410\ k.ft}{|-1650\ k.ft|} = 25\%$$

Unfortunately, the shakedown limit load calculated for this span does not match closely with any of the load levels applied during the experimental testing. Thus, this was rounded to the nearest load level used, or $P_{D\ SD\ limit} = 191\ k$ and $P_{B,C\ SD\ limit} = 220\ k$, for purposes of presenting the results in Chapter 5.

A.3.5 Predictions under Ultimate Strength Loading

Ultimate strength testing was conducted in the south span of the first specimen under the application of only Load D. The associated moment diagram under a unit load P is shown in Figure A-9. This is identical to that for the north span, but mirrored across the interior support.

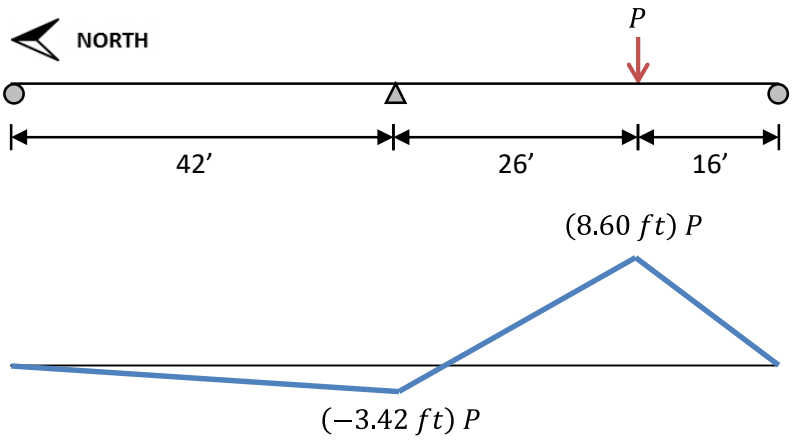

Figure A-9: Ultimate Strength Loading for the South Span of the First Specimen

Predicting the plastic limit load was done in the same manner as for the north span. The only possible mechanism for this applied load is shown in Figure A-10 and is identical to that for shakedown loading:

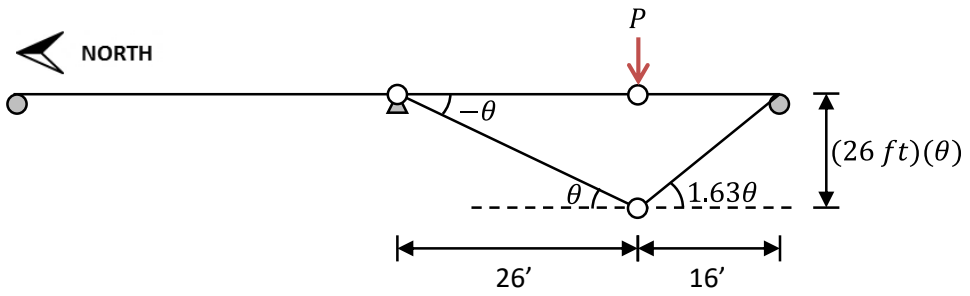

Figure A-10: Ultimate Strength Mechanism for the South Span of the First Specimen

$$\delta W_{internal} = (M_{p\ span} - DL_{span})(1.63\theta + \theta) + \left(-M_{p\ pier} - DL_{pier}\right)(-\theta) = (1910\ k.ft - 76.6\ k.ft)(2.63\theta) + (-1240\ k.ft - (-136\ k.ft)\ )(-\theta) = (5930\ k.ft)(\theta)$$

$$\delta W_{external} = (26\ ft)(\theta)(P)$$

$$\delta W_{internal} = \delta W_{external} \quad \rightarrow \quad (5650\ k.ft)(\theta) = (26\ ft)(\theta)(P_{ULT}) \quad \rightarrow \quad P_{ULT} = 227\ k$$

A.4 SECOND SPECIMEN

The material properties for the second specimen are given in Table A-4.

Table A-4: Material Properties for the Second Specimen

Steel yield stress in positive moment regions ($F_{y\ span}$, ksi)	56.3
Steel yield stress in negative moment regions ($F_{y\ pier}$, ksi)	56.3
Elastic modulus of steel beams (E_s, ksi)	29000
Compressive strength of concrete (f'_c, ksi)	2.5
Elastic modulus of concrete (E_c, ksi)	2850

A.4.1 Properties of Non-Composite Section at Interior Support

Yield Moment

The yield moment of the section in negative bending at the interior support is calculated in the same manner as for the first specimen:

$$M_{y\_pier} = S_x \, F_{y\,pier} = (245\ ksi)(56.3\ ksi)\left(\frac{1\ ft}{12\ in}\right) = 1150\ k.ft$$

Moment Capacity and Shape Factor

The moment capacity and shape factor of the section in negative bending at the interior support is calculated in the same manner as for the first specimen:

$$M_{p\_pier} = Z_x \, F_{y\,pier} = (283\ ksi)(56.3\ ksi)\left(\frac{1\ ft}{12\ in}\right) = 1330\ k.ft$$

$$k_{pier} = \frac{M_{p\,pier}}{M_{y\,pier}} = \frac{1330\ k.ft}{1150\ k.ft} = 1.16$$

Neutral Axis

As with the first specimen, the neutral axis for a doubly symmetric non-composite section at all levels of load in the elastic and inelastic range is expected to be located at mid-depth of the web.

A.4.2 Properties of Partially Composite Section in the Span

Elastic Properties and Yield Moment

The yield moment of this partially composite section is calculated in the same manner as for the first specimen. For this girder, there are 5 pairs of connectors, so $N = 10$. The stress distribution at the plastic moment capacity is identical to that shown in Figure A-1:

$$n = \frac{E_s}{E_c} = \frac{29000\ ksi}{2850\ ksi} = 10.2$$

$$y_{NA\ tr} = \frac{A_s\left(\frac{d}{2}\right) - \frac{A_{deck}}{n}\left(\frac{t_{deck}}{2}\right)}{A_s + \frac{A_{deck}}{n}}$$
$$= \frac{(26.3\ in^2)\left(\frac{29.5\ in}{2}\right) - \frac{(507\ in^2)}{10.2}\left(\frac{6.5\ in}{2}\right)}{(26.3\ in) + \frac{(507\ in^2)}{10.2}} = 2.98\ in$$

$$I_{tr} = I_x + A_s\left(\frac{d}{2} - y_{NA\ tr}\right)^2 + \frac{I_{deck}}{n} + \frac{A_{deck}}{n}\left(\frac{t_{deck}}{2} + y_{NA\ tr}\right)^2$$
$$= 3610\ in^4 + (26.3\ in^2)\left(\frac{29.5\ in}{2} - 2.98\ in\right)^2$$
$$+ \frac{(1790\ in^4)}{10.2} + \frac{(507\ in^2)}{10.2}\left(\frac{6.5\ in}{2} + 2.98\ in\right)^2 = 9360\ in^4$$

$$S_{tr} = \frac{I_{tr}}{d - y_{NA\ tr}} = \frac{9360\ in^4}{(29.5\ in) - (2.98\ in)} = 353\ in^3$$

$$C_{f\ FC} = min\begin{Bmatrix} 0.85 f_c' A_{deck} \\ A_s F_y \end{Bmatrix} = min\begin{Bmatrix} 0.85(2.5\ ksi)(507\ in^2) \\ (26.3\ in^2)(56.3\ ksi) \end{Bmatrix} = min\begin{Bmatrix} 1080\ k \\ 1480\ k \end{Bmatrix}$$
$$= 1080\ k$$

$$N_{FC} = \frac{C_{f\ FC}}{Q_n} = \frac{1080\ k}{30.1\ k} = 35.9$$

$$\eta = \frac{N}{N_{FC}} = \frac{10}{35.9} = 0.279$$

$$I_{eff} = I_x + \sqrt{\eta}(I_{tr} - I_x)$$
$$= (3610\ in^4) + \sqrt{0.279}\big((9360\ in^4) - (3610\ in^4)\big)$$
$$= 6650\ in^4$$

$$S_{eff} = S_x + \sqrt{\eta}(S_{tr} - S_x) = (245\ in^3) + \sqrt{0.279}\big((353\ in^3) - (245\ in^3)\big)$$
$$= 302\ in^3$$

$$M_{y\ span} = S_{eff}F_{y\ span} = (302\ in^3)(56.3\ ksi)\left(\frac{1\ ft}{12\ in}\right) = 1420\ k.ft$$

Moment Capacity and Shape Factor

The moment capacity and shape factor of a partially composite section is calculated in the same manner as for the first specimen:

$$C_f = min\begin{Bmatrix} 0.85f_c'A_{deck} \\ A_sF_{y\_span} \\ N\ Q_n \end{Bmatrix} = min\begin{Bmatrix} 0.85(2.5\ ksi)(507\ in^2) \\ (26.3\ in^2)(56.3\ ksi) \\ (10)(30.1\ k) \end{Bmatrix} = min\begin{Bmatrix} 1080\ k \\ 1480\ k \\ 301\ k \end{Bmatrix}$$
$$= 301\ k$$

$$P_{y\ web} = A_{web}F_{y\_span} = \big(A_s - 2A_f\big)F_{y\_span}$$
$$= (26.3\ in^2 - 2(6.34\ in^2))(56.3\ ksi) = 767\ k$$

$$767\ k > 301\ k \ \rightarrow\ P_{y\ web} > C_f \ \rightarrow\ Plastic\ neutral\ axis\ is\ in\ the\ web$$

$$a = \frac{C_f}{0.85f_c'b_{eff}} = \frac{301\ k}{0.85(2.5\ ksi)(78\ in)} = 1.82\ in$$

$$T_s = zt_w\big(2F_{y\_span}\big) = (z)(0.470\ in)\big(2(56.3\ ksi)\big) = \left(52.9\frac{k}{in}\right)(z)$$

$$M_{p\ steel} = Z_xF_{y\_span} = (283\ in^3)(56.3\ ksi) = 15900\ k.in$$

$$\Sigma F = 0 \ \rightarrow\ T_s - C_f = 0 \ \rightarrow\ \left(52.9\frac{k}{in}\right)(z) - 301\ k = 0 \ \rightarrow\ z = 5.69\ in$$

$$M_{p\,span} = \Sigma M_{interface} = T_s\left(\frac{d}{2} - \frac{z}{2}\right) + C_f\left(t_{deck} - \frac{a}{2}\right) + M_{p\,steel}$$
$$= \left(\left(52.9\frac{k}{in}\right)(5.69\ in)\right)\left(\frac{(29.5\ in)}{2} - \frac{(5.69\ in)}{2}\right)$$
$$+ (301\ k)\left(6.5\ in - \frac{1.82\ in}{2}\right) + 15900\ k.in$$
$$= (21200\ k.in)\left(\frac{1\ ft}{12\ in}\right) = 1760\ k.ft$$

$$k_{span} = \frac{M_{p\,span}}{M_{y\,span}} = \frac{1760\ k.ft}{1420\ k.ft} = 1.24$$

Neutral Axis

As discussed previously for the first specimen, locating the neutral axis in a partially composite cross section is difficult because plane sections do not remain plane due to the interface slip. Thus, the location of the neutral axis at the plastic moment is plotted as the "predicted location" in Figure 5-11 and Figure 5-22 for comparison to the experimental data. For this case, the plastic neutral axis was calculated to be 5.69 inches above mid-depth of the web, or 9.06 inches below the interface.

A.4.3 Dead Load Analysis

The dead load moments are calculated in the same manner as for the first specimen. The only difference in this analysis between the two specimens is the span length. The dead load moments are plotted in Figure A-11. At the critical locations, the dead load moments are:

$$DL_{span} = 117\ k.ft \qquad DL_{pier} = -209\ k.ft$$

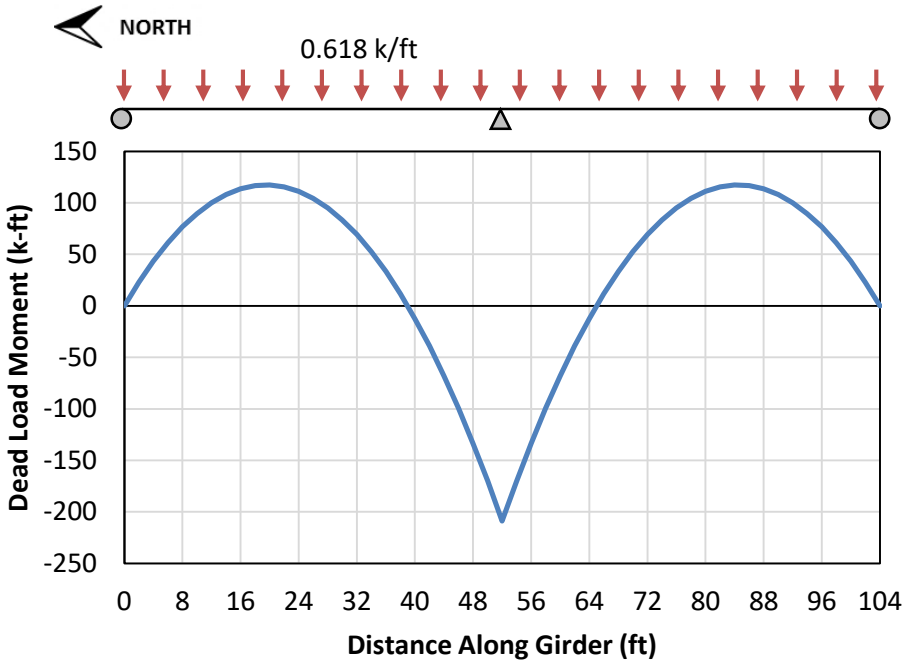

Figure A-11: Dead Load Moments for Second Specimen

A.4.4 Predictions under Shakedown Loading

For this specimen, the same load was applied at all four load locations, so the load ratio was 1.0. The associated moment diagrams under unit loads of *P* are shown in Figure A-12. Note that the first and last load steps are identical, but mirrored across the interior support.

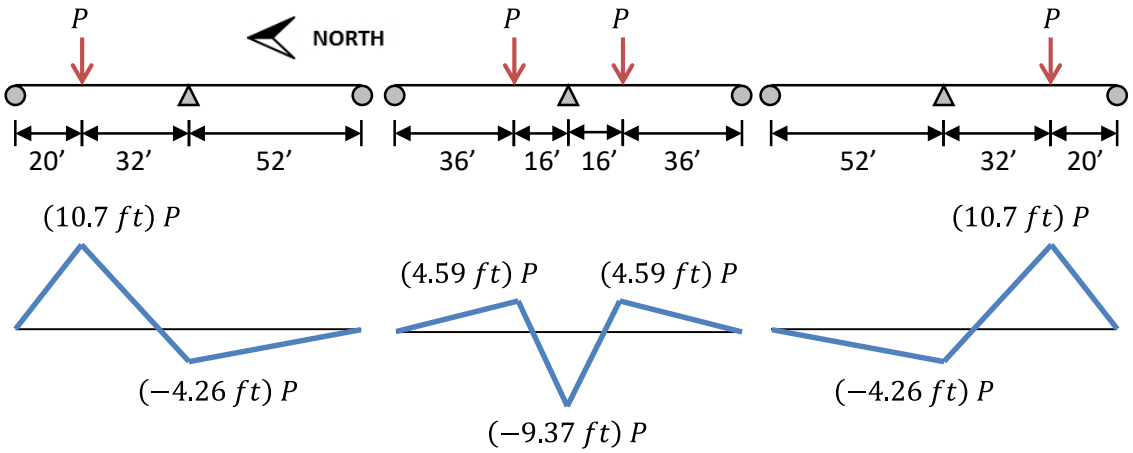

Figure A-12: Load Pattern and Moment Diagrams for Shakedown Testing of the Second Specimen

Elastic Limit Load

First yield in the specimen under the loading pattern shown in Figure A-12 can occur either at the location of Load A and Load D in positive bending or at the interior support in negative bending. The following calculates the load (P_y) that causes first yield to occur at both locations:

$$At\ Load\ A\ or\ Load\ D\text{:}\quad (10.7\ ft)\ P_y + DL_{span} = M_{y\ span}$$

$$\rightarrow\ P_y = \frac{M_{y\ span} - DL_{span}}{10.7\ ft} = \frac{1420\ k.ft - 117\ k.ft}{10.7\ ft}$$

$$= 122\ k$$

$$At\ Interior\ Support\text{:}\quad (-9.37\ ft)\ P_y + DL_{pier} = -M_{y\ pier}$$

$$\rightarrow\quad P_y = \frac{M_{y\ pier} + DL_{pier}}{9.37\ ft} = \frac{1150\ k.ft - 209\ k.ft}{9.37\ ft}$$

$$= 100\ k$$

The smaller of these two values for P_y controls, indicating that first yield is predicted to occur at the interior support at a load of $P_{B,C\ EL\ limit} = 100\ k$.

Shakedown Limit Load

Predicting the shakedown limit load and calculating the actual amount of moment redistribution are done in the same manner as for the first specimen. The only possible mechanism for this loading pattern is shown in Figure A-13:

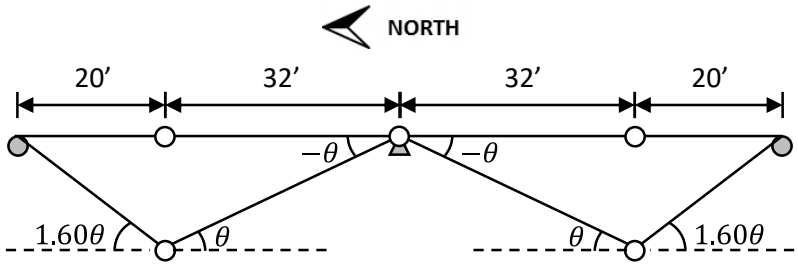

Figure A-13: Shakedown Mechanism for the Second Specimen

$$\delta W_{internal} = 2 * ((M_{p\,span} - DL_{span})(1.60\theta + \theta) + \big(-M_{p\,pier} - DL_{pier}\big)(-\theta)) = 2 * ((1760\ k.ft - 117\ k.ft)(2.60\theta) + \big(-1330\ k.ft - (-209\ k.ft)\big)(-\theta)) = (10800\ k.ft)(\theta)$$

$$\delta W_{external} = 2 * \big((10.7\ ft)\ P\big)(1.60\theta + \theta) + \big((-9.37\ ft)\ P\big)(-\theta)) = \big((74.4\ ft)\ P\big)(\theta)$$

$$\delta W_{internal} = \delta W_{external} \quad \rightarrow \quad (10800\ k.ft)(\theta) = \big((74.4\ ft)\ P_{SD}\big)(\theta) \rightarrow \quad P_{SD} = 145\ k$$

$$P_{A\ SD\ limit} = P_{B,C\ SD\ limit} = P_{D\ SD\ limit} = P = 145\ k$$

$$M_{el} = (-9.37\ ft)P_{B,C\ SD\ limit} + DL_{pier} = (-9.37\ ft)(145\ k) - 209\ k.ft = -1570\ k.ft$$

$$M_{rd} = |M_{el}| - M_{p\,pier} = |-1570\ k.ft| - 1330\ k.ft = 240\ k.ft$$

$$\frac{M_{rd}}{|M_{el}|} = \frac{240\ k.ft}{|-1570\ k.ft|} = 15\%$$

A.4.5 Predictions under Ultimate Strength Loading

Ultimate strength testing was conducted on the second specimen under the application of both Load A and Load D. The associated moment diagram under unit loads of P is shown in Figure A-14.

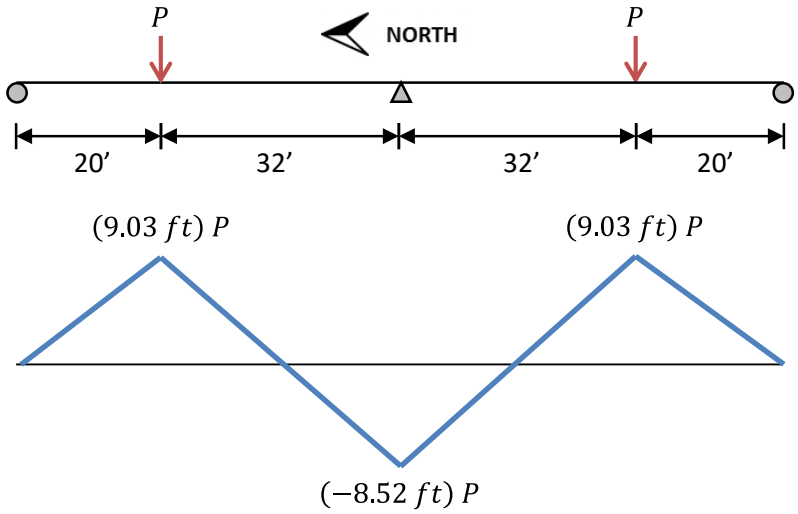

Figure A-14: Ultimate Strength Loading for the Second Specimen

Predicting the plastic limit load was done in the same manner as for the first specimen. The only possible mechanism for this applied load is shown in Figure A-15:

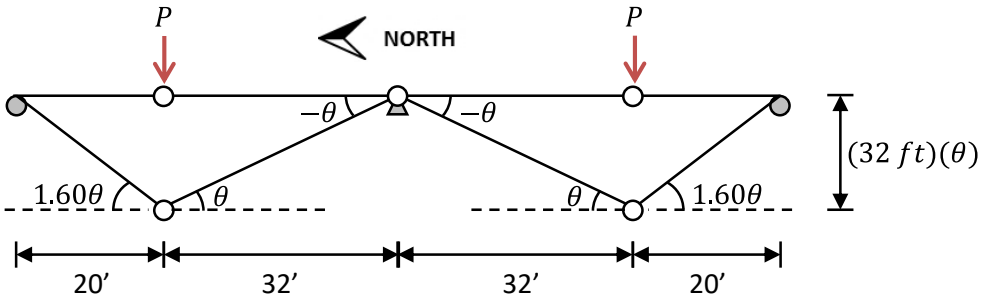

Figure A-15: Ultimate Strength Mechanism for the Second Specimen

$$\delta W_{internal} = 2 * ((M_{p\,span} - DL_{span})(1.60\theta + \theta) + \left(-M_{p\,pier} - DL_{pier}\right)(-\theta)) = 2 * ((1760\ k.ft - 117\ k.ft)(2.60\theta) + \left(-1330\ k.ft - (-209\ k.ft)\right)(-\theta)) = (10800\ k.ft)(\theta)$$

$$\delta W_{external} = 2 * (32\ ft)(\theta)(P) = (64\ ft)(\theta)(P)$$

$$\delta W_{internal} = \delta W_{external} \quad \rightarrow \quad (10800\ k.ft)(\theta) = (64\ ft)(\theta)(P_{ULT}) \rightarrow \quad P_{ULT} = 169\ k$$

APPENDIX B: EQUATIONS USED IN FURTHER ANALYSIS OF EXPERIMENTAL RESULTS

B.1 Overview

This appendix contains the equations for the deflected shapes and redistribution moments used in the analysis discussed in Section 6.2.1.

B.2 Residual Deflections and Redistribution Moments

Figure B-1 shows the deflected shapes and associated residual moment diagrams resulting from rotation of a plastic hinge in three different critical locations along a symmetric two-span continuous girder. This figure is analogous to Figure 6-1. The equations describing these deflected shapes and redistribution moments (M_{rd}) are given in the following sections. For simplicity in deriving these equations, the deflection at the hinge point (δ) was used in lieu of the hinge rotation (θ) for cases in which the hinge was located in one of the spans.

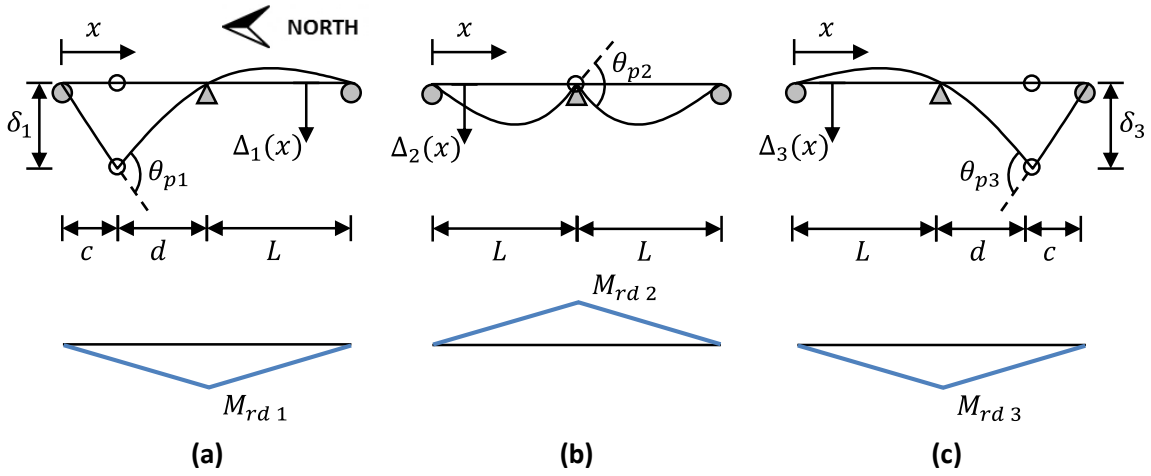

Figure B-1: Deflected Shapes from Rotation of Plastic Hinges (a) at Load A in North Span, (b) at Interior Support, and (c) at Load D in South Span

B.2.1 Plastic Hinge at Load A in North Span

For $0 \le x \le c$*:* $$\Delta_1(x) = \left(\frac{-cx^3 + (4L^3 - 5L^2c + 2c^3)x}{cd(2L^2 + 3Ld - d^2)}\right)\delta_1$$

$$For\ c \le x \le L: \qquad \Delta_1(x) = \left(\frac{x^3 - 5L^2x + 4L^3}{d(2L^2 + 3Ld - d^2)}\right)\delta_1$$

$$For\ L \le x \le 2L: \qquad \Delta_1(x) = \left(\frac{-x^3 + 6Lx^2 - 11L^2x + 6L^3}{d(2L^2 + 3Ld - d^2)}\right)\delta_1$$

$$M_{rd\,1} = -\left(\frac{3EI}{d(L+d)}\right)\delta_1 \qquad \delta_1 = \left(\frac{d(2L^3 + L^2d - dLd^2 - d^3)}{2(3L^3 - L^2d + d^3)}\right)\theta_1$$

B.2.2 Plastic Hinge at Interior Support

$$For\ 0 \le x \le L: \qquad \Delta_2(x) = \left(\frac{-x^3 + L^2x}{4L^2}\right)\theta_2$$

$$For\ L \le x \le 2L: \qquad \Delta_2(x) = \left(\frac{x^3 - 6Lx^2 + 11L^2x - 6L^3}{4L^2}\right)\theta_2$$

$$M_{rd\,2} = -\left(\frac{3EI}{2L}\right)\theta_2$$

B.2.3 Plastic Hinge at Load D in South Span

$$For\ 0 \le x \le L: \qquad \Delta_3(x) = \left(\frac{x^3 - L^2x}{d(2L^2 + 3Ld - d^2)}\right)\delta_3$$

$$For\ L \le x \le 2L - c: \qquad \Delta_3(x) = \left(\frac{-x^3 + 6Lx^2 - 7L^2x + 2L^3}{d(2L^2 + 3Ld - d^2)}\right)\delta_3$$

$$For\ 2L - c \le x \le 2L: \qquad \Delta_1(x) = \left(\frac{-c(2L - x)^3 + (4L^3 - 5L^2c + 2c^3)(2L - x)}{cd(2L^2 + 3Ld - d^2)}\right)\delta_3$$

$$M_{rd\,3} = -\left(\frac{3EI}{d(L+d)}\right)\delta_3 \qquad \delta_3 = \left(\frac{d(2L^3 + L^2d - dLd^2 - d^3)}{2(3L^3 - L^2d + d^3)}\right)\theta_3$$

B.3 Elastic Deflections under Applied Loads

Figure B-2 shows the deflected shapes resulting from the three different loading cases used in the shakedown testing. This figure is analogous to Figure 6-2. The equations describing these deflected shapes are given in the following sections.

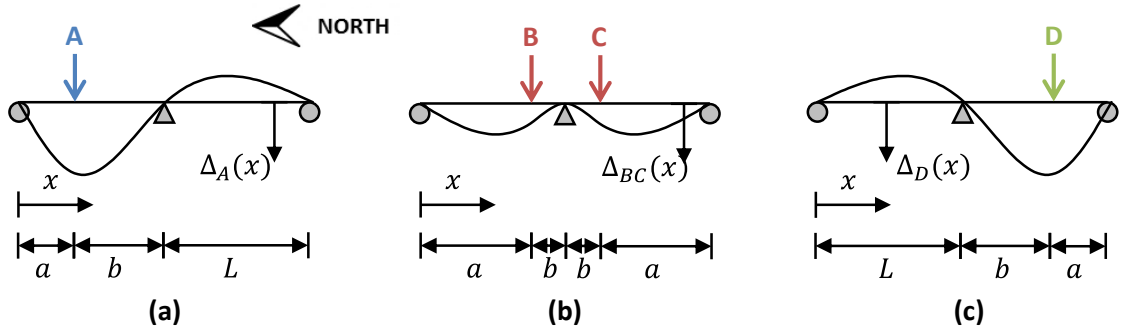

Figure B-2: Elastic Deflected Shapes from Applied Load for (a) Load A in North Span, (b) Loads B and C in Both Spans, and (c) Load D in South Span

B.3.1 Applied Load A in North Span

For $0 \le x \le a$*:*

$$\Delta_A(x) = \left(\frac{P_A b}{24EIL^3}\right)\left((a^2 + La - 4L^2)x^3 + (7L^3a - 5L^2a^2)x\right)$$

For $a \le x \le L$*:*

$$\Delta_A(x) = \left(\frac{P_A a}{24EIL^3}\right)\left((5L^2 - a^2)x^3 - 12L^3x^2 + (7L^4 + 5L^2a^2)x - 4L^3a^2\right)$$

For $L \le x \le 2L$*:*

$$\Delta_A(x) = \left(\frac{P_A ab(L+a)}{24EIL^3}\right)(-x^3 + 6Lx^2 - 11L^2x + 6L^3)$$

B.3.2 Applied Loads B and C in Both Spans

For $0 \le x \le a$*:*

$$\Delta_{BC}(x) = \left(\frac{P_{BC}b^2}{12EIL^3}\right)\left((-3L+b)x^3 + (3L^3 - 3L^2b)x\right)$$

For $a \le x \le L$*:*

$$\Delta_{BC}(x) = \left(\frac{P_{BC}a}{12EIL^3}\right)\left((3L^2 - a^2)x^3 - 6L^3x^2 + (3L^4 + 3L^2a^2)x - 2L^3a^2\right)$$

For $L \le x \le 2L - a$*:*

$$\Delta_{BC}(x) = \left(\frac{P_{BC}a}{12EIL^3}\right)\left((-3L^2 + a^2)x^3 + (12L^3 - 6La^2)x^2 + (-15L^4 + 9L^2a^2)x + 6L^5 - 4L^3a^2\right)$$

For $2L - a \le x \le 2L$*:*

$$\Delta_{BC}(x) = \left(\frac{P_{BC}b^2}{12EIL^3}\right)\left((3L-b)x^3 + (-18L^2 + 6Lb)x^2 + (33L^3 - 9L^2b)x - 18L^4 + 2L^3b\right)$$

B.3.3 Applied Load D in South Span

For $0 \le x \le L$*:*

$$\Delta_D(x) = \left(\frac{P_D ab(L+a)}{24EIL^3}\right)(x^3 - L^2x)$$

For $L \le x \le 2L - a$*:*

$$\Delta_D(x) = \left(\frac{P_D a}{24EIL^3}\right)\left((-5L^2 + a^2)x^3 + (18L^3 - 6La^2)x^2 + (-19L^4 + 7L^2a^2)x + 6L^5 - 2L^3a^2\right)$$

For $2L - a \le x \le 2L$*:*

$$\Delta_D(x) = \left(\frac{P_A b}{24EIL^3}\right)\left((a^2 + La - 4L^2)(2L - x)^3 + (7L^3a - 5L^2a^2)(2L - x)\right)$$

APPENDIX C: FULL RESULTS OF PARAMETRIC STUDY

C.1 OVERVIEW

This appendix provides graphs showing all of the results from the parametric study discussed in Chapter 7. That chapter presents the results from only one of the three girder geometries used in the study, because the trends in the results were very similar. Results for all three girders, including that from the girder presented in Chapter 7, are shown here.

C.2 RESULTS FROM PARAMETRIC STUDY

Figure D-1, Figure C-2, and Figure C-3 show the results from the parametric study for Girders A, B, and C, respectively. Note that Figure D-1 is identical to Figure 7-10. The trends are similar for all three girder geometries.

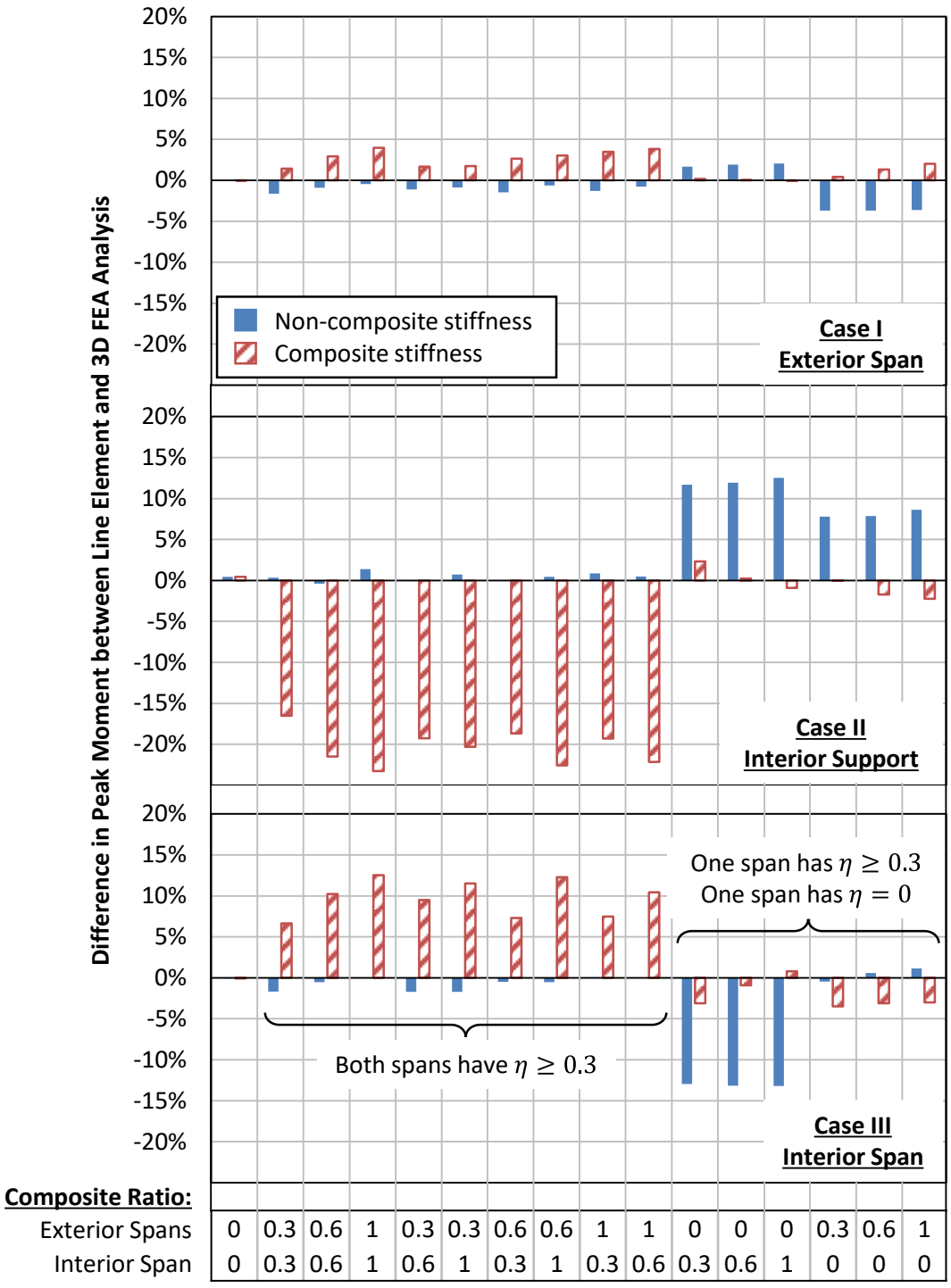

Figure C-1: Comparison of Peak Moments from 2D and 3D Analyses for Non-Composite and Strengthened Girder A

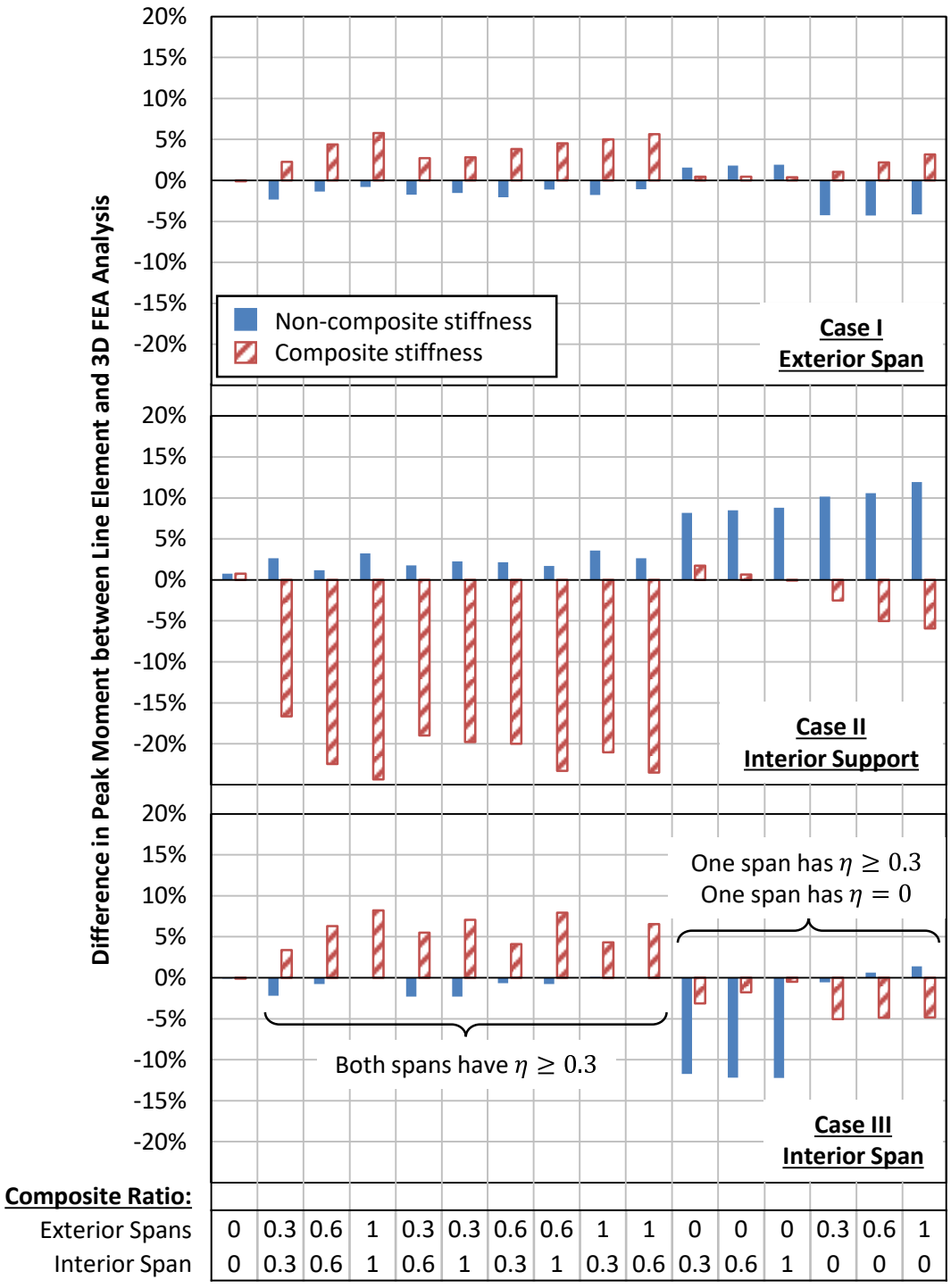

Figure C-2: Comparison of Peak Moments from 2D and 3D Analyses for Non-Composite and Strengthened Girder B

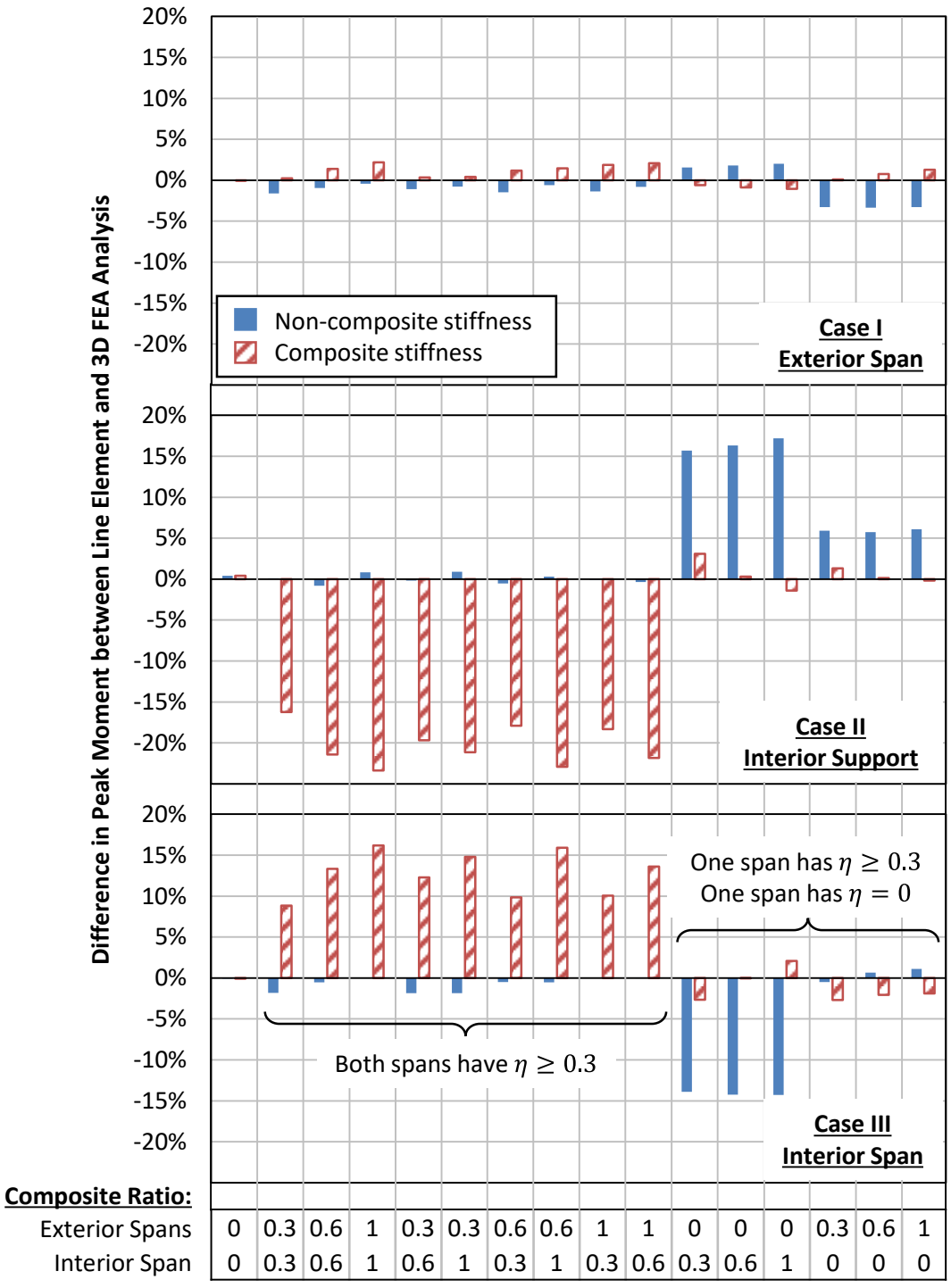

Figure C-3: Comparison of Peak Moments from 2D and 3D Analyses for Non-Composite and Strengthened Girder C

APPENDIX D: DESIGN EXAMPLE

D.1 OVERVIEW

This example addresses the strengthening design for a three-span continuous steel girder unit comprising a portion of an existing non-composite bridge in Texas.

D.1.1 Description of Bridge

The two-lane bridge was originally constructed in 1943 with four steel beams through the cross section. In 1961, the bridge was widened to four lanes by adding two steel beams to either side of the original structure. The steel unit from this bridge is symmetric in both the transverse and longitudinal directions. A half-cross section view of the bridge is shown Figure D-1. A general half-elevation view of a typical girder is shown in Figure D-2. Because of symmetry, only one-half of each girder needs to be analyzed.

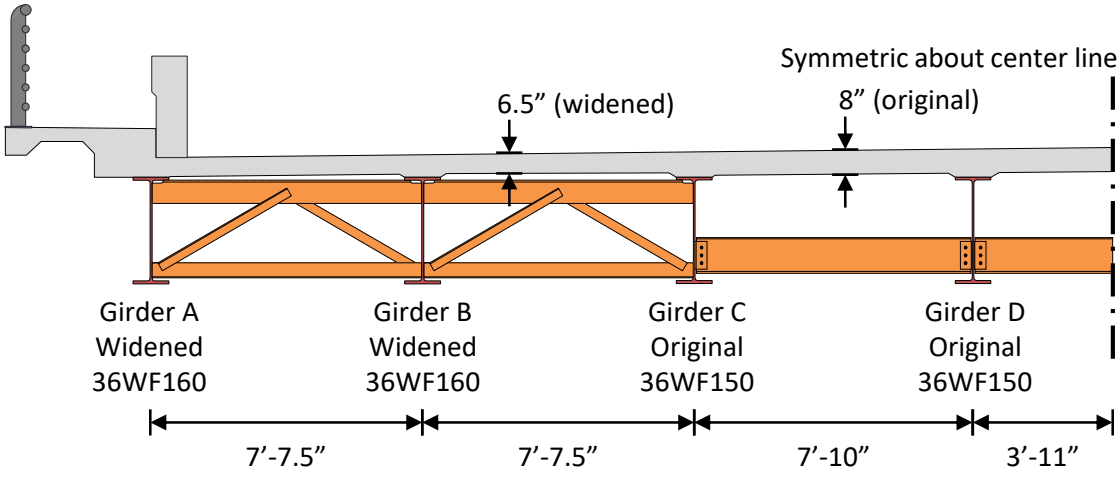

Figure D-1: Cross Section View of Bridge

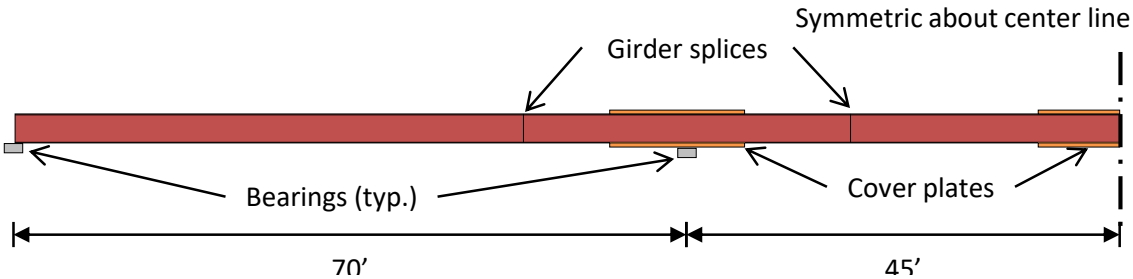

Figure D-2: Half-Elevation View of Typical Girder

D.1.2 General Design Information

The majority of the strength calculations and analyses are conducted using the load factor design method in the *Standard Specifications for Highway Bridges* (AASHTO 2002). All table, section, and equation references also refer to this document, unless otherwise specified. Although this is not the current design specification in the United States, it is often common practice to use the Standard specifications to evaluate bridges that were designed using those specifications.

However, the moment redistribution and fatigue provisions are taken from the *LRFD Bridge Design Specifications* for this example (AASHTO 2010). The moment redistribution provisions in the LRFD specifications are much simpler to use and apply to a wider range of geometries than those in the Standard specifications. Additionally, the fatigue design is conducted using the LRFD specifications to more accurately reflect the effect of realistic truck traffic at the time of the strengthening design.

Note that this design example is focused on the flexural strength of the non-composite and partially composite girders as well as the fatigue strength of the post-installed shear connectors. Although it is not explicitly shown here, a full strengthening design would consider all possible limit states for all members of the bridge. This includes but is not limited to the following:

- Shear strength of the steel beams
- Strength of the substructure and foundations
- Strength of the approach spans

The following material properties are used in these calculations. Because these properties were not directly specified on the available design drawings, the values used here are based on typical materials used at the time of construction and recommendations in the *Manual for Bridge Evaluation* (AASHTO 2011):

- Yield stress of steel beams, $F_y = 33\ ksi$ (ASTM A7 steel)
- Elastic modulus of steel beams, $E_s = 29000\ ksi$
- 28-day compressive strength of concrete deck, $f_c' = 3\ ksi$
- Elastic modulus of concrete deck,

$$E_c(ksi) = 57\sqrt{f'c\ (psi)} = 57\sqrt{3000\ psi} = 3222\ ksi$$

D.1.3 Scope of Design Example

Detailed design calculations and discussion are provided here for Girder B. A summary of the results for the other three girders are also provided in less detail, as the process is nearly identical.

The general process for the design is as follows: (1) conduct structural analysis, (2) evaluate existing non-composite structure, (3) set strengthening targets, (4) check negative moment regions and redistribute moments as necessary, (5) design connectors for strength requirements in positive moment regions, and (6) locate connectors and check fatigue.

D.2 Detailed Design of Girder B

A half-elevation view of Girder B, which is equivalent to Girder A, is shown in Figure D-3. This girder was added as part of the widening of the bridge in 1961. It is constructed of a 36WF160 rolled steel shape, with cover plates welded to the top and bottom flange at the interior pier and in the middle of the interior span. Table D-1 summarizes the section properties for design for the steel beam (Section 1), as well as for the steel beam with cover plates at the interior pier (Section 2) and in the interior span (Section 3).

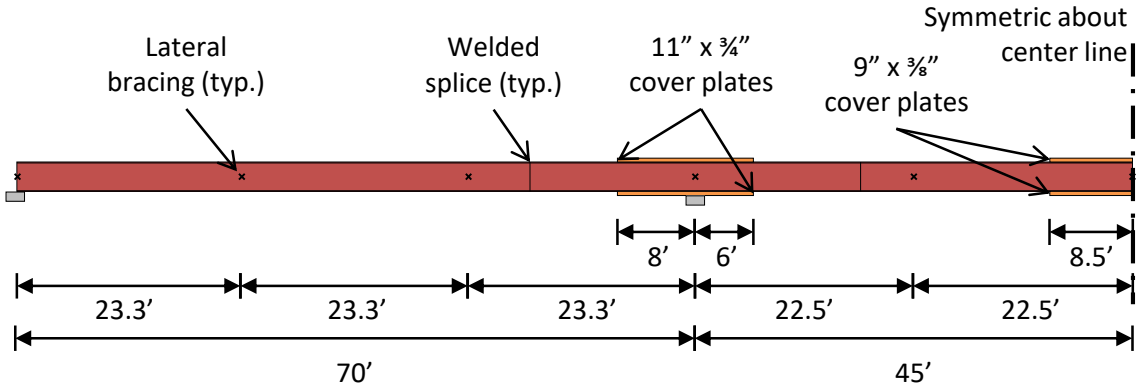

Figure D-3: Half-Elevation View of Girders A and B

Table D-1: Section Properties for Girders A and B

	Section 1	Section 2	Section 3
Cover plate width (b_{pl}, in)	0	11.0	9.00
Cover plate thickness (t_{pl}, in)	0	0.750	0.375
Flange width (b_f, in)	12.0	12.0	12.0
Flange thickness (t_f, in)	1.02	1.02	1.02
Flange area (A_f, in^2)	12.2	20.5	15.6
Flange moment of inertia (I_{yc}, in^4)	147	230	170
Total depth (d, in)	36.0	37.5	36.8
Web thickness (t_w, in)	0.650	0.650	0.650
Area (A_s, in^2)	47.0	63.5	53.8
Moment of inertia (I_x, in^4)	9760	15300	12000
Elastic section modulus (S_x, in^3)	542	818	653
Plastic section modulus (Z_x, in^3)	624	927	747
Radius of gyration (r_y, in)	2.51	2.70	2.52
Polar moment of inertia (J, in^4)	12.4	15.5	12.7
Web depth (D, in)	34.0	34.0	34.0
Depth of web in compression, elastic (D_c, in)	17.0	17.0	17.0
Depth of web in compression, plastic (D_{cp}, in)	17.0	17.0	17.0
Effective deck width (b_{deck}, in) and girder spacing (S, in)	91.5	91.5	91.5
Deck thickness (t_{deck}, in)	6.5	6.5	6.5
Deck area (A_{deck}, in^2)	595	595	595
Deck moment of inertia (I_{deck}, in^4)	2090	2090	2090

D.2.1 Conduct Structural Analysis

The structural analysis was done using a line girder analysis with the software BAR7. This software, which is commonly used for load rating of bridges, outputs the unfactored dead and live load moments, given the geometry of a given bridge girder, the

magnitude of the live load, and the appropriate distribution factor. The load factor design and rating procedures are used in this example, so an HS 20 live load was chosen for the analysis.

The dead load was taken as the self-weight of the girder (including cover plates), the self-weight of the deck, the weight of a 4-inch asphalt overlay, and a portion of the curb, sidewalk, and railing weights. The tributary area for the deck and overlay was taken as half of the distance to the adjacent girders, and the overlay was assumed to contribute a load of 12 psf per inch of thickness. The weight of the curb, sidewalk, and railings was even distributed over all of the girders, according to the recommendation in Section 3.23.2.3.1.1.

The vehicular live load used in the analysis was an HS 20 load, which is the target load rating for the bridge after strengthening. The distribution factor for moment, is calculated as follows. Note that this calculated distribution factor represents the fraction of a wheel line of the design truck that is distributed to the girder of interest. The software BAR7 defines the distribution factor as the fraction of the total design truck distributed to the girder of interest. Thus, the distribution factor entered into the software is one-half of this calculated value:

$$DF = \frac{S}{5.5} = \frac{(91.5\ in)\left(\frac{1\ ft}{12\ in}\right)}{5.5} = 1.39$$ *Table 3.23.1*

The unfactored dead load moments and live load moment envelope are plotted in Figure D-4. Table D-2 indicates the values of these moments at the critical sections of the girder. The critical sections for flexural strength are at the points of maximum positive moment near the center of each span, at the points of maximum negative moment at the centerline of each interior support, and at the points of section transitions, which only occur on this girder at the termination of the cover plates. The moments at the lateral brace points in the unbraced lengths adjacent to the interior pier are also given in the table. Recall that because of symmetry, only one-half of the girder is analyzed here. Each section is denoted by its location relative to the end of the continuous steel unit. Thus, the section at the centerline of the interior pier is denoted as 70'.

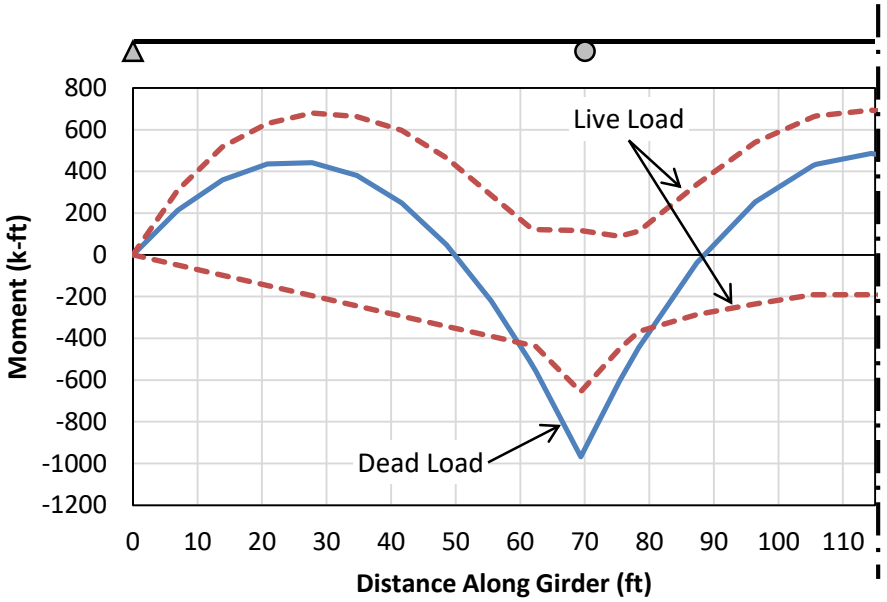

Figure D-4: Plot of Unfactored Moments for Girder B

Table D-2: Unfactored Moments at Critical Sections and at Lateral Brace Locations around the Interior Pier Section in Girder B

Location (ft)	Section Type	Section Number	Unfactored Moment (k-ft)		
			Dead Load	Live Load	
				Pos.	Neg.
28	Critical, Span	1	442	679	-195
46.7	Lateral Brace	1	121	514	-324
62	Critical, Transition	1	-503	136	-432
70	Critical, Pier Lateral Brace	2	-967	116	-657
76	Critical, Transition	1	-606	89	-452
92.5	Lateral Brace	1	108	439	-261
106.5	Critical, Transition	1	434	666	-191
115	Critical, Span	3	486	694	-191

D.2.2 Evaluate Existing Non-Composite Girder

The evaluation of the non-composite girder is done through a load rating at the critical sections listed in Table D-2 using the Load Factor Rating method. The rating factor (RF) is calculated using the following equation:

$$RF = \frac{C - A_1\, DL}{A_2(LL + I)}$$

MBE Equation 6B.4.1-1

where C represents the capacity of the section, DL is the dead load force effect, $LL + I$ is the live load force effect including the dynamic impact factor, and A_1 and A_2 are constants depending on the type of rating and the limit state considered.

This rating factor represents the fraction of the live load applied during the structural analysis that can be safely resisted by the girder, which in this case is an HS 20 live load. The corresponding load factor rating (RT) is determined by multiply the rating factor by the magnitude of the live load used in the analysis in tons, which in this case is 20.

$$RT = (RF)(W) = (RF)(20)$$

MBE Equation 6B.4.1-2

Both the Overload and Maximum Load limit states are considered here. The values of the coefficients A_1 and A_2 for an inventory-level rating for the two limit states are as follows:

$$Overload: \quad A_1 = 1.0; \quad A_2 = 1.67$$

$$Maximum\ Load: \quad A_1 = 1.3; \quad A_2 = 2.17$$

MBE Equation 6B.4.3

The capacity at the Overload limit state is based on a limiting value for the stresses in the steel beam. Because the entire girder is non-composite at this point, the stress in the extreme fiber of the steel beam is limited to 80% of the yield stress. This is equivalent to limiting the moment to 80% of the yield moment (M_y) because all of the stresses are carried by the non-composite section. Thus, in general, the flexural capacity at the Overload limit state (C_{OL}) is:

$$C_{OL} = 0.80\, M_y = 0.80\, S_x\, F_y$$

Section 10.57.1

The capacity at the Maximum Load limit state (C_{ML}) is the smaller of the local buckling capacity, lateral-torsional buckling capacity, and the plastic moment of the section, as defined in Section 10.48. The following calculations determine the capacity at both the Overload and Maximum Load limit states for the critical sections listed in Table D-2:

Critical Location at 28' (Section #1)

The Overload capacity is calculated as:

$$C_{OL\,28'} = 0.80\,S_x\,F_y = 0.80(542\ in^3)(33\ ksi)\left(\frac{1\ ft}{12\ in}\right) = 1190\ k.ft$$

To calculate the Maximum Load capacity, the compression (top) flange can be considered to be continuously braced by the deck so that lateral-torsional buckling will not control the strength. Thus, the steel section is classified as compact if:

$$\frac{b_f}{t_f} \le \frac{4{,}100}{\sqrt{F_y}} \rightarrow \frac{12.0\ in}{1.02\ in} \le \frac{4{,}100}{\sqrt{33{,}000\ psi}} \rightarrow 11.8 \le 22.6 \qquad \textit{Equation 10-93}$$

$$\rightarrow \textit{compression flange is compact}$$

$$\frac{D}{t_w} \le \frac{19{,}230}{\sqrt{F_y}} \rightarrow \frac{34.0\ in}{0.650\ in} \le \frac{19{,}230}{\sqrt{33{,}000\ psi}} \rightarrow 52.3 \qquad \textit{Equation 10-94}$$

$$\le 106 \rightarrow \textit{web is compact}$$

This section qualifies as a compact section, so the flexural strength is defined as the plastic moment of the section. The Maximum Load capacity is:

$$C_{ML\,28'} = Z_x\,F_y = (624\ in^3)(33\ ksi)\left(\frac{1\ ft}{12\ in}\right) = 1720\ k.ft \qquad \textit{Section 10.48.1}$$

The rating factor and load rating for the Overload and Maximum Load limit states for this critical location are:

$$RF_{OL\,28'} = \frac{1190\ k.ft - (1.0)(442\ k.ft)}{(1.67)(679\ k.ft)} = 0.660$$

$$RT_{OL\ 28'} = (0.660)(20) = 13.2 \quad \rightarrow \quad HS\ 13.2$$

$$RF_{ML\ 28'} = \frac{1720\ k.ft - (1.3)(442\ k.ft)}{(2.17)(679\ k.ft)} = 0.777$$

$$RT_{ML\ 28'} = (0.777)(20) = 15.5 \quad \rightarrow \quad HS\ 15.5$$

Critical Location at 62' (Section #1)

The Overload capacity is equivalent to that at 28', although it will be given a negative sign since this location is dominated by negative flexure:

$$C_{OL\ 62'} = -1190\ k.ft$$

The unbraced length (L_b) for the compression (bottom) flange is 23.3 feet, or 280 inches. The steel section is the same as that at 28', so the compression flange and web meet the compact limits. Thus, the steel section is classified as compact if:

$$\frac{L_b}{r_y} \leq \frac{\left[3.6 - 2.2\left(\frac{M_1}{M_p}\right)\right] x10^3}{F_y} \qquad \textit{Equation 10-96}$$

$$M_1 = (1.3)(121\ k.ft) + (2.17)(-324\ k.ft) = -546\ k.ft$$

$$M_p = -Z_{x\ 70'}\ F_y = (927\ k.ft)(33\ ksi)\left(\frac{1\ ft}{12\ in}\right) = -2550\ k.ft$$

$$\rightarrow \quad \frac{280\ in}{2.51\ in} \leq \frac{\left[3.6 - 2.2\left(\frac{-546\ k.ft}{-2550\ k.ft}\right)\right] x10^3}{33\ ksi} \quad \rightarrow \quad 111 \not\leq 94.8$$

$$\rightarrow \quad LTB\ not\ OK$$

In the above equation for the lateral-torsional buckling check, M_1 is the smaller of the brace moments and M_p is the plastic moment capacity at the other brace point. The

ratio of M_1 to M_p is taken as positive if the factored moments cause single curvature within the unbraced length, which is the case here.

Because the unbraced length is too large, the section is not compact. The steel section is classified as a braced noncompact section if the following equation is true. Note that because the compression flange and web are known to meet the compact limits, only the lateral-torsional buckling check needs to be done here:

$$L_b \leq \frac{20{,}000 A_f}{F_y\, d} \quad \rightarrow \quad 280\ in \leq \frac{20{,}000(12.2\ in^2)}{(33\ ksi)(36.0\ in)}$$

$$\rightarrow \quad 280\ in \not\leq 205\ in \quad \rightarrow \quad LTB\ not\ OK$$

Equation 10-101

Again, because the unbraced length is too large, the section does not qualify as a braced noncompact section. Thus, it is a partially braced member, and the capacity is calculated as follows:

$$C_{ML\,62'} = -M_r R_b$$

Equation 10-103a

$$M_r = (91\ x\ 10^3) C_b \left(\frac{I_{yc}}{L_b}\right) \sqrt{0.772 \frac{J}{I_{yc}} + 9.87 \left(\frac{d}{L_b}\right)^2} \leq M_y$$

Equation 10-103c

$$C_b = 1.75 + 1.05\left(-\frac{M_1}{M_2}\right) + 0.3\left(-\frac{M_1}{M_2}\right)^2 \leq 2.3$$

$$M_1 = (1.3)(121\ k.ft) + (2.17)(-324\ k.ft) = -546\ k.ft$$

$$M_2 = (1.3)(-967\ k.ft) + (2.17)(-657\ k.ft) = -2680\ k.ft$$

$$C_b = 1.75 + 1.05\left(-\frac{-546\ k.ft}{-2680\ k.ft}\right) + 0.3\left(-\frac{-546\ k.ft}{-2680\ k.ft}\right)^2 = 1.55$$

$$M_y = S_x F_y = (542\ in^3)(33\ ksi)\left(\frac{1\ ft}{12\ in}\right) = 1490\ k.ft$$

$$M_r = (91x10^3)(1.55)\left(\frac{147\ in^4}{280\ in}\right)\sqrt{0.772\left(\frac{12.4\ in^4}{147\ in^4}\right) + 9.87\left(\frac{36.0\ in}{280\ in}\right)^2}$$

$$= 35400\ k.in\left(\frac{1\ ft}{12\ in}\right) = 2950\ k.ft \nleq M_y \quad \rightarrow \quad M_r$$

$$= 1490\ k.ft$$

$$R_b = 1 - 0.002\left(\frac{D_c\ t_w}{A_f}\right)\left[\frac{D_c}{t_w} - \frac{\lambda}{\sqrt{\frac{M_r}{S_x}}}\right] \leq 1.0$$

$$= 1 - 0.002\frac{(17.0\ in)(0.650\ in)}{12.2\ in^2}\left[\frac{17.0\ in}{0.650\ in} - \frac{15{,}400}{\sqrt{33{,}000\ psi}}\right]$$

$$= 1.11 \nleq 1.0 \quad \rightarrow \quad R_b = 1.0$$

$$C_{ML\ 62'} = -(1490\ k.ft)(1.0) = -1490\ k.ft$$

Note that because M_r is equal to M_y, the ratio of M_r to S_x under the square root in the equation for R_b is simply equal to F_y. In the equation for C_b, M_1 and M_2 are the smaller and larger of the factored brace point moments, respectively. The ratio of M_1 to M_2 is taken as negative if the moments cause single curvature, which is the case here.

The rating factor and load rating for the Overload and Maximum Load limit states for this critical location are:

$$RF_{OL\ 62'} = \frac{-1190\ k.ft - (1.0)(-503\ k.ft)}{(1.67)(-432\ k.ft)} = 0.952$$

$$RT_{OL\ 62'} = (0.952)(20) = 19.0 \quad \rightarrow \quad HS\ 19.0$$

$$RF_{ML\ 62'} = \frac{-1490\ k.ft - (1.3)(-503\ k.ft)}{(2.17)(-432\ k.ft)} = 0.892$$

$$RT_{ML\ 62'} = (0.892)(20) = 17.8 \quad \rightarrow \quad HS\ 17.8$$

Critical Location at 70' (Section #2)

The Overload capacity is calculated as:

$$C_{OL\,70'} = -0.80\,S_x\,F_y = 0.80(818\,in^3)(33\,ksi)\left(\frac{1\,ft}{12\,in}\right) = -1800\,k.ft$$

Because there is a cross frame at this location, the unbraced lengths on both sides of this critical location need to be checked. The unbraced length (L_b) for the compression (bottom) flange is 23.3 feet, or 280 inches, in the direction of the exterior span and 22.5 feet, or 270 inches, in the direction of the interior span. However, from the calculations at 62', it is already known that the unbraced length adjacent to the interior pier in the exterior span is classified as a partially braced member, so the compact and braced noncompact checks do not need to be made here. The capacity for a partially braced member is calculated for the unbraced lengths on either side of the interior pier are:

$$C_{ML\,70'} = -M_r R_b \qquad \textit{Equation 10-103a}$$

$$M_r = (91\,x\,10^3)C_b\left(\frac{I_{yc}}{L_b}\right)\sqrt{0.772\frac{J}{I_{yc}} + 9.87\left(\frac{d}{L_b}\right)^2} \leq M_y \qquad \textit{Equation 10-103c}$$

$$C_b = 1.75 + 1.05\left(-\frac{M_1}{M_2}\right) + 0.3\left(-\frac{M_1}{M_2}\right)^2 \leq 2.3$$

$$M_{1\,ext} = -546\,k.ft$$

$$M_{1\,int} = (1.3)(108\,k.ft) + (2.17)(-261\,k.ft) = -426\,k.ft$$

$$M_2 = -2680\,k.ft$$

$$C_{b\,ext} = 1.55$$

$$C_{b\,int} = 1.75 + 1.05\left(-\frac{-426\ k.ft}{-2680\ k.ft}\right) + 0.3\left(-\frac{-426\ k.ft}{-2680\ k.ft}\right)^2 = 1.59$$

$$M_y = S_x F_y = (818\ in^3)(33\ ksi)\left(\frac{1\ ft}{12\ in}\right) = 2250\ k.ft$$

$$M_{r\,ext} = (91x10^3)(1.55)\left(\frac{230\ in^4}{280\ in}\right)\sqrt{0.772\left(\frac{15.5\ in^4}{230\ in^4}\right) + 9.87\left(\frac{36.0\ in}{280\ in}\right)^2}$$
$$= 57300\ k.in\left(\frac{1\ ft}{12\ in}\right) = 4480\ k.ft \not\leq M_y \quad \rightarrow \quad M_{r\,ext}$$
$$= 2250\ k.ft$$

$$M_{r\,int} = (91x10^3)(1.59)\left(\frac{230\ in^4}{270\ in}\right)\sqrt{0.772\left(\frac{15.5\ in^4}{230\ in^4}\right) + 9.87\left(\frac{36.0\ in}{270\ in}\right)^2}$$
$$= 58800\ k.in\left(\frac{1\ ft}{12\ in}\right) = 4900\ k.ft \not\leq M_y \quad \rightarrow \quad M_{r\,int}$$
$$= 2250\ k.ft$$

$$R_b = 1 - 0.002\left(\frac{D_c\ t_w}{A_f}\right)\left[\frac{D_c}{t_w} - \frac{\lambda}{\sqrt{\frac{M_r}{S_x}}}\right] \leq 1.0$$
$$= 1 - 0.002\,\frac{(17.0\ in)(0.650\ in)}{20.5\ in^2}\left[\frac{17.0\ in}{0.650\ in} - \frac{15{,}400}{\sqrt{33{,}000\ psi}}\right]$$
$$= 1.06 \not\leq 1.0 \quad \rightarrow \quad R_b = 1.0$$

$$C_{ML\,70'} = -(2250\ k.ft)(1.0) = -2250\ k.ft$$

The rating factor and load rating for the Overload and Maximum Load limit states for this critical location are:

$$RF_{OL\,70'} = \frac{-1800\ k.ft - (1.0)(-967\ k.ft)}{(1.67)(-657\ k.ft)} = 0.759$$

$$RT_{OL\,70'} = (0.759)(20) = 15.2 \quad \rightarrow \quad HS\ 15.2$$

$$RF_{ML\,70'} = \frac{-2250\ k.ft - (1.3)(-967\ k.ft)}{(2.17)(-657\ k.ft)} = 0.696$$

$$RT_{ML\,70'} = (0.696)(20) = 13.9 \quad \rightarrow \quad HS\ 13.9$$

Critical Location at 76' (Section #1)

The Overload capacity is equivalent to that at 62':

$$C_{OL\,76'} = -1190\ k.ft$$

The unbraced length (L_b) for the compression (bottom) flange is 22.5 feet, or 270 inches. The steel section is the same as that at 28' and 62', so the compression flange and web meet the compact limits. Some calculations for the unbraced length were conducted previously for the critical location at 70' and will not be repeated in detail here. The steel section is classified as compact if:

$$\frac{L_b}{r_y} \leq \frac{\left[3.6 - 2.2\left(\frac{M_1}{M_p}\right)\right] x10^3}{F_y} \qquad \textit{Equation 10-96}$$

$$M_1 = -426\ k.ft$$

$$M_p = -Z_{x\,70'}\ F_y = (927\ k.ft)(33\ ksi)\left(\frac{1\ ft}{12\ in}\right) = -2550\ k.ft$$

$$\rightarrow \quad \frac{270\ in}{2.51\ in} \leq \frac{\left[3.6 - 2.2\left(\frac{-426\ k.ft}{-2550\ k.ft}\right)\right] x10^3}{33\ ksi} \quad \rightarrow \quad 108 \not\leq 98.0$$

$$\rightarrow \quad LTB\ not\ OK$$

Because the unbraced length is too large, the section is not compact. Because the compression flange and web already satisfy the compact limits, the steel section is classified as a braced noncompact section if:

$$L_b \leq \frac{20{,}000 A_f}{F_y\, d} \quad \rightarrow \quad 270\ in \leq \frac{20{,}000(12.2\ in^2)}{(33\ ksi)(36.0\ in)} \qquad \textit{Equation 10-101}$$

$$\rightarrow \quad 270\ in \not\leq 205\ in \quad \rightarrow \quad LTB\ not\ OK$$

Again, because the unbraced length is too large, the section does not qualify as a braced noncompact section. Thus, it is a partially braced member, and the capacity is calculated as follows:

$$C_{ML\ 76'} = -M_r R_b \qquad \textit{Equation 10-103a}$$

$$M_r = (91\ x\ 10^3) C_b \left(\frac{I_{yc}}{L_b}\right) \sqrt{0.772 \frac{J}{I_{yc}} + 9.87 \left(\frac{d}{L_b}\right)^2} \leq M_y \qquad \textit{Equation 10-103c}$$

$$C_b = 1.59$$

$$M_y = S_x F_y = (542\ in^3)(33\ ksi)\left(\frac{1\ ft}{12\ in}\right) = 1490\ k.ft$$

$$M_r = (91x10^3)(1.59)\left(\frac{147\ in^4}{270\ in}\right)\sqrt{0.772\left(\frac{12.4\ in^4}{147\ in^4}\right) + 9.87\left(\frac{36.0\ in}{270\ in}\right)^2}$$

$$= 38600\ k.in\left(\frac{1\ ft}{12\ in}\right) = 3220\ k.ft \not\leq M_y \quad \rightarrow \quad M_r$$

$$= 1490\ k.ft$$

$$R_b = 1 - 0.002\left(\frac{D_c\ t_w}{A_f}\right)\left[\frac{D_c}{t_w} - \frac{\lambda}{\sqrt{\frac{M_r}{S_x}}}\right] \leq 1.0$$

$$= 1 - 0.002\frac{(17.0\ in)(0.650\ in)}{12.2\ in^2}\left[\frac{17.0\ in}{0.650\ in} - \frac{15{,}400}{\sqrt{33{,}000\ psi}}\right]$$

$$= 1.11 \nleq 1.0 \quad \rightarrow \quad R_b = 1.0$$

$$C_{ML\ 76'} = -(1490\ k.ft)(1.0) = -1490\ k.ft$$

The rating factor and load rating for the Overload and Maximum Load limit states for this critical location are:

$$RF_{OL\ 76'} = \frac{-1190\ k.ft - (1.0)(-606\ k.ft)}{(1.67)(-452\ k.ft)} = 0.774$$

$$RT_{OL\ 76'} = (0.774)(20) = 15.5 \quad \rightarrow \quad HS\ 15.5$$

$$RF_{ML\ 76'} = \frac{-1490\ k.ft - (1.3)(-606\ k.ft)}{(2.17)(-452\ k.ft)} = 0.716$$

$$RT_{ML\ 76'} = (0.716)(20) = 14.3 \quad \rightarrow \quad HS\ 14.3$$

Critical Location at 106.5' (Section #1)

The Overload capacity is equivalent to that at 28':

$$C_{OL\ 106.5'} = 1190\ k.ft$$

To calculate the Maximum Load capacity, the compression flange and web have already been shown to meet the compact limits. Additionally, the compression (top) flange can be considered to be continuously braced by the deck so that lateral-torsional buckling will not control the strength. Thus, the steel section is classified as compact and the capacity is:

$$C_{ML\ 106.5'} = Z_x\ F_y = (624\ in^3)(33\ ksi)\left(\frac{1\ ft}{12\ in}\right) = 1720\ k.ft$$ *Section 10.48.1*

The rating factor and load rating for the Overload and Maximum Load limit states for this critical location are:

$$RF_{OL\ 106.5'} = \frac{1190\ k.ft - (1.0)(434\ k.ft)}{(1.67)(666\ k.ft)} = 0.680$$

$$RT_{OL\ 106.5'} = (0.680)(20) = 13.6 \quad \rightarrow \quad HS\ 13.6$$

$$RF_{ML\ 106.5'} = \frac{1720\ k.ft - (1.3)(434\ k.ft)}{(2.17)(666\ k.ft)} = 0.800$$

$$RT_{ML\ 106.5'} = (0.800)(20) = 16.0 \quad \rightarrow \quad HS\ 16.0$$

Critical Location at 115' (Section #3)

The Overload capacity is calculated as:

$$C_{OL\ 115'} = 0.80\ S_x\ F_y = 0.80(653\ in^3)(33\ ksi)\left(\frac{1\ ft}{12\ in}\right) = 1440\ k.ft$$

To calculate the Maximum Load capacity, the compression flange and web have already been shown to meet the compact limits. Additionally, the compression (top) flange can be considered to be continuously braced by the deck so that lateral-torsional buckling will not control the strength. Thus, the steel section is classified as compact and the capacity is:

$$C_{ML\ 115'} = Z_x\ F_y = (747\ in^3)(33\ ksi)\left(\frac{1\ ft}{12\ in}\right) = 2050\ k.ft$$ *Section 10.48.1*

The rating factor and load rating for the Overload and Maximum Load limit states for this critical location are:

$$RF_{OL\ 115'} = \frac{1440\ k.ft - (1.0)(486\ k.ft)}{(1.67)(694\ k.ft)} = 0.823$$

$$RT_{OL\ 115'} = (0.823)(20) = 16.5 \quad \rightarrow \quad HS\ 16.5$$

$$RF_{ML\ 115'} = \frac{2050\ k.ft - (1.3)(486\ k.ft)}{(2.17)(694\ k.ft)} = 0.942$$

$$RT_{ML\ 115'} = (0.942)(20) = 18.8 \quad \rightarrow \quad HS\ 18.8$$

Summary of Load Rating of Existing Non-Composite Girder

Table D-3 summarizes the results of the load rating calculations for the existing girder at the critical locations from Table D-2. The controlling load rating is HS 13.2, which occurs at the Overload limit state at the critical section at the maximum positive moment in the exterior span (28').

Table D-3: Load Rating Results of Existing Non-Composite Girder B

Location (ft)	Section Type	Capacity (k-ft)		Inventory Load Rating	
		Overload	Maximum Load	Overload	Maximum Load
28	Critical, Span	1190	1720	HS 13.2	HS 15.5
62	Critical, Transition	-1190	-1490	HS 19.0	HS 17.8
70	Critical, Pier	-1800	-2250	HS 15.2	HS 13.9
76	Critical, Transition	-1190	-1490	HS 15.5	HS 14.3
106.5	Critical, Transition	1190	1720	HS 13.6	HS 16.0
115	Critical, Span	1440	2050	HS 16.5	HS 18.8

D.2.3 Set Strengthening Targets

The bridge owner would like to ***increase the inventory load factor rating to HS 20***, which corresponds to the minimum strength of a new bridge designed using the Standard specifications. At a minimum, a ***remaining life of 25 years*** is desired for the

purposes of fatigue design of the post-installed shear connectors. It is expected that an ***average annual daily truck traffic ($(ADTT)_{SL}$) of 1160 trucks per day*** will cross the bridge over the next 25 years.

D.2.4 Check Negative Moment Regions and Redistribute Moments

To start the strengthening process, first the strength of the negative moment regions at the interior piers (70') is evaluated and compared to the factored moments (M_u) to determine whether or not moment redistribution is necessary. As with the evaluation of the existing girder, both the Overload and Maximum Load limit states are considered here. The factored moments for these limit states are as follows, where DL is the dead load force effect and $LL + I$ is the live load force effect, including the dynamic impact factor:

$$M_{u\,OL} = 1.0DL + (1.67)(LL + I)$$
$$= 1.0(-967\ k.ft) + (1.67)(-657\ k.ft)$$
$$= -2060\ k.ft$$

Section 10.57

$$M_{u\,ML} = 1.3DL + 2.17(LL + I)$$
$$= 1.3(-967\ k.ft) + 2.17(-657\ k.ft)$$
$$= -2680\ k.ft$$

Table 3.22.1A

If the factored moment at the interior pier exceeds the capacity of the section at that interior pier, moment redistribution can be considered to increase the load rating at that location. The capacity at both limit states was calculated during the evaluation of the existing non-composite girder:

$$C_{OL\,70'} = -1800\ k.ft$$

$$C_{ML\,70'} = -2250\ k.ft$$

The magnitude of the factored moments exceed the calculated capacities at the interior pier section (70') for both the Overload (2060 k-ft > 1800 k-ft) and Maximum Load (2680 k-ft > 2250 k-ft) limit states. This means that ***moment redistribution should be considered at both limit states***.

The findings of this research recommend using the simple, rational moment redistribution provisions from Appendix B6 of the LRFD specifications, rather than the provisions that cover moment redistribution in the Standard specifications. The provisions in the LRFD specifications are much simpler to use and apply to a wider range of cases than those in the Standard specifications, based on research done in the mid-1990s (Barth et al. 2004). The following requirements are given in Section B6.2 of the LRFD specifications, and must be satisfied to allow for moment redistribution:

1. The bridge must be straight with supports not skewed more than 10° $\rightarrow$ OK
2. The specified minimum yield stress does not exceed 70 ksi $\rightarrow$ OK
3. Holes in the tension flange may not be present within a distance of twice the web depth from each interior pier section from which moments are redistributed $\rightarrow$ OK
4. The web proportions cannot violate the following requirements:
   $\frac{D}{t_w} \leq 150 \rightarrow \frac{34.0\ in}{0.650\ in} \leq 150 \rightarrow 52.3 \leq 150 \rightarrow OK$
   $\frac{2D_c}{t_w} \leq 6.8\sqrt{\frac{E}{F_y}} \rightarrow \frac{2(17.0\ in)}{0.650\ in} \leq 6.8\sqrt{\frac{29000\ ksi}{33\ ksi}} \rightarrow 52.3 \leq 202 \rightarrow OK$
   $D_{cp} \leq 0.75D \rightarrow 17.0\ in \leq 0.75(34.0\ in) \rightarrow 17.0\ in \leq 25.5\ in \rightarrow OK$
5. The compression flange proportions cannot violate the following requirements, the first of which ensures that the flange is compact:
   $\frac{b_f}{2t_f} \leq 0.38\sqrt{\frac{E}{F_y}} \rightarrow \frac{12.0\ in}{2(1.02\ in)} \leq 0.38\sqrt{\frac{29000\ ksi}{33\ ksi}} \rightarrow 5.88 \leq 11.3 \rightarrow OK$
   $b_f \geq \frac{D}{4.25} \rightarrow 12.0\ in \geq \frac{34.0\ in}{4.25} \rightarrow 12.0\ in \geq 8\ in \rightarrow OK$
   Note that the flange proportions here are checked without considering the contributions of the cover plates. Engineering judgement can be used to include any contribution from the cover plates, if desired.
6. The compression flange must be adequately braced to prevent lateral-torsional buckling and allow the section to achieve enough plastic rotation to adequately redistribute moments:
   $L_b \leq \left[0.1 - 0.06\left(\frac{M_1}{M_2}\right)\right]\frac{r_t E}{F_y}$

The cover plate terminates within the unbraced length, so that two different sets of section properties are valid within the unbraced lengths in question. To be conservative, the section properties of the smaller section (Section #1) are used. The effective radius of gyration for lateral-torsional buckling is defined in Appendix A6 of the LRFD specifications (Equation A6.3.3-10), and is calculated for Section #1 as:

$$r_t = \frac{b_f}{\sqrt{12\left(1 + \frac{1}{3}\frac{D_c t_w}{b_f t_f}\right)}} = \frac{12.0\ in}{\sqrt{12\left(1 + \frac{1}{3}\frac{(17.0\ in)(0.650\ in)}{(12.0\ in)(1.02\ in)}\right)}} = 3.04\ in$$

Because both the unbraced length and the brace point moments are different on either side of the interior pier, both must be checked at the Overload and Maximum Load limit states. However, because the load factors for the Maximum Load limit state are exactly 30% greater than those for the Overload limit state, the ratio of the factored brace moments (M_1 and M_2) will be the same for both limit states. Thus, only the Maximum Load limit state will be used here.

$$L_{b\,ext} \leq \left[0.1 - 0.06\left(\frac{1.3(121\ k.ft) + (2.17)(-324\ k.ft)}{1.3(-967\ k.ft) + (2.17)(-657\ k.ft)}\right)\right]\frac{(3.04\ in)(29000\ ksi)}{33\ ksi}$$

$$= (235\ in)\left(\frac{1\ ft}{12\ in}\right) = 19.5\ ft$$

$$L_{b\,int} \leq \left[0.1 - 0.06\left(\frac{1.3(108\ k.ft) + (2.17)(-261\ k.ft)}{1.3(-967\ k.ft) + (2.17)(-657\ k.ft)}\right)\right]\frac{(3.04\ in)(29000\ ksi)}{33\ ksi}$$

$$= (242\ in)\left(\frac{1\ ft}{12\ in}\right) = 20.1\ ft$$

In the above calculations, M_1 is the smaller of the brace point moments, while M_2 is the larger of the brace point moments. The ratio of M_1 to M_2 is taken as a positive value if the factored moments cause single curvature within the unbraced length, which is the case here.

The actual unbraced lengths exceed these calculated limiting values:

$L_{b\,ext} = 23.3\,ft > 19.5\,ft \;\rightarrow\; NOT\ OK$

$L_{b\,int} = 22.5\,ft > 20.1\,ft \;\rightarrow\; NOT\ OK$

Thus, the existing cross frames do not provide adequate lateral bracing to allow for moment redistribution. To redistribute moments in this girder, ***additional cross frames must be added on either side of the interior pier to reduce the unbraced length***. These cross frames must be located such that they reduce the unbraced length so that this requirement is satisfied.

In this design, the cross frames will be added at 10 feet from the interior pier in the exterior span and at 10.5 feet from the interior pier in the interior span. These locations are chosen to match the existing cross frame locations on Girders C and D, which are different from those in Girders A and B because they were constructed at different times. Repeating the calculations for the limiting unbraced lengths using the new brace point moments, shown later in Table D-4, shows that the new unbraced lengths satisfy the lateral bracing requirements:

$L_{b\,ext} = 10.0\,ft < 15.1\,ft \;\rightarrow\; OK$

$L_{b\,int} = 10.5\,ft < 16.0\,ft \;\rightarrow\; OK$

7. There shall be no section transitions within the unbraced length of the interior pier section $\rightarrow\ NOT\ OK$

   Because the cover plates at the interior pier terminate within the adjacent unbraced lengths from the pier, this requirement is not satisfied. Although the exact reason for this requirement is unclear in the specification, it is likely there for a few reasons, which are discussed here.

   Firstly, if the section changes within the unbraced length, it is unclear which section properties should be used to check the lateral-torsional buckling capacity within that unbraced length. To be conservative, the properties of the smallest section within the unbraced length are used here (see number 6 on this list).

   Secondly, the moment redistribution provisions are based on the assumption that the critical section for negative flexure is at the centerline of the interior pier. If there is a section transition near the interior pier, that location could be the critical location for negative flexure instead. This means that the location of the section transition might reach its capacity first, and moments would be redistributed from that location instead of from the centerline of

the interior pier. However, when evaluating the existing bridge, it was found that the load rating was in fact controlled by the section at the centerline of the interior pier, rather than at the ends of the cover plates, indicating that this will not be a concern for this bridge.

Finally, and most importantly, the LRFD specifications eliminate the requirements to satisfy flexural stress checks at the Overload limit state within the entire negative moment region as well as flexural capacity checks at the Maximum Load limit state within the unbraced lengths adjacent to the interior pier from which moments are redistributed (LRFD Sections B6.3.2.1 and B.6.4.1.1). Thus, if there is a transition to a smaller section within that unbraced length, it is possible that the reduced flexural strength of that section may be exceeded by the factored moments or stresses. However, a simple additional check that the flexural capacity at both the Overload and Maximum Load limit states exceeds the factored moment after redistribution at any section transitions within the unbraced length adjacent to the interior pier will eliminate this possibility. Note that for the Overload limit state, the stress limits should be abolished and the capacity should be taken as the same nominal moment capacity used in the check for at Maximum Load limit state.

Because of the conservative use of section properties in calculating the maximum unbraced length to prevent lateral-torsional buckling and the assessment that the controlling section in negative flexure will be the centerline of the interior pier, rather than at any nearby section transitions, this requirement that no section transitions occur within the unbraced lengths of the pier section is ignored. The reduced flexural capacity at each transition will be checked against the factored moments after redistribution to ensure that the section has adequate strength.

Note that alternatively, this requirement could be directly satisfied by placing the additional cross frames that are needed to reduce the unbraced length (see number 6 on this list) at the location of the section transition or at a location even closer to the interior pier.

8. The shear limit state must not be exceeded within the unbraced length adjacent to the interior pier regions. → OK

Although a check for shear is not shown here, the shear strength requirements are satisfied for this girder.

9. Bearing stiffeners must be present at the interior pier locations $\rightarrow$ $NOT\ OK$

   Thus, bearing stiffeners must be added at the interior pier to allow for inelastic moment redistribution. It is recommended that these stiffeners are should be designed according to the provision in Article 6.10.11.2 of the LRFD specifications. These provisions require double-sided stiffeners that extend over the full depth of the web and as close to the outer edges of the flanges as is practical. Thus, choose a stiffener width of 5 inches and calculate the minimum thickness using the following equation from the LRFD specifications:

$$b_t \leq 0.48 t_p \sqrt{\frac{E}{F_y}} \rightarrow t_p \geq \frac{b_t}{0.48}\sqrt{\frac{F_y}{E}} \rightarrow t_p \geq \frac{(5\ in)}{0.48}\sqrt{\frac{33\ ksi}{29000\ ksi}} \rightarrow t_p \geq 0.35\ in$$

   Choose a thickness of 3/8 inches so that ***double-sided 5-inch by 3/8-inch bearing stiffeners should be installed at the interior pier sections of Girder B***. Strength considerations for the bearing stiffeners can be addressed by investigating the effects of the concentrated reaction force at the interior piers. Equations for the strength of the stiffeners can also be found in Article 6.10.11.2 of the LRFD specifications.

Assuming that additional cross frames and bearing stiffeners are added, moment redistribution can be allowed for this girder. Following the provisions in Section B6.5 of the LRFD specifications, the effective plastic moment for the section is calculated, which accounts for the slenderness of the section to ensure an adequate amount of inelastic rotation capacity can be attained. This effective plastic moment differs for the Overload and Maximum Load limit states, which are referred to as the Service II and Strength I limit states, respectively, in the LRFD specifications. Sections that have "ultracompact" webs have been shown to exhibit enhanced moment-rotation characteristics and thus have a larger effective plastic moment. The section is classified as having an ultracompact web if:

$$\frac{2D_{cp}}{t_w} \leq 2.3\sqrt{\frac{E}{F_y}} \rightarrow \frac{2(17.0\ in)}{0.650\ in} \leq 2.3\sqrt{\frac{29000\ ksi}{33\ ksi}} \rightarrow 52.3 \leq 68.2 \rightarrow web\ is\ ultracompact$$

LRFD Equation B6.5.1-1

The effective plastic moment at both the Overload and Maximum Load limit state is calculated as follows. Note that for the Overload limit state, the capacity is simply the nominal moment capacity of the section (M_n). Because the section has an ultracompact web, a compact flange (as determined in number 5 of the moment redistribution requirements), and additional lateral bracing will be added to satisfy the moment redistribution requirements, this nominal capacity is simply the plastic moment capacity (M_p) of the section. For the Maximum Load limit state, the capacity is equal to a calculated fraction of the nominal capacity:

$$M_{pe\ OL} = M_n = M_p = F_y Z_x = (33\ ksi)(927\ in^3)\left(\frac{1\ ft}{12\ in}\right) = 2550\ k.ft$$

LRFD Equation B6.5.1-2

$$M_{pe\ ML} = \left(2.78 - 2.3\frac{b_f}{t_f}\sqrt{\frac{F_y}{E}} - 0.35\frac{D}{b_f} + 0.39\frac{b_f}{t_f}\sqrt{\frac{F_y}{E}\frac{D}{b_f}}\right)M_n \leq M_n$$

LRFD Equation B6.5.1-3

$$\rightarrow \left(2.78 - 2.3\left(\frac{12.0\ in}{1.02\ in}\right)\sqrt{\frac{33\ ksi}{29000\ ksi}} - 0.35\left(\frac{34.0\ in}{12.0\ in}\right) + 0.39\left(\frac{12.0\ in}{1.02\ in}\right)\sqrt{\frac{33\ ksi}{29000\ ksi}}\left(\frac{34.0\ in}{12.0\ in}\right)\right)(2550\ k.ft)$$

$$= 3350\ k.ft > 2550\ k.ft \rightarrow 2550\ k.ft$$

In this case, the capacity at both the Overload and Maximum Load limit states considering moment redistribution is equal to the full plastic moment capacity of the section. This is common for girders comprised of rolled steel sections.

Once the effective plastic moment has been calculated, the redistribution moment at the interior pier is calculated for both limit states. The redistribution moment represents the portion of the factored moment that exceeds the effective plastic moment. Thus, the redistribution moment must be positive, as redistribution is only necessary when the factored moment is greater than the effective plastic moment. Note that only gravity loads are considered in this design, so no lateral forces are included in this calculation.

$$M_{rd\,OL} = |M_{u\,OL}| - M_{pe\,OL} = |-2060\ k.ft| - 2550\ k.ft$$
$$= -490\ k.ft \quad \rightarrow \quad 0\ k.ft$$

LRFD Equation B6.4.2.1-1

$$M_{rd\,ML} = |M_{u\,ML}| - M_{pe\,ML} = |-2680\ k.ft| - 2550\ k.ft$$
$$= 130\ k.ft$$

LRFD Equation B6.4.2.1-1

Although it was determined previously that moment redistribution is necessary at both the Overload and the Maximum Load limit states, the redistribution moment at Overload is calculated to be zero. This is because of the significant increase in the strength that is attributed to this section from the original capacity, defined as 80% of the moment at first yield, and the effective plastic moment, which in this case is the full plastic moment capacity. Thus, although moment redistribution needs to be considered at the Overload limit state, and all of the requirements from Section B6.2 of the LRFD specifications must be satisfied, no actual redistribution of moments is needed at the Overload limit state.

At the Maximum Load limit state, however, the effective plastic moment is only slightly larger than the capacity calculated prior to considering moment redistribution. In fact, with the addition of the extra cross frames required to satisfy the redistribution requirements, there would be no difference in the capacity prior to considering redistribution and the effective plastic moment, at least in this case. This is because the girder at 70' would be classified as a compact section and would have a capacity equal to the plastic moment of the steel section.

The calculated redistribution moment is limited to 20% of the factored moment, which is confirmed by the following check. The actual percentage of the factored elastic moment that is redistributed is also calculated here:

$$M_{rd\,ML} \leq 0.2|M_{u\,ML}| = 0.2|-2680\ k.ft| = 536\ k.ft$$
$$\rightarrow \quad 130\ k.ft < 536\ k.ft \quad \rightarrow \quad OK$$

LRFD Equation B6.4.2.1-3

$$\frac{M_{rd\ ML}}{|M_{u\ ML}|} = \frac{130\ k.ft}{2680\ k.ft} = 4.9\%$$

The redistribution moment diagram is constructed by first plotting the redistribution moments calculated at the interior piers, and then connecting them by straight lines, with zero moment at the end of the girder. Figure D-5 plots the redistribution moment diagram at the Maximum Load limit state, along with the same dead load and live load moments from Figure D-4. Table D-4 summarizes the value of the redistribution moment at each of the critical sections, along with the dead and live load moments at the critical sections from Table D-2. For the remainder of the design, the redistribution moments will be added to the dead and live load moments for the Maximum Load limit state. Note that the redistribution moments always have a load factor of 1.0.

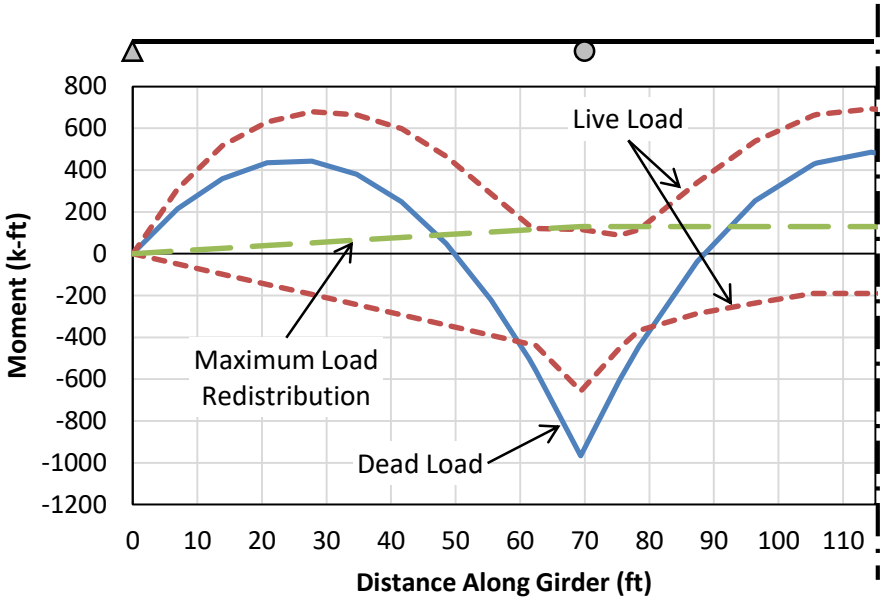

Figure D-5: Plot of Unfactored and Redistribution Moments for Girder B

Table D-4: Unfactored and Redistribution Moments at Critical Sections in Girder B

Location (ft)	Section Type	Section Number	Unfactored Moment (k-ft)			Redistribution Moment (k-ft)	
			Dead Load	Live Load			
				Pos.	Neg.	OL	ML
28	Critical, Span	1	442	679	-195	0	52
60	Lateral Brace	1	-405	188	-418	0	111
62	Critical, Trans.	1	-503	136	-432	0	115
70	Critical, Pier Lateral Brace	2	-967	116	-657	0	130
76	Critical, Trans.	1	-606	89	-452	0	130
80.5	Lateral Brace	1	-378	151	-354		130
106.5	Critical, Trans.	1	434	666	-191	0	130
115	Critical, Span	3	486	694	-191	0	130

Finally, check that the factored moment at the section transitions near the interior pier do not exceed the capacity after redistribution at the Maximum Load limit state. This is a necessary check in this case because the cover plates terminate within the unbraced length adjacent to the interior pier section from which moments are redistributed.

Critical Location at 62' (Section #1)

After the addition of a cross frame at 10 feet from the interior pier section in the exterior span, the unbraced length (L_b) for the compression (bottom) flange is now 10 feet, or 120 inches. The compression flange and web have already been shown to meet the compact limits. Thus, the steel section is classified as compact if:

$$\frac{L_b}{r_y} \leq \frac{\left[3.6 - 2.2\left(\frac{M_1}{M_p}\right)\right] x10^3}{F_y}$$ *Equation 10-96*

$$M_1 = (1.3)(-405\ k.ft) + (2.17)(-418\ k.ft) = -1430\ k.ft$$

$$M_p = -Z_{x\,70'}\,F_y = (927\ k.ft)(33\ ksi)\left(\frac{1\ ft}{12\ in}\right) = -2550\ k.ft$$

$$\rightarrow \quad \frac{120\ in}{2.51\ in} \leq \frac{\left[3.6 - 2.2\left(\frac{-1430\ k.ft}{-2550\ k.ft}\right)\right] x10^3}{33\ ksi} \quad \rightarrow \quad 47.8 \leq 71.7$$

$$\rightarrow \quad LTB\ OK$$

Thus, the steel section is classified as compact and the Maximum Load capacity is:

$$C_{ML\ 62'} = -Z_x\ F_y = -(624\ in^3)(33\ ksi)\left(\frac{1\ ft}{12\ in}\right) = -1720\ k.ft$$

Section 10.48.1

The factored moment at the Maximum Load limit state at this location is:

$$M_{u\ ML\ 62'} = 1.3(-503\ k.ft) + 2.17(-432\ k.ft) + 1.0(111\ k.ft) = -1480\ k.ft$$

Table 3.22.1A

Because the capacity exceeds the factored moment at this section transition, the calculated 130 k-ft redistribution moment can be allowed.

Critical Location at 76' (Section #1)

After the addition of a cross frame at 10.5 feet from the interior pier section in the interior span, the unbraced length (L_b) for the compression (bottom) flange is now 10.5 feet, or 126 inches. The compression flange and web have already been shown to meet the compact limits. Thus, the steel section is classified as compact if:

$$\frac{L_b}{r_y} \leq \frac{\left[3.6 - 2.2\left(\frac{M_1}{M_p}\right)\right] x10^3}{F_y}$$

Equation 10-96

$$M_1 = (1.3)(-378\ k.ft) + (2.17)(-354\ k.ft) = -1260\ k.ft$$

$$M_p = -Z_{x\ 70'}\ F_y = (927\ k.ft)(33\ ksi)\left(\frac{1\ ft}{12\ in}\right) = -2550\ k.ft$$

$$\rightarrow \quad \frac{126\ in}{2.51\ in} \leq \frac{\left[3.6 - 2.2\left(\frac{-1260\ k.ft}{-2550\ k.ft}\right)\right] x10^3}{33\ ksi} \quad \rightarrow \quad 50.2 \leq 76.1$$

$$\rightarrow \quad LTB\ OK$$

Thus, the steel section is classified as compact and the Maximum Load capacity is:

$$C_{ML\ 76'} = -Z_x\ F_y = -(624\ in^3)(33\ ksi)\left(\frac{1\ ft}{12\ in}\right) = -1720\ k.ft$$

Section 10.48.1

The factored moment at the Maximum Load limit state at this location is:

$$M_{u\ ML\ 76'} = 1.3(-606\ k.ft) + 2.17(-452\ k.ft) + 1.0(130\ k.ft) = -1638\ k.ft$$

Table 3.22.1A

Because the capacity exceeds the factored moment at this section transition, the calculated 130 k-ft redistribution moment can be allowed.

D.2.5 Design Connectors for Positive Moment Regions

Now that the redistribution moments are known, the partially composite positive moment regions are designed and checked at both the Overload and Maximum Load limit states. For this girder, a different design needs to be conducted for the exterior span, which has a critical section at 28', and for the middle span, which has a critical section at 115'. The design for the interior span also needs to be checked at the transition location at the termination of the cover plate at 106.5'. The Overload limit state involves stress-based calculations on the non-composite, short term composite, and long term composite sections which can make for a complicated way to begin the design. Thus, it is recommended to begin the design with the Maximum Load limit state.

Design for the Maximum Load Limit State – Exterior Spans

The factored moment, including redistribution moments, for the critical section in the exterior spans (28') at the Maximum Load limit state is:

$$M_{u\,ML\,28'} = 1.3(442\ k.ft) + 2.17(679\ k.ft) + 1.0(52\ k.ft)$$
$$= 2100\ k.ft$$

The capacity at the Maximum Load limit state is simply the nominal moment capacity of the section (M_n). This is usually equal to the plastic moment of the partially composite cross section, because the deck provides continuous lateral support for the top flange of the girder to prevent lateral-torsional buckling, and little to none of the steel section is required to resist large compressive forces so local buckling tends not to control.

First, the fully composite section is analyzed to determine the number of connectors required for full-composite action as well as the strength and stiffness of the fully composite section, indicated by the subscript "FC". The number of connectors needed is simply the compression force in the deck (C_f) divided by the strength of a single connector (Q_n), which is calculated from the effective cross-sectional area (A_{sc}) and the ultimate tensile strength ($F_{u\,sc}$) of the ASTM A193 B7 threaded rod comprising the connector (Kwon et al. 2007):

$$A_{sc} = 0.8\frac{\pi\ {d_{sc}}^2}{4} = 0.8\left(\frac{\pi\left(\frac{7}{8}in\right)^2}{4}\right) = 0.481\ in^2$$

$$Q_n = 0.5\ A_{sc}\ F_{u\,sc} = 0.5(0.481\ in^2)(125\ ksi) = 30.1\ kips$$

Simple plastic cross-sectional analysis, is used to determine the properties of the fully composite section:

$$C_{f\,FC} = min\begin{Bmatrix}0.85f_c'A_{deck}\\ A_sF_y\end{Bmatrix} = min\begin{Bmatrix}0.85(3\ ksi)(595\ in^2)\\ (47.0\ in^2)(33\ ksi)\end{Bmatrix} = min\begin{Bmatrix}1520\ k\\ 1550\ k\end{Bmatrix}$$
$$= 1520\ k$$

$$N_{FC} = \frac{C_{f\,FC}}{Q_n} = \frac{1520\ k}{30.1\ k} = 50.5$$

Generally, the number of connectors in a design should be rounded up to the next even number, as they are installed in pairs. However, since the final design is unlikely to

be fully composite, the number of connectors required for a fully composite girder can remain as a decimal for now. Also, because the first term in the equation for C_f is the smallest, the plastic neutral axis will be either in the top flange or top portion of the web of the steel beam. If the plastic neutral axis is in the web of the steel beam, the net plastic force in the top and bottom flanges will cancel out, since the section is doubly symmetric. Thus, the plastic neutral axis can only be in the web of the steel beam if the maximum plastic force that can be developed in the web ($P_{y\,web}$) is greater than the compressive force in the slab (C_f). Otherwise, the plastic neutral axis is located in the top flange of the steel beam, as is the case here, indicated by the following calculations:

$$P_{y\,web} = A_{web}F_y = \left(A_s - 2A_f\right)F_y = \left(A_s - 2b_f t_f\right)F_y$$
$$= \left(47.0\ in^2 - 2(12.0\ in)(1.02\ in)\right)(33\ ksi) = 743\ k$$

$$743\ k < 1520\ k \ \rightarrow\ P_{y\,web} < C_{f\,FC}$$
$$\rightarrow\ \textit{Plastic neutral axis is in the top flange}$$

The stress distribution at the plastic moment capacity is shown in Figure D-6. Force resultants, which act at mid-height of the corresponding stress block, are indicated by filled arrowheads and bold labels. For simplicity, an equivalent stress distribution, shown in the far right portion of the figure, will be used for the calculations. In this equivalent stress distribution, the entirety of the steel beam is shown under tensile yield stress, while the portion of the top flange above the plastic neutral axis is subjected to twice the yield stress in compression. Using the equivalent stress distribution helps to simplify the calculations while keeping the same net stresses on the section. The unknown distance "y" represents the depth of the top flange that is in compression and can be solved for by summing forces on the cross-section. The plastic moment capacity (M_p) is then calculated by summing moments on the section. Since there is no net axial force on the section, moments can be summed about any point. Here, the steel-concrete interface is chosen, and counterclockwise moments are taken as positive:

$$T_s = A_s F_y = (47.0\ in^2)(33\ ksi) = 1550\ k$$

$$C_s = b_f y F_y = (12.0\ in)(y)(33\ ksi) = \left(396\frac{k}{in}\right)(y)$$

$$\Sigma F = 0 \;\rightarrow\; T_s - C_s - C_{f\,FC} = 0$$
$$\rightarrow\; (1550\ k) - \left(396\frac{k}{in}\right)(y) - (1520\ k) = 0$$
$$\rightarrow\; y = 0.0758\ in$$

$$M_{p\,FC} = \Sigma M_{interface} = T_s\left(\frac{d}{2}\right) - C_s\left(\frac{y}{2}\right) + C_{f\,FC}\left(\frac{t_{deck}}{2}\right)$$
$$= (1550\ k)\left(\frac{36.0\ in}{2}\right) - \left(396\frac{k}{in}\right)(0.0758\ in)\left(\frac{0.0758\ in}{2}\right)$$
$$+ (1520\ k)\left(\frac{6.5\ in}{2}\right) = (32800\ k.in)\left(\frac{1\ ft}{12\ in}\right) = 2740\ k.ft$$

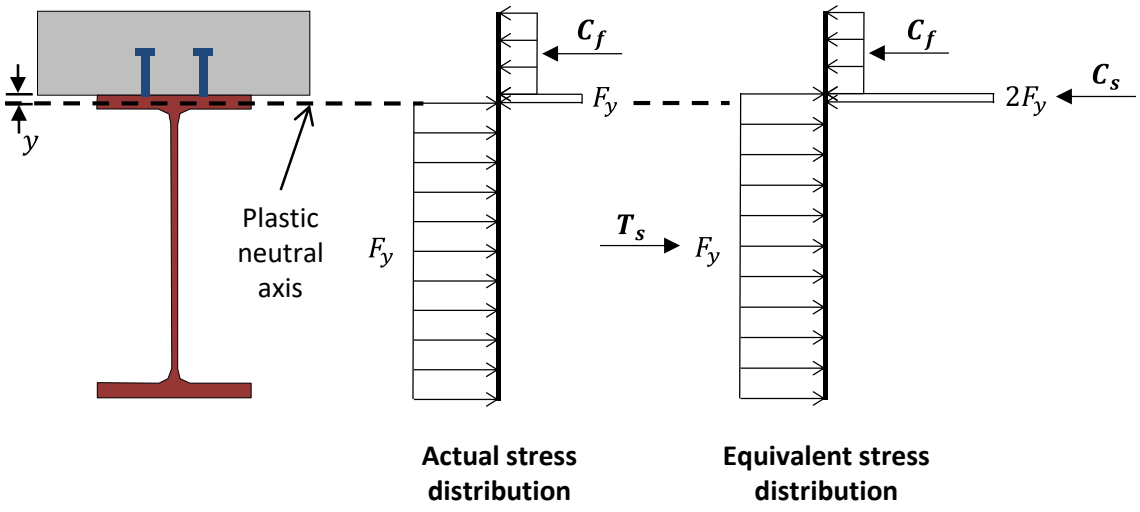

Figure D-6: Stress Distribution at Plastic Moment of Fully Composite Section – Exterior Span of Girder B

The transformed moment of inertia (I_{tr}) and elastic section modulus to the extreme bottom fiber of the steel beam (S_{tr}) of the fully composite section can also be calculated using basic concepts of mechanics of materials after locating the elastic neutral axis (at a distance of y_{NA} below the interface). Two sets of calculations follow, one of which corresponds to the short-term composite section and the other of which corresponds to the long-term composite section. The short-term composite section properties, indicated by the subscript "*ST*", are calculated using the short-term modular ratio of n while the long-

term composite section properties, indicated by the subscript "LT", are calculated using the long-term modular ratio of $3n$:

Short-term section:

$$n = \frac{E_s}{E_c} = \frac{29000\ ksi}{3122\ ksi} = 9.3$$

$$y_{NA\ ST} = \frac{A_s\left(\frac{d}{2}\right) - \frac{A_{deck}}{n}\left(\frac{t_{deck}}{2}\right)}{A_s + \frac{A_{deck}}{n}} = \frac{(47.0\ in^2)\left(\frac{36.0\ in}{2}\right) - \frac{(595\ in^2)}{9.3}\left(\frac{6.5\ in}{2}\right)}{(47.0\ in) + \frac{(595\ in^2)}{9.3}} = 5.75\ in$$

$$I_{tr\ ST} = I_s + A_s\left(\frac{d}{2} - y_{NA}\right)^2 + \frac{I_{deck}}{n} + \frac{A_{deck}}{n}\left(\frac{t_{deck}}{2} + y_{NA}\right)^2$$
$$= 9760\ in^4 + (47.0\ in^2)\left(\frac{36.0\ in}{2} - 5.75\ in\right)^2 + \frac{(2090\ in^4)}{9.3} + \frac{(595\ in^2)}{9.3}\left(\frac{6.5\ in}{2} + 5.75\ in\right)^2$$
$$= 22200\ in^4$$

$$S_{tr\ ST} = \frac{I_{tr\ ST}}{d - y_{NA}} = \frac{22200\ in^4}{(36.0\ in) - (5.75\ in)} = 734\ in^3$$

Long-term section:

$$3n = 3(9.3) = 27.9$$

$$y_{NA\ LT} = \frac{A_s\left(\frac{d}{2}\right) - \frac{A_{deck}}{3n}\left(\frac{t_{deck}}{2}\right)}{A_s + \frac{A_{deck}}{3n}} = \frac{(47.0\ in^2)\left(\frac{36.0\ in}{2}\right) - \frac{(595\ in^2)}{27.9}\left(\frac{6.5\ in}{2}\right)}{(47.0\ in) + \frac{(595\ in^2)}{27.9}} = 11.4\ in$$

$$I_{tr\,LT} = I_s + A_s\left(\frac{d}{2} - y_{NA}\right)^2 + \frac{I_{deck}}{3n} + \frac{A_{deck}}{3n}\left(\frac{t_{deck}}{2} + y_{NA}\right)^2$$
$$= 9760\ in^4 + (47.0\ in^2)\left(\frac{36.0\ in}{2} - 11.4\ in\right)^2 + \frac{(2090\ in^4)}{27.9} + \frac{(595\ in^2)}{27.9}\left(\frac{6.5\ in}{2} + 11.4\ in\right)^2$$
$$= 16500\ in^4$$

$$S_{tr\,LT} = \frac{I_{tr\,LT}}{d - y_{NA}} = \frac{16500\ in^4}{(36.0\ in) - (11.4\ in)} = 671\ in^3$$

Now that the analysis of the fully composite section is complete, the iterative process of designing the partially composite section can be done. Since the plastic strength of the fully composite section (2740 k-ft) is greater than the factored moments at the Maximum Load limit state (2130 k-ft), the girder can be strengthened using partial-composite design. To begin, choose an approximate composite ratio, and calculate the number of connectors required and the strength of the partially composite section, indicated by a subscript "PC". Recall that because the connectors are installed in pairs, the number of connectors should be rounded up to the nearest even number. The strength calculations are conducted in the exact same manner as for the fully composite section, except the interface shear (C_f) will now be controlled by the strength of the partially composite shear connection. This means that the plastic neutral axis will always be located in the steel beam.

A composite ratio (η) of approximately 30% will be chosen to start. This value represents the minimum recommended for design. The stress distribution for this partially composite case is shown in Figure D-7. Because the plastic neutral axis is now located in the web, a different equivalent stress distribution is used to simplify the calculations. In this case, the top half of the steel is shown under the yield stress in compression, while the bottom half of the steel is subjected to the yield stress in tension. This stress distribution creates two equal force resultants that form a force couple with the same magnitude as the plastic moment of the steel section ($M_{p\,steel}$). The portion of the steel above mid-depth of the beam and below the plastic neutral axis is also under a tensile stress of twice the yield stress. The unknown distance z represents the height of the web above mid-depth of the steel section but below the plastic neutral axis. Since the interface shear ($C_{f\,PC}$) is no longer

controlled by the plastic force in the deck, only the top portion of the deck is assumed to be under compressive stress. The depth of the concrete compression block is denoted as a.

$$N = \eta\, N_{FC} = (0.3)(50.5) = 15.15 \;\rightarrow\; N = 16 = 8\, pairs$$

$$\eta_{actual} = \frac{N}{N_{FC}} = \frac{16}{50.5} = 0.317$$

$$C_{f\,PC} = min\begin{Bmatrix} 0.85 f_c' A_{deck} \\ A_s F_y \\ N\, Q_n \end{Bmatrix} = min\begin{Bmatrix} 0.85(3\ ksi)(595\ in^2) \\ (47.0\ in^2)(33\ ksi) \\ (16)(30.1\ k) \end{Bmatrix} = min\begin{Bmatrix} 1520\ k \\ 1550\ k \\ 482\ k \end{Bmatrix}$$
$$= 482\ k$$

$$743\ k > 482\ k \;\rightarrow\; P_{y\,web} > C_f \;\rightarrow\; Plastic\ neutral\ axis\ is\ in\ the\ web$$

$$a = \frac{C_{f\,PC}}{0.85 f_c' b_{eff}} = \frac{482\ k}{0.85(3\ ksi)(91.5\ in)} = 2.07\ in$$

$$T_s = z t_w \left(2F_y\right) = (z)(0.650\ in)\left(2(33\ ksi)\right) = \left(42.9 \frac{k}{in}\right)(z)$$

$$M_{p\,steel} = Z_x F_y = (624\ in^3)(33\ ksi) = 20600\ k.in$$

$$\Sigma F = 0 \;\rightarrow\; T_s - C_{f\,PC} = 0 \;\rightarrow\; \left(42.9 \frac{k}{in}\right)(z) - 482\ k = 0 \;\rightarrow\; z$$
$$= 11.2\ in$$

$$M_{p\,PC} = \Sigma M_{interface} = T_s\left(\frac{d}{2} - \frac{z}{2}\right) + C_{f\,PC}\left(t_{deck} - \frac{a}{2}\right) + M_{p\,steel}$$

$$= \left(\left(42.9\frac{k}{in}\right)(11.2\ in)\right)\left(\frac{(36.0\ in)}{2} - \frac{(11.2\ in)}{2}\right)$$

$$+ (482\ k)\left(6.5\ in - \frac{2.07\ in}{2}\right) + 20600\ k.in$$

$$= (29200\ k.in)\left(\frac{1\ ft}{12\ in}\right) = 2430\ k.ft$$

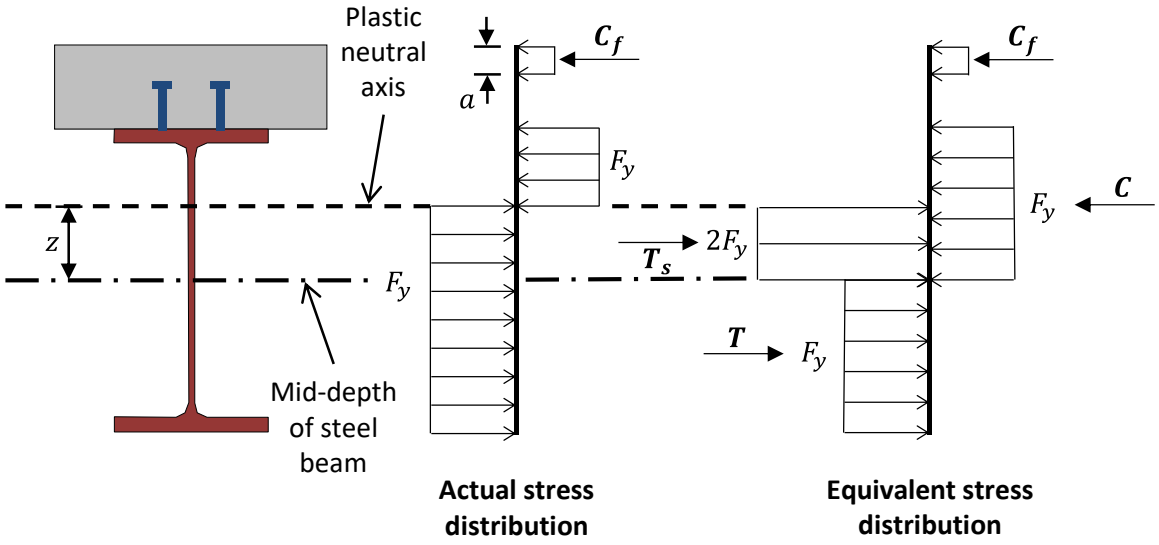

Figure D-7: Stress Distribution at Plastic Moment of Partially Composite Section – Exterior Span of Girder B

The plastic moment capacity of the approximately 30% partially composite section (2430 k-ft) exceeds the maximum factored moment at the Maximum Load limit state in the exterior spans (2130 k-ft). Because 30% is the minimum recommended composite ratio, choose $N = 16$ for the exterior spans to satisfy the requirements of the Maximum Load limit state.

Check the Design at the Overload Limit State – Exterior Spans

Next, check the Overload limit state with $N = 16$ in the exterior spans. This requires the computation of steel stresses due to bending moments and requires the use of different values of the section modulus for the different load types. For bridges

strengthened with post-installed shear connectors, all dead load present prior to the installation of the connectors is applied to the non-composite section. Any dead load applied after the connectors are installed, such as an overlay of the driving surface, is applied to the long-term composite section, along with any redistribution moments at the Overload limit state, of which there are none in this case. The live load is applied to the short-term composite section. The short- and long-term effective elastic moduli of the partially composite section (S_{eff}) are calculated by interpolation between the properties of the non-composite steel beam and the properties of the transformed fully composite section (AISC 2010). Note that because there are no redistribution moments at the Overload limit state, the long-term effective elastic section modulus will not be used in any calculations, but is shown here as an example:

$$S_{eff\ ST} = S_x + \sqrt{\eta_{actual}}(S_{tr\ ST} - S_x)$$
$$= (542\ in^3) + \sqrt{0.317}\big((734\ in^3) - (542\ in^3)\big) = 650\ in^3$$

$$S_{eff\ LT} = S_x + \sqrt{\eta_{actual}}(S_{tr\ LT} - S_x)$$
$$= (542\ in^3) + \sqrt{0.317}\big((671\ in^3) - (542\ in^3)\big) = 615\ in^3$$

The following factored stress is calculated at the Overload limit state in positive bending at the critical section at 28':

$$\sigma_{u\ OL} = 1.0\left(\frac{442\ k.ft}{542\ in^3}\right)\left(\frac{12\ in}{1\ ft}\right) + (1.67)\left(\frac{679\ k.ft}{650\ in^3}\right)\left(\frac{12\ in}{1\ ft}\right) = 30.7\ ksi$$

For a composite section, the extreme stress in the steel beam is limited to 95% of the yield stress at the Overload limit state. Note that this requirement applies to only fully composite sections in the LRFD specifications, which do not currently allow for partial-composite design. The difference in stress limits between non-composite (80%) and fully composite (95%) sections is primarily due to the vast difference in the ratio of maximum moment capacity (M_n) to yield moment (M_y) for the two types of sections. Because even with low composite ratios, partially composite sections have maximum moment-to-yield moment ratios much closer to fully composite sections than to non-composite sections, the 95% stress limit is recommended for use with partially composite strengthened girders. Thus, the capacity, or maximum allowed stress ($\sigma_{mx\ OL}$), at the Overload limit state is calculated as:

$$\sigma_{max\ OL} = 0.95F_y = 0.95(33\ ksi) = 31.4\ ksi$$

This maximum allowed stress (31.4 ksi) exceeds the stress from the factored loads, indicating that the requirements of the Overload limit state are satisfied by $N = 16$.

Thus, to satisfy the requirements of both the Overload and Maximum Load limit states, ***use $N = 16$ in the exterior spans on Girder B***. Note that N is the number of shear connectors required between points of zero and maximum moment. Thus, each of the exterior spans spans will contain two sets of 16 connectors.

Design for the Maximum Load and Overload Limit States – Interior Span

The same procedure is followed for the design of the connectors in the interior span. Table D-5 summarizes the results of the calculations for the critical section in the interior span (115') and for the location of cover plate termination in the interior span (106.5') at the Maximum Load limit state. Again, the minimum recommended composite ratio of 0.3 is used for the partially composite calculations.

Table D-5: Results from Partially Composite Design Calculations for the Interior Span of Girder B

	115'	**106.5'**
Section number	3	1
Factored Maximum Load moment ($M_{u\,ML}$, k-ft)	2310	2180
Deck force, fully composite ($C_{f\,FC}$, k)	1520	1520
Number of connectors, fully composite (N_{FC})	50.5	50.5
Plastic web force ($P_{y\,web}$, k)	743	743
Plastic neutral axis location, fully composite	Flange	Flange
Plastic moment, fully composite ($M_{p\,FC}$, k-ft)	3120	2740
Short term moment of inertia, fully composite ($I_{tr\,ST}$, in^4)	25400	22200
Short term section modulus, fully composite ($S_{tr\,ST}$, in^3)	839	734
Long term moment of inertia, fully composite ($I_{tr\,ST}$, in^4)	19000	16500
Long term section modulus, fully composite ($S_{tr\,ST}$, in^3)	765	671
Number of connectors, partially composite (N_{PC})	16	16
Actual composite ratio	0.317	0.317
Deck force, partially composite ($C_{f\,PC}$, k)	482	482
Plastic neutral axis location, partially composite	Web	Web
Plastic moment, partially composite ($M_{p\,PC}$, k-ft)	2780	2430
Short term section modulus, partially composite ($S_{eff\,ST}$, in^3)	1060	650
Long term section modulus, partially composite ($S_{eff\,LT}$, in^3)	866	615
Factored Overload stress ($\sigma_{u\,OL}$, ksi)	22.0	30.1
Maximum allowed Overload stress ($\sigma_{max\,OL}$, ksi)	31.4	31.4

The plastic moment capacity exceeds the factored moment at the Maximum Load limit state at both locations. The maximum allowed stress also exceeds the factored stress at the Overload limit state at both locations. Thus, the requirements for both limit states are satisfied with this design, so ***use $N = 16$ in the interior spans on Girder B***.

D.2.6 Locate Connectors and Check Fatigue

Before checking the fatigue behavior of the post-installed shear connectors, a connector layout must be chosen. Based on the recommendations given by Ghiami Azad

(2016), the layout in Figure D-8 is proposed. Because the girder is symmetric, only the left half is shown in the figure. Within a group, the connectors are spaced at 12 inches, which is equal to the transverse rebar spacing in the deck. The connector nearest to the end of the girder is located 6 inches away from the centerline of the support, while the connectors nearest to the interior support are located a distance equal to 15% of the span length from that support.

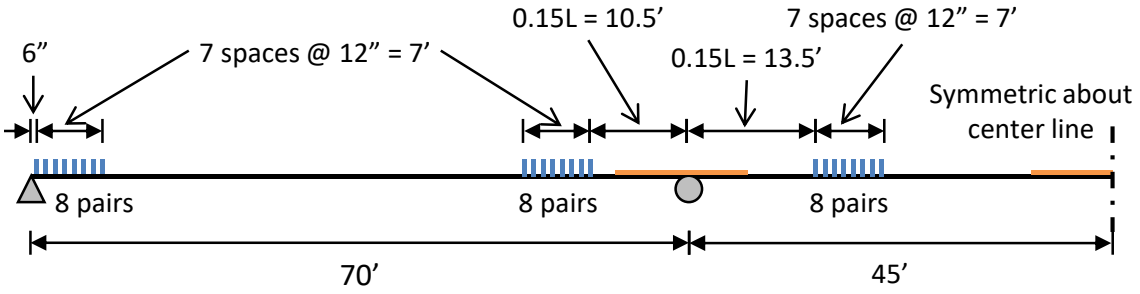

Figure D-8: Connector Layout for Girder B

In addition to the recommendations provided for locating the connectors, it is important to consider constructability and field conditions when choosing a connector layout, paying particular attention to the accessibility of the locations along the girder in which the connectors are to be installed. Because small changes in the connector layout will likely not significantly affect the behavior, some adjustments can be made in the field when necessary. It is highly recommended to use a rebar locator to find the transverse deck reinforcement in the locations where the connectors will be installed. Once the bars are located, modify the connector layout so that the connectors are installed approximately halfway between reinforcing bars and use a connector spacing equal to a multiple of the bar spacing. This should prevent conflicts with reinforcing bars when drilling into the deck to install the connectors.

The first step in checking the connectors for fatigue is to determine which load combination from the AASHTO LRFD specifications is to be used, by comparing the projected daily truck traffic in a single lane to the limiting value calculated from the provisions:

$$(ADTT)_{SL} = p\,(ADTT) = (0.8)\left(1160\frac{trucks}{day}\right) = 928\frac{trucks}{day} \qquad \textit{LRFD Equation 3.6.1.4.2-1}$$

$$(ADTT)_{SL\ limit} = \frac{8{,}700{,}000}{Y} = \frac{8{,}700{,}000}{25} = 348{,}000\,\frac{trucks}{day}$$

Because the projected truck traffic is below the limiting value, the Fatigue II load combination is used to design for finite life. Note that as discussed in Section 8.2.8, the above equation results in a very high limiting $(ADTT)_{SL}$ value, indicating that the Fatigue II load combination will essentially always control the design. Thus, the nominal fatigue resistance is calculated as follows:

$$\begin{aligned} N &= (365)(Y)(n)(ADTT)_{SL} \\ &= \left(365\,\frac{days}{year}\right)(25\ years)\left(1.0\,\frac{cycles}{truck}\right)\left(928\,\frac{trucks}{day}\right) \\ &= 8{,}470{,}000\ cycles \end{aligned}$$

$$(\Delta F)_n = \left(\frac{A}{N}\right)^{1/m} = \left(\frac{4.24\ x\ 10^{15}\ ksi^7}{8{,}470{,}000\ cycles}\right)^{1/7} = 17.5\ ksi$$

Figure D-9 shows the results from the fatigue analysis, conducted in a manner that explicitly considers the interface slip. This analysis was carried out using an Excel-based program, which was developed during the course of this research and models the connectors as linear springs (Ghiami Azad 2016). The recommended stiffness of 900 kips per inch was used for the spring representing each individual connector. The figure plots the stress range in each connector induced by the fatigue loading defined in the Fatigue II load combination in the LRFD specifications. Because of symmetry, only one-half of the girder is shown.

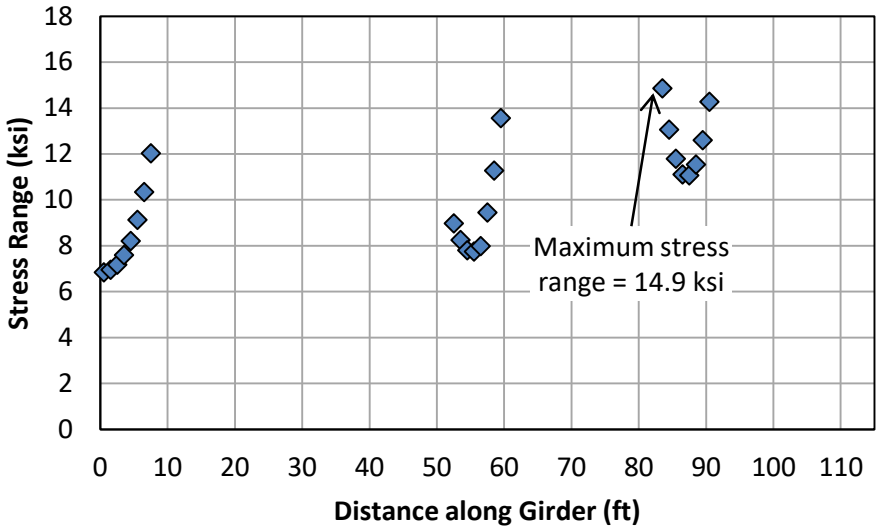

Figure D-9: Results from Fatigue Analysis for Girder B

The maximum stress range (ΔF) that a connector undergoes during fatigue loading is 14.9 ksi. As shown in the figure, this critical connector is the closest connector to the interior support in the interior span. This maximum stress range is less than the nominal fatigue resistance (17.5 ksi), indicating that ***the connectors have adequate fatigue life to satisfy the design requirement of a 25-year remaining life***.

The actual remaining life can be estimated by reversing the design equations to solve for the number of cycles and corresponding number of years that can be resisted at a given stress range. These calculations indicate that ***the connectors in Girder B are estimated to have a remaining fatigue life of 77 years***:

$$N_{actual} = \frac{A}{(\Delta F)^m} = \frac{4.24\ x\ 10^{15}\ ksi^7}{(14.9\ ksi)^7} = 26{,}000{,}000\ cycles$$

$$Y_{actual} = \frac{N_{actual}}{(365)(n)(ADTT)_{SL}} = \frac{26{,}000{,}000\ cycles}{\left(365\,\frac{days}{year}\right)\left(1.0\,\frac{cycles}{truck}\right)\left(928\,\frac{trucks}{day}\right)}$$

$$= 77\ years$$

D.2.7 Conduct Load Rating of Strengthened Girder

Following the strengthening a load rating of each of the critical sections can be done in the same manner as the initial evaluation of the existing non-composite structure. A slight modification should be made to the equation to calculate the rating factor to include the redistribution moment at a section (RD):

$$RF = \frac{C - A_1\, DL - (1.0)RD}{A_2(LL + I)}$$

Modified MBE Equation 6B.4.1-1

Critical Location at 28' (Section #1, N = 16):

The Overload limit state must be addressed in terms of stresses now, because different types of loads are resisted by different sections. The capacity, or limiting stress, for the Overload limit state of a composite section was calculated previously as:

$$C_{OL\ 28'} = 31.4\ ksi$$

The dead load is resisted by the non-composite section, while the live load is resisted by the short-term partially composite section. If there were any redistribution moments at the Overload limit state, these would be resisted by the long-term partially composite section. Thus, the unfactored stresses for each of these load types are:

$$\sigma_{DL\ 28'} = \frac{M_{DL\ 28'}}{S_x} = \frac{442\ k.ft}{542\ in^3}\left(\frac{12\ in}{1\ ft}\right) = 9.79\ ksi$$

$$\sigma_{LL\ 28'} = \frac{M_{LL\ 28'}}{S_{eff\ ST}} = \frac{679\ k.ft}{650\ in^3}\left(\frac{12\ in}{1\ ft}\right) = 12.5\ ksi$$

The Maximum Load limit state is always evaluated in terms of moment. The unfactored moments are given in Table D-4, and the capacity is the plastic moment capacity of the partially composite section:

$$C_{ML\ 28'} = M_{p\ PC} = 2430\ k.ft$$

The rating factor and load rating for the Overload and Maximum Load limit states for this critical location are:

$$RF_{OL\ 28'} = \frac{31.4\ ksi - (1.0)(9.79\ ksi)}{(1.67)(12.5\ ksi)} = 1.03$$

$$RT_{OL\ 28'} = (1.03)(20) = 20.7 \quad \rightarrow \quad HS\ 20.7$$

$$RF_{ML\ 28'} = \frac{2430\ k.ft - (1.3)(442\ k.ft) - (1.0)(52\ k.ft)}{(2.17)(679\ k.ft)} = 1.22$$

$$RT_{ML\ 28'} = (1.22)(20) = 24.5 \quad \rightarrow \quad HS\ 24.5$$

Critical Location at 62' (Section #1):

Because moments are redistributed from the adjacent interior pier section, the Overload capacity is not subjected to the stress limits and is simply the nominal moment capacity of the section. Thus, the capacity for both the Overload and Maximum Load limit states are the same. This capacity was calculated in Section D.2.4 after the addition of the new cross frames around the interior pier:

$$C_{OL\ 62'} = C_{ML\ 62'} = -1720\ k.ft$$

The unfactored moments are given in Table D-4. The rating factor and load rating for the Overload and Maximum Load limit states for this critical location are:

$$RF_{OL\ 62'} = \frac{-1720\ k.ft - (1.0)(-503\ k.ft)}{(1.67)(-432\ k.ft)} = 1.69$$

$$RT_{OL\ 62'} = (1.69)(20) = 33.7 \quad \rightarrow \quad HS\ 33.7$$

$$RF_{ML\ 62'} = \frac{-1720\ k.ft - (1.3)(-503\ k.ft) - (1.0)(111\ k.ft)}{(2.17)(-432\ k.ft)} = 1.26$$

$$RT_{ML\ 62'} = (1.26)(20) = 25.1 \quad \rightarrow \quad HS\ 25.1$$

Critical Location at 70' (Section #2):

Because moments are redistributed from this interior pier section, the Overload and Maximum Load capacities are the effective plastic moments calculated in Section D.2.4:

$$C_{OL\,70'} = M_{pe\,OL} = -2550\ k.ft$$

$$C_{ML\,70'} = M_{pe\,ML} = -2550\ k.ft$$

The unfactored moments are given in Table D-4. The rating factor and load rating for the Overload and Maximum Load limit states for this critical location are:

$$RF_{OL\,70'} = \frac{-2550\ k.ft - (1.0)(-967\ k.ft)}{(1.67)(-657\ k.ft)} = 1.44$$

$$RT_{OL\,70'} = (1.44)(20) = 28.9 \quad \rightarrow \quad HS\ 28.9$$

$$RF_{ML\,70'} = \frac{-2550\ k.ft - (1.3)(-967\ k.ft) - (1.0)(130\ k.ft)}{(2.17)(-657\ k.ft)} = 1.00$$

$$RT_{ML\,70'} = (1.00)(20) = 20.0 \quad \rightarrow \quad HS\ 20.0$$

Critical Location at 76' (Section #1):

Because moments are redistributed from the adjacent interior pier section, the Overload capacity is not subjected to the stress limits and is simply the nominal moment capacity of the section. Thus, the capacity for both the Overload and Maximum Load limit states are the same. This capacity was calculated in Section D.2.4 after the addition of the new cross frames around the interior pier:

$$C_{OL\,76'} = C_{ML\,76'} = -1720\ k.ft$$

The unfactored moments are given in Table D-4. The rating factor and load rating for the Overload and Maximum Load limit states for this critical location are:

$$RF_{OL\ 76'} = \frac{-1720\ k.ft - (1.0)(-606\ k.ft)}{(1.67)(-452\ k.ft)} = 1.48$$

$$RT_{OL\ 76'} = (1.48)(20) = 29.5 \quad \rightarrow \quad HS\ 29.5$$

$$RF_{ML\ 76'} = \frac{-1720\ k.ft - (1.3)(-606\ k.ft) - (1.0)(130\ k.ft)}{(2.17)(-452\ k.ft)} = 1.08$$

$$RT_{ML\ 76'} = (1.08)(20) = 21.7 \quad \rightarrow \quad HS\ 21.7$$

Critical Location at 106.5' (Section #1, N = 16):

The Overload limit state must be addressed in terms of stresses again, because different types of loads are resisted by different sections. The capacity, or limiting stress, for the Overload limit state of a composite section was calculated previously as:

$$C_{OL\ 106.5'} = 31.4\ ksi$$

The unfactored dead and live load stresses are:

$$\sigma_{DL\ 106.5'} = \frac{M_{DL\ 106.5'}}{S_x} = \frac{434\ k.ft}{542\ in^3}\left(\frac{12\ in}{1\ ft}\right) = 9.61\ ksi$$

$$\sigma_{LL\ 106.5'} = \frac{M_{LL\ 106.5'}}{S_{eff\ ST}} = \frac{666\ k.ft}{650\ in^3}\left(\frac{12\ in}{1\ ft}\right) = 12.3\ ksi$$

The Maximum Load limit state is always evaluated in terms of moment. The unfactored moments are given in Table D-4, and the capacity is the plastic moment capacity of the partially composite section:

$$C_{ML\ 106.5'} = M_{p\ PC} = 2430\ k.ft$$

The rating factor and load rating for the Overload and Maximum Load limit states for this critical location are:

$$RF_{OL\ 106.5'} = \frac{31.4\ ksi - (1.0)(9.61\ ksi)}{(1.67)(12.3\ ksi)} = 1.06$$

$$RT_{OL\ 106.5'} = (1.06)(20) = 21.2 \quad \rightarrow \quad HS\ 21.2$$

$$RF_{ML\ 106.5'} = \frac{2430\ k.ft - (1.3)(434\ k.ft) - (1.0)(130\ k.ft)}{(2.17)(666\ k.ft)} = 1.20$$

$$RT_{ML\ 106.5'} = (1.20)(20) = 24.0 \quad \rightarrow \quad HS\ 24.0$$

Critical Location at 115' (Section #3, N = 16):

The Overload limit state must be addressed in terms of stresses again, because different types of loads are resisted by different sections. The capacity, or limiting stress, for the Overload limit state of a composite section was calculated previously as:

$$C_{OL\ 115'} = 31.4\ ksi$$

The unfactored dead and live load stresses are:

$$\sigma_{DL\ 115'} = \frac{M_{DL\ 115'}}{S_x} = \frac{486\ k.ft}{653\ in^3}\left(\frac{12\ in}{1\ ft}\right) = 8.93\ ksi$$

$$\sigma_{LL\ 115'} = \frac{M_{LL\ 115'}}{S_{eff\ ST}} = \frac{694\ k.ft}{757\ in^3}\left(\frac{12\ in}{1\ ft}\right) = 11.0\ ksi$$

The Maximum Load limit state is always evaluated in terms of moment. The unfactored moments are given in Table D-4, and the capacity is the plastic moment capacity of the partially composite section:

$$C_{ML\ 115'} = M_{p\ PC} = 2780\ k.ft$$

The rating factor and load rating for the Overload and Maximum Load limit states for this critical location are:

$$RF_{OL\ 115'} = \frac{31.4\ ksi - (1.0)(8.93\ ksi)}{(1.67)(11.0\ ksi)} = 1.22$$

$$RT_{OL\ 115'} = (1.22)(20) = 24.5 \quad \rightarrow \quad HS\ 24.5$$

$$RF_{ML\ 115'} = \frac{2780\ k.ft - (1.3)(486\ k.ft) - (1.0)(130\ k.ft)}{(2.17)(694\ k.ft)} = 1.34$$

$$RT_{ML\ 115'} = (1.34)(20) = 26.8 \quad \rightarrow \quad HS\ 26.8$$

The results of this load rating for the strengthened girder are summarized in Table D-6. After post-installing the shear connectors and considering moment redistribution, the ***inventory load factor rating of Girder B is increased from HS 13.3 to HS 20.0***. This load rating is controlled by the section at the interior piers at the Maximum Load limit state.

Table D-6: Load Rating Results of Strengthened Girder B

Location (ft)	Section Type	Inventory Load Factor Rating	
		Overload	Maximum Load
28	Critical, Span	HS 20.7	HS 24.5
62	Critical, Transition	HS 33.7	HS 25.1
70	Critical, Pier	HS 28.9	HS 20.0
76	Critical, Transition	HS 29.5	HS 21.7
106.5	Critical, Transition	HS 21.2	HS 24.0
115	Critical, Span	HS 24.5	HS 26.8

D.2.8 Summary of Strengthening Design for Girder B

To strengthen Girder B to a minimum inventory load factor rating of HS 20, a total of 96 adhesive anchor shear connectors should be post-installed and approximately 5% of the factored moment at the interior piers must be redistributed at the Maximum Load limit state. In order to allow for moment redistribution, double-sided 5-inch by 3/8-inch bearing stiffeners need to be installed at the interior piers. Additionally, new cross frames must be

installed to reduce the unbraced length at the interior piers to satisfy the requirements of Appendix B6 of the LRFD specifications. These cross frames should be placed 10 feet into the exterior span and 10.5 feet into the interior span, measured from the interior pier.

The connectors are installed in pairs on opposite sides of the web of the steel beam in a cross section, as illustrated in Figure D-10. The transverse spacing of 6 inches was determined by approximately centering the connectors on the protruding portion of the flange. The connectors are grouped in six locations, with one group located near each end of the positive moment regions in all three spans. The specific connector layout is shown in Figure D-8. This layout can be modified slightly due to constraints in the field during installation, such as transverse deck reinforcing bars or other obstacles.

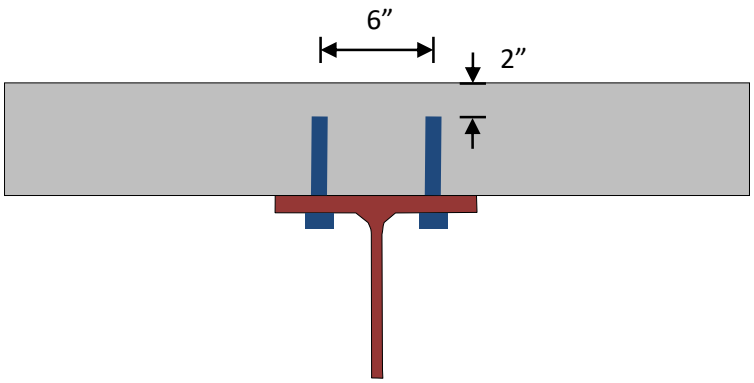

Figure D-10: Cross-Sectional Connector Layout

D.3 Summary of Design Process and Results for Girder A

Girder A is identical to Girder B, so refer to the half-elevation view shown in Figure D-3 and the section properties in Table D-1.

D.3.1 Conduct Structural Analysis

The distribution factor for Girder A is calculated using the lever rule, assuming that the deck acts as a simple span between the girders (Section 3.23.2.3.1.2). This calculation is illustrated in Figure D-11. The wheels of the design truck are spaced 6 feet apart in the transverse direction, and the centerline of the wheel cannot be closer than 2 feet from the curb. The distribution factor for Girder A is thus calculated to be 0.607. Figure D-12 and Table D-7 summarize the results of the structural analysis for Girder A.

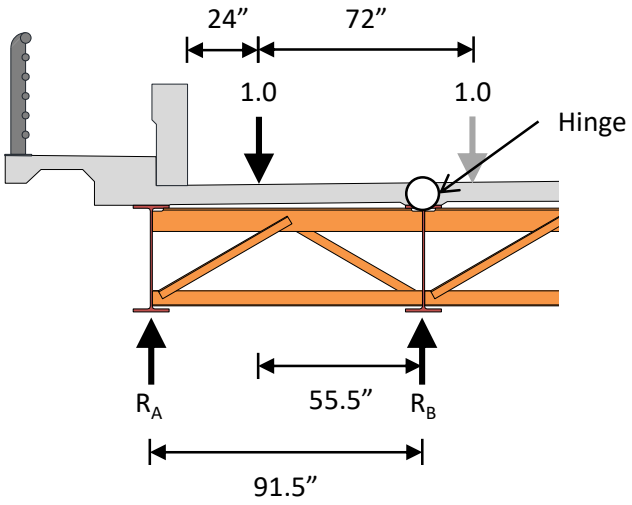

$$\Sigma M_{hinge} = 0 = R_A(91.5\ in) - (1.0)(55.5\ in)$$

$$\rightarrow \quad R_A = DF = 0.607$$

Figure D-11: Lever Rule for Distribution Factor Calculation for Girder A

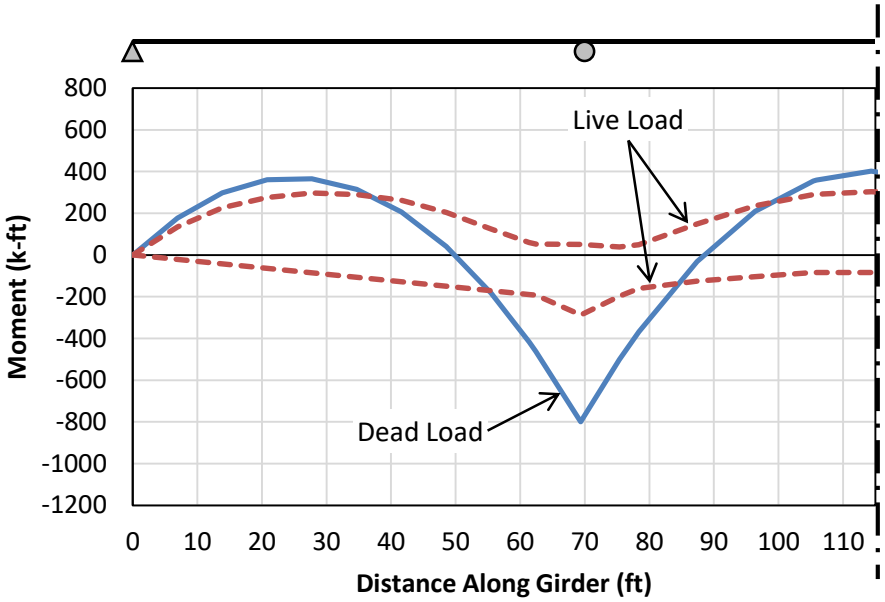

Figure D-12: Plot of Unfactored Moments for Girder A

Table D-7: Unfactored Moments at Critical Sections and at Lateral Brace Locations around the Interior Pier Section in Girder B

Location (ft)	Section Type	Section Number	Unfactored Moment (k-ft)		
			Dead Load	Live Load	
				Pos.	Neg.
28	Critical, Span	1	366	297	-85.4
46.7	Lateral Brace	1	100	225	-142
62	Critical, Transition	1	-416	59.3	-189
70	Critical, Pier and Lateral Brace	2	-800	50.8	-287
76	Critical, Transition	1	-501	29	-198
92.5	Lateral Brace	1	89.5	192	-114
106.5	Critical, Transition	1	359	291	-83.4
115	Critical, Span	3	402	303	-83.4

D.3.2 Evaluate Existing Non-Composite Girder

All of the capacity calculations are for Girder A are identical to those for Girder B. The results of the load rating for Girder A are summarized in Table D-8. The controlling load rating is HS 33.2, which occurs at the Overload limit state at the critical section at the maximum positive moment in the exterior span (28'). All of the load ratings are greater than the target value of HS 20, so no strengthening is necessary for this girder. This is because it is subjected to minimal amounts of traffic load in comparison to the other girders. Although the check is not shown here, the girder is also adequate for the combination of sidewalk and traffic loading in the Standard specifications.

Table D-8: Load Rating Results of Existing Non-Composite Girder A

Location (ft)	Section Type	Capacity (k-ft)		Inventory Load Rating	
		Overload	Maximum Load	Overload	Maximum Load
28	Critical, Span	1190	1720	HS 33.2	HS 38.1
62	Critical, Transition	-1190	-1490	HS 49.0	HS 45.7
70	Critical, Pier	-1800	-2250	HS 41.7	HS 38.3
76	Critical, Transition	-1190	-1490	HS 41.7	HS 38.5
106.5	Critical, Transition	1190	1720	HS 34.2	HS 39.2
115	Critical, Span	1440	2050	HS 41.0	HS 45.8

D.3.3 Summary of Strengthening Design for Girder A

The ***existing non-composite Girder A has an inventory load factor rating of HS 33.2***. Thus, ***no strengthening is necessary*** for this girder.

D.4 Summary of Design Process and Results for Girder C

A half-elevation view of Girder C is shown in Figure D-13. This girder was built as part of the original bridge in 1943. It is constructed of a 36WF150 rolled steel shape, with cover plates riveted to the top and bottom flange at the interior pier and in the middle of the interior span. Table D-9 summarizes the section properties for design for the steel beam (Section 1), as well as for the steel beam with cover plates at the interior pier (Sections 2 and 3) and in the interior span (Section 3). Note that because this girder sits on the boundary between the original and widened portions of the bridge, the deck thickness and girder spacing are different on either side of the girder. Thus, average values of the deck properties are used here.

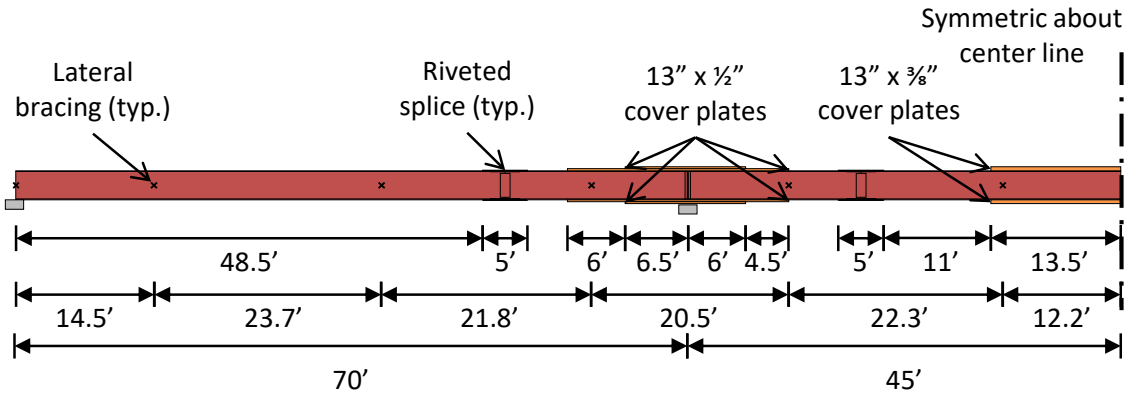

Figure D-13: Half-Elevation View of Girder C

Table D-9: Section Properties for Girder C

	Section 1	Section 2	Section 3	Section 4
Cover plate width (b_{pl}, in)	0	13.0	13.0	13.0
Cover plate thickness (t_{pl}, in)	0	0.500	1.00	0.375
Flange width (b_f, in)	12.0	12.0	12.0	12.0
Flange thickness (t_f, in)	0.940	0.940	0.940	0.940
Flange area (A_f, in^2)	11.3	17.8	24.3	16.2
Flange moment of inertia (I_{yc}, in^4)	135	227	318	204
Total depth (d, in)	35.9	36.9	37.9	36.7
Web thickness (t_w, in)	0.625	0.625	0.625	0.625
Area (A_s, in^2)	44.3	57.3	70.3	54.1
Moment of inertia (I_x, in^4)	9040	13300	17900	12200
Elastic section modulus (S_x, in^3)	504	723	944	668
Plastic section modulus (Z_x, in^3)	581	818	1060	758
Radius of gyration (r_y, in)	2.47	2.81	3.01	2.75
Polar moment of inertia (J, in^4)	10.1	11.2	18.8	10.6
Web depth (D, in)	34.0	34.0	34.0	34.0
Depth of web in compression, elastic (D_c, in)	17.0	17.0	17.0	17.0
Depth of web in compression, plastic (D_{cp}, in)	17.0	17.0	17.0	17.0
Effective deck width (b_{deck}, in) and girder spacing (S, in)	92.8	92.8	92.8	92.8
Deck thickness (t_{deck}, in)	7.25	7.25	7.25	7.25
Deck area (A_{deck}, in^2)	673	673	673	673
Deck moment of inertia (I_{deck}, in^4)	2950	2950	2950	2950

D.4.1 Conduct Structural Analysis

The distribution factor for interior Girder C is calculated to be 1.41. Figure D-14 and Table D-10 summarize the results of the structural analysis for Girder C.

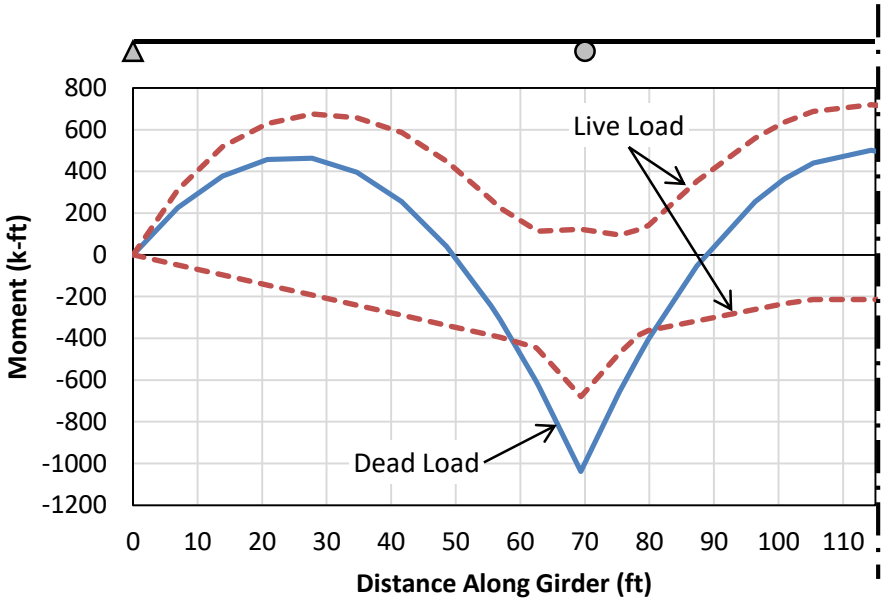

Figure D-14: Plot of Unfactored Moments for Girder C

Table D-10: Unfactored Moments at Critical Sections and at Lateral Brace Locations around the Interior Pier Section in Girder C

Location (ft)	Section Type	Section Number	Unfactored Moment (k-ft)		
			Dead Load	Live Load	
				Pos.	Neg.
28	Critical, Span	1	463	676	-193
38.2	Lateral Brace	1	338	628	-261
57.5	Critical, Transition	1	-311	225	-395
60	Lateral Brace	2	-438	179	-417
63.5	Critical, Transition	2	-630	114	-457
70	Critical, Pier	3	-1038	123	-679
76	Critical, Transition	2	-655	94.7	-470
80.5	Critical, Transition and Lateral Brace	1	-404	142	-363
101.5	Critical, Transition	1	363	635	-234
102.8	Lateral Brace	4	384	649	-229
115	Critical, Span	4	502	720	-215

D.4.2 Evaluate Existing Non-Composite Girder

All of the capacity calculations for Girder C are done in the same manner to those for Girder B. The results of these and of the load rating calculations for Girder C are summarized in Table D-11. The controlling load rating is HS 11.5, which occurs at the Overload limit state at the critical section at the maximum positive moment in the exterior span (28'). In fact, this is the controlling load rating for all of the steel beams.

Table D-11: Load Rating Results of Existing Non-Composite Girder C

Location (ft)	Section Type	Capacity (k-ft)		Inventory Load Rating	
		Overload	Maximum Load	Overload	Maximum Load
28	Critical, Span	1110	1600	HS 11.5	HS 13.4
57.5	Critical, Transition	-1110	-1390	HS 24.2	HS 22.7
63.5	Critical, Transition	-1590	-1990	HS 25.2	HS 23.3
70	Critical, Pier	-2080	-2600	HS 18.4	HS 16.7
76	Critical, Transition	-1590	-1990	HS 23.8	HS 22.0
80.5	Critical, Transition	-1110	-1390	HS 23.3	HS 21.7
101.5	Critical, Transition	1110	1600	HS 14.1	HS 16.2
115	Critical, Span	1470	2080	HS 16.1	HS 18.0

D.4.3 Set Strengthening Targets

The same strengthening targets are used for Girder C as for Girder B. Thus, the goals of the strengthening design are to increase the inventory load factor rating to HS 20, and to provide a minimum remaining life of 25 years for the purposes of fatigue design of the post-installed shear connectors. The same average annual daily truck traffic ($(ADTT)_{SL}$) of 1160 trucks per day will be used.

D.4.4 Check Negative Moment Regions and Redistribute Moments

In a similar manner to Girder B, the capacity of the negative moment regions at the interior piers (70') of Girder C is evaluated and compared to the factored moments at the Overload and Maximum Load limit states to determine whether or not inelastic moment redistribution is needed. The factored moments are calculated from those given in Table

D-10. Because these regions will remain non-composite, the capacities are the same as those in Table D-11. A summary of these values is given in Table D-12.

Table D-12: Necessity of Moment Redistribution for Girder C

Factored Overload moment ($M_{u\ OL}$, k-ft)	-2170
Factored Maximum Load moment ($M_{u\ ML}$, k-ft)	-2840
Overload capacity (C_{OL}, k-ft)	-2080
Maximum Load capacity (C_{ML}, k-ft)	-2600

The factored moment at the interior pier section exceeds the capacity at both the Overload and Maximum Load limit states. This means that ***moment redistribution should be considered at both limit states***. As with the design of Girder B, the requirements from Appendix B6 of the LRFD specifications must be satisfied to allow for moment redistribution:

1. The bridge must be straight with supports not skewed more than 10° $\rightarrow$ OK
2. The specified minimum yield stress does not exceed 70 ksi $\rightarrow$ OK
3. Holes in the tension flange may not be present within a distance of twice the web depth from each interior pier section from which moments are redistributed $\rightarrow$ $NOT\ OK$

   Because this girder has riveted cover plates on the top and bottom flanges at the interior pier section, this requirement is not satisfied, although the holes are filled completely with rivets. Although there is little to no literature available about the inelastic moment-rotation behavior of wide flange steel beams with riveted cover plates, tests on riveted plate connections have not indicated any significant lack of ductility or otherwise poor behavior that would adversely impact the moment-rotation behavior. In this case, engineering judgement is used to eliminate this requirement, and allow for moment redistribution. Additionally, essentially no redistribution is actually necessary (as is calculated later), and the extent of inelastic behavior in this region is expected to be minimal.
4. Web proportion requirements $\rightarrow$ OK
5. Compression flange proportion requirements $\rightarrow$ OK
6. Compression flange bracing requirements

As with Girder B, because one the cover plates terminates within the unbraced length, the properties of the smallest section (Section 2) are used to be conservative. The calculations result in:

$L_b = 20.5\ ft > 10.3\ ft = L_{b\ limiting} \ \rightarrow \ NOT\ OK$

Thus, the existing cross frames do not provide adequate lateral bracing to allow for moment redistribution. To redistribute moments in this girder, ***at least one additional cross frame must be added at or near the interior pier to reduce the unbraced length***.

Recall that there is not a cross frame located at the centerline of this interior support, although there are cross frames at this location on Girders A and B which were constructed at a later date. Thus, ***add a cross frame at the centerline of the interior pier*** for this girder. This reduces the unbraced length to 10 feet in the exterior span and to 10.5 feet in the interior span. Repeating the calculations for the limiting unbraced lengths with an additional cross frame located at the interior pier shows that the new unbraced lengths satisfy the lateral bracing requirements:

$L_{b\ ext} = 10.0\ ft < 15.3\ ft \ \rightarrow \ OK$

$L_{b\ int} = 10.5\ ft < 16.1\ ft \ \rightarrow \ OK$

7. There shall be no section transitions within the unbraced length of the interior pier section $\rightarrow \ NOT\ OK$

   Because the cover plates at the interior pier terminate within the adjacent unbraced lengths from the pier, this requirement is actually not satisfied. However, for the same reasons discussed in the design for Girder B, namely that the section properties used in calculating the lateral-torsional buckling requirements and that the controlling section in negative flexure is the centerline of the interior pier, not the section transitions at the ends of the cover plates, this requirement is ignored. The reduced flexural capacity at each transition need to be checked against the factored moments after redistribution to ensure that the section has adequate strength.

   Note that alternatively, this requirement could be directly satisfied by adding two cross frames and placing each at or closer to the interior pier than the ends of the cover plate.

8. The shear limit state must not be exceeded within the unbraced lengths adjacent to the interior pier regions. $\rightarrow \ OK$

Although a check for shear is not shown here, the shear strength requirements are satisfied for this girder.

9. Bearing stiffeners must be present at the interior pier locations $\rightarrow$ OK

   Riveted bearing stiffeners constructed of L-shapes are present at the interior support on this girder

Assuming that at least one additional cross frame is added at or near the interior support to satisfy number 6 in the preceding list, moment redistribution can be allowed for this girder. Table D-13 summarizes the results of calculations for the redistribution moment, following the provisions in Section B6.5 of the LRFD specifications in a similar manner to the design of Girder B.

Table D-13: Results from Moment Redistribution Calculations for Girder C

Ultracompact web?	Yes
Effective plastic moment at Overload ($M_{pe\ OL}$, k-ft)	2920
Effective plastic moment at Maximum Load ($M_{pe\ ML}$, k-ft)	2920
Overload redistribution moment ($M_{rd\ OL}$, k-ft)	-750 → 0
Maximum Load redistribution moment (M_{rd_ML}, k-ft)	-80.0 → 0

Although it was determined previously that moment redistribution is necessary at both the Overload and the Maximum Load limit states, in fact no moment redistribution is actually needed at either limit state. For the Overload limit state, this is again because of the significant increase in the strength that is attributed to the section when considering moment redistribution from the strength defined by the stress limit of 80% of the yield stress. For the Maximum Load limit state, this is a result of the addition of at least one cross frame that allows the section to reach the full plastic moment capacity without lateral-torsional buckling occurring. Thus, while moment redistribution needs to be considered and the aforementioned requirements of Section B6.2 of the LRFD specifications should be followed including the addition of one or more cross frames, ***no redistribution moments are necessary for the design of Girder C***.

D.4.5 Design Connectors for Positive Moment Regions

In a similar manner to Girder B, the partially composite positive moment regions are now designed and checked at both the Overload and Maximum Load limit states. For this girder, a different design needs to be conducted for the exterior span, which has a critical section at 28', and for the middle span, which has a critical section at 115'. The design is also checked at the transition location at the termination of the cover plate in the interior span at 101.5'.

Table D-14 summarizes the results from these calculations. As with Girder B, the partially composite design was begun with the minimum recommended composite ratio of 0.3, which ended up controlling the design in the interior span. However, in the exterior spans, a composite ratio of 0.66 is necessary to satisfy the requirements of the Overload limit state.

Table D-14: Results from Partially Composite Design Calculations for Girder C

	28'	**115'**	**101.5'**
Section number	1	4	1
Factored Maximum Load moment ($M_{u\,ML}$, k-ft)	2090	2340	1870
Deck force, fully composite ($C_{f\,FC}$, k)	1710	1710	1710
Number of connectors, fully composite (N_{FC})	48.6	57.0	48.6
Plastic web force ($P_{y\,web}$, k)	717	717	717
Plastic neutral axis location, fully composite	Deck	Flange	Deck
Plastic moment, fully composite ($M_{p\,FC}$, k-ft)	2690	3240	2690
Short term moment of inertia, fully composite ($I_{tr\,ST}$, in^4)	22200	27000	22200
Short term section modulus, fully composite ($S_{tr\,ST}$, in^3)	707	869	707
Long term moment of inertia, fully composite ($I_{tr\,ST}$, in^4)	16400	20100	16400
Long term section modulus, fully composite ($S_{tr\,ST}$, in^3)	642	793	642
Number of connectors, partially composite (N_{PC})	32	18	18
Actual composite ratio	0.658	0.316	0.370
Deck force, partially composite ($C_{f\,PC}$, k)	962	541	541
Plastic neutral axis location, partially composite	Flange	Web	Web
Plastic moment, partially composite ($M_{p\,PC}$, k-ft)	2590	2890	2390
Short term section modulus, partially composite ($S_{eff\,ST}$, in^3)	669	781	627
Long term section modulus, partially composite ($S_{eff\,LT}$, in^3)	616	739	588
Factored Overload stress ($\sigma_{u\,OL}$, ksi)	31.3	21.9	22.0
Maximum allowed Overload stress (σ_{max}, ksi)	31.4	31.4	31.4

The plastic moment capacity exceeds the factored moment at the Maximum Load limit state at all three locations. The maximum allowed stress also exceeds the factored stress at the Overload limit state at all three locations. Thus, the requirements for both limit

states are satisfied with this design, so ***use $N = 32$ in the exterior spans and $N = 18$ in the interior span on Girder C***.

D.4.6 Locate Connectors and Check Fatigue

The connector layout in Figure D-15 is proposed, based on the same recommendations given in previous research as were used in the design of Girder B. However, the layout has been modified to avoid the splice plates, shown as green lines in the figure, and cover plates, shown as orange lines in the figure. It is not practical to post-install adhesive anchor shear connectors through these riveted plates. Thus, the connector groups nearest to the interior support in the exterior span have to be located farther than the recommended 15% of the span length. The connector groups in the interior span have been shifted closer than the recommended 15% of the span length to the interior support to compensate. Additionally, there is a 6-ft gap within each connector group to avoid the splice plates. The final positioning of the connector groups was determined by trial and error to determine the minimum overall fatigue demand on the connectors while keeping all connectors outside of the splice and cover plate regions. Because the girder is symmetric, only the left half is shown in the figure. Within a group, the connectors are spaced at 12 inches, which is equal to the transverse rebar spacing in the deck. The connector nearest to the end of the girder is located 6 inches away from the centerline of the support, and no connector is closer than 6 inches to a cover plate.

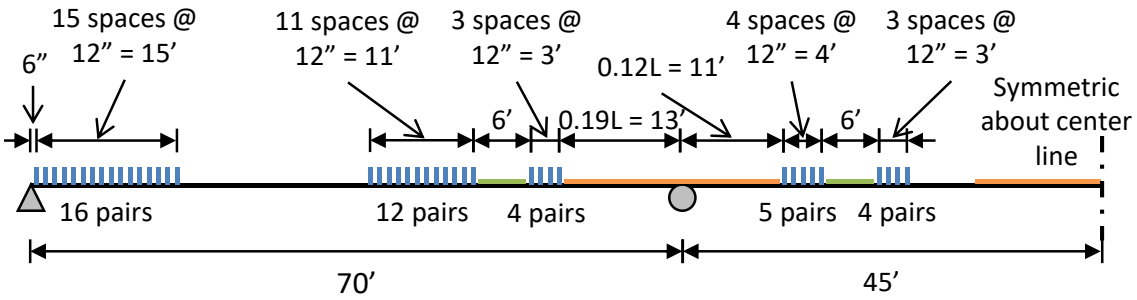

Figure D-15: Connector Layout for Girder C

The fatigue check is conducted in the same manner as for Girder B. Because the predicted truck traffic and required remaining life are the same as for Girder B, the nominal fatigue resistance of a single connector is also the same ($(\Delta F)_n = 17.5\ ksi$).

Figure D-16 shows the results from the fatigue analysis, conducted in the same way as for Girder B, which explicitly considers the interface slip and uses a stiffness of 900 kips per inch for the linear springs that represent each shear connector. The figure plots the stress range in each connector induced by the fatigue loading defined in the Fatigue II load combination in the LRFD specifications. Because of symmetry, only one-half of the girder is shown.

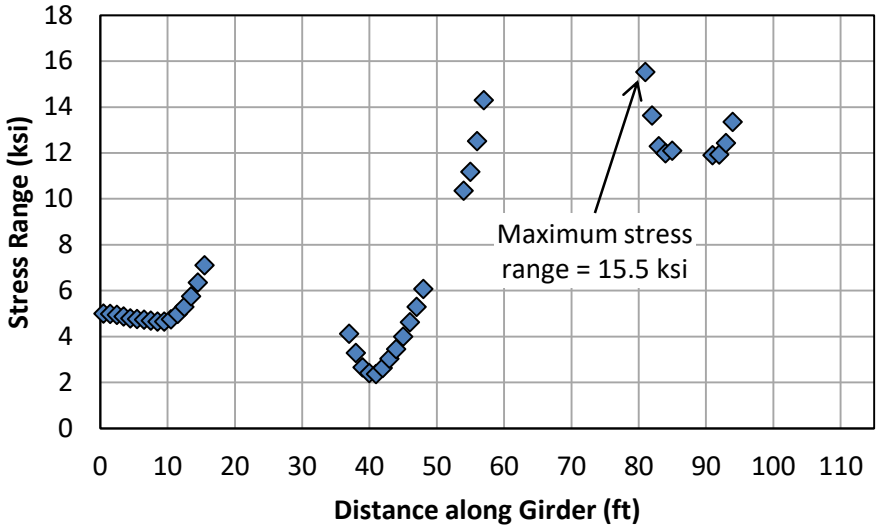

Figure D-16: Results from Fatigue Analysis for Girder C

The maximum stress range (ΔF) that a connector undergoes during fatigue loading is 15.5 ksi. As shown in the figure, this critical connector is the closest connector to the interior support in the interior span. This maximum stress range is less than the nominal fatigue resistance (17.5 ksi), indicating that ***the connectors have adequate fatigue life to satisfy the design requirement of a 25-year remaining life***. By reversing the design equations, ***the connectors in Girder C are estimated to have a remaining fatigue life of 58 years***.

D.4.7 Conduct Load Rating of Strengthened Girder

A load rating of the strengthened girder is carried out in the same manner as for Girder B. The results of this load rating are summarized in Table D-15. After post-installing the shear connectors and considering moment redistribution, the ***inventory load***

factor rating of Girder C is increased from HS 11.5 to HS 20.1. This load rating is controlled by the section near the middle of the exterior spans at the Overload limit state.

Table D-15: Load Rating Results of Strengthened Girder C

Location (ft)	Section Type	Inventory Load Factor Rating	
		Overload	Maximum Load
28	Critical, Span	HS 20.1	HS 27.1
57.5	Critical, Transition	HS 24.2	HS 27.8
63.5	Critical, Transition	HS 42.5	HS 28.8
70	Critical, Pier	HS 33.2	HS 21.3
76	Critical, Transition	HS 40.7	HS 27.4
80.5	Critical, Transition	HS 23.3	HS 27.3
101.5	Critical, Transition	HS 22.3	HS 27.8
115	Critical, Span	HS 24.2	HS 28.7

D.4.8 Summary of Design for Girder C

To strengthen Girder C to a minimum inventory load factor rating of HS 20, ***a total of 164 adhesive anchor shear connectors should be post-installed.*** While moment redistribution does need to be considered, ***no actual moments need to be redistributed at either the Overload or Maximum Load limit state***. However, ***additional lateral bracing must be provided to the girder at the interior piers*** to reduce the unbraced length to satisfy the requirements of Appendix B6 of the LRFD specifications.

The connectors are installed in pairs on opposite sides of the web of the steel beam through a cross section, as illustrated in Figure D-10. They are grouped in six locations, with one group located near each end of the positive moment regions in all three spans. The specific connector layout is shown in Figure D-15. This layout can be modified slightly due to constraints in the field during installation, such as transverse deck reinforcing bars or other obstacles.

After post-installing the shear connectors and considering moment redistribution, the ***inventory load factor rating of Girder C is increased from HS 11.5 to HS 20.1***. This load rating is controlled in the strengthened bridge by the section near the middle of the exterior spans at the Overload limit state.

D.5 Summary of Design Process and Results for Girder D

A half-elevation view of Girder D is shown in Figure D-17. This girder was built as part of the original bridge in 1943. It is constructed of a 36WF150 rolled steel shape, with cover plates riveted to the top and bottom flange at the interior pier and in the middle of all three spans. Table D-16 summarizes the section properties for design for the steel beam (Section 1), as well as for the steel beam with cover plates in the exterior spans (Section 2), at the interior pier (Sections 3 and 4) and in the interior span (Section 3).

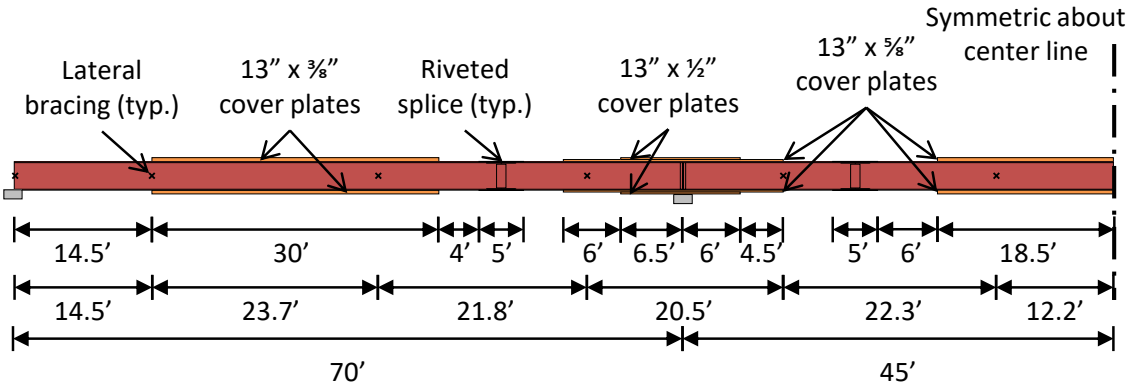

Figure D-17: Half-Elevation View of Girder D

Table D-16: Section Properties for Girder D

	Section 1	Section 2	Section 3	Section 4
Cover plate width (b_{pl}, in)	0	13.0	13.0	13.0
Cover plate thickness (t_{pl}, in)	0	0.375	0.625	1.125
Flange width (b_f, in)	12.0	12.0	12.0	12.0
Flange thickness (t_f, in)	0.940	0.940	0.940	0.940
Flange area (A_f, in^2)	11.3	16.2	19.4	25.9
Flange moment of inertia (I_{yc}, in^4)	135	204	250	341
Total depth (d, in)	35.9	36.7	37.2	38.2
Web thickness (t_w, in)	0.625	0.625	0.625	0.625
Area (A_s, in^2)	44.3	54.1	60.6	73.6
Moment of inertia (I_x, in^4)	9040	12200	14500	19100
Elastic section modulus (S_x, in^3)	504	668	778	999
Plastic section modulus (Z_x, in^3)	581	758	878	1120
Radius of gyration (r_y, in)	2.47	2.75	2.87	3.04
Polar moment of inertia (J, in^4)	10.1	10.6	12.2	22.4
Web depth (D, in)	34.0	34.0	34.0	34.0
Depth of web in compression, elastic (D_c, in)	17.0	17.0	17.0	17.0
Depth of web in compression, plastic (D_{cp}, in)	17.0	17.0	17.0	17.0
Effective deck width (b_{deck}, in) and girder spacing (S, in)	94.5	94.5	94.5	94.5
Deck thickness (t_{deck}, in)	8	8	8	8
Deck area (A_{deck}, in^2)	756	756	756	756
Deck moment of inertia (I_{deck}, in^4)	4030	4030	4030	4030

D.5.1 Conduct Structural Analysis

The distribution factor for interior Girder D is calculated to be 1.43. Figure D-18 and Table D-17 summarize the results of the structural analysis for Girder D.

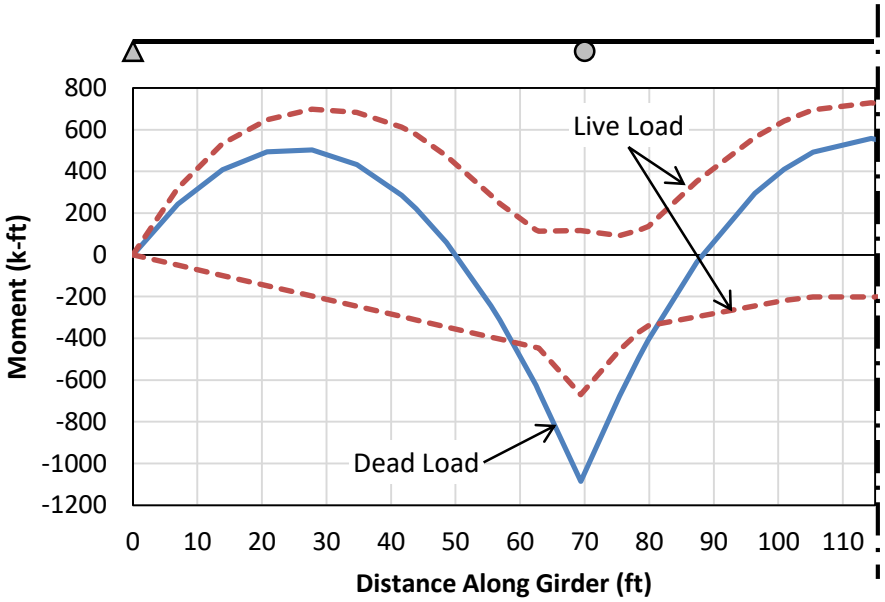

Figure D-18: Plot of Unfactored Moments for Girder D

Table D-17: Unfactored Moments at Critical Sections and at Lateral Bracing in Girder D

Location (ft)	Section Type	Section Number	Unfactored Moment (k-ft)		
			Dead Load	Live Load	
				Pos.	Neg.
14.5	Critical, Transition	1	408	533	-98.6
28	Critical, Span	2	503	698	-197
38.2	Lateral Brace	2	372	654	-267
44.5	Critical, Transition	1	221	577	-312
57.5	Critical, Transition	1	-313	246	-394
60	Lateral Brace	3	-454	189	-422
63.5	Critical, Transition	3	-652	114	-447
70	Critical, Pier	4	-1090	117	-670
76	Critical, Transition	3	-677	92.4	-458
80.5	Critical, Transition and Lateral Brace	1	-408	137	-340
96.5	Critical, Transition	1	295	563	-245
102.8	Lateral Brace	3	433	657	-214
115	Critical, Span	3	558	729	-202

D.5.2 Evaluate Existing Non-Composite Girder

All of the capacity calculations for Girder D are done in the same manner to those for Girder B. The results of these and of the load rating calculations for Girder D are summarized in Table D-18. The ***controlling load rating is HS 15.8***, which occurs at the Overload limit state at the end of the cover plate in the exterior span nearest the exterior support (14.5').

Table D-18: Load Rating Results of Existing Non-Composite Girder D

Location (ft)	Section Type	Capacity (k-ft)		Inventory Load Rating	
		Overload	Maximum Load	Overload	Maximum Load
14.5	Critical, Transition	1110	1600	HS 15.8	HS 18.2
28	Critical, Span	1470	2080	HS 16.6	HS 18.6
44.5	Critical, Transition	1110	1600	HS 18.5	HS 20.7
57.5	Critical, Transition	-1110	-1600	HS 24.2	HS 27.5
63.5	Critical, Transition	-1710	-2140	HS 28.3	HS 26.3
70	Critical, Pier	-2200	-2750	HS 19.8	HS 18.1
76	Critical, Transition	-1710	-2140	HS 27.0	HS 25.0
80.5	Critical, Transition	-1110	-1390	HS 24.7	HS 23.0
96.5	Critical, Transition	1110	1600	HS 17.3	HS 19.6
115	Critical, Span	1710	2410	HS 18.9	HS 21.0

D.5.3 Set Strengthening Targets

The same strengthening targets are used for Girder D as for Girder B. Thus, the goals of the strengthening design are to increase the inventory load factor rating to HS 20, and to provide a minimum remaining life of 25 years for the purposes of fatigue design of the post-installed shear connectors. The same average annual daily truck traffic ($(ADTT)_{SL}$) of 1160 trucks per day will be used.

D.5.4 Check Negative Moment Regions and Redistribute Moments

In a similar manner to Girder B, the capacity of the negative moment regions at the interior piers (70') of Girder D is evaluated and compared to the factored moments at the Overload and Maximum Load limit states to determine whether or not inelastic moment redistribution is needed. The factored moments are calculated from those given in Table D-18. Because these regions will remain non-composite, the capacities are the same as those in Table D-17. A summary of these values is given in Table D-19.

Table D-19: Necessity of Moment Redistribution for Girder D

Factored Overload moment ($M_{u\,OL}$, k-ft)	-2210
Factored Maximum Load moment ($M_{u\,ML}$, k-ft)	-2890
Overload capacity (C_{OL}, k-ft)	-2200
Maximum Load capacity (C_{ML}, k-ft)	-2750

The factored moment at the interior pier section exceeds the capacity at both the Overload and Maximum Load limit states. This means that ***moment redistribution should be considered at both limit states***. As with the design of Girder B, the requirements from Appendix B6 of the LRFD specifications must be satisfied to allow for moment redistribution:

1. The bridge must be straight with supports not skewed more than 10° $\rightarrow$ OK
2. The specified minimum yield stress does not exceed 70 ksi $\rightarrow$ OK
3. Holes in the tension flange may not be present within a distance of twice the web depth from each interior pier section from which moments are redistributed $\rightarrow$ $NOT\ OK$

   As with Girder C, because this girder has riveted cover plates on the top and bottom flanges at the interior pier section, this requirement is not satisfied. However, in a similar manner as with Girder C, engineering judgement is used to eliminate this requirement in this case. This is partially because limited experimental testing of riveted connections has not indicated a lack of ductility, and only a minimal amount of redistribution is actually necessary in this case so the extent of inelastic behavior is expected to be minimal.
4. Web proportion requirements $\rightarrow$ OK
5. Compression flange proportion requirements $\rightarrow$ OK
6. Compression flange bracing requirements

   As with Girder B, because one the cover plates terminates within the unbraced length, the properties of the smallest section (Section 2) are used to be conservative. The calculations result in:

   $L_b = 20.5\ ft > 10.9\ ft = L_{b\ limiting}$ $\rightarrow$ $NOT\ OK$

   Thus, the existing cross frames do not provide adequate lateral bracing to allow for moment redistribution. To redistribute moments in this girder, ***at***

least one additional cross frame must be added at or near the interior pier to reduce the unbraced length.

Recall that there is not a cross frame located at the centerline of this interior support, although there are cross frames at this location on Girders A and B which were constructed at a later date. Thus, ***add a cross frame at the centerline of the interior pier*** for this girder. This reduces the unbraced length to 10 feet in the exterior span and to 10.5 feet in the interior span. Repeating the calculations for the limiting unbraced lengths with an additional cross frame located at the interior pier shows that the new unbraced lengths satisfy the lateral bracing requirements:

$L_{b\,ext} = 10.0\,ft < 15.2\,ft \;\rightarrow\; OK$

$L_{b\,int} = 10.5\,ft < 16.3\,ft \;\rightarrow\; OK$

7. There shall be no section transitions within the unbraced length of the interior pier section $\rightarrow\; NOT\ OK$

   Because the cover plates at the interior pier terminate within the adjacent unbraced lengths from the pier, this requirement is actually not satisfied. However, for the same reasons discussed in the design for Girder B, namely that the section properties used in calculating the lateral-torsional buckling requirements and that the controlling section in negative flexure is the centerline of the interior pier, not the section transitions at the ends of the cover plates, this requirement is ignored. The reduced flexural capacity at each transition need to be checked against the factored moments after redistribution to ensure that the section has adequate strength.

   Note that alternatively, this requirement could be directly satisfied by adding two cross frames and placing each at or closer to the interior pier than the ends of the cover plate.

8. The shear limit state must not be exceeded within the unbraced lengths adjacent to the interior pier regions. $\rightarrow\; OK$

   Although a check for shear is not shown here, the shear strength requirements are satisfied for this girder.

9. Bearing stiffeners must be present at the interior pier locations $\rightarrow\; OK$

   Riveted bearing stiffeners constructed of L-shapes are present at the interior support on this girder

Assuming that at least one additional cross frame is added at or near the interior support to satisfy number 6 in the preceding list, moment redistribution can be allowed for this girder. Table D-20 summarizes the results of calculations for the redistribution moment, following the provisions in Section B6.5 of the LRFD specifications in a similar manner to the design of Girder B.

Table D-20: Results from Moment Redistribution Calculations for Girder D

Ultracompact web?	Yes
Effective plastic moment at Overload ($M_{pe\ OL}$, k-ft)	3080
Effective plastic moment at Maximum Load ($M_{pe\ ML}$, k-ft)	3080
Overload redistribution moment ($M_{rd\ OL}$, k-ft)	-870 → 0
Maximum Load redistribution moment (M_{rd_ML}, k-ft)	-190 → 0

Although it was determined previously that moment redistribution is necessary at both the Overload and the Maximum Load limit states, in fact no moment redistribution is actually needed at either limit state. For the Overload limit state, this is again because of the significant increase in the strength that is attributed to the section when considering moment redistribution from the strength defined by the stress limit of 80% of the yield stress. For the Maximum Load limit state, this is a result of the addition of at least one cross frame that allows the section to reach the full plastic moment capacity without lateral-torsional buckling occurring. Thus, while moment redistribution needs to be considered and the aforementioned requirements of Section B6.2 of the LRFD specifications should be followed including the addition of one or more cross frames, ***no redistribution moments are necessary for the design of Girder D***.

D.5.5 Design Connectors for Positive Moment Regions

In a similar manner to Girder B, the partially composite positive moment regions are now designed and checked at both the Overload and Maximum Load limit states. For this girder, a different design needs to be conducted for the exterior span, which has a critical section at 28', and for the middle span, which has a critical section at 115'. The design is also checked at the transition locations at the termination of the cover plate in the exterior span at 14.5' and 44.5', as well as in the interior span at 96.5'.

Table D-21 summarizes the results from these calculations. As with Girder B, the partially composite design was begun with the minimum recommended composite ratio of 0.3, which ended up controlling the design.

Table D-21: Results from Partially Composite Design Calculations for Girder D

	28'	**14.5'**	**44.5'**	**115'**	**96.5'**
Section number	2	1	1	3	1
Factored moment ($M_{u\,ML}$, k-ft)	2190	1700	1560	2330	1620
Deck force, fully composite ($C_{f\,FC}$, k)	1780	1460	1460	1920	1460
Number of connectors, fully composite (N_{FC})	59.3	48.6	48.6	63.8	48.6
Plastic web force ($P_{y\,web}$, k)	717	717	717	717	717
Plastic neutral axis location, fully composite	Deck	Deck	Deck	Flange	Deck
Plastic moment, fully composite ($M_{p\,FC}$, k-ft)	3360	2790	2790	3730	2790
Short term moment of inertia, fully composite ($I_{tr\,ST}$, in^4)	28300	23300	23300	31600	23300
Short term section modulus, fully composite ($S_{tr\,ST}$, in^3)	1540	1300	1300	1700	1300
Long term moment of inertia, fully composite ($I_{tr\,ST}$, in^4)	2110	17300	17300	23600	17300
Long term section modulus, fully composite ($S_{tr\,ST}$, in^3)	1150	962	962	1270	962
Number of connectors, partially composite (N_{PC})	18	18	18	20	20
Actual composite ratio	0.303	0.370	0.370	0.314	0.411
Deck force, partially composite ($C_{f\,PC}$, k)	541	541	541	601	601
Plastic neutral axis location, partially composite	Web	Web	Web	Web	Web
Plastic moment, partially composite ($M_{p\,PC}$, k-ft)	2920	2420	2420	3320	2470
Short term section modulus, partially composite ($S_{eff\,ST}$, in^3)	1080	986	986	1290	1010
Long term section modulus, partially composite ($S_{eff\,LT}$, in^3)	859	782	782	1050	797
Factored Overload stress ($\sigma_{u\,OL}$, ksi)	16.8	16.2	12.3	15.4	13.7
Maximum allowed Overload stress (σ_{max}, ksi)	31.4	31.4	31.4	31.4	31.4

The plastic moment capacity exceeds the factored moment at the Maximum Load limit state at all five locations. The maximum allowed stress also exceeds the factored stress at the Overload limit state all five locations. Thus, the requirements for both limit states are satisfied with this design, so ***use $N = 18$ in the exterior spans and $N = 20$ in the interior span on Girder D***.

D.5.6 Locate Connectors and Check Fatigue

The connector layout in Figure D-19 is proposed, based on the same recommendations given in previous research as were used in the design of Girder B. However, in a similar manner as with Girder C, the layout has been modified to avoid the splice plates, shown as green lines in the figure, and cover plates, shown as orange lines in the figure. It is not practical to post-install adhesive anchor shear connectors through these riveted plates. Thus, the connector groups nearest to the interior support in the exterior span have to be located farther than the recommended 15% of the span length. The connector groups in the interior span have been shifted closer than the recommended 15% of the span length to the interior support to compensate. Additionally, there is a 5-ft 8-in gap within the connector group nearest the interior support in the exterior span and a 6-ft gap within the connector group nearest the interior support in the interior span to avoid the splice plates. Due to the limited available space between plates in the exterior span, the connectors nearest the interior support in this span are spaced at 10 inches, which is not a multiple of the transverse rebar spacing in the deck. During installation, minor adjustments can be made to this spacing to avoid the reinforcement as needed. Use of a rebar locater is highly recommended. All other connectors are spaced at 12 inches, which is equal to the transverse rebar spacing. The final positioning of the connector groups was determined by trial and error to determine the minimum overall fatigue demand on the connectors while keeping all connectors outside of the splice and cover plate regions. Because the girder is symmetric, only the left half is shown in the figure. The connector nearest to the end of the girder is located 6 inches away from the centerline of the support, and no connector is closer than 6 inches to a cover plate.

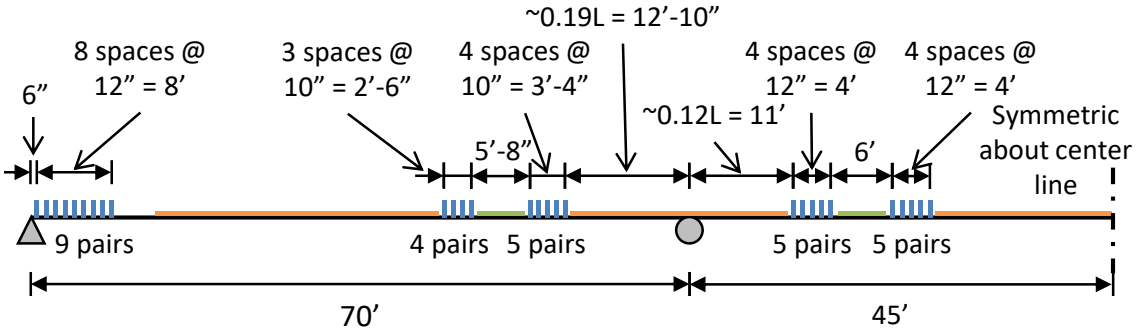

Figure D-19: Connector Layout for Girder D

The fatigue check is conducted in the same manner as for Girder B. Because the predicted truck traffic and required remaining life are the same as for Girder B, the nominal fatigue resistance of a single connector is also the same ($(\Delta F)_n = 17.5\ ksi$).

Figure D-20 shows the results from the fatigue analysis, conducted in the same way as for Girder B, which explicitly considers the interface slip and uses a stiffness of 900 kips per inch for the linear springs that represent each shear connector. The figure plots the stress range in each connector induced by the fatigue loading defined in the Fatigue II load combination in the LRFD specifications. Because of symmetry, only one-half of the girder is shown.

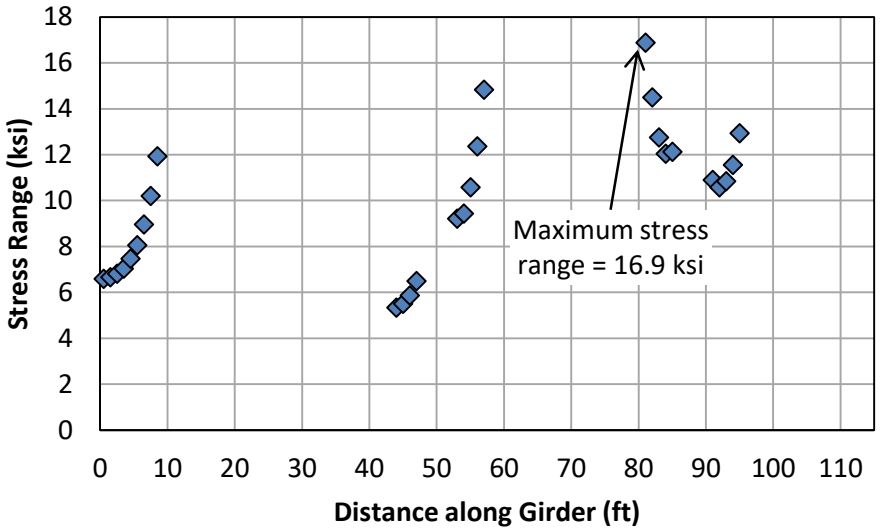

Figure D-20: Results from Fatigue Analysis for Girder D

The maximum stress range (ΔF) that a connector undergoes during fatigue loading is 16.9 ksi. As shown in the figure, this critical connector is the closest connector to the interior support in the interior span. This maximum stress range is less than the nominal fatigue resistance (17.5 ksi), indicating that ***the connectors have adequate fatigue life to satisfy the design requirement of a 25-year remaining life***. By reversing the design equations, ***the connectors in Girder D are estimated to have a remaining fatigue life of 32 years***.

D.5.7 Conduct Load Rating of Strengthened Girder

A load rating of the strengthened girder is carried out in the same manner as for Girder B. The results of this load rating are summarized in Table D-22. After post-installing the shear connectors and considering moment redistribution, the ***inventory load factor rating of Girder C is increased from HS 15.8 to HS 22.9***. This load rating is controlled by the section near the middle of the exterior spans at the Overload limit state.

Table D-22: Load Rating Results of Strengthened Girder D

Location (ft)	Section Type	Inventory Load Factor Rating	
		Overload	Maximum Load
14.5	Critical, Transition	HS 26.0	HS 32.7
28	Critical, Span	HS 22.9	HS 30.0
44.5	Critical, Transition	HS 28.7	HS 34.1
57.5	Critical, Transition	HS 23.6	HS 27.1
63.5	Critical, Transition	HS 47.3	HS 32.3
70	Critical, Pier	HS 35.9	HS 23.1
76	Critical, Transition	HS 45.5	HS 30.9
80.5	Critical, Transition	HS 24.7	HS 29.0
96.5	Critical, Transition	HS 27.8	HS 34.2
115	Critical, Span	HS 28.1	HS 32.8

D.5.8 Summary of Design for Girder D

To strengthen Girder D to a minimum inventory load factor rating of HS 20, ***a total of 112 adhesive anchor shear connectors should be post-installed***. While moment

redistribution does need to be considered, ***no actual moments need to be redistributed at either the Overload or Maximum Load limit state***. However, ***additional lateral bracing must be provided to the girder at or near the interior piers*** to reduce the unbraced length to satisfy the requirements of Appendix B6 of the LRFD specifications.

The connectors are installed in pairs on opposite sides of the web of the steel beam through a cross section, as illustrated in Figure D-10. They are grouped in six locations, with one group located near each end of the positive moment regions in all three spans. The specific connector layout is shown in Figure D-19. This layout can be modified slightly due to constraints in the field during installation, such as transverse deck reinforcing bars or other obstacles.

After post-installing the shear connectors and considering moment redistribution, the ***inventory load factor rating of Girder D is increased from HS 15.8 to HS 22.9***. This load rating is controlled in the strengthened bridge by the section near the middle of the exterior spans at the Overload limit state.

D.6 SUMMARY OF DESIGN FOR ALL GIRDERS

The results of the design are summarized in Figure D-21. A total of 372 post-installed adhesive anchor shear connectors are required to satisfy both strength and fatigue requirements for the entire steel unit of this bridge. Only small amounts of moment redistribution, not exceeding 5% of the factored design moment, is required from the interior pier sections for this bridge. The controlling inventory load factor rating for the girders in the strengthened bridge is HS 20.0, occurring at the interior pier sections of Girder B. This is an increase of nearly 75% over the HS 11.5 rating of the existing non-composite steel girder unit.

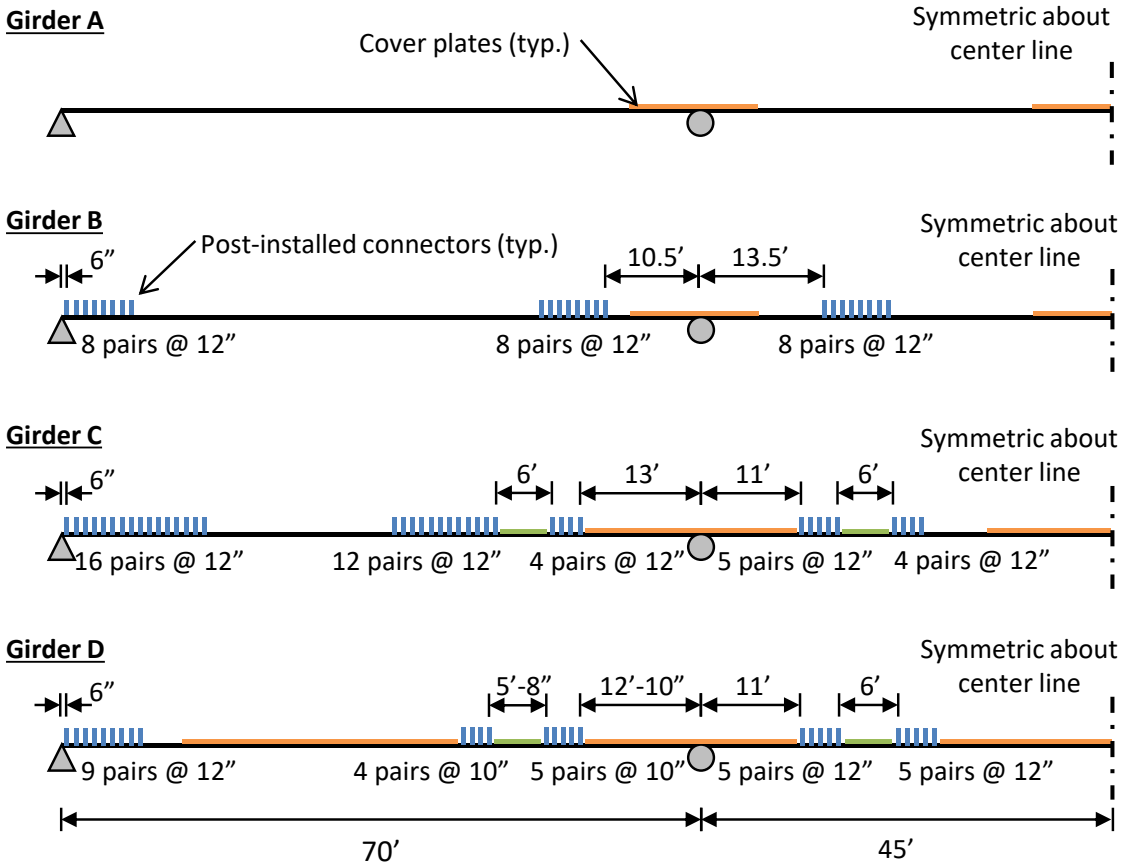

Figure D-21: Summary of Design for All Girders

The post-installed shear connectors satisfy the remaining fatigue life requirement of at least 25 years. Unlike conventional shear stud design, the fatigue demands did not control the design of these post-installed shear connectors. The maximum stress range expected to be experienced by any connector along the bridge corresponds to an actual predicted remaining fatigue life of 32 years. Note that the connectors are concentrated in groups near the ends of the positive moment regions in each span. This has been shown to improve the ductility of partially composite girders and to reduce the maximum demand on connectors under elastic levels of load (Kwon et al. 2007, Ghiami Azad 2016).

For strength purposes, the number of shear connectors required in each span was generally controlled by the minimum recommended composite ratio of 0.3. This is a practical limit which is often suggested by various design guidelines to ensure that both the steel beam and the shear connectors behave elastically under service-level loads and that significant ductility is provided beyond the ultimate strength (AISC 2010). Most of the

load ratings in positive bending exceed the HS 20 requirement because of this minimum composite ratio. The exception to this is the exterior spans of Girder C, which requires a composite ratio of 0.66 to reach a load rating of just greater than HS 20.

Because moment redistribution is required at the interior pier sections of Girders B, C, and D, particular requirements outlined in Appendix B6 of the *LRFD Bridge Design Specifications* must be fulfilled to allow the steel section to undergo plastic rotation required for moment redistribution, without premature local or lateral-torsional buckling (AASHTO 2010). Additional cross frames need to be added around the interior piers. Details and suggestions for locating these additional cross frames are provided in the design calculations in the Appendix. A double-sided bearing stiffener must also be installed at the interior pier of Girder B. Bearing stiffeners are already present at the interior pier sections of Girders C and D.

References

AASHTO 1973, *Standard Specifications for Highway Bridges*, 11th edition, American Association of State Highway Officials, Washington, DC.

AASHTO 1986, *Guide Specifications for Alternate Load Factor Design Procedures for Steel Beam Bridges Using Braced Compact Sections*, 1st edition, American Association of State Highway and Transportation Officials, Washington, DC.

AASHTO 1994, *AASHTO LRFD Bridge Design Specifications*, 1st edition, American Association of State Highway and Transportation Officials, Washington, DC.

AASHTO 2002, *Standard Specifications for Highway Bridges*, 17th edition, American Association of State Highway Officials, Washington, DC.

AASHTO 2004, *AASHTO LRFD Bridge Design Specifications*, 3rd edition, American Association of State Highway and Transportation Officials, Washington, DC.

AASHTO 2010, *AASHTO LRFD Bridge Design Specifications*, 5th edition, American Association of State Highway and Transportation Officials, Washington, DC.

AASHTO 2011, *The Manual for Bridge Evaluation*, 2nd edition, American Association of State Highway and Transportation Officials, Washington, DC.

AISC 2010, *Commentary on the Specification for Structural Steel Buildings*, American Institute of Steel Construction, Chicago, Illinois.

ANSYS 2012, *ANSYS (software)*, ANSYS, Inc., Version 14.5, Canonsburg, PA.

ASCE-WRC 1971, *Plastic Design in Steel: A Guide and Commentary*, 2nd edition, American Society of Civil Engineers and the Welding Research Council, New York, New York.

Barth, KE, Hartnagel, BA, White, DW & Barker, MG 2004, 'Recommended Procedures for Simplified Inelastic Design of Steel I-Girder Bridges', *Journal of Bridge Engineering*, vol. 9, no. 3, pp. 230-242.

Bergson, PM 1994, *Shakedown and Ultimate Load Tests of a One-Third Scale Three-Span Composite Bridge*, MS Thesis, University of Minnesota, Minneapolis, Minnesota.

Bleich, H 1932, 'Über die bemessung statisch unbestimmter stahltragwerke unter berücksichtigung des elastisch-plastischen verhaltens des baustoffes (The design of statically indeterminate steel frames considering the elastic-plastic behavior of the material)', *Bauingenieur*, vol. 13, pp. 261-267.

Buckby, R, Johnson, RP, Ogle, M & Harvey, D 1997, 'The Performance of Coiled Spring Pin Connectors under Static and Fatigue Loading', *Conference Report: Composite Construction – Conventional and Innovative*, Innsbruck, Austria.

Carskadden PS 1980, *Autostress Design of Highway Bridges, Phase 3: Interior-Support Model Test*, Technical Report, United States Steel Corporation Research Laboratory, American Iron and Steel Institute (AISI) Project No. 188.

Chapman, JC & Balakrishnan, S 1964, 'Experiments on Composite Beams', *The Structural Engineer*, vol. 42, no. 11, pp. 369-383.

CSI 2011, *SAP2000 (software)*, Computers and Structures, Inc., Version 15, Walnut Creek, CA.

Culver, C & Coston, R 1961, 'Tests of Composite Beams with Stud Shear Connectors', *Journal of the Structural Division, Proceedings of the American Society of Civil Engineers*, vol. 87, no. ST1, pp. 1-17.

Dionne, G, Picard, A, & Beaulieu, D 1997, 'Development of Composite Action in Existing Non-Composite Bridges', *Conference Report: Composite Construction – Conventional and Innovative*, Innsbruck, Austria.

Eyre, DG & Galambos, TV 1970 , 'Shakedown Tests on Steel Bars and Beams', *Journal of the Structural Division, Proceedings of the American Society of Civil Engineers*, vol. 96, no. ST7, pp. 1287-1304.

Flemming, DJ 1994, *Experimental Verification of Shakedown Loads for Composite Bridges*, PhD Thesis, University of Minnesota, Minneapolis, Minnesota.

Fukumoto, Y & Yoshida, H 1969, 'Deflection Stability of Beams Under Repeated Loads', *Journal of the Structural Division, American Society of Civil Engineers*, vol. 95, no. ST7, pp.1443-1458.

Ghiami Azad, AR 2016, *Fatigue Behavior of Post-Installed Shear Connectors used to Strengthen Continuous Non-Composite Steel Bridge Girders*, PhD Dissertation, The University of Texas at Austin, Austin, Texas.

Gozum, AT 1954, *Experimental "Shakedown" of Continuous Steel Beams*, Research report no. 205G.1, Fritz Engineering Laboratory, Lehigh University, Bethlehem, Pennsylvania.

Grant Jr., JA, Fisher, JW, & Slutter, RG 1977, 'Composite Beams with Formed Steel Deck', *AISC Engineering Journal*, vol. 14, no. 1, pp. 24-43.

Grubb, MA & Carskaddan, PS 1979, *Autostress Design of Highway Bridges, Phase 3: Initial Moment-Rotation Tests*, Research Report 97-H-045(019-4), American Iron and Steel Institute (AISI), Project 188.

Grubb, MA & Carskaddan, PS 1981, *Autostress Design of Highway Bridges, Phase 3: Moment-Rotation Requirements*, Research Report 97-H-045(018-1), American Iron and Steel Institute (AISI), Project 188.

Grüning, M 1926, Die Tragfähigkeit statisch unbestimmter Tragwerke aus Stahl bei beliebig häufig wiederholter Belastung (The carrying capacity of statically indeterminate steel frames subjected to arbitrarily repeated loading), Julius Springer, Berlin, Germany.

Hansell, WG & Viest, IM 1971, 'Load Factor Design for Steel Highway Bridges', *AISC Engineering Journal*, vol. 8, no. 4, pp. 113-123.

Hartnagel, BA 1997, *Inelastic Design and Experimental Testing of Compact and Noncompact Steel Girder Bridges*, PhD Dissertation, University of Missouri-Columbia, Columbia, Missouri.

Hungerford, BE 2004, *Methods to Develop Composite Action in Non- Composite Bridge Floor Systems: Part II*, MS Thesis, University of Texas at Austin, Austin, Texas.

Kayir, H 2006, *Methods to Develop Composite Action in Non-Composite Bridge Floor Systems: Fatigue Behavior of Post-Installed Shear Connectors*, MS Thesis, University of Texas at Austin, Austin, Texas.

Klaiber, FW, Dedic, DJ, Dunker, KF & Sanders Jr., WW 1983, *Strengthening of Existing Single Span Steel Beam and Concrete Deck Bridges*, Engineering Research Institute, Iowa State University, Ames, Iowa.

Klöppel, K 1936, 'Contribution to the Question of Utilising Plasticity in Continuous Girders Subject to Repeated Stresses', *Second Congress Report of the International Association for Bridge and Structural Engineering*, pp. 77-81.

Kreitman, K, Ghiami Azad, AR, Patel, H, Engelhardt, M, Helwig, T, Williamson, E & Klingner, R 2015, *Strengthening Existing Continuous Non-Composite Steel Girder Bridges Using Post-Installed Shear Connectors*, Research report no. 0-6719-1, Center for Transportation Research, Austin, Texas.

Kreitman, K, Ghiami Azad, AR, Engelhardt, MD, Helwig, TA & Williamson, EB 2016 (expected), *Implementation Project: Strengthen Continuous Steel Girder Bridge with Post-Installed Shear Connectors, Phase I – Bridge Strengthening Design and Load Testing*, Research report no. 5-6719-1, Center for Transportation Research, Austin, Texas.

Kwon, G 2008, *Strengthening Existing Steel Bridge Girders by the Use of Post-Installed Shear Connectors*, PhD Dissertation, University of Texas at Austin, Austin, Texas.

Kwon, G, Engelhardt, M & Klingner, R 2009, *Implementation Project: Strengthening of a Bridge near Hondo, Texas using Post-Installed Shear Connectors*, Research report no. 5-4124-01-1, Center for Transportation Research, Austin, Texas.

Kwon, G, Hungerford, B, Kayir, H, Schaap, B, Ju, YK, Klingner, R & Engelhardt, M 2007, *Strengthening Existing Non-Composite Steel Bridge Girders Using Post-Installed Shear Connectors*, Research report no. 0-4124-1, Center for Transportation Research, Austin, Texas.

MathWorks 2015, *MATLAB (software)*, The MathWorks, Inc., Version R2015b, Natick, MA.

Massonnet, C 1953, 'Essais d'adaptation et de stabilization plastiques sur des poutrelles laminees (Plastic collapse and shake-down tests on small rolled beams)', *Publications of the International Association for Bridge and Structural Engineering*, vol. 13, pp. 239-282.

Melan, E 1936, 'Theorie statisch unbestimmter systeme aus ideal plastischen baustoff (The theory of statically indeterminate systems made of ideally plastic material)', *Sitzungsberichte der Akademie der Wissenschaften*, vol. 2a, no. 145, pp. 195-218.

Mertz, DR 2004, 'Service Limit State Control of Permanent Deflection for Steel Sections in Flexure', *Structures Congress 2000: Advanced Technology in Structural Engineering*, May 2000, Philadelphia, PA.

Moore, M & Grubb, MA 1990, 'Behavior of a Two-Span Continuous Plate Girder Bridge Designed by the Alternate Load Factor Method', *AISC Engineering Journal*, vol. 27, no. 4, pp. 132-149.

National Cooperative Highway Research Program (NCHRP) 2012, *Fatigue Evaluation of Steel Bridges*, Report 721, Transportation Research Board, Washington, DC.

Neal, BG 1977, *The Plastic Methods of Structural Analysis*, 3rd (S.I.) edition, Chapman and Hall, New York, New York.

Newmark, NM, Seiss, CO & Veist, IM 1951, 'Tests and analysis of composite beams with incomplete interactions,' *Proceedings of the Society for Experimental Stress Analysis*, vol. 4, no. 1, pp. 75-92.

Oehlers, DJ & Bradford, MA 1995, *Composite Steel and Concrete Structural Members: Fundamental Behavior*, 1st edition, Elsevier Science Inc., Tarrytown, New York.

Patel, HV 2013, *Strengthening of Noncomposite Steel Girder Bridges with Post-Installed Shear Connectors: Fatigue Behavior of the Adhesive Anchor*, MS Thesis, University of Texas at Austin, Austin, Texas.

PennDOT 2010, *BAR7 Bridge Analysis and Rating (software)*, Version 7.13.0.0, Commonwealth of Pennsylvania Department of Transportation.

Proctor, MH 1963, *Analytical and Experimental Study of Lightweight Concrete-Steel Composite Beams*, MS Thesis, University of Missouri, Columbia, Missouri.

RISA 2002, *RISA-2D Educational (software)*, RISA Technologies, Version 1.0, Foothill Ranch, CA.

Roeder, CW & Eltvik, L 1985, 'An Experimental Evaluation of Autostress Design,' *Transportation Research Record*, vol. 1044, pp. 35-42.

Schaap, BA 2004, Methods to Develop Composite Action in Non-Composite Bridge Floor Systems: Part I, MS Thesis, University of Texas at Austin, Austin, Texas.

Seracino, R, Lee, CT, Lim, TC & Lim JY 2004, 'Partial Interaction Stresses in Continuous Composite Beams under Serviceability Loads', *Journal of Constructional Steel Research*, vol. 60, no. 10, pp. 1525-1543.

Seracino, R, Lee, CT & Tan Z 2006, 'Partial Interaction Shear Flow Forces in Continuous Composite Steel-Concrete Beams', *Journal of Structural Engineering*, vol. 132, no. 2, pp. 227-236.

Sherbourne, AN 1963, 'Some Preliminary Experiments on the Behavior of Ductile Structures Under Repeated Loads', *Experimental Mechanics*, vol. 3, no. 5, pp. 119-128.

Slutter, RG & Driscoll Jr., GC 1963, *The Flexural Strength of Steel and Concrete Composite Beams*, Paper 549, Fritz Laboratory Reports, Lehigh University, Bethlehem, Pennsylvania.

Texas Highway Department (THD) 1951, *Standard Specifications for Road and Bridge Construction*, Texas Highway Department.

Thirugnanasundralingam, K 1991, *Continuous Composite Beams under Moving Loads*, PhD Dissertation, Monash University, Victoria, Australia.

von Mises, R 1913, 'Mechanik der festen Körper im plastisch deformaglen Zustand (Mechanics of solid bodies in the plastically-deformable state)', *Nachrichten von der Akademie der Wissenschaften in Göttingen, Math-Physics Klasse*, vol. 1, pp. 582-592.

Weber, DC 1994, *Experimental Verification of Inelastic Load and Resistance Factor Design Limits*, MS Thesis, University of Missouri-Columbia, Columbia, Missouri.

Vita

Kerry Lynn Kreitman is from Houston, Texas. After graduating from Cypress Falls High School, she attended Washington University in St. Louis, where she earned a Bachelor of Science in Civil Engineering and played varsity softball for four years. Kerry then returned to her home state to enroll at the University of Texas at Austin, where she worked as a research assistant at the Phil M. Ferguson Structural Engineering Laboratory. She received both a Master of Science and a Doctor of Philosophy in Civil Engineering. After completing her academic studies, she will continue on to a career in structural forensics and engineering.

Permanent email address: kerry.kreitman@utexas.edu

This dissertation was typed by the author.